



HAL
open science

Magnetic field in laser plasmas: non-local electron transport and reconnection

Raphaël Riquier

► **To cite this version:**

Raphaël Riquier. Magnetic field in laser plasmas: non-local electron transport and reconnection. Plasma Physics [physics.plasm-ph]. Université Paris Saclay (COMUE), 2016. English. NNT: 2016SACLX004. tel-01355188

HAL Id: tel-01355188

<https://pastel.hal.science/tel-01355188>

Submitted on 22 Aug 2016

HAL is a multi-disciplinary open access archive for the deposit and dissemination of scientific research documents, whether they are published or not. The documents may come from teaching and research institutions in France or abroad, or from public or private research centers.

L'archive ouverte pluridisciplinaire **HAL**, est destinée au dépôt et à la diffusion de documents scientifiques de niveau recherche, publiés ou non, émanant des établissements d'enseignement et de recherche français ou étrangers, des laboratoires publics ou privés.

NNT : 2016SACLX004

THÈSE DE DOCTORAT
DE
L'UNIVERSITÉ PARIS-SACLAY
PRÉPARÉE À
L'ÉCOLE POLYTECHNIQUE

ÉCOLE DOCTORALE N°572
Ondes et matières

Spécialité de doctorat : Physique des plasmas

Par

M. Raphaël RIQUIER

Magnetic field in laser plasmas:
non-local electron transport and reconnection

Thèse présentée et soutenue à Palaiseau, le 28 Janvier 2016 :

Composition du Jury :

M. Jean-Marcel RAX	Professeur, École Polytechnique	Président du Jury
M. Stephano ATZENI	Professeur, Università di Roma, La Sapienza	Rapporteur
M. Robert CAUBLE	Directeur de JLF, LLNL	Rapporteur
M. Xavier RIBEYRE	Ingénieur-chercheur, CEA	Examineur
M. Roch SMETS	Maître de conférence, UPMC	Examineur
M. Julien FUCHS	Directeur de recherche, CNRS	Directeur de thèse
M. Alain GRISOLLET	Ingénieur-chercheur, CEA	Encadrant

Contents

Notations	1
Introduction	3
1 Modeling the heat flux in hydro-radiative simulations	13
1.1 FCI2: A Resistive MHD hydro-radiative code (and more)	14
1.1.1 The physics included in FCI2	14
1.1.2 Hydrodynamics of a solid foil irradiated by a nanosecond laser pulse	16
1.2 The limited Spitzer-Härm heat flux	18
1.2.1 Kinetic equation	19
1.2.2 P1 system (isotropisation)	20
1.2.3 The Spitzer-Härm heat flux (Maxwellianisation)	22
1.2.4 Limited heat flux	23
1.3 The Braginskii heat flux	25
1.3.1 Linear transport	25
1.3.2 Braginskii's notation	26
1.3.3 The Righi-Leduc effect	28
1.4 The magneto-hydrodynamic framework	28
1.4.1 Momentum equation, the Laplace (Lorentz) force	29
1.4.2 Energy equation	30
1.4.3 Ohm's law and B-field induction equation	31
1.4.4 Nernst effect	32
1.5 Modeling the non-local heat flux in FCI2	34
1.5.1 Presentation of the model	37
1.5.2 B-field – Heat flux coupling strategies	42
1.5.3 Comparison with a Fokker-Planck code: ALADIN	44
1.6 Conclusions	54
1.7 Useful equations	58
2 Experiments	61
2.1 Single laser beam experiments	64
2.1.1 LULI2000 (2008)	65
2.1.2 JLF-Titan (2011)	67

2.2	Comparison integrated measurements – post-processors	69
2.2.1	Interferometry	70
2.2.2	Polarimetry	78
2.2.3	X-ray pinhole	82
2.2.4	Proton-Radiography	84
2.3	Comparison of the heat flux models with the LULI2000 experiment.	100
2.4	Conclusions	105
3	Analysis using FCI2	107
3.1	Magnetic field topology	109
3.1.1	Topology of the magnetic field	109
3.1.2	Source and confinement of the magnetic field	111
3.1.3	Transport regimes	114
3.2	Parametric study of the laser parameters	116
3.2.1	Reference and high energy cases	116
3.2.2	Focal spot : Flat-top and high intensity cases	117
3.2.3	Laser wavelength : 3ω case	118
3.3	Effects of the magnetic field on the interaction	120
3.3.1	Effects on the heat flux	121
3.3.2	Effects on the hydrodynamics	126
3.3.3	Energy balance	131
3.4	Extrapolation to ICF conditions	134
3.4.1	Driving laser : LMJ or NIF quad	134
3.4.2	Full scale ICF experiment	135
3.5	Conclusions	137
4	Reconnection of the magnetic field in high energy density plasmas	139
4.1	State of the art of magnetic reconnection	142
4.1.1	The Sweet-Parker model	143
4.1.2	The magnetic field reconnection in various plasma physics contexts	146
4.1.3	Experimental platforms for the study of reconnection	149
4.2	Motivation for the experiments : study using HECKLE	154
4.2.1	Different methods to simulate the reconnection	154
4.2.2	Hall component of the magnetic field	156
4.2.3	Effects of an angle between the irradiation spots	157
4.3	Reconnection experiments using laser driven plasmas	161
4.3.1	Phelix	161
4.3.2	LULI2000	164
4.3.3	Interpretation of the results	171
4.3.4	LMJ-Petal	176

4.4 Conclusions	178
Conclusion	181
Bibliography	185
List of Figures	198
Role of the author	199
List of publications and presentations	201

Notations

Notation	Description
N_e	electron density
N_c	critical density
$T_{e,i}$	electron (resp. ion) temperature
D_t	Lagrangian derivative $\frac{\partial}{\partial t} + (u \cdot \nabla)$
ρ	mass density
\mathbf{u}	fluid velocity
$P_{e,i}$	electron (resp. ion) pressure
P_{mag}	magnetic pressure
\mathbf{Q}	heat flux
$\mathcal{E}_{e,i}$	electron (resp. ion) internal energy
$\nu_{ei,ee}$	electron-ion (resp. electron-electron) collision frequency
\mathbf{j}	electron current density
\mathbf{v}	electron velocity
e	elementary charge
$m_{e,i}$	electron (resp. ion) mass
Z	atomic number
c	speed of light
f	electron distribution function
f_0	scalar distribution function
\mathbf{f}_1	vectorial distribution function
f_0^m	Maxwellian distribution function
h	correction to the scalar Maxwellian
\mathbf{y}	correction to the vectorial Maxwellian
\mathbf{E}	electric field
\mathbf{B}	magnetic field
\mathbf{b}	magnetic field's direction
K_{SH}	Spitzer-Härm diffusion coefficient
$C_{0,1}$	collisional operators
$E(v), D(v)$	Rosenbluth coefficients
$\bar{\alpha}, \bar{\beta}, \bar{\kappa}$	Braginskii's coefficients

Notation	Description
χ	thermal electron magnetization (Hall parameter)
χ_v	velocity dependant electron magnetization (Hall parameter)
β_{th}	thermal beta parameter P/P_{mag}
β_{kin}	kinetic beta parameter $\rho u^2/2P_{mag}$
σ	electric conductivity
η	electric resistivity
$\lambda_{ei,ee}$	electron-ion (resp. electron-electron) collision mean free path
d_E	electron stopping length in an electric field
I	laser intensity
λ_L	Laser wavelength
$\Delta\phi$	Phase difference
N	Optical index
$\omega_{pe,i}$	electron(resp. ion) plasma frequency
$\omega_{ce,i}$	electron (resp. ion) cyclotron frequency
R_L	Larmor radius
M_a	Mach number
K_n	Knudsen number
R_e	Reynolds number
R_m	magnetic Reynolds number
V_A	Alfvén velocity
S	Lundquist number
E_p	proton energy (proton radiography)

Introduction

Basics of inertial confinement fusion

The principle of inertial confinement fusion (ICF) [1] is to maintain a dense fuel, composed of low mass number nuclei, in a compressed state for a time long enough, such that fusion reactions consume the fuel before it disassembles due to its own pressure. Since the reaction rates depend on the cross-sections between the two fusing ion species, most of the efforts are currently toward the fusion of deuterium ($D = {}^2H$) and tritium ($T = {}^3H$) as they present the best cross section $\langle\sigma v\rangle_{DT}$ in an accessible range of temperature. The first is an abundant isotope of hydrogen, mostly found in water, while tritium can be produced from lithium irradiated by neutrons, themselves produced by the D-T reaction: $D + T \rightarrow {}^4He(3.5MeV) + n(14.1MeV)$. The goals of ICF are multiple:

- From a societal point of view, it could be a source of energy, if the repetition rate and gain G are high enough to compensate for the efficiency η_D of the energy driver (an array of nanosecond lasers in the most common approach), the thermal to electrical power conversion efficiency η_{th} and the fraction f of the output power used to run the driver. Then, with $f = 0.25$, $\eta_D = 0.1$ and $\eta_{th} = 0.4$, and because of the relation $Gf\eta_D\eta_{th} = 1$, this leads to a required Gain $G > 100$ for ICF to be an efficient power source.
- From a scientific point of view, achieving high gains, in accordance with numerical simulations, is the proof of a good understanding of the many physical processes at play and their modeling. Moreover, investigating the physics at play and the properties of matter in such a state of high energy density is of interest for many branches of science, such as laboratory astrophysics [2, 3]. Finally, the research on high gain ICF experiments is a drive for technological progress, yielding applications in various fields (material processing, laser technologies *etc.*)

The feasibility of a self-sustained heating through nuclear reactions is characterized by the Lawson criteria, $n\tau_c$, which represents the required conditions on the confinement. For example, in a tokamak the plasma's density n is small ($\sim 10^{15} \text{ cm}^{-3}$) but the confinement time τ_c is long ($> 1 \text{ s}$) [4], while in ICF τ_c is short ($< 100 \text{ ps}$) but n is large ($10^{24} - 10^{26} \text{ cm}^{-3}$). In fact, in ICF, rather than a confinement time, τ_c represents the time taken by the fusing fuel to disassemble due to its high pressure and its inertia.

Let us consider a sphere of high pressure fuel of homogeneous density ρ and radius R . The confinement time can be estimated as the time required for a rarefaction wave, traveling at the sound velocity C_s , to reach the center [5]. Let $\tau_c(r') = (R - r')/C_s$ be the time at which the fuel at r' starts its outward motion. The global confinement time is found by mass averaging over the entire sphere:

$$\tau_c = \frac{\int_0^R \rho 4\pi r'^2 [(R - r')/C_s] dr'}{\rho (4/3) \pi R^3} = R/4C_s. \quad (0.1)$$

To estimate the fraction f_b of the fuel which is burned before the sphere disassembles, let first denote n_D and n_T the number density of deuterium and tritium. The rate at which the deuterium or tritium are burned is then:

$$dn_{D,T}/dt = -n_D n_T \langle \sigma v \rangle_{DT},$$

or considering $n_D = n_T = n/2$ with n the total fuel number density:

$$dn/dt = - (n^2/2) \langle \sigma v \rangle_{DT}.$$

Once integrated over τ_c , we have:

$$1/n - 1/n_0 = (\tau_c/2) \langle \sigma v \rangle_{DT}.$$

Considering the burned fraction $f_b = 1 - (n/n_0)$, $\tau_c = R/4C_s$ (Eq.0.1) and $n_0 = \rho/m_{DT}$ the initial fuel density, where $m_{DT} = 2.5 [amu]$ leads to:

$$f_b = \rho R / [\rho R + \beta(T)], \quad \text{with } \beta(T) = 8m_{DT}C_s / \langle \sigma v \rangle_{DT}. \quad (0.2)$$

In typical burn conditions, a burned fraction of 1/3 requires a fuel surface density $\rho R = 3 g/cm^2$, or for an uncompressed DT fuel ($\rho = 0.21 g/cm^3$), a mass of 2.6 kg. Yet, the problem is that with 17.6 MeV released per fusion reaction, the total energy output is $2.9 \times 10^{14} J$, *i.e.* 70 kt of TNT, which is commonly admitted to be too much for a laboratory experiment.

If we want a lower output, we have to compress the target so that the mass is reduced but keeping ρR constant. For example, compressing the target to $190 g/cm^3$ gives a mass of 5 mg, for a yield of 500 MJ.

Indirect drive ICF

In laser driven ICF, the best way to achieve a high compression is through a spherical implosion, as the density will scale as R^3 . Yet, as we ultimately want to heat the fuel using the accumulated kinetic pressure, an initially homogeneous solid sphere of fuel is no more possible. Instead of that, the fuel is formed of a plastic capsule filled with the D-T, which, once cooled down to a few Kelvin, forms a layer of *ice* inside the capsule enclosing a low density gas. The *in-flight aspect ratio* ($IFAR = R/\Delta R$) is then a compromise between a thin capsule converging at high velocity and a thick capsule resilient to hydrodynamic instabilities.

The mechanism to accelerate the target is the *rocket effect*: the outer plastic layer of the pellet is quickly heated, becoming a high pressure plasma which expands outward at high velocity and thus pushes the remaining capsule inward, just like a rocket for which the exhaust gases accelerate the payload (cryogenic D-T in ICF) as well as the remaining fuel (the plastic *ablator*).

Upon reaching convergence, the kinetic energy of the D-T fuel accumulated by the $P \cdot dV$ work is converted into internal energy, heating a point of the low density fuel to a high temperature, initiating nuclear fusion reactions. The electronic conduction and the α particles produced by the fusion reactions then ablate the inner face of the solid fuel, forming a *hot-spot* of increasing mass. Fig.0.1(top) shows the different transport processes at play in this *hot-spot*. Knowing that the temperature has to stay high enough to maintain the fusion reactions, it is clear that to keep this *deflagration* (reaction-

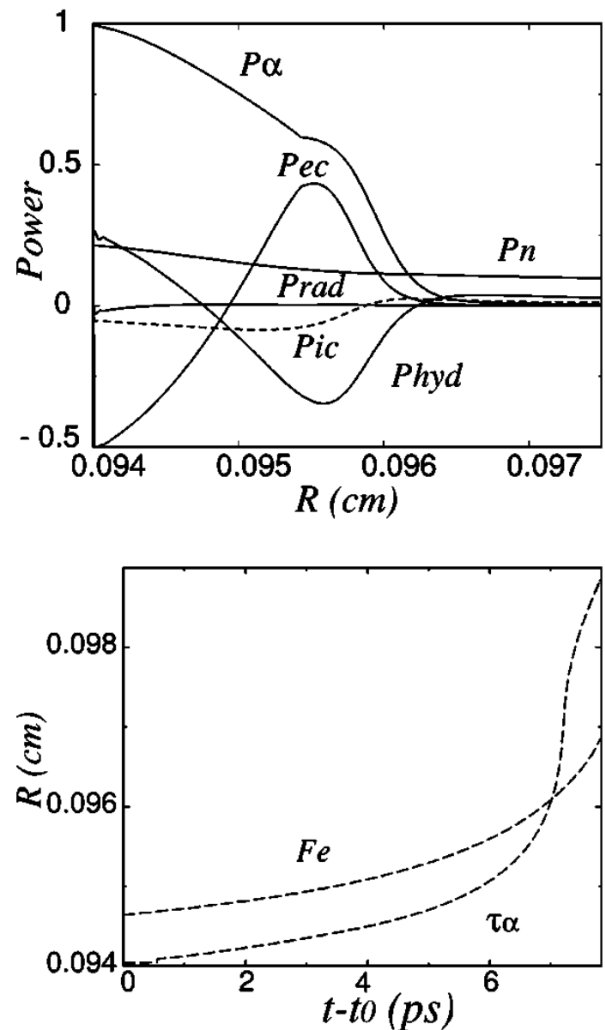


Figure 0.1: (Top) Specific energy variation in the hot-spot as a function of space. P_α , P_{rad} , P_{hyd} , P_{ec} , P_{ic} and P_n refer to the contribution of the α particles, radiations, hydrodynamic, electronic conduction, ion conduction and neutrons.

(Bottom) Position of the maximum reaction rate τ_α and electronic flux F_e . From [6].

diffusion) ongoing, the α -heating has to overcome the cooling of the hot-spot by electron conduction. Note that at some point, volumic heating of the dense D-T fuel by the neutrons reduces the stopping power of the suprathemal ions so much, that they heat the shell deeper than the electronic ablation front (see Fig.0.1,bottom), leading to a supersonic reaction wave and thus a transition from the *deflagration* into a *detonation* (reaction-compression) [6].

As we saw, the principle of ICF is based on the very quick deposition of energy on the target, to compress it using the *rocket effect*. Different methods have been envisioned to do so, but currently, the use of lasers is the most realistic way. Two schemes are heavily studied: the direct drive and the indirect one. In the first case the lasers are directly irradiating the target, depositing energy at the critical electronic density ($N_c = 8.9 \times 10^{21} \text{ cm}^{-3}$ for a laser with a wavelength of $0.351 \mu\text{m}$). On the opposite, in the indirect drive scheme, the capsule is placed in a high Z cavity also called *hohlraum* which acts like a x-ray oven: the lasers heat the inner face of the cavity's walls, converting the laser light to soft x-rays [7]. These x-rays are then rapidly absorbed and re-emitted, producing a pseudo *black body* heating the target with a much better homogeneity than in the direct drive scheme.

To illustrate this particular set-up, a 2D simulation of an indirect drive experiment, using the FCI2 code², is presented in Fig.0.2. Looking clockwise: the mass density map (upper left) shows the capsule which outside is being ablated. It is placed in a rugby shaped [8] gold cavity, filled with a gas to prevent the gold plasma ablated by the lasers (upper right) to reach the capsule: this color-map of absorbed laser power density also puts into light the interface between the gold and the gas, as well as the electronic ablation front (supposed close to the critical density where the laser radiation cannot propagate). The laser energy is then converted to x-rays trapped in the enclosure (lower right), producing a very homogeneous radiative flux which drives the capsule. Finally, the kinetic energy density map (lower left) shows, from the center to the outside: the capsule accelerating inward by the radiatively ablated plastic and the steady electronic ablation front. Note that most of the kinetic energy is located in the imploding capsule.

Self-generated magnetic fields in ICF

Up to now, four years of full scale experiments on the National Ignition Facility (NIF) have remained unsuccessful in terms of overall gain [9], proving that something (either technical or physical) is missing in the modeling, since a gain of more than 10 MJ was

¹Reducing the laser wavelength from first ($1.053 \mu\text{m}$) to third ($0.351 \mu\text{m}$) harmonic allows for a laser absorption at a higher density, and thus a better absorption (and better conversion into x-rays for indirect drive).

²FCI2 is a 2D hydro-radiative code, developed at CEA for the design and interpretation of laser-plasma and ICF experiments. See sec. 1.1.

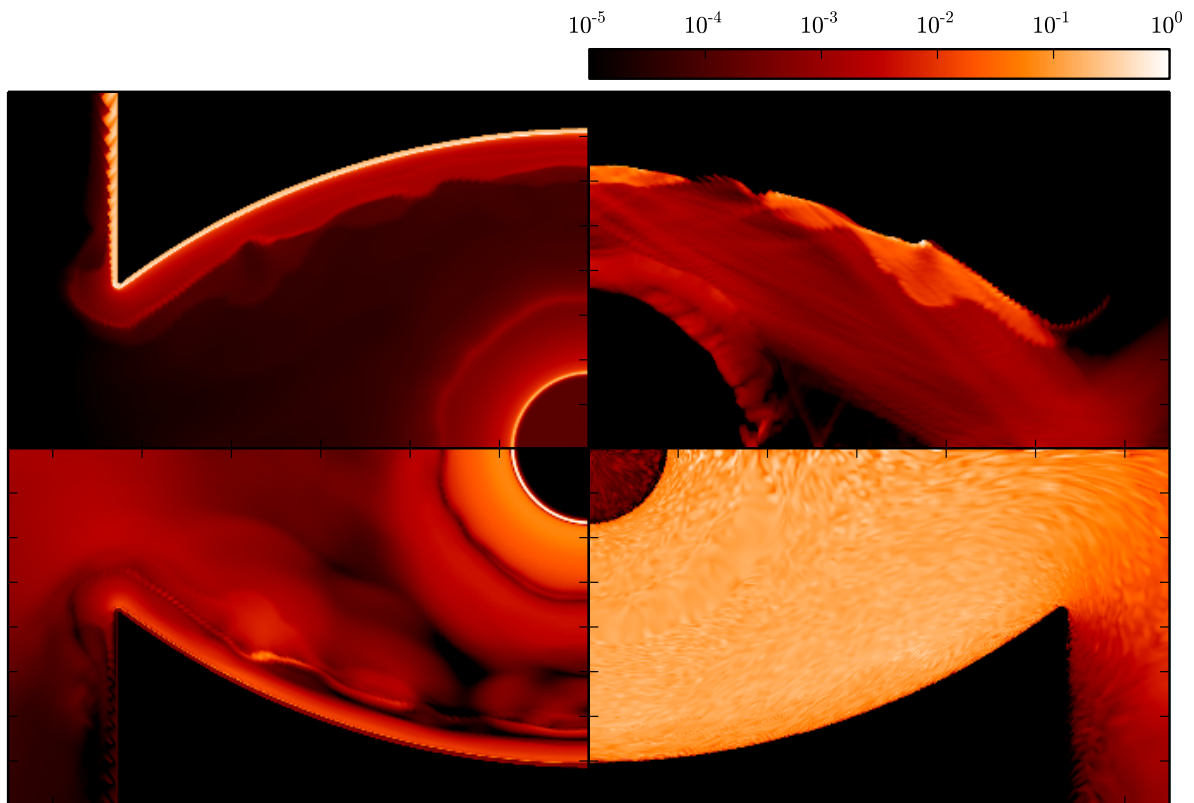


Figure 0.2: *2D axi-symmetrical FCI2 simulation of a full scale ICF experiment in indirect drive. (All quantities are shown in log scale, normalized to their maximum)*
Top Left: mass density.
Top Right : absorbed laser power density
Lower Left: kinetic energy density.
Lower Right: radiative energy density.

predicted [10] based on LASNEX simulations [11]. For the “technical” issues, heavy 3D simulations of capsule implosions [12] have pointed out that geometric effects (the surface roughness of the capsule, the tent holding it, the tube filling the capsule with D-T, etc) drastically deteriorate the implosion. This thesis is part of another approach, namely the study of physical phenomena, supposed to have little effects on the overall interaction and thus previously neglected.

When the lasers irradiate the inner wall of the cavity, the expanding gold plasma self-generates magnetic field loops of the order of the MegaGauss ($1\text{ MG} = 100\text{ T}$) around the irradiation spots, due to thermo-electric effects [13] *i.e.* the non-collinear electron density and temperature gradients (see. Fig.0.3). This induces a magnetization of the plasma that was supposed to be of small importance. Nonetheless, as we will see, this magnetic field is strong enough to drastically alter the heat flux by turning it (*Righi-Leduc* effect [14]) and reducing the effective range of the fast electron population (*relocalization*), which carries the heat in the plasma. In return, the magnetic field is transported both by

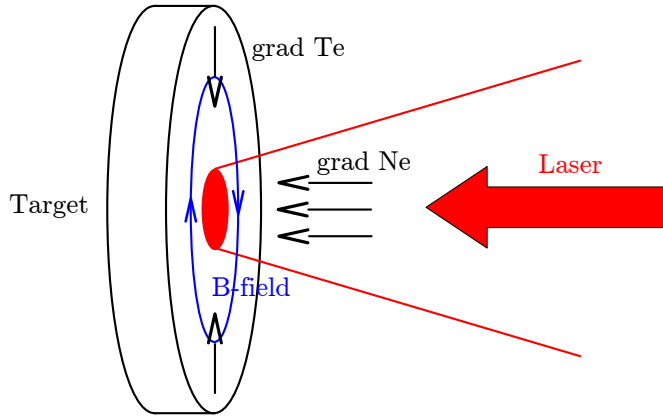


Figure 0.3: *Illustration of the self-generation of the magnetic field in laser-solid interaction.*

the plasma motion (*frozen in field*) and the heat flux (*Nernst effect* [15]).

While the overall hydrodynamics of an indirect drive experiment is driven by radiations, we observe (as will be detailed in this manuscript) that the model used for the heat flux alters the resulting electron temperature of the plasma filling the cavity, and thus the way the lasers propagate from the *laser entrance holes (LEH)* to the cavity’s wall. Indeed, the modelization of laser-plasma interactions (LPI), filamentation and energy deposition in the cavity relies on an accurately defined electronic temperature of the filling gas [16].

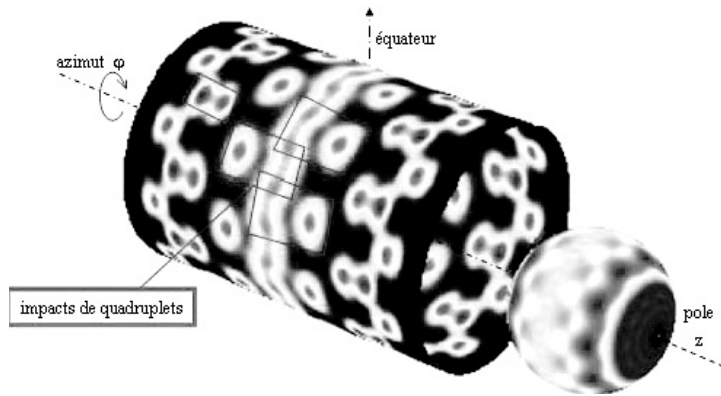


Figure 0.4: *Illustration of the laser irradiation in a former LMJ design (cylinder hohlraum).* From [17].

Moreover, the cavity’s wall being irradiated by multiple close-by laser spots (see Fig. 0.4), numerous magnetic field loops are generated, growing in size and amplitude with the expanding gold plasma bubbles. At some point, the field lines of neighboring loops will be compressed toward each other, leading to a strong gradient of magnetic field, as the field lines are anti-parallel. This is the setup for magnetic reconnection events, where the magnetic field energy is converted back to kinetic energy [18]. Thus, if the reconnection is fast and localized enough, this may lead to inhomogeneities in the x-ray emission from the

gold wall and, ultimately, to asymmetries in the capsule implosion. More generally, the magnetic reconnection is of interest in the study of plasma physics, solar physics (coronal mass ejections, heating of the solar corona *etc.*), space physics (reconnection between the interplanetary magnetic field and the Earth's magnetosphere) or laboratory discharge plasma physics.

Structure of the thesis

The goal of the thesis will thus be to investigate the growth and evolution of magnetic fields in ICF plasmas, as well as investigate the reconnection processes that could take place between two neighboring magnetic field structures.

The first chapter of this thesis is dedicated to the presentation of different models of heat flux, starting with the most common one: the flux limited *Spitzer-Härm* (S-H) [19]. It has been used for decades due to its simplicity, but because of its assumption of a local heat flux (diffusion), it relies on an arbitrary parameter to fit experimental results. In the presence of magnetic field, there exists another approach, the *Braginskii* treatment [20] that provides numerical fits of the conductivity tensors to model the interplay between the local heat flux and the magnetic field transport.

In laser generated plasmas, the validity of the local heat flux fails as, in the electronic conduction zone, the mean free path of the heat-carrying electrons (traveling at 3-4 times the thermal velocity, while the mean free path is function of v^4) is higher than the electronic temperature gradient length, *i.e.* the transport is no more diffusive. To correctly calculate the heat flux, a *Fokker-Planck* code (in which the kinetic equations, discretized over space and velocity, are solved to determine the electron distribution function) would be needed. Yet, its calculation cost is much too important for the simulation of the interactions of our interest: indeed, we would need a millimetric simulation box, with micrometric cells, over nanoseconds. To account “online” for non-local effects in hydro-radiative codes, different methods have been proposed. The convolution over space of the S-H flux by a kernel [21], is affordable in 1D but still too expensive in 2D. Schurtz, Nicolaï and Busquet [22] then proposed a multi-group diffusion model, based on the assumption of an electron distribution function with a small deformation from the Maxwellian. We will describe how this model can be coupled to the *magneto-hydrodynamic* (MHD) approach, in which the equations of evolution of a single fluid are linked with those of electromagnetic fields. To conclude this chapter, we will present comparisons of different coupling strategies with a Fokker-Planck code through a simplified case (without hydrodynamics).

The second chapter is dedicated to the comparison between measurements performed at the JLF-Titan facility (2011) with post-processed results from FCI2 simulations, in order to assess the validity of the code. More specifically, we will discuss the possibility to perform comparisons on deconvolved measurements with physical quantities. For example,

the electron density given by the simulation may be compared with the experimental one after Abel inversion of the measured phase map through interferometry, or one can calculate a phase map from the simulated electron density. The most important diagnostic being proton radiography [23] (the only one able to probe the magnetic field deep inside the dense part of the plasma), we will detail how the integrated magnetic field modulates the proton dose on our detector and will study the sensibility of this diagnostic to the proton energy, to the laser energy, to the laser focal spot or to the scattering of the protons through the solid matter. Finally, we will show that the magnetic fields topology calculated by FCI2 using our model gives proton radiography results in agreement with the measurements, for both low and high Z targets, all along the interaction. The chapter will be concluded with a comparison of the different models presented in chapter 1, but this time against an experimental measurement performed on the LULI2000 facility (2008).

The third chapter is dedicated to the study of the growth and transport of the field, and its effects on the overall interaction. Using the FCI2 code, a study of the source and transport of the B-field, as well as the influence of the laser parameters, is performed for both low and high Z targets. The resulting topology of the magnetic field being understood, a study of the feedback of the field over the interaction is performed, showing that the field strongly affects the heat flux due to a strong dependence of the magnetization of the electrons through their velocity. Moreover, the effects on the ion motion (*i.e.* the hydrodynamics of the plasma) and the energy balance are studied. The chapter will be concluded by an extrapolation to multi-kiloJoule scales (LMJ or NIF quad irradiating a foil³) and full scale ICF experiments.

The last chapter aims at studying the reconnection of the magnetic field in the framework of our collisional laser-generated plasmas. First, a state of the art of the knowledge of the reconnection is presented, as well as the different types of codes (resistive MHD, Particle in Cell and hybrid) that can be used to investigate the physics at play, leading to the HECKLE code from LPP which will be used to design and analyse our experiments in parallel with FCI2. Indeed, a previous numerical study performed with HECKLE pointed out that the quadrupolar structure of the magnetic field in the reconnection zone (called the Hall component) may be a cause and not a consequence of the reconnection [24]. Thus, artificially inhibiting it using bended foils could reduce the reconnection rate. We will then present experiments performed at Phelix (GSI) and LULI2000, which aimed at assessing the reconnection rate in laser generated plasmas, as well as the preliminary interpretation of the experimental results using both FCI2 (simulation of a single irradiation spot) and HECKLE (simulation of the reconnection). The chapter will end with the presentation

³LMJ (*Laser MegaJoule*, France) and NIF (*National Ignition Facility*, USA) are the two currently operating MegaJoule class laser facilities, designed to demonstrate the feasibility of high gain ICF experiments. A quadruplet (or quad) is a bunch of 4 co-propagating laser beams, resulting in a 10-20 kJ laser energy in a single focal spot.

of an oncoming LMJ-Petal experiment.

1 Modeling the heat flux in hydro-radiative simulations

Introduction

In *Inertial Confinement Fusion* (ICF) and *High Energy Density Plasmas* (HEDP) experiments, the typical scales are as follow (in *c.g.s.*): object size of 10^{-1} *cm*, gradient lengths in the order of 10^{-4} *cm* and duration ranging from 10^{-10} *s* to 10^{-8} *s*. With a characteristic fluid velocity of $10^7 - 10^8$ *cm/s*, this results in a characteristic time around 10^{-13} *s*. Simulating this kind of experiments is thus not affordable with a Fokker-Planck code, which would describe the distribution function of the electrons and ions (or only one of them in the case of a hybrid code). Therefore, the most common method is to assume that the system is at the *Local Thermodynamic Equilibrium* (LTE), leading to Maxwell-Boltzmann distribution functions and hence allowing to describe the system through the different momenta of the distribution functions. This is the fluid (or hydrodynamic) framework.

While the physics at play in hydro-radiative simulations is very vast, the electron thermal transport plays a major role in laser produced HEDP experiments. In the case of ICF plasmas, electron conduction strongly affects the electronic ablation front (*i.e.* the limit where the solid target is heated by the electron heat transport and is thus vaporized) in direct drive, as well as the x-ray emission from the high *Z* materials in indirect drive hohlraum. Moreover, hydrodynamics and parametric instabilities (coupling and energy transfer between electro-magnetic, ionic and electronic waves) are also sensitive to thermal conduction. Hence, an accurate modeling of electron transport in hydro-radiative codes is of great importance, as it may affect both the way laser energy is deposited in ICF experiments and the way internal energy is transported in the target.

Most commonly, the electron conduction model used in this kind of code (*i.e.* hydrodynamic) is the Spitzer-Härm (S-H) linear theory, which will be described below. Yet, because the laser energy is deposited in a very small area near the critical density ($N_c \simeq 1.1 \times 10^{21}$ [*cm*⁻³] / λ_{laser}^2 [μm]), the temperature profile exhibits very sharp temperature gradients, leading to an overestimated heat flux due to the non-validity of the linear theory in this area. Thus, in order to correctly reproduce experimental measurements, the S-H heat flux has to be artificially limited to a maximum value [21]. This method,

while allowing to fit the results of the various observables that can be recorded independently in HEDP experiments (*e.g.* x-ray emission, electron temperature, hydro-motion *etc.*), does not allow to match every measurements of an experiment with a single value of the flux limiter. Furthermore, it turns out that the limitation has to be adjusted from an experiment to the other, depending on the laser parameters.

In this chapter, we will describe the different electron conduction models which can be used in our FCI2 code, starting from the Spitzer-Härm model, which depends only on the local hydrodynamics parameters. Then, we will present the various approaches aiming at improving the treatment of the heat flux : artificial limitation, linear theory in the case of a magnetized plasma, and finally, non-local models coupled with a MHD module.

1.1 FCI2: A Resistive MHD hydro-radiative code (and more)

The physics studied in this thesis takes place in the framework of the interaction of high-power laser beams on either the wall of a high Z (such as gold) cavity in indirect drive ICF (ID-ICF), or a low Z (such as plastic) *ablator* of a direct drive ICF (DD-ICF) target. To be more synthetic, we have reduced the field of the first part of our study to the interaction of a single laser beam with solid foils of different atomic number. The targets, based on experimental constrains, will be presented in details in chapter 2.

1.1.1 The physics included in FCI2

The numerical simulations of the interaction of a single laser beam with a foil, that we are going to present and discuss here, were all performed with FCI2 (in French: code de *Fusion par Confinement Inertiel*), an hydro-radiative code [25] developed at CEA (French Commission for Alternate Energy and Atomic Energy), used routinely to design ICF experiments. FCI2 is a 2D axi-symmetrical hydrodynamic code (r - z cylindrical geometry), solving the equations of the classical (for laser studies) two temperature-one fluid model of the plasma [26, 27]. Indeed, because the laser deposits its energy on the electrons, this leads to a system where electrons and ions are co-moving (such as to keep the quasi-neutrality of the system), but have different temperatures. Once the laser is turned off, removing the large energy source on the electrons, the two temperatures eventually equilibrate by the action of electron-ions collisions. The FCI2 code uses the Lagrangian

formalism where $D_t = \frac{\partial}{\partial t} + (\mathbf{u} \cdot \nabla)$ is the Lagrangian derivative:

$$\begin{aligned}
D_t \mathbf{r} &= \mathbf{u} \\
D_t \rho + \rho \nabla \cdot \mathbf{u} &= 0 && \text{Mass conservation,} \\
\rho D_t \mathbf{u} + \nabla P &= 0 && \text{Momentum conservation,} \\
D_t \mathcal{E}_e + P_e \nabla \cdot \mathbf{u} + \nabla \cdot \mathbf{Q}_e &= S_e - \nu_{ei} (T_e - T_i) + H_{rad} && \text{Energy conservation (electrons),} \\
D_t \mathcal{E}_i + P_i \nabla \cdot \mathbf{u} + \nabla \cdot \mathbf{Q}_i &= S_i + \nu_{ei} (T_e - T_i) && \text{Energy conservation (ions),} \quad (1.1)
\end{aligned}$$

where \mathbf{u} is the fluid velocity, ρ is its mass density and $P = P_i + P_e$ is its total scalar pressure. $\mathcal{E}_{i,e}$ is the internal energy of the ions (respectively electrons), $\mathbf{Q}_{i,e}$ is the heat flux, $S_{i,e}$ is the external energy source, H_{rad} represents the electron-photon energy exchange (through a radiative equation), $T_{i,e}$ is the ion (resp. electron) temperature and ν_{ei} the electron-ion collision frequency.

Because in ICF, and more generally in laser-solid interaction, the fluid is rapidly expanding or contracting, it is convenient to use the Lagrangian description, for which the reference frame moves with the flow velocity of the fluid. Indeed, in this co-moving frame, D_t reduces to $\frac{\partial}{\partial t}$, allowing to get rid of the advection terms $(\mathbf{u} \cdot \nabla)$ of the Eulerian formalism. Nonetheless, because in the Lagrangian description the mesh is embedded with the fluid, shear flows or vortices will lead to highly deformed meshes preventing the continuation of the simulation. In the ‘‘simple’’ case of a laser irradiated foil, the large variation of density at the ablation front results in highly elongated meshes and thus a small spatial resolution in the ablated part of the plasma. To solve this problem, FCI2 uses an ALE (*Arbitrary Lagrangian-Eulerian*) module, to transform the deformed mesh into a more regularized one.

Furthermore, to close the system (Eqs. 1.1), one needs equations of state (EOS) to calculate $P_{i,e}(\rho, T_{i,e})$ and $\mathcal{E}_{i,e}(\rho, T_{i,e})$, which, in FCI2, are interpolated from tabulated calculations. The difficulty comes again from the various states of the matter in this kind of experiment, from the (possibly) degenerated dense cold plasma to the hot one, having a low collisionality.

The heat transport in the system ($\nabla \cdot \mathbf{Q}_e$ in the energy equation of 1.1) can use either a flux-limited Spitzer-Härm, Braginskii or a non-local multi-group diffusion model coupled to the self-generated magnetic field. This part will be developed afterwards in this chapter. Note that because the ionic heat flux is much smaller than the electronic one, it is treated as a linear diffusion: $\mathbf{Q}_i = -\kappa_i \nabla T_i$.

In the case of high Z materials, the transport of energy through radiation becomes dominant in the equation of energy. This is a long lasting subject of research and many different models have been proposed, starting, in the approximation of an optically thick

plasma, with the simplest *grey diffusion*¹, in which a mean frequency is used. However, in our case, there is a continuous transition from the optically thick solid part of the target to the optically thin low density corona. Hence, FCI2 contains a multi-group Monte-Carlo transport module [28], using tabulated opacities, corrected to account for *Non-Local Thermodynamic Equilibrium* (NLTE) [29]. Note that the transport of energy in hydro-radiative simulations is a particularly complex subject (especially in 2D), as both the electronic and radiative transports may have a long range, leading to a set of non-linear equations to solve in order to calculate the energy of the system. To be exhaustive, note that the photonic module may be coupled to an atomic physics one, in order to improve the accuracy of the opacities and ionization states.

The laser energy deposition ($S_{e,Laser}$) is simulated through a 3D geometric optics ray-tracing package, modeling absorption through inverse bremsstrahlung. Finally, in the case of full scale ICF simulations, one has to use packages for nuclear reactions, supra-thermal ions and neutron transport.

1.1.2 Hydrodynamics of a solid foil irradiated by a nanosecond laser pulse

Before looking further in details into the issue of heat transport, we will present here the dynamics of a solid foil irradiated by a $\sim 10^{14} W/cm^2$ *nanosecond* laser pulse. The heating from the laser launches a thermal wave in the target, heating and ionizing it, resulting in an ablation of the foil.

Fig. 1.1 illustrates in one dimension the laser which deposits its energy through inverse bremsstrahlung up to the critical density (the electron density at which the electron plasma frequency is higher than that of the laser). The thermal energy is transported toward the dense target by electron conduction until the *electronic ablation front*, and deeper inside the target by radiation conduction, up to the *radiative ablation front* [30, 31]. The resulting ablation pressure launches a shock through the target, which, upon reaching its rear face, accelerates it. Because of the fast and localized laser heating, the temperature gradient in the electron conduction zone may be very steep, resulting in electrons carrying the heat with a mean free path longer than the corresponding gradient length. This leads to the delocalization of the heat flux.

Fig. 1.2 to Fig. 1.5 present 2D FCI2 simulations with non-local electron conduction and MHD for typical HEDP parameters: 23 μm thick Mylar or 5 μm thick gold targets, irradiated by a 400 J, 2 ns, 300 μm FWHM focal spot and $\lambda = 1 \mu m$ (1ω) laser pulse,

¹A *grey diffusion* corresponds to a diffusion mechanism for an equilibrated population (*e.g.* Planckian for a population of photons or Maxwellian for a population of electrons) for which a fine description of the distribution function is not necessary.

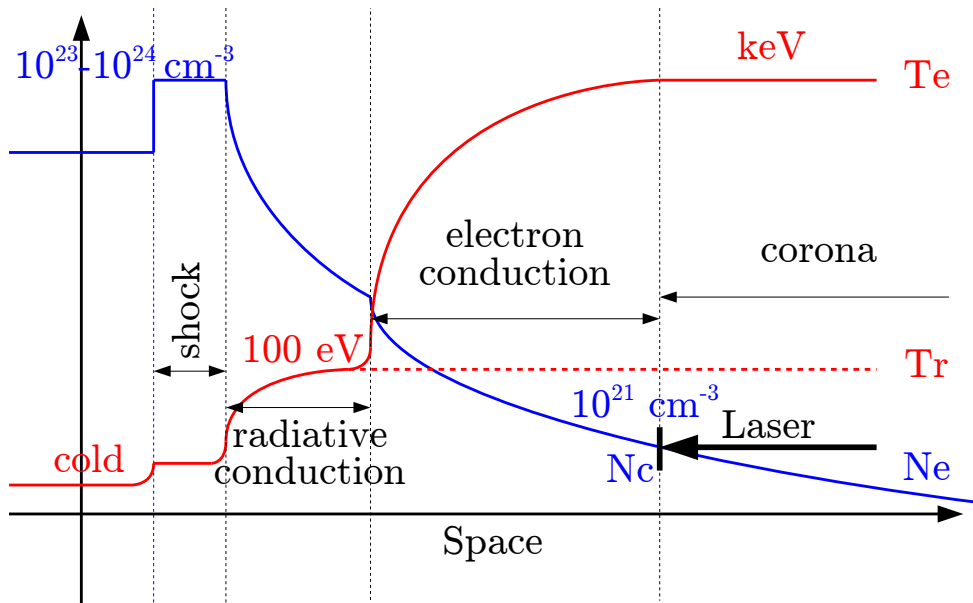


Figure 1.1: 1D scheme of the irradiation of a solid foil by a $\sim 10^{14} \text{ W/cm}^2$ nanosecond laser pulse.

giving an intensity of $\sim 3 \times 10^{14} \text{ W/cm}^2$. It illustrates the dynamics of the foil from the hydrodynamics point of view. First of all, because of the lower inertia of the plastic target, thus characterized by a faster plasma motion, the electron conduction length (see Fig. 1.2 at 2.0 ns) is much longer than for the gold target. Secondly, one can see the gold target being ablated deeply by radiative energy transport (see the large region of plasma at $0.1 - 1 \text{ g/cm}^3$). Note also the decreasing temperature in the corona, a typical result given by non-local electron conduction models, opposed to the classical isothermal corona of the flux-limited conduction model.

Fig. 1.3 and Fig. 1.5 exhibit the repartition of energy in the system (upper/lower is the internal/kinetic energy), as it governs its evolution. It shows that in overall, the energy is lower for the gold target, as a significant fraction of the energy is lost through radiations, because of the “open” geometry of the foil (opposed to an ICF cavity). Moreover, it is important to understand that despite the high temperature of the corona, its low density implies a low internal energy. In fact, most of the system’s energy is split between internal energy at the ablation front, and kinetic energy in the accelerated foil. Most of the hydrodynamics of the foil is then determined by the dense part of the plasma. The solid iso-line represents $M_a = 1$ ($M_a \simeq \sqrt{\frac{[\text{Kinetic energy}]}{[\text{Internal energy}]}}$ being the Mach number), *i.e.* the separation between compressible and incompressible fluids.

To conclude this basic introduction concerning the hydrodynamics of a laser irradiated foil, we point out that one significant peculiarity of high Z targets is the apparition of a radiative ablation front, ahead of the electronic one, resulting in a *double ablation front* (DAF) structure [32]: this results in an area of almost constant density and temperature,

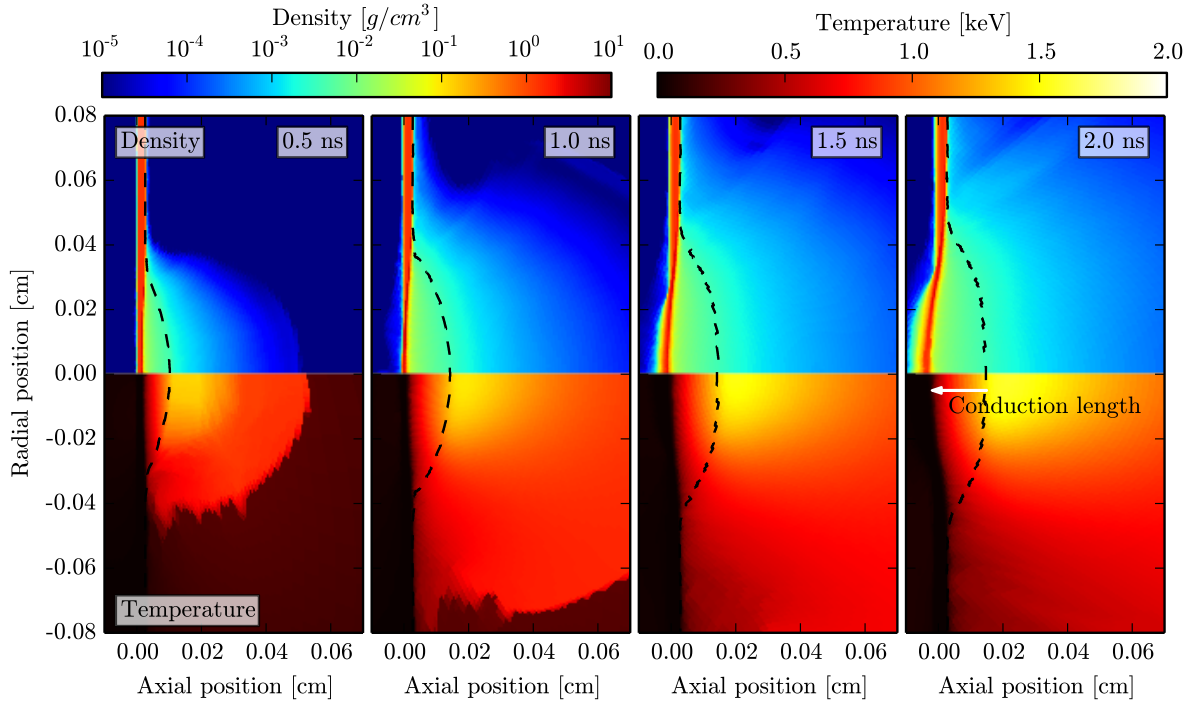


Figure 1.2: *Density* [g/cm^3] (up) and *electron temperature* [keV] (down) for a $23\ \mu m$ thick Mylar target irradiated by a $400\ J$, $2\ ns$, $300\ \mu m$ FWHM focal spot and $1\ \mu m$ wavelength laser pulse. From left to right : 0.5 , 1.0 , 1.5 and $2.0\ ns$. The dotted line represents the critical density.

between the two fronts². Because an ablation front marks a separation between the accelerated foil (moving toward $x < 0$) and the ablated plasma (moving toward $x > 0$), it appears as a local minimum of the kinetic energy. On Fig. 1.3 one can clearly see a single ablation front, while on Fig. 1.5 there are two.

1.2 The limited Spitzer-Härm heat flux

As we saw above in (Eqs. 1.1), solving the equation of energy requires to calculate a heat flux \mathbf{Q} , for which different assumptions may be made. First of all, because of the high mobility of electrons, we will here neglect the ions' contribution in the heat transport. Next, for simplicity, one could assume that the transport is much faster than the system's evolution (*i.e.* infinite heat flux), leading to an homogeneous temperature (*isothermal* assumption) or, on the opposite, that the heat transport is much slower than the system's evolution (*i.e.* null heat flux, *adiabatic* assumption). Both assumptions strongly simplify the resolution of the electron energy's equation, but are too restrictive for our kind of

²*n.b.* Because, in our case, the electron temperature is lower than $200\ eV$ in this region, it is hardly visible on the colormap.

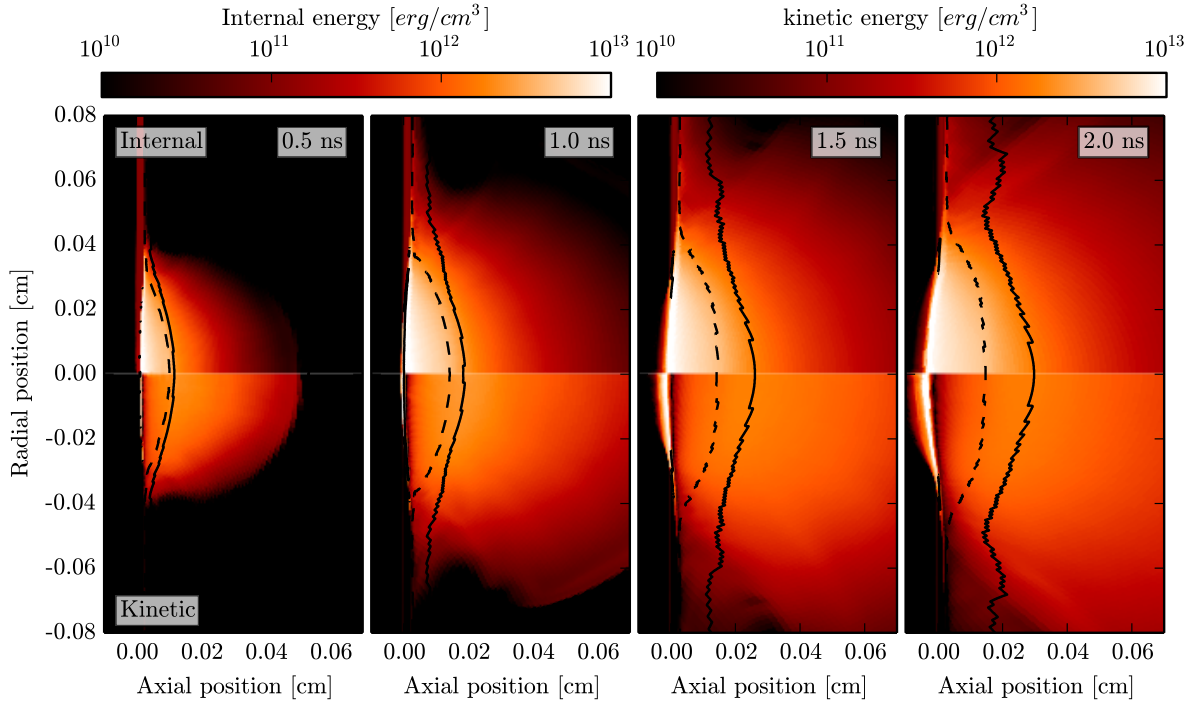


Figure 1.3: Internal (up) and kinetic (down) energy density [erg/cm^3] for a $23 \mu\text{m}$ thick Mylar target irradiated by a 400 J , 2 ns , $300 \mu\text{m}$ FWHM focal spot and $1 \mu\text{m}$ wavelength laser pulse, with isolines for the critical density (dashed) and $M_a = 1$ (solid). From left to right : 0.5 , 1.0 , 1.5 and 2.0 ns .

experiments in which the heat flux ranges from one extreme to the other, depending on time and space. We thus have to calculate a finite heat flux.

1.2.1 Kinetic equation

Let us start with $f(\mathbf{x}, \mathbf{v}, t)$ the electron distribution function (as said above the ion contribution is negligible). Its velocity moments, from which the plasma's characteristics can be evaluated, are:

$$\begin{aligned}
 N_e &= \int f d^3\mathbf{v} && 0^{\text{th}} \text{ moment : Electron density,} \\
 \mathbf{j} &= -e \int f \mathbf{v} d^3\mathbf{v} && 1^{\text{st}} \text{ moment : Electron current,} \\
 \mathcal{E} &= \frac{m_e}{2} \int f \mathbf{v}^2 d^3\mathbf{v} && 2^{\text{nd}} \text{ moment : Energy,} \\
 \mathbf{Q} &= \frac{m_e}{2} \int f \mathbf{v}^3 d^3\mathbf{v} && 3^{\text{rd}} \text{ moment : Heat flux,}
 \end{aligned} \tag{1.2}$$

where, in cylindrical symmetry, $\mathbf{x} = (z, r)$ and $\mathbf{v} = (v_z, v_r)$.

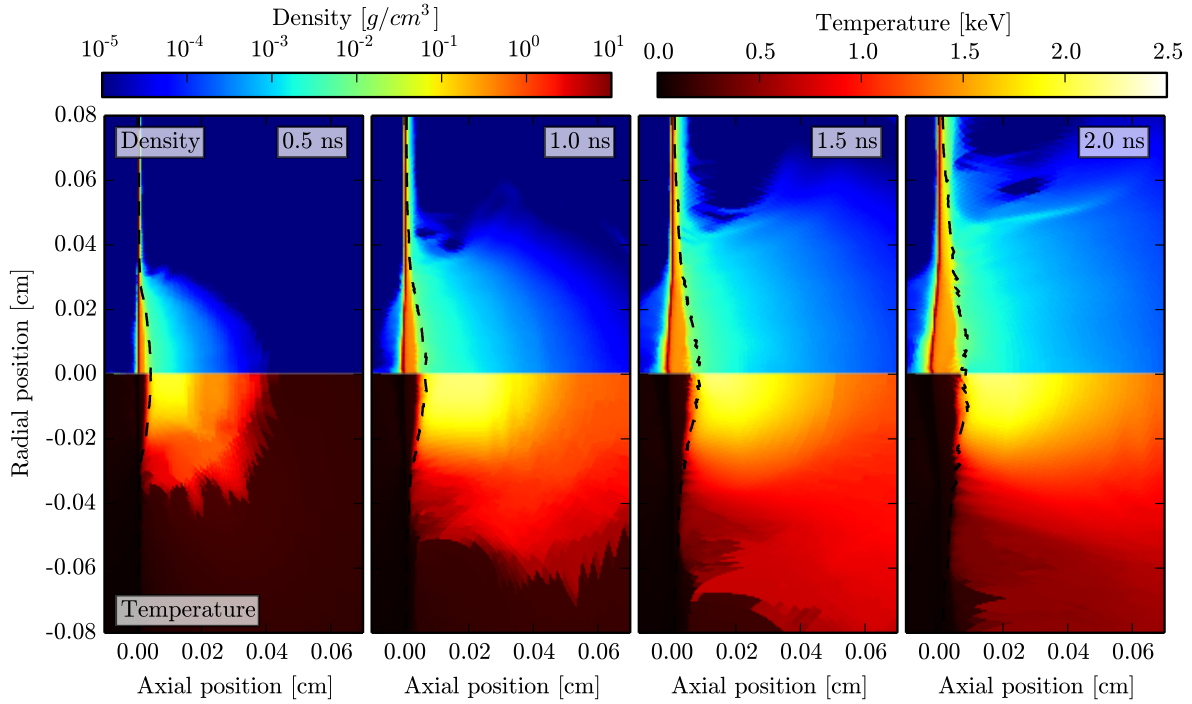


Figure 1.4: Density [g/cm^3] (up) and electron temperature [keV] (down) for a $5 \mu m$ thick gold target irradiated by a $400 J$, $2 ns$, $300 \mu m$ FWHM focal spot and $1 \mu m$ wavelength laser pulse. From left to right : 0.5 , 1.0 , 1.5 and $2.0 ns$. The dotted line represents the critical density.

$f(\mathbf{x}, \mathbf{v}, t)$ is solution of the *Vlasov-Fokker-Planck-Landau* equation:

$$\frac{\partial f}{\partial t} + \mathbf{v} \cdot \nabla_{\mathbf{x}} f - \frac{e}{m_e} \left(\mathbf{E} + \frac{\mathbf{v}}{c} \times \mathbf{B} \right) \cdot \nabla_{\mathbf{v}} f = Q^{ee}(f, f) + Q^{ei}(f, f^i), \quad (1.3)$$

where $\nabla_{\mathbf{x}}$ and $\nabla_{\mathbf{v}}$ represent respectively the gradients over the spatial and velocity dimensions, $-e$ is the electron charge, m_e the electron mass, (\mathbf{E}, \mathbf{B}) the electromagnetic field, c the speed of light and $Q^{ee}(f, f) + Q^{ei}(f, f^i)$ are the electron-electron and electron-ion collision operators.

1.2.2 P1 system (isotropisation)

Assuming that the distribution function is close to isotropy, we expand the distribution function in spherical harmonics [33] up to the first order [34], with $v = \|\mathbf{v}\|$ and $\boldsymbol{\Omega} = \frac{\mathbf{v}}{v}$:

$$f(\mathbf{x}, \mathbf{v}, t) = \frac{f_0(\mathbf{x}, v, t)}{4\pi} + \frac{3\boldsymbol{\Omega} \cdot \mathbf{f}_1(\mathbf{x}, v, t)}{4\pi} + \dots \quad (1.4)$$

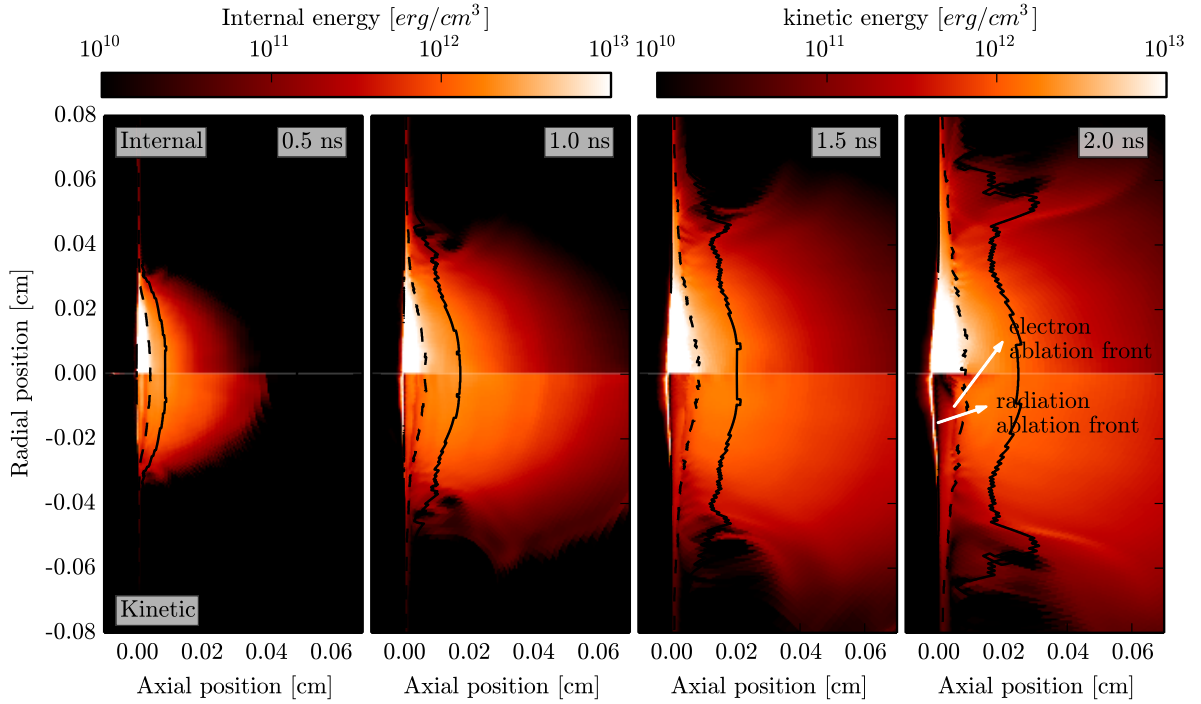


Figure 1.5: Internal (up) and kinetic (down) energy density [erg/cm^3] for a $5 \mu\text{m}$ thick gold target irradiated by a 400 J , 2 ns , $300 \mu\text{m}$ FWHM focal spot and $1 \mu\text{m}$ wavelength laser pulse, with isolines for the critical density (dashed) and $M_a = 1$ (solid). From left to right : 0.5 , 1.0 , 1.5 and 2.0 ns .

f_0 represents the isotropic part of the distribution function (even moments : density, energy, *etc.*), while \mathbf{f}_1 represents the anisotropic part (odd moments : velocity/current, heat flux, *etc.*). Therefore, with $d^3\mathbf{v} = v^2 dv d\Omega$, the moments of f (Eq. 1.2) become:

$$\begin{aligned} N_e &= \int f_0 v^2 dv, & \mathcal{E} &= \frac{m_e}{2} \int f_0 v^4 dv, \\ \mathbf{j} &= -e \int \mathbf{f}_1 v^3 dv, & \mathbf{Q} &= \frac{m_e}{2} \int \mathbf{f}_1 v^5 dv. \end{aligned} \quad (1.5)$$

Substituting the distribution function (Eq. 1.4), expanded up to the first order, in the VFPL equation (Eq. 1.3), directs to:

$$\frac{\partial f_0}{\partial t} + v \nabla_{\mathbf{x}} \cdot \mathbf{f}_1 - \frac{e\mathbf{E}}{m_e} \cdot \frac{1}{v^2} \frac{\partial}{\partial v} (v^2 \mathbf{f}_1) = C_0, \quad (1.6)$$

$$\frac{\partial \mathbf{f}_1}{\partial t} + \frac{v}{3} \nabla_{\mathbf{x}} f_0 - \frac{e\mathbf{E}}{3m_e} \frac{\partial f_0}{\partial v} - \frac{e}{m_e} \frac{\mathbf{B}}{c} \times \mathbf{f}_1 = \mathbf{C}_1. \quad (1.7)$$

C_0 and \mathbf{C}_1 are respectively the scalar and vectorial (approximated from the Lorentz

model) collisional operators [35, 36]:

$$C_0 = C_0(f_0) = \frac{\nu_{ee}}{N_e} \frac{\partial}{\partial v} \left(v f_0(v) E(v) + D(v) \frac{\partial f_0(v)}{\partial v} \right), \quad (1.8)$$

$$\mathbf{C}_1 = \mathbf{C}_1(\mathbf{f}_1) = -\nu_{ei}^* \mathbf{f}_1, \quad (1.9)$$

where $\nu_{ee} = \frac{4\pi N_e e^4 \ln \Lambda_{ee}}{v^3 m_e^2}$ and $\nu_{ei} = \frac{4\pi N_i e^4 Z^2 \ln \Lambda_{ei}}{v^3 m_e^2}$ are respectively the electron-electron (ee) and electron-ion (ei) collision frequencies with N_e and N_i the electron and ion density, Z the ions' charge state and $\Lambda_{ee}, \Lambda_{ei}$ the Coulomb logarithms corresponding to e - e and e - i collisions. Note that ν_{ei} is valid only in the limit of high Z [37]. For an arbitrary Z , ν_{ei} is corrected as $\nu_{ei}^* = \alpha \nu_{ei} = \frac{Z + 4.2}{Z + 0.24} \nu_{ei}$. $E(v)$ and $D(v)$ are the isotropic Rosenbluth coefficients [38]:

$$E(v) = 4\pi \int_0^v f_0(v') v'^2 dv', \quad (1.10)$$

$$D(v) = \frac{4\pi}{3} v^3 \left(\int_0^v f_0(v') v'^4 dv' + \int_v^\infty f_0(v') v' dv' \right). \quad (1.11)$$

1.2.3 The Spitzer-Härm heat flux (Maxwellianisation)

Next, we assume that f_0 varies slowly in space, *i.e.* the *mean free path (mfp)* of the electrons $\lambda(v) = v/\nu(v)$ is smaller than a characteristic length. In other words, one can define a small parameter $\epsilon = \lambda(v)/L_{th}$, with $L_{th} = T_e/|\nabla T_e|$ the temperature gradient scale length. This allows us to replace f_0 by the Maxwellian distribution, function of the momenta N_e and T_e (the fluid velocity is neglected, being much lower than the thermal velocity):

$$f_0 = f_0^m = 4\pi N_e \left(\frac{m_e}{2\pi k_b T_e} \right)^{\frac{3}{2}} e^{-(m_e v^2 / 2k_b T_e)}. \quad (1.12)$$

Using (Eq. 1.7) and (Eq. 1.9) under stationary conditions (\mathbf{f}_1 is slowly varying compared to the hydrodynamics time scale, $\frac{\partial \mathbf{f}_1}{\partial t} = 0$) and null magnetic field hypothesis, leads to:

$$\frac{v}{3} \nabla_{\mathbf{x}} f_0^m - \frac{e\mathbf{E}}{3m_e} \frac{\partial f_0^m}{\partial v} = -\nu_{ei}^* \mathbf{f}_1. \quad (1.13)$$

At this point, the electric field \mathbf{E} is the only remaining unknown we need to calculate the heat flux (3^{rd} order moment of \mathbf{f}_1). To do so, assuming a null electric current ($\mathbf{j} = \vec{0}$, 1^{st} order moment of \mathbf{f}_1) to prevent any accumulation of charge, we can write using (Eq. 1.13)

in (Eq. 1.5) and keeping in mind that $\nu_{ei}^* \propto v^{-3}$:

$$\mathbf{j}_{null} = \int_0^\infty \left(v \nabla_{\mathbf{x}} f_0^m - \frac{e \mathbf{E}}{m_e} \frac{\partial f_0^m}{\partial v} \right) v^6 dv = \vec{0} \quad (1.14)$$

and therefore, after integration:

$$\mathbf{E}_{SH} = -\frac{k_b T_e}{e} \left(\frac{\nabla N_e}{N_e} + \frac{5}{2} \frac{\nabla T_e}{T_e} \right). \quad (1.15)$$

Using this ‘‘Spitzer-Härm electric field’’ \mathbf{E}_{SH} in (Eq. 1.7), still without magnetic field, gives access to \mathbf{f}_1^m :

$$\mathbf{f}_1^m = -\frac{v}{3\nu_{ei}^*} \left(\frac{m_e v^2}{2k_b T_e} - 4 \right) f_0^m \frac{\nabla T_e}{T_e} \quad (1.16)$$

and finally, to the Spitzer-Härm heat flux [19]:

$$\mathbf{Q}_{SH} = -K_{SH} \nabla (k_b T_e) = -\frac{64}{Y_{ei}^*} \sqrt{\frac{2}{\pi}} \left(\frac{k_b T_e}{m_e} \right)^{\frac{5}{2}} \nabla (k_b T_e), \quad (1.17)$$

with $Y_{ei}^* = \alpha \left(\frac{4\pi e^4 Z^2 \ln \Lambda_{ei}}{m_e^2} \right)$.

1.2.4 Limited heat flux

As one can note, the Spitzer-Härm model leads to an implementation in the codes of a ‘‘grey diffusion’’, *i.e.* the electrons are supposed to be at equilibrium (Maxwellian distribution function), and the transport coefficient $K_{SH}(\mathbf{r})$ depends only on the *local* thermodynamics variables $T_e(\mathbf{r})$ and $\nabla T_e(\mathbf{r})$. This treatment is the simplest and easiest thermal conduction model to implement in codes. This explains why the Spitzer-Härm heat flux has been, in hydro-radiative codes, the most commonly used model for decades.

Yet, it appeared very early that simulations using this model could not reproduce all the experimental measurements [39], proving that at least one of the assumptions used above is not justified. The first one which is made is that the vectorial part of the electron distribution function is a perturbation of the isotropic one : $\|3\boldsymbol{\Omega} \cdot \mathbf{f}_1^m\| \ll f_0^m$.

Let us introduce $\beta = \frac{m_e v^2}{2k_b T_e}$ the reduced energy, $L_{th} = \frac{T_e}{\nabla T_e}$ the temperature gradient length, and $\lambda_{ei}^{th} = \frac{(k_b T_e)^2}{4\pi e^4 N_e \ln \Lambda_{ei}}$ the mean free path for an electron moving at the thermal velocity. From the expression of \mathbf{f}_1^m (Eq. 1.16) we have:

$$\boldsymbol{\Omega} \cdot \mathbf{f}_1^m(v) = -\frac{\lambda_{ei}^{th}}{3L_{th}} \beta^2 (\beta - 4) f_0^m(v), \quad (1.18)$$

which implies:

$$\frac{\lambda_{ei}^{th}}{L_{th}} \beta^2 |\beta - 4| \ll 1. \quad (1.19)$$

Clearly, this condition is doomed to fail with increasing β , *i.e.* v^2 . Nevertheless, one could question the contribution of the high energy part of the distribution function to the heat flux, because of its small value. Let $q(v)$ be the differential heat flux, defined from $Q = \int q(v)dv$. From (Eq. 1.16) in (Eq. 1.5) and with $\nu_{ei}^* \propto v^{-3}$, it comes:

$$q(v) \propto \left(\frac{m_e v^2}{2k_b T_e} - 4 \right) v^9 f_0^m. \quad (1.20)$$

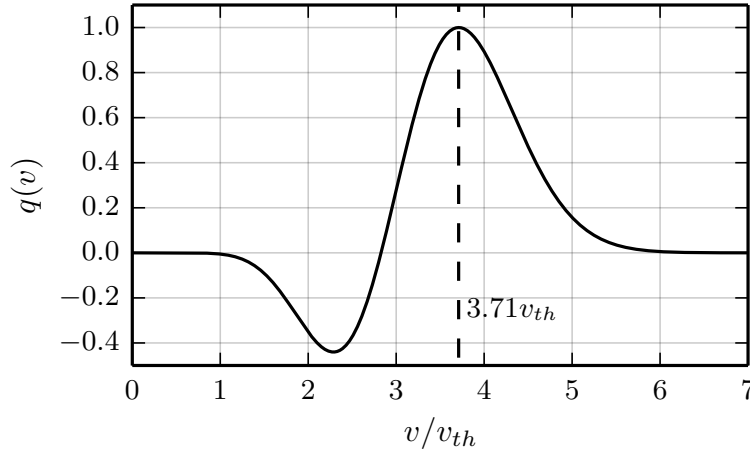


Figure 1.6: Normalized differential heat flux $q(v)$ from (Eq. 1.20).

Plotting $q(v)$ from (Eq. 1.20) shows a maximum at $3.71v_{th}$ (see Fig. 1.6). Using this value of v/v_{th} for β in (Eq. 1.19) gives us the condition:

$$\frac{\lambda_{ei}^{th}}{L_{th}} < 2 \times 10^{-3}. \quad (1.21)$$

While this could seem very low compared to the condition $\lambda_{ei} < L_{th}$, one has to keep in mind that the mean free path is function of v^4 , and thus $\lambda_{ei}(3.71v_{th}) \simeq 200\lambda_{ei}^{th}$.

Because of the very steep temperature gradients encountered in laser generated plasmas (mostly in the electron conduction area, between the ablation front and the critical density, as seen in sec. 1.1.2), this condition fails. As such, the Spitzer-Härm may result in an unphysical, over-estimated heat flux, even larger than the free-streaming heat flux:

$$Q_{FS} = N_e m_e v_{th}^3. \quad (1.22)$$

Hence, as often with diffusive processes, the Spitzer-Härm heat flux may be limited to a fraction f of the free streaming flux, either, for example, by a *sharp cut-off*, or an *harmonic limitation* (see Fig. 1.7):

$$Q = \min(Q_{SH}, f \cdot Q_{FS}) \quad \text{or} \quad \frac{1}{Q} = \frac{1}{Q_{SH}} + \frac{1}{f \cdot Q_{FS}}.$$

Note that there is no precise rule to determine the value of f in the simulations. It is chosen depending on the target's material and the laser's intensity and wavelength, such as to fit experimental data and is typically low, around 0.05 – 0.1 for a sharp cut-off [40, 41, 42]. This shows that the limited Spitzer-Härm heat flux, while convenient from a numerical point of view, cannot be predictive as the parameter f has to be adjusted *a-posteriori*.

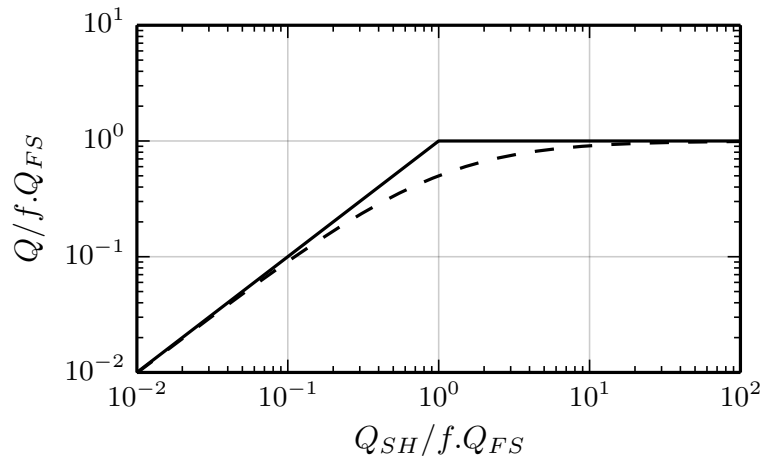


Figure 1.7: Sharp (solid) and harmonic (dashed) cut-off.

1.3 The Braginskii heat flux

1.3.1 Linear transport

As we saw in (Eq. 1.17), the Spitzer-Härm heat flux is a linear transport model: it is proportional to ∇T_e through a *transport coefficient* K_{SH} . In this section we will present the so-called *Braginskii* heat flux, which in fact describes the heat flux within the linear theory when the plasma is magnetized.

First, we start from the kinetic equation under the assumption of a small anisotropy (P1 system, Eq. 1.6 and 1.7). Because we are in the framework of a close to local thermodynamic equilibrium (LTE), f_0 is set to the Maxwellian, and thus the 0^{th} and 2^{nd}

order moment (density and energy) are known. The principle of the linear theory is then to express the electric and thermal currents as linear functions of (magneto-)hydrodynamics quantities such as the electric field \mathbf{E} , the electron temperature gradient ∇T_e or the electron density gradient ∇N_e .

The difficult part is to solve the equation for \mathbf{f}_1 (Eq. 1.7) as it depends on Z , the ionization of the plasma, and on $\chi \equiv \omega_{ce}\tau_{ei}$, its magnetization, where $\omega_{ce} = \frac{e|\mathbf{B}|}{m_e c}$ is the electron gyro-frequency and $\tau_{ei} = 1/\nu_{ei}$ the mean collision time. To do so, the equation is solved for given (Z, χ) couples to fill a table, which is then interpolated to give an approximated continuous expression of the coefficients, *e.g.* the $\alpha = \frac{Z + 4.2}{Z + 0.24}$, in the K_{SH} of the Spitzer-Härm heat flux (Eq. 1.17).

1.3.2 Braginskii's notation

As said above, we keep the small anisotropy assumption with the scalar part of the electron distribution function set to the Maxwellian:

$$f_{Br} = \frac{f_0^m}{4\pi} + \frac{3\boldsymbol{\Omega} \cdot \mathbf{f}_1}{4\pi}. \quad (1.23)$$

Then, the equation for \mathbf{f}_1 from the Spitzer-Härm model (Eq. 1.13), but accounting for the magnetic field through the $-\frac{e}{m_e} \frac{\mathbf{B}}{c} \times \mathbf{f}_1$ term reads:

$$\mathbf{f}_1 = -\tau_{ei} \left(\frac{v}{3} \nabla f_0^m - \frac{e\mathbf{E}}{3m_e} \frac{\partial f_0^m}{\partial v} \right) - \chi (\mathbf{b} \times \mathbf{f}_1). \quad (1.24)$$

Following, just like in the S-H case, one needs to calculate the electric field, which this time comes from the generalized Ohm's law [20]:

$$eN_e \mathbf{E}_{Br} = -\nabla P_e - eN_e \mathbf{u} \times \frac{\mathbf{B}}{c} + \mathbf{j} \times \frac{\mathbf{B}}{c} + \bar{\alpha} \cdot \frac{\mathbf{j}}{N_e} - N_e k_b \bar{\beta} \cdot \nabla T_e, \quad (1.25)$$

while the heat flux is expressed as a function of ∇T_e and \mathbf{j} :

$$\mathbf{Q}_{Br} = -\frac{k_b T_e \bar{\beta}}{e} \cdot \mathbf{j} - \bar{\kappa} \cdot \nabla T_e. \quad (1.26)$$

The transport coefficients are :

- $\bar{\alpha}$ the electrical resistivity,

- $\overline{\beta}$ the thermo-electric conductivity tensor,
- $\overline{\kappa}$ the thermal conductivity tensor,
- χ the plasma's magnetization (also called Hall parameter), function of the thermal velocity v^{th} in the linear theory.

Using Braginskii vectorial notation [20], the components of these tensors are given for any vector \mathbf{s} and $\mathbf{b} = \frac{\mathbf{B}}{\|\mathbf{B}\|}$ as:

$$\overline{\psi} \cdot \mathbf{s} = \psi_{\parallel} \mathbf{b}(\mathbf{b} \cdot \mathbf{s}) + \psi_{\perp} \mathbf{b} \times (\mathbf{s} \times \mathbf{b}) + \psi_{\wedge} \mathbf{b} \times \mathbf{s}, \quad (1.27)$$

i.e. \parallel is the direction of \mathbf{b} , \perp is the direction perpendicular to \mathbf{b} but collinear to \mathbf{s} , and \wedge is the direction perpendicular to both vectors. For example, in an axi-symmetrical geometry, with \mathbf{b} being on the (O_{θ}) axis and ∇T_e in the (O_z, O_r) plane, Q_{\perp} denotes the heat flux in the direction of ∇T_e , while Q_{\wedge} denotes the heat flux in the direction perpendicular to ∇T_e (see Fig. 1.8).

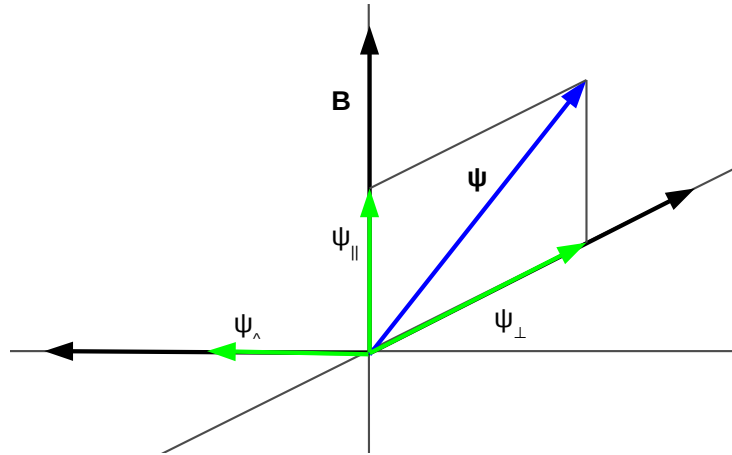


Figure 1.8: *Braginskii's vectorial notations.*

Solving equations (Eq. 1.24 – 1.26) requires to calculate the set of coefficients $(\overline{\alpha}, \overline{\beta}, \overline{\kappa})$ for fixed (Z, χ) couples. In order to do so, different methods have been proposed. Some are analytical, involving an expansion of f_1 in polynomials with a truncation after a number of terms [43, 44]. Others [45] computed the solution through finite differences. Once a table of coefficients is filled for discrete Z and χ , one can fit the results to estimate a continuous $c_i(Z, \chi)$ (c_i representing one of any coefficient listed above). Note that the resulting coefficients can only be used in a validity domain restricted by the hypothesis made to solve f_1 . One could cite for example the Hubbard thermal conductivity [46] valid for fully degenerated plasmas ($T_e < T_F \equiv \frac{\hbar^2}{3m_e} (3\pi^2 N_e)^{2/3}$) in the limit $Z \rightarrow \infty$, or Lee and More who calculated a set of coefficients for the liquid and solid phases within an arbitrary magnetic field [47].

1.3.3 The Righi-Leduc effect

In this subsection we will introduce the so-called Righi-Leduc (R-L) effect. As we saw, when the plasma is magnetized, the thermal conductivity coefficient becomes a tensor $K_{SH} \rightarrow \bar{\kappa}$, *i.e.* the conduction is anisotropic. This tensor can be expressed as a function of the Spitzer-Härm conductivity: $\bar{\kappa} = K_{SH} \bar{X}$, and thus, the Braginskii heat flux (Eq. 1.26) can be rewritten as a function of the Spitzer-Härm one:

$$\begin{aligned} \mathbf{Q}_{Br} &= -\frac{k_b T_e \bar{\beta}}{e} \cdot \mathbf{j} + \bar{X} \cdot \mathbf{Q}_{SH} \\ &= \left(-\frac{k_b T_e}{e} \beta_{\perp} \mathbf{j} + X_{\perp} \mathbf{Q}_{SH} \right) + \mathbf{b} \times \left(-\frac{k_b T_e}{e} \beta_{\wedge} \mathbf{j} + X_{\wedge} \mathbf{Q}_{SH} \right). \end{aligned} \quad (1.28)$$

Fig. 1.9 is plotting, in the limit $Z \rightarrow \infty$ (Lorentz model) and under a null electrical current hypothesis, both the components and the module of \mathbf{Q}_{Br} normalized to $\|\mathbf{Q}_{SH}\|$ as a function of the Hall parameter (magnetization, see page 26) $\chi(N_e, T_e, B)$. It illustrates the behavior of the heat flux in the presence of a magnetic field :

- In the limit $\chi \rightarrow 0$, $\mathbf{Q}_{Br} \rightarrow \mathbf{Q}_{SH}$.
- For $0.01 < \chi < 0.1$ (weakly magnetized plasma), the module of the heat flux stays close to the non-magnetized case, but its direction is rotated toward $\mathbf{b} \times \nabla T_e$, up to $\sim 45^\circ$.
- For $\chi > 0.1$ (magnetized plasma), the heat flux is even more rotated toward $\mathbf{b} \times \nabla T_e$, but it starts to be inhibited due to $\omega_{ce} \simeq \nu_{ei}$.
- In the limit $\chi \rightarrow \infty$, $\|\mathbf{Q}_{Br}\| \rightarrow 0$, the thermal transport is completely inhibited as the electrons are trapped by the magnetic field ($\omega_{ce} > \nu_{ei}$): even if the collisions are still at play, the electrons don't have enough mobility to transport the heat.

RIGHI-LEDUC EFFECT

In the regime of a weakly magnetized plasma, the heat flux is rotated in the $\mathbf{b} \times \nabla T_e$ direction, without a significant loss in strength.

1.4 The magneto-hydrodynamic framework

In the last section we saw that the behavior of the electron conduction in the plasma is strongly modified in the presence of a magnetic field. Yet, it only appeared in the equations in the form of a magnetization χ and a direction \mathbf{b} . In this section we will look in more details at the magnetic field induction $\partial \mathbf{B} / \partial t$, *i.e.* which are the physical mechanisms that are at the source of the field, its transport and its relaxation.

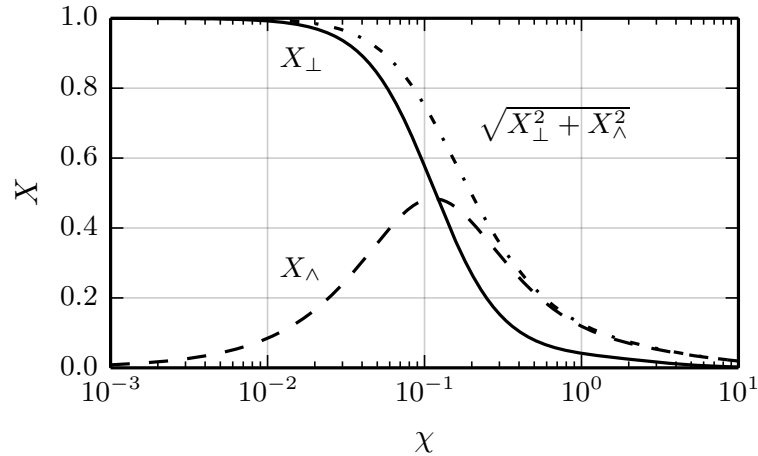


Figure 1.9: X_{\perp} , X_{\parallel} and $\sqrt{X_{\perp}^2 + X_{\parallel}^2}$ as a function of the magnetization χ , for $Z \rightarrow \infty$ and $\mathbf{j} = \vec{0}$.

Taking into account the electro-magnetic field in the fluid equations leads to the *Magneto-Hydrodynamic* (MHD) framework, *i.e.* a single fluid (and two temperatures in our case) model in which the thermodynamic and electro-magnetic quantities (ρ , P , \mathbf{u} , \mathbf{j} , \mathbf{B} , \mathbf{E}) are determined via the simultaneous resolution of the equations of mass conservation, momentum conservation, generalized Ohm's law, Ampere's law and Faraday's law, completed by a set of equations of state.

1.4.1 Momentum equation, the Laplace (Lorentz) force

Let us start with the momentum equations for the ions and electrons which are affected by the pressure of the other total ion population P_i (respectively electron population P_e), the Lorentz force and R_{ie} the electron-ion collision term:

$$N_i m_i D_t \mathbf{u}_i = -\nabla P_i + e Z N_i \left(\mathbf{E} + \frac{\mathbf{u}_i}{c} \times \mathbf{B} \right) - R_{ie}, \quad (1.29)$$

$$N_e m_e D_t \mathbf{u}_e = -\nabla P_e - e N_e \left(\mathbf{E} + \frac{\mathbf{u}_e}{c} \times \mathbf{B} \right) + R_{ie}, \quad (1.30)$$

with $D_t = \frac{\partial}{\partial t} + (\mathbf{u} \cdot \nabla)$ the Lagrangian derivative. Adding (Eq. 1.29) to (Eq. 1.30) when $m_e/m_i \rightarrow 0$ (hence $\mathbf{u} = \mathbf{u}_i$) and $e N_e (u_i - u_e) = \mathbf{j}$, gives the fluid's momentum equation:

$$\rho D_t \mathbf{u} = -\nabla P + \frac{1}{c} \mathbf{j} \times \mathbf{B}, \quad (1.31)$$

where on the right hand side of the equation, the “ $-4\pi (\mathbf{j} \cdot \nabla) \mathbf{j} / \omega_{pe}^2$ ” term has been neglected³ ($\omega_{pe}^2 = 4\pi N_e e^2 / m_e$ is the plasma frequency).

The fluid’s motion is then governed not only by the fluid pressure but also by the Laplace (Lorentz) force. Note that using Ampère’s law, the Laplace force may be written :

$$\begin{aligned} F_{Laplace} &= \frac{1}{c} \mathbf{j} \times \mathbf{B} \\ &= \frac{1}{4\pi} (\nabla \times \mathbf{B}) \times \mathbf{B} \\ &= \frac{1}{4\pi} (\mathbf{B} \cdot \nabla) \times \mathbf{B} - \nabla \frac{\|\mathbf{B}\|^2}{8\pi}. \end{aligned}$$

The second term corresponds to the magnetic pressure $P_{mag} = \frac{\|\mathbf{B}\|^2}{8\pi}$, while the first corresponds to a magnetic tension. Because of the cylindrical geometry ($\|\mathbf{B}\| = \mathbf{B} \cdot \mathbf{e}_\theta$), the magnetic tension may be rewritten $T_{mag} = -\frac{2P_{mag}}{r} \mathbf{e}_r$, with $r = \mathbf{r} \cdot \mathbf{e}_r$ [48, 49]. The momentum equation then reads:

$$\rho D_t \mathbf{u} = -\nabla P - \nabla P_{mag} + T_{mag}. \quad (1.32)$$

1.4.2 Energy equation

The presence of magnetic fields in the system also implies a modification in the energy equation(s). Indeed, some energy is taken from the hydrodynamics to build up the magnetic field (see the magnetic pressure term in the momentum equation), and on the opposite side, the magnetic field releases some energy back to the hydrodynamics. The evolution of the magnetic energy then reads:

$$D_t P_{mag} = D_t \frac{B^2}{8\pi} = \frac{1}{8\pi} \left[\frac{\partial B^2}{\partial t} + \mathbf{u} \cdot \nabla B^2 + B^2 \nabla \cdot \mathbf{u} \right] = \frac{1}{8\pi} \left[\frac{\partial B^2}{\partial t} + \nabla \cdot (B^2 \mathbf{u}) \right].$$

Using Ohm’s law (Eq. 1.25), one may write the equations for the internal, kinetic and magnetic energies. (For visibility, only the exchange terms are shown, not the transport

³If L is a characteristic length of the system then, with Ampere’s law $\mathbf{j} = \frac{c}{4\pi} \nabla \times \mathbf{B}$, the $\frac{1}{c} \mathbf{j} \times \mathbf{B}$ term has the dimension $[B^2/L]$, while the $-4\pi (\mathbf{j} \cdot \nabla) \mathbf{j} / \omega_{pe}^2$ term has the dimension $[c^2 B^2 / L^3 \omega_{pe}^2]$. The ratio of the two gives the dimension $[L^2 \omega_{pe}^2 / c^2]$, yet $L \gg c / \omega_{pe} = \delta_{nc}$, where δ_{nc} is the non-collisional skin depth.

ones such as the heat flux *etc.*)

$$\rho D_t \mathcal{E} = -P \nabla \cdot \mathbf{u} + \frac{j^2}{\sigma} - \mathbf{j} \cdot \frac{1}{eN_e} \nabla P_e + \dots \quad (1.33)$$

$$\frac{\rho}{2} D_t u^2 = +P \nabla \cdot \mathbf{u} - \mathbf{j} \cdot \left(\frac{\mathbf{u}}{c} \times \mathbf{B} \right) + \dots \quad (1.34)$$

$$D_t P_{mag} = -\frac{j^2}{\sigma} + \mathbf{j} \cdot \frac{1}{eN_e} \nabla P_e + \mathbf{j} \cdot \left(\frac{\mathbf{u}}{c} \times \mathbf{B} \right) + \dots \quad (1.35)$$

where:

- $P \nabla \cdot \mathbf{u}$ is the pressure's work that links the internal and kinetic energies,
- $\frac{j^2}{\sigma}$ is the resistive dissipation of the magnetic field (Joule effect),
- $\mathbf{j} \cdot \frac{1}{eN_e} \nabla P_e$ is the thermo-electric source of the magnetic field,
- $\mathbf{j} \cdot \left(\frac{\mathbf{u}}{c} \times \mathbf{B} \right)$ is the magnetic field induction (dynamo effect).

1.4.3 Ohm's law and B-field induction equation

The B-field induction equation comes from Faraday's law:

$$\frac{\partial \mathbf{B}}{\partial t} = -c \nabla \times \mathbf{E}. \quad (1.36)$$

Using \mathbf{E} from Ohm's law, formulated with Braginskii's notations (Eq. 1.25), and \mathbf{j} replaced using Ampere's law

$$\mathbf{j} = \frac{c}{4\pi} \nabla \times \mathbf{B}, \quad (1.37)$$

where the displacement current $\partial \mathbf{E} / \partial t$ has been neglected (the two terms are in the ratio u^2/c^2 [49]), we get:

$$\frac{\partial \mathbf{B}}{\partial t} = \nabla \times \left[\frac{c}{eN_e} \nabla P_e + (\mathbf{u} \times \mathbf{B}) - \frac{c}{4\pi} \bar{\alpha} \nabla \times \mathbf{B} - \frac{c(\nabla \times \mathbf{B}) \times \mathbf{B}}{4\pi eN_e} + \frac{k_b c \bar{\beta}}{e} \nabla T_e \right]. \quad (1.38)$$

Let us detail each term of (Eq. 1.38):

- $\nabla \times \left(\frac{c}{eN_e} \nabla P_e \right) = \frac{k_b c}{e} \frac{\nabla T_e \times \nabla N_e}{N_e}$ is the thermo-electric source term (Biermann battery effect),
- $\nabla \times (\mathbf{u} \times \mathbf{B})$ is the advection of the magnetic field by the fluid,

- $-\frac{c}{4\pi}\nabla \times (\bar{\alpha}\nabla \times \mathbf{B})$ is the $\frac{\mathbf{j}}{\sigma}$ resistive diffusion (Joule effect),
- $-\frac{c}{4\pi e}\nabla \times \left(\frac{(\nabla \times \mathbf{B}) \times \mathbf{B}}{N_e}\right)$ is the $\mathbf{j} \times \mathbf{B}$ Hall source term,
- $\frac{k_b c}{e}\nabla \times (\bar{\beta}\nabla T_e)$ is the Nernst source term, which will be described in the following subsection.

Nonetheless, the thermo-electric and Hall source terms are in the ratio:

$$\frac{|\nabla \times (P_e/eN_e)|}{|\nabla \times (\mathbf{j} \times \mathbf{B}/eN_e)|} \propto \frac{|(P_e/eN_e)L|}{|(B^2/eN_e)|} \propto \frac{P_e}{P_{mag}}.$$

Hence, because laser generated plasmas are expected to be in a regime where $P_e \gg P_{mag}$, the Hall source term will be neglected hereafter.

1.4.4 Nernst effect

As we saw, the magnetic field induction equation presents a term arising from thermo-electric effects, the Nernst source term, which may be expanded as:

$$\frac{\partial \mathbf{B}}{\partial t}_{Nernst} = \frac{k_b c}{e}\nabla \times (\beta_{\perp}\nabla T_e + \beta_{\parallel}\mathbf{b} \times \nabla T_e). \quad (1.39)$$

In the hypothesis of a Lorentz plasma⁴ ($Z \rightarrow \infty$, $\chi \rightarrow 0$), $\beta_{\perp} \rightarrow 3/2$ (see the asymptote for $\chi \rightarrow 0$ in Fig. 1.10): hence, under this hypothesis, β_{\perp} is constant. Moreover, from the vectorial property $\nabla \times \nabla x = 0$, we have $\nabla \times (\beta_{\perp}\nabla T_e) = 0$, which gives:

$$\begin{aligned} \frac{\partial \mathbf{B}}{\partial t}_{Nernst} &= \frac{k_b c}{e}\nabla \times (\beta_{\parallel}\mathbf{b} \times \nabla T_e) \\ &\equiv \nabla \times (\mathbf{u}_{Nernst} \times \mathbf{B}), \end{aligned} \quad (1.40)$$

where $\mathbf{u}_{Nernst} \approx -\frac{k_b c}{e}\frac{\beta_{\parallel}}{\|\mathbf{B}\|}\nabla T_e$ is assimilated to a velocity.

The Nernst effect may then be assimilated to an advection of the magnetic field at a characteristic velocity \mathbf{u}_{Nernst} which may be included in the advection term of the B-field induction equation (Eq. 1.38):

$$\frac{\partial \mathbf{B}}{\partial t} = \nabla \times \left[\frac{c}{eN_e}\nabla P_e + (\mathbf{U} \times \mathbf{B}) - \frac{c}{4\pi}\bar{\alpha}\nabla \times \mathbf{B} - \frac{c(\nabla \times \mathbf{B}) \times \mathbf{B}}{4\pi eN_e} \right], \quad (1.41)$$

where the magnetic field is advected with a velocity $\mathbf{U} = \mathbf{u}_{flow} + \mathbf{u}_{Nernst}$.

⁴In the Lorentz plasma approximation, the electrons are supposed to collide only with fixed ions. Therefore, because $\nu_{ei} = Z\nu_{ee}$, it correspond to the limit $Z \rightarrow \infty$. [37]

Still under the Lorentz plasma hypothesis, β_λ may be linked to $\kappa_\perp = K_{SH}$ as:

$$\beta_\lambda \approx \frac{e}{k_b c} \frac{\|\mathbf{B}\| K_{SH}}{\frac{3}{2} N_e k_b T_e}. \quad (1.42)$$

Injecting (Eq. 1.42) into (Eq. 1.40) leads to a *thermal Nernst velocity*, where the 3/2 term comes from $1/(\gamma - 1)$ with $\gamma = 5/3$:

$$\mathbf{u}_{Nernst} \approx \frac{-K_{SH} \nabla T_e}{\frac{3}{2} P_e} = \frac{\mathbf{Q}_{SH}}{\frac{3}{2} P_e}. \quad (1.43)$$

One may question the validity of this thermal Nernst effect, as we assumed $\chi \rightarrow 0$. Using kinetic calculations, Kho and Haines [14] have shown that the Nernst effect is strongly linked to \mathbf{u}_T , the velocity associated with the heat-flow: the ratio $\mathbf{u}_{Nernst}/\mathbf{u}_T$ is varying from 1 in the case of a Lorentz plasma to 0.7 for $\chi \gg 1$. While this deviation by a factor 0.7 from the kinetic results may seem quite important, one has to keep in mind that while both χ and \mathbf{Q} can extend over several orders of magnitude, this ratio remains close to unity, showing a strong correlation between the heat flux and the Nernst effect.

By extension of (Eq. 1.43), we define the Nernst velocity for any heat flux \mathbf{Q} :

$$\mathbf{u}_{Nernst} \approx \mathbf{u}_T = \frac{\mathbf{Q}}{\frac{3}{2} P_e}. \quad (1.44)$$

Note that hereafter, unless specified, the Nernst velocity is referring to \mathbf{u}_T .

NERNST EFFECT

Advection of the magnetic field by the heat flux:

the electrons carrying the heat, while in small number, are less collisional and thus more efficient at transporting the B-field through the plasma.

Finally, one may think that the ‘‘Braginskii’s’’ Nernst velocity, as defined in (Eq. 1.40), may be more robust than the thermal one (Eq. 1.44). Nonetheless, for the first, the hypothesis of a weakly magnetized plasma may be very restrictive. Indeed, as we will see, the non-locality of the heat flux is due to the low collisionality of the electrons carrying the heat flux, which means that they are easily magnetized (as $\chi = \omega_{ce} \tau_{ei} \propto v^3$). On the contrary, the second has been validated *a-posteriori* by kinetic calculations, and while not fully capturing the physics, expresses the main effect: that the low collisional electrons are more efficient at transporting the magnetic field.

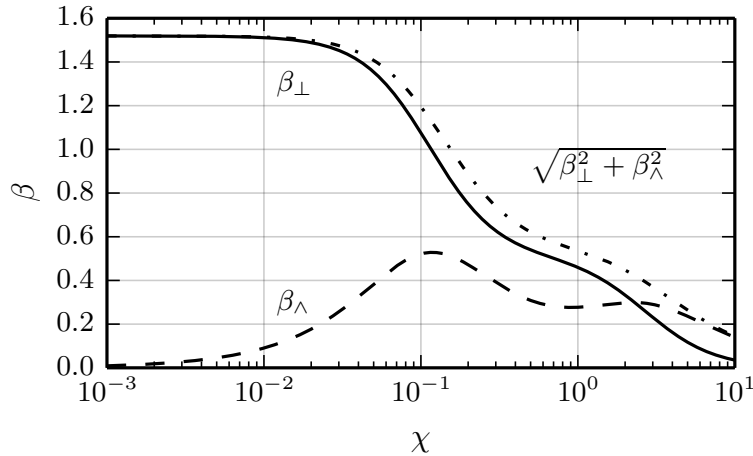


Figure 1.10: Thermoelectric coefficients β_{\perp} , β_{\parallel} and $\sqrt{\beta_{\perp}^2 + \beta_{\parallel}^2}$ as a function of the magnetization χ , for $Z \rightarrow \infty$.

1.5 Modeling the non-local heat flux in FCI2

As we saw in sec. 1.2.4, the linear theory is not valid for laser-solid interactions because of the long mean free path of the heat carrying electrons, larger than the temperature gradient lengths, having led physicists to the use of flux limiters for decades. To overcome this arbitrary truncation, Luciani, Mora and Virmont [21] proposed the intuitive idea to convolve the Spitzer-Härm heat flux by a delocalization kernel W , mimicking the dependence of hydrodynamic parameters at long range. The heat flux in one dimension then reads:

$$Q(x) = \int_{-\infty}^{+\infty} W(x, x') Q_{SH}(x') dx'. \quad (1.45)$$

Note that the kernel has to fall back to a Dirac function in the case of a small mean free path (optically thick plasma, by analogy with radiation transport). Hence, the authors proposed this first convolution kernel (illustrated in Fig. 1.11)

$$W(x, x') \equiv \frac{1}{a\lambda_e(x')} \exp\left(-\frac{\tau(x, x')}{a\lambda_e(x')}\right), \quad \text{with } \tau(x, x') = \frac{\left|\int_x^{x'} N_e(x'') dx''\right|}{N_e(x')}, \quad (1.46)$$

where $\lambda_e = \sqrt{\lambda_{ee}^{th} \lambda_{ei}^{th}} = \frac{(k_b T_e)^2}{4\pi e^4 N_e \sqrt{Z} \ln \Lambda}$ is the mean free path of the thermal electrons.

The use of such a convolution kernel gives a good agreement with 1D Fokker-Plank calculations [50]. Other kernels have been proposed [51, 52, 53] and the concept has been expanded to more dimensions [22]. Yet, the convolution in more than one dimension is too long to calculate, as for each point one has to convolve the heat flux all over the simu-

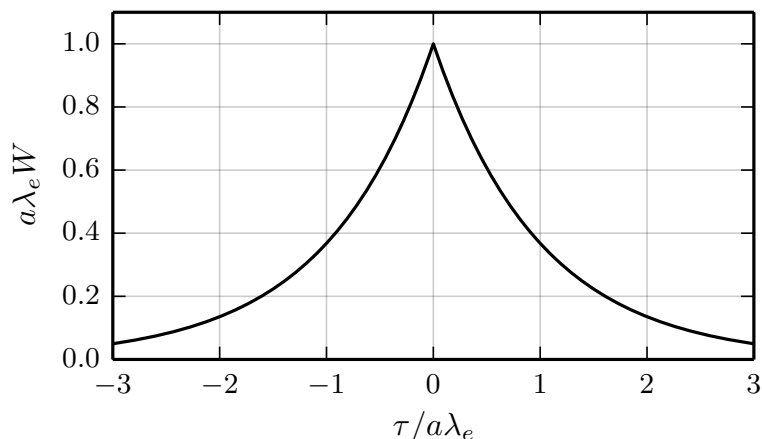


Figure 1.11: *LMV delocalization kernel*

lation box by a function which is itself an integral. Moreover, note that none of the most common proposed kernels have been derived from first principles, but have been adjusted to fit Fokker-Planck simulations. The extension to 2D and 3D by Schurtz, Nicolaï and Busquet (sometimes called SNB) [22], leads to a multi-group diffusion model in which the kernel associated to each group becomes symmetrical. It was first implemented in FCI2 and is now used in many hydro-radiative codes such as CHIC (CELIA), HYDRA (LLNL), LILAC (LLE) and DUED (U. Roma) [54, 55, 56].

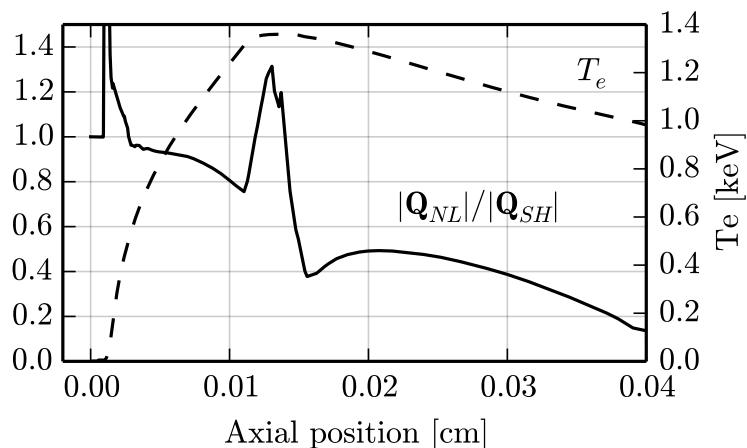


Figure 1.12: *2D FCI2 simulation using a non-local heat flux with B-field for a plastic target irradiated by a $\sim 10^{14} \text{ W/cm}^2$, 1ω laser pulse. Lineout over the symmetry axis at 0.6 ns of the ratio $\|Q_{NL}\| / \|Q_{SH}\|$ (solid) and of T_e (dashed). The laser comes from the right.*

Using a non-local model for the heat flux leads to a significant improvement in the calculation of the energy equation, as it accounts for kinetic effects which reduce the heat flux in the sharp temperature gradient areas, as well as pre-heat the plasma at the foot of the

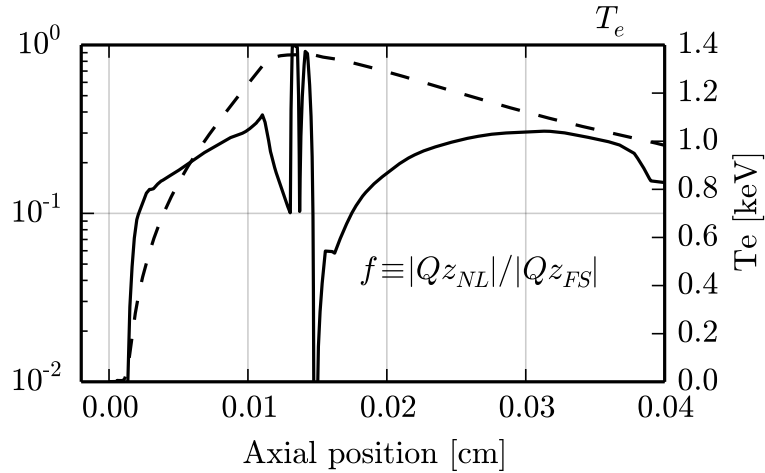


Figure 1.13: *2D FCI2 simulation using a non-local heat flux with B-field for a plastic target irradiated by a $\sim 10^{14} \text{ W/cm}^2$, 1ω laser pulse. Lineout over the symmetry axis at 0.6 ns of the ratio $f \simeq \|\mathbf{Q}_{z,NL}\| / \|\mathbf{Q}_{z,FS}\|$ (solid) and of T_e (dashed). The laser comes from the right and the “z” subscript denotes the axial component.*

conduction zone. More generally, such non-local models allow for a decoupling between the local temperature gradient and the heat flux.

These effects are illustrated in Fig. 1.12. Typically, for laser-foil interactions, they result in a temperature gradient in the corona (right side of Fig. 1.12), in agreement with Fokker-Planck simulations, and opposed to the well-known isothermal corona of flux-limited simulations. Finally, Fig. 1.13 shows the ratio of the axial component of the non-local heat flux over the free streaming one, giving a rough estimate of a flux limiter to apply. Hence, it illustrates the most important feature of a non-local heat flux model which is the absence of an arbitrary, constant, isotropic and global flux limiter parameter.

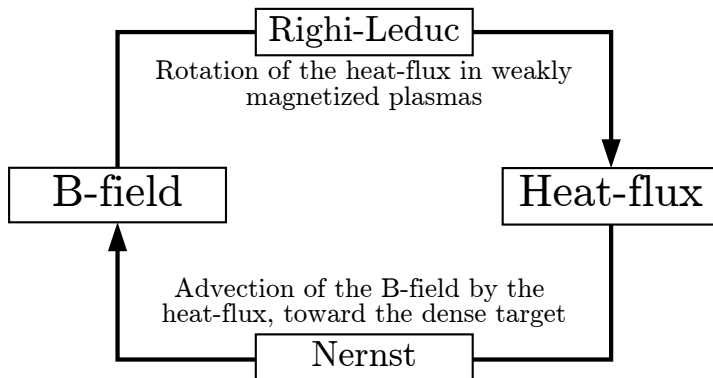


Figure 1.14: *Scheme of the coupling between the magnetic field and the heat flux*

Before presenting how the non-local heat flux is modeled in FCI2, let us introduce the context. In the framework of a solid foil irradiated by a nanosecond, $\sim 10^{14} \text{ W/cm}^2$ laser

pulse, it is useful to recall that the non-colinear density and temperature gradients of the expanding plasma are the source of a magnetic field (Biermann battery, see first term in Eq. 1.38). The geometry of this field is toroidal, due to the axi-symmetry of the expanding plasma (see Fig. 1.2 and Fig. 1.15 for example), and polarized clock-wise when facing the irradiated face of the target. Because of the advection of the field with the heat flux (Nernst effect, Eq. 1.44), the B-field is subjected to a convective amplification toward the dense part of the target. Simultaneously, depending of the magnetization of the electrons, the heat flux may be either unaffected, inhibited, or rotated (Righi-Leduc effect, Eq. 1.28). As we will see, the difficulty is thus to couple consistently the non-local heat flux with the magneto-hydrodynamics, as illustrated in Fig. 1.14.

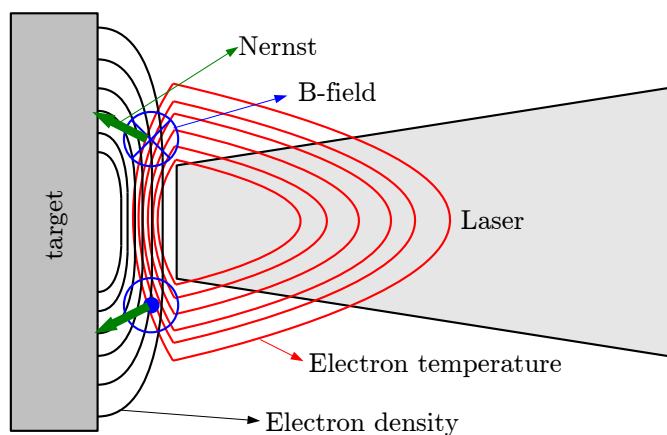


Figure 1.15: Scheme of the thermo-electric source of magnetic field

1.5.1 Presentation of the model

As we saw, the linear theory for the heat flux relies on two major hypotheses: the local thermodynamic equilibrium, *i.e.* the electron distribution function (*EDF*) is a Maxwellian and the small anisotropy of the electron distribution function (P1 system). Nevertheless, the distribution function relaxes to the Maxwellian in a characteristic time given by the electron-electron collision time $\tau_{ee} = \frac{\lambda_{ee}}{v} \propto v^3$, which is longer by a factor Z than that for electron-ions τ_{ei} (see ν_{ee} and ν_{ei} page 22) which characterizes the isotropization time. Therefore, we consider here that the P1 approximation $f(\mathbf{x}, \mathbf{v}, t) = \frac{f_0(\mathbf{x}, v, t)}{4\pi} + \frac{3\boldsymbol{\Omega} \cdot \mathbf{f}_1(\mathbf{x}, v, t)}{4\pi}$ is still valid, but use a perturbative treatment to account for an incomplete equilibration of the distribution function:

$$\begin{aligned}
 f_0 &= f_0^m + h, \\
 \mathbf{f}_1 &= \mathbf{f}_1^m + \mathbf{y}.
 \end{aligned}
 \tag{1.47}$$

The hypothesis of a small departure of the EDF from the Maxwellian is also justified by the fact that, here, we calculate a heat flux for the energy equation of a hydrodynamic code. If h and \mathbf{y} were too important, the whole hydrodynamics reduction would fail as, then, one could not define the system according to the distribution function momenta decomposition. Therefore, more than a hypothesis, this is a requirement.

Let us start back with the kinetic equations (Eq. 1.6 and 1.7), under stationary conditions, and with $\mathbf{C}_1(\mathbf{f}_1) = -\nu_{ei}^* \mathbf{f}_1$:

$$v \nabla \cdot \mathbf{f}_1 - \frac{e\mathbf{E}}{m_e} \cdot \frac{1}{v^2} \frac{\partial}{\partial v} (v^2 \mathbf{f}_1) = C_0(f_0), \quad (1.48)$$

$$\frac{v}{3} \nabla f_0 - \frac{e\mathbf{E}}{3m_e} \frac{\partial f_0}{\partial v} - \frac{e}{m_e} \frac{\mathbf{B}}{c} \times \mathbf{f}_1 = -\nu_{ei}^* \mathbf{f}_1. \quad (1.49)$$

Using the following relations:

- $\mathbf{f}_1^m = -\frac{v}{3\nu_{ei}^*} \left(\frac{m_e v^2}{2k_b T_e} - 4 \right) f_0^m \frac{\nabla T_e}{T_e}$,
- $\nabla f_0^m = f_0^m \left[\frac{\nabla N_e}{N_e} - \frac{3}{2} \cdot \frac{\nabla T_e}{T_e} + \frac{m_e v^2}{2k_b T_e} \cdot \frac{\nabla T_e}{T_e} \right]$,
- $\frac{\partial f_0^m}{\partial v} = -f_0^m \frac{m_e v}{k_b T_e}$,
- $\frac{\nabla N_e}{N_e} + \frac{5}{2} \cdot \frac{\nabla T_e}{T_e} + \frac{e\mathbf{E}_{SH}}{k_b T_e} = 0$ (*i.e.* the null current hypothesis, with $\mathbf{E} = \mathbf{E}_{SH}$),

we can then express (Eq. 1.48 and Eq. 1.49) as:

$$\nu_{ee} h + v \nabla \mathbf{f}_1^m + v \nabla \cdot \mathbf{y} = \frac{e\mathbf{E}}{m_e} \cdot \frac{1}{v^2} \frac{\partial}{\partial v} (v^2 (\mathbf{f}_1^m + \mathbf{y})), \quad (1.50)$$

$$\frac{1}{3} \nabla h = - \left(\frac{\nu_{ei}^*}{v} + \frac{1}{d_E} \right) \mathbf{y} + \frac{\omega_{ce}}{v} \mathbf{b} \times (\mathbf{f}_1^m + \mathbf{y}), \quad (1.51)$$

where:

- \mathbf{f}_1^m and \mathbf{E} come from the Spitzer-Härm model (see Eqs. 1.15 and 1.16, on page 23).
- $C_0(f_0^m + h)$ has been replaced by the Bhatnagar-Gross-Kook (BGK) linear operator $-\nu_{ee} h$ [57]. One may also use the high velocity (HV) approximation $C_0 = v \nu_{ee} \frac{\partial h}{\partial v}$ which couples the different energy groups, or a linear combination of BGK and HV. Finally, FCI2 includes a collision term with a more accurate formulation, close to the Compton term in radiative transport, solved using a modified Young method [58].
- $\frac{eE}{3m_e v} \cdot \frac{\partial h}{\partial v}$ has been replaced by $-\frac{1}{d_E} \cdot \mathbf{y}$ [22, 59, 48], with $d_E = \frac{m_e v^2}{2e \|\mathbf{E}\|}$ the stopping length of an electron of velocity v in an electric field. The $\left(\frac{\nu_{ei}^*}{v} + \frac{1}{d_E} \right) \mathbf{y}$ term is then

equivalent to an harmonic limitation of the mean free path by the electric stopping length: $\left(\frac{1}{\lambda_{ei}} + \frac{1}{d_E}\right) \mathbf{y} = \frac{1}{\lambda} \mathbf{y}$.

The use of the Spitzer-Härm electric field in the non-local model could seem questionable. Its validity is justified because while the high velocity electrons transport the heat flux, they are in very weak number and thus have a small influence on the electric field (see Fig. 1.16 from [22]). This electric field accelerates the low velocity electrons while slowing down the high velocity ones, ensuring the null current condition and a limitation on the electrons' mean free path. Nonetheless, note that the ‘‘SNB’’ non-local model does allow calculating an electric field corrected for the deformed Maxwellian [48, 22, 59]. Yet, unless specified otherwise, we used the Spitzer-Härm electric field $\mathbf{E}_{SH} = \frac{k_b T_e}{e} \left[\frac{\nabla N_e}{N_e} + \frac{5}{2} \cdot \frac{\nabla T_e}{T_e} \right]$ as it allows the simplifications of the different terms in Eq. 1.48 and Eq. 1.49.

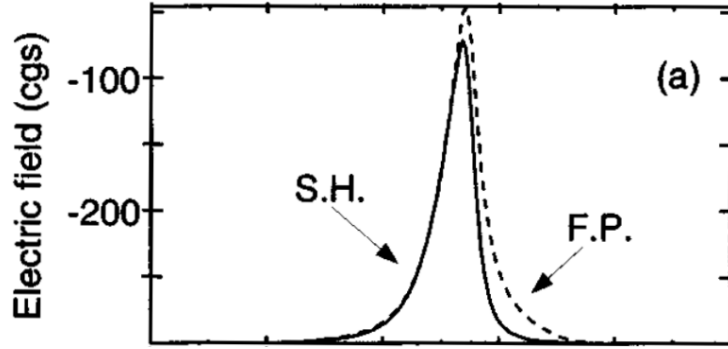


Figure 1.16: *Electric field from Spitzer-Härm (solid) and from a 1D Fokker-Planck calculation (Dashed), as a function of the axial position. From [22].*

Using $\frac{1}{\lambda} = \left(\frac{1}{\lambda_{ei}} + \frac{1}{d_E}\right)$, $\frac{\omega_{ce}}{v} = \frac{\chi_v}{\lambda_{ei}}$ and the vectorial identity $\mathbf{b} \times (\mathbf{b} \times \mathbf{y}) = -\mathbf{y}$ when $\mathbf{b} \perp \mathbf{y}$ allows to write (Eq. 1.51) and $\mathbf{b} \times$ (Eq. 1.51) as:

$$\frac{1}{3} \nabla h = -\frac{1}{\lambda} \mathbf{y} + \frac{\chi_v}{\lambda_{ei}} \mathbf{b} \times \mathbf{f}_1^m + \frac{\chi_v}{\lambda_{ei}} \mathbf{b} \times \mathbf{y}, \quad (1.52)$$

$$\mathbf{b} \times \mathbf{y} = -\lambda \left[\frac{1}{3} \mathbf{b} \times \nabla h + \frac{\chi_v}{\lambda_{ei}} \mathbf{f}_1^m + \frac{\chi_v}{\lambda_{ei}} \mathbf{y} \right]. \quad (1.53)$$

Substituting (Eq. 1.53) in (Eq. 1.52) gives \mathbf{y} as a function of ∇h :

$$\begin{aligned} \mathbf{y} = & -\frac{\chi_v^2}{\lambda_{ei}^2} \cdot \left(\frac{1}{\lambda^2} + \frac{\chi_v^2}{\lambda_{ei}^2} \right)^{-1} \cdot \mathbf{f}_1^m & + \frac{\chi_v}{\lambda \lambda_{ei}} \cdot \left(\frac{1}{\lambda^2} + \frac{\chi_v^2}{\lambda_{ei}^2} \right)^{-1} \cdot \mathbf{b} \times \mathbf{f}_1^m \\ & - \frac{1}{3\lambda} \cdot \left(\frac{1}{\lambda^2} + \frac{\chi_v^2}{\lambda_{ei}^2} \right)^{-1} \cdot \nabla h & - \frac{\chi_v}{3\lambda_{ei}} \cdot \left(\frac{1}{\lambda^2} + \frac{\chi_v^2}{\lambda_{ei}^2} \right)^{-1} \cdot \mathbf{b} \times \nabla h, \end{aligned} \quad (1.54)$$

or in a more concise form:

⁵ $\chi_v \equiv \chi(v)$ refers to a velocity dependent magnetization, opposed to $\chi \equiv \chi(v^{th})$ previously used in Braginskii's model

$$\mathbf{y} = -a_1 \mathbf{f}_1^{\mathbf{m}} + a_2 \mathbf{b} \times \mathbf{f}_1^{\mathbf{m}} - \lambda_1 \nabla h - \lambda_2 \mathbf{b} \times \nabla h. \quad (1.55)$$

Back to (Eq. 1.50) and noting that its right hand side is proportional to $\mathbf{E} \cdot \mathbf{j}$ when integrated over $v^5 dv$ and thus null because of the null current condition, it now writes:

$$\frac{h}{\lambda_{ee}} - \nabla \cdot (\lambda_1 \nabla h + \lambda_2 \mathbf{b} \times \nabla h) = -\nabla \cdot [(1 - a_1) \mathbf{f}_1^{\mathbf{m}} + a_2 \mathbf{b} \times \mathbf{f}_1^{\mathbf{m}}] \quad (1.56)$$

This diffusion equation is solved in the current version of FCI2 using a new solver, adapted to integrate the $\nabla \cdot (\lambda_2 \mathbf{b} \times \nabla h)$ cross term which used to be neglected. This is one of the major improvements from older versions of FCI2 [58].

h and ∇h being solved, the heat flux can be calculated by integrating $\mathbf{f}_1 = \mathbf{f}_1^{\mathbf{m}} + \mathbf{y}$ (Eq. 1.55) over $v^5 dv$.

$$\begin{aligned} \mathbf{Q}_{NL} &= \frac{1}{2} m_e \int_0^\infty (\mathbf{f}_1^{\mathbf{m}} + \mathbf{y}) v^5 dv \\ \mathbf{Q}_{NL} &= \underbrace{+\frac{1}{2} m_e \int_0^\infty (1 - a_1) \mathbf{f}_1^{\mathbf{m}} v^5 dv}_{(1)} \quad \underbrace{+\frac{1}{2} m_e \int_0^\infty a_2 \mathbf{b} \times \mathbf{f}_1^{\mathbf{m}} v^5 dv}_{(2)} \\ &\quad \underbrace{-\frac{1}{2} m_e \int_0^\infty \lambda_1 \nabla h v^5 dv}_{(3)} \quad \underbrace{-\frac{1}{2} m_e \int_0^\infty \lambda_2 \mathbf{b} \times \nabla h v^5 dv}_{(4)} \quad (1.57) \end{aligned}$$

The non-local heat flux then appears as:

- (1) The inhibited Spitzer-Härm heat flux.
- (2) The Righi-Leduc component of the local heat flux.
- (3) The correction for non-local effects
- (4) The Righi-Leduc component of the non-local correction.

Note that both non-local corrections are not proportional to the Spitzer-Härm integrand $\mathbf{f}_1^{\mathbf{m}}$, but to ∇h . As such, even without magnetic field, the resulting non-local heat flux is not collinear to ∇T_e : hence the thermal conduction is always anisotropic.

Fig. 1.17 plots a_1 , a_2 , λ_1 and λ_2 as a function of the velocity dependent Hall parameter χ_v (in the limit $\lambda \rightarrow \lambda_{ei}$). Their shape is very similar to those of X_\perp and X_\wedge (see Fig. 1.9 on page 29), yet because (3) and (4) are corrections to the Spitzer-Härm heat flux, their effect on the heat flux are different.

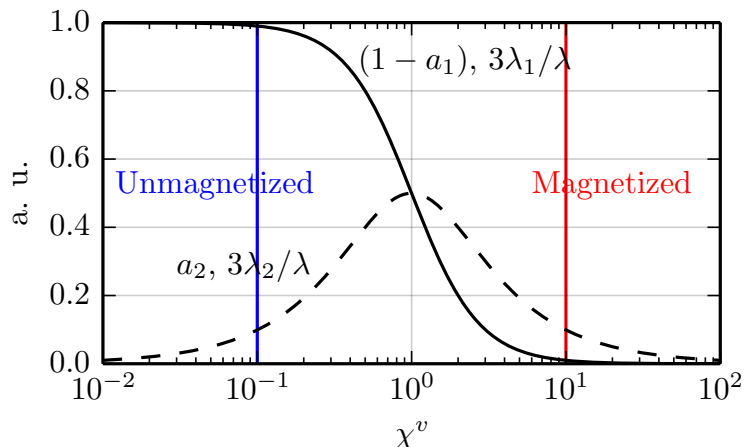


Figure 1.17: $(1 - a_1)$, a_2 , $3\lambda_1/\lambda$ and $3\lambda_2/\lambda$ as functions of the velocity dependent Hall parameter χ_v (in the limit $\lambda \rightarrow \lambda_{ei}$)

- In the limit $\chi_v \rightarrow 0$ (no B-field) and $\mathbf{f}_1 \rightarrow \mathbf{f}_1^{\mathbf{m}}$ ($\nabla h = 0$, no non-local effects), the heat flux falls back to Spitzer-Härm, the base of this heat flux model.
- For $\chi_v \rightarrow 0$ and $\nabla h \neq 0$, the heat flux corresponds to \mathbf{Q}_{SH} , corrected for non-local effects.
- Without non-local effects ($\nabla h = 0$), our model is similar to Braginskii, as the heat flux will be rotated and eventually inhibited as the magnetization increases. Nonetheless, note that the model differs from Braginskii as it uses the Spitzer-Härm integrand $\mathbf{f}_1^{\mathbf{m}}$ and is a multi-group diffusion, even for the local part of the heat flux. As such, every velocity group uses its own magnetization instead of a mean one in the Braginskii model.

Therefore, this new treatment of the non-local heat flux in FCI2 accounts for the close interplay between the magnetic field and non-locality. Indeed, on the one hand, the magnetization (velocity dependent) may inhibit both the local and the non-local effects by reducing the mobility of the electrons or rotate the heat flux through a non-local Righi-Leduc correction. On the other hand, because the Nernst advection of the magnetic field is linked to the heat flux, a correct modeling of the later is crucial as a fast advection may drastically reduce the magnetic field somewhere and compress it somewhere else. As such, it is possible that, at a given point, the heat flux would have been local due to a strong magnetization, but with the fast advection of the field, the magnetization would drop, and cause a re-emergence of non-locality [60].

1.5.2 Different coupling strategies between the magnetic field and the heat flux

To illustrate the importance of this \mathbf{B} -field- \mathbf{Q}_{NL} coupling, we will compare different treatments with results from Fokker-Planck simulations.

Current treatment: Non-Local Spitzer-Härm heat flux (NLSH):

Hereafter, the model presented before is denoted “NLSH” for *Non-Local Spitzer-Härm*, as it is derived from the Spitzer-Härm model, through the use of its integrand \mathbf{f}_1^m and the corresponding electric field \mathbf{E}_{SH} . The Nernst advection velocity uses the thermal definition (Eq. 1.44):

$$\begin{aligned} \mathbf{Q}_{NLSH} = & \frac{1}{2}m_e \int_0^\infty (1 - a_1) \mathbf{f}_1^m v^5 dv & + \frac{1}{2}m_e \int_0^\infty a_2 \mathbf{b} \times \mathbf{f}_1^m v^5 dv \\ & - \frac{1}{2}m_e \int_0^\infty \lambda_1 \nabla h v^5 dv & - \frac{1}{2}m_e \int_0^\infty \lambda_2 \mathbf{b} \times \nabla h v^5 dv \end{aligned} \quad (1.58)$$

$$\mathbf{u}_{Nernst} = \frac{\mathbf{Q}_{NLSH}}{\frac{3}{2}P_e} \quad (1.59)$$

Alternative treatment: Non-Local Braginskii heat flux (“NLBR” model):

As one could see, the “NLSH” model relies on the hypothesis of a heat flux close to the Spitzer-Härm one. As such, the isotropic and anisotropic distribution functions, f_0 and \mathbf{f}_1 , are based on the non-magnetized Maxwellian from the S-H model, f_0^m and \mathbf{f}_1^m , corrected by h and \mathbf{y} such as to solve the kinetic equations including the magnetic field. Therefore, \mathbf{y} includes:

1. The correction relative to the magnetic field, for the Maxwellian part of the distribution function: the $\mathbf{y}_B = -a_1 \mathbf{f}_1^m + a_2 \mathbf{b} \times \mathbf{f}_1^m$ term in Eq.1.55.
2. The correction for non-local effects (themselves affected by the B-field): the $\mathbf{y}_{NL} = -\lambda_1 \nabla h - \lambda_2 \mathbf{b} \times \nabla h$ term in Eq.1.55.

In the “NLBR” (*Non-Local Braginskii*) model presented here, another approach is used. This time, the anisotropic part of the Maxwellian distribution function comes from Braginskii’s model, where \mathbf{f}_1^{Br} is proportional to ∇T_e , $\mathbf{b} \times \nabla T_e$, \mathbf{j} and $\mathbf{b} \times \mathbf{j}$ through transport coefficients, as presented in [59]:

$$\mathbf{f}_1^{Br} = -C_\perp \frac{\mathbf{j}}{v_{th} e N_e} - C_\wedge \mathbf{b} \times \frac{\mathbf{j}}{v_{th} e N_e} - D_\perp \frac{v_{th}}{\nu_{th}} \frac{\nabla T_e}{T_e} - D_\wedge \mathbf{b} \times \frac{v_{th}}{\nu_{th}} \frac{\nabla T_e}{T_e}, \quad (1.60)$$

Once integrated over $v^5 dv$, \mathbf{f}_1^{Br} gives the Braginskii heat flux \mathbf{Q}_{Br} .

The equations for h and \mathbf{y} are thus:

$$\frac{h}{\lambda_{ee}} - \nabla \cdot (\lambda_1 \nabla h + \lambda_2 \mathbf{b} \times \nabla h) = -\nabla \cdot \mathbf{f}_1^{\text{Br}} \quad (1.61)$$

and

$$\mathbf{y} = -\lambda_1 \nabla h - \lambda_2 \mathbf{b} \times \nabla h. \quad (1.62)$$

Moreover, it is possible in the ‘‘SNB’’ non-local formalism to correct the Spitzer-Härm electric field such as to calculate a so-called ‘‘kinetic’’ electric field \mathbf{E}_{kin} , that reduces to \mathbf{E}_{Br} if $h \rightarrow 0$ (see Eq. 35 in [59]). Finally, opposed to the CHIC code, in which the evolution of the magnetic field is calculated using Faraday’s law involving \mathbf{E}_{kin} , we use in the NLBR model a Nernst velocity deduced from the term identified as the Nernst effect in the expression of \mathbf{E}_{kin} . This Nernst velocity is then reported in our magnetic field induction equation (Eq. 1.41 on page 32).

In summary, the heat flux and the Nernst velocity read:

$$\mathbf{Q}_{NLBR} = \mathbf{Q}_{Br} - \frac{1}{2} m_e \int_0^\infty \lambda_1 \nabla h v^5 dv - \frac{1}{2} m_e \int_0^\infty \lambda_2 \mathbf{b} \times \nabla h v^5 dv, \quad (1.63)$$

$$\left. \frac{\partial \mathbf{B}}{\partial t} \right|_{Nernst} \equiv \nabla \times (\mathbf{u}_{Nernst} \times \mathbf{B}) = \nabla \times \mathbf{E}_{kin, Nernst}. \quad (1.64)$$

Non-local heat flux without Nernst effect (‘‘No Nernst’’):

While being unphysical, this method allows to shed light onto the importance of the advection of the field by the heat flux, *i.e.* the re-emergence of non-locality because of the field being swept away by the Nernst effect.

$$\begin{aligned} \mathbf{Q}_{NLSH} = & \frac{1}{2} m_e \int_0^\infty (1 - a_1) \mathbf{f}_1^{\text{m}} v^5 dv & + \frac{1}{2} m_e \int_0^\infty a_2 \mathbf{b} \times \mathbf{f}_1^{\text{m}} v^5 dv \\ & - \frac{1}{2} m_e \int_0^\infty \lambda_1 \nabla h v^5 dv & - \frac{1}{2} m_e \int_0^\infty \lambda_2 \mathbf{b} \times \nabla h v^5 dv \end{aligned} \quad (1.65)$$

$$\mathbf{u}_{Nernst} = 0 \quad (1.66)$$

Braginskii (“Br” Model):

Being the most used model when studying self-generated magnetic fields in laser-generated plasmas, we will also include the Braginskii model for the sake of comparison.

$$\begin{aligned}\mathbf{Q}_{Br} &= -\frac{k_b T_e \bar{\beta}}{e} \cdot \mathbf{j} - \bar{X} \cdot \mathbf{Q}_{SH} \\ &= \left(-\frac{k_b T_e}{e} \beta_{\perp} \mathbf{j} - X_{\perp} \mathbf{Q}_{SH} \right) + \mathbf{b} \times \left(-\frac{k_b T_e}{e} \beta_{\wedge} \mathbf{j} - X_{\wedge} \mathbf{Q}_{SH} \right)\end{aligned}\quad (1.67)$$

$$\mathbf{u}_{Nernst} = \frac{\mathbf{Q}_{Br}}{\frac{3}{2} P_e} \quad (1.68)$$

1.5.3 Comparison with a Fokker-Planck code: ALADIN

The first step in the validation of the new magnetized non-local treatment model in FCI2 was, as is usual in any study on electron transport, to benchmark it against Fokker-Planck simulations. For this, the ALADIN code, developed at CEA, has been used.

ALADIN is a planar 2D Vlasov-Fokker-Planck-Landau code dedicated to the study of electron transport and its interplay with electro-magnetic fields. As such it solves the kinetic equation for the non-degenerated electron population in the P1 system (Eq. 1.6 and Eq. 1.7) and the ions are supposed to be infinitely heavy (no fluid motion). As opposed to other codes [61], there is no hypothesis of quasi-neutrality of the plasma, hence allowing high electric fields to originate from charge separation. The evolution of the electric field is governed by Ampère’s law, where the displacement current is accounted for. To complete the electro-magnetic equations, the magnetic field evolution follows Faraday’s law.

The system of equations to solve is thus:

$$\frac{\partial f_0}{\partial t} + v \nabla \cdot \mathbf{f}_1 - \frac{e \mathbf{E}}{m_e} \cdot \frac{1}{v^2} \frac{\partial}{\partial v} (v^2 \mathbf{f}_1) = C_0 + C_{ei}^L, \quad (1.69)$$

$$\frac{\partial \mathbf{f}_1}{\partial t} + \frac{v}{3} \nabla f_0 - \frac{e \mathbf{E}}{3 m_e} \frac{\partial f_0}{\partial v} - \frac{e}{m_e} \frac{\mathbf{B}}{c} \times \mathbf{f}_1 = \mathbf{C}_1, \quad (1.70)$$

$$\frac{\partial \mathbf{E}}{\partial t} = c \nabla \times \mathbf{B} - 4\pi \mathbf{j}, \quad (1.71)$$

$$\frac{\partial \mathbf{B}}{\partial t} = -c \nabla \times \mathbf{E}, \quad (1.72)$$

with the current:

$$\mathbf{j} = -e \int \mathbf{f}_1 v^3 dv$$

and where the scalar collision term (thermalization) is defined from the Rosenbluth coefficients [38]:

$$\begin{aligned} C_0(f_0) &= \frac{\nu_{ee}}{N_e} \frac{\partial}{\partial v} \left(v f_0(v) E(v) + D(v) \frac{\partial f_0(v)}{\partial v} \right), \\ E(v) &= 4\pi \int_0^v f_0(v') v'^2 dv', \\ D(v) &= \frac{4\pi}{3} v^3 \left(\int_0^v f_0(v') v'^4 dv' + \int_v^\infty f_0(v') v' dv' \right), \end{aligned} \quad (1.73)$$

the vectorial collision term (isotropization) being:

$$\mathbf{C}_1(\mathbf{f}_1) = -\nu_{ei}^* \mathbf{f}_1. \quad (1.74)$$

The laser absorption is described through the inverse bremsstrahlung effect, whose kinetic description is given by Langdon [62]:

$$C_{ei}^L(f_0) = \frac{A_L}{v^2} \frac{\partial}{\partial v} \left(\frac{l(v)}{v} \frac{\partial f_0}{\partial v} \right), \quad (1.75)$$

where $A_L = \frac{4\pi e^4 N_i Z^4 \ln \Lambda_{ei}}{6m_e^2} \cdot \frac{v_0^2}{v_{th}^2}$, v_0 is the mean velocity of the electrons in the laser electric field, such that $\frac{v_0^2}{v_{th}^2} \simeq 4 \cdot 10^{-16} \frac{I_l \lambda_l}{k_b T_e}$. I_l [W/cm^2] is the laser intensity and λ_l [cm] its wavelength.

Benchmark parameters

For the sake of comparison with previously published results [22], the different FCI2 non-local models have been benchmarked against ALADIN using a test case close to the one proposed by Epperlein [63]. It reproduces a simplified ideal laser-foil experiment: the target is a $25 \mu m$ thick Beryllium foil with an uniform initial electron temperature of $250 eV$, ensuring the full ionization of the plasma ($Z = 4$). The electron density exponentially decreases from $10^{23} cm^{-3}$ at $x = 25 \mu m$ to $4.2 \times 10^{20} cm^{-3}$ at $x = 150 \mu m$ and is constant for $x > 150 \mu m$, mimicking the hydrodynamic expansion of the foil (see Fig. 1.18).

The target is irradiated from the increasing x direction, by a 3^{rd} harmonic laser pulse ($\lambda_L = 0.35 \mu m$), thus propagating to the critical density $N_c \simeq 9 \times 10^{21} cm^{-3}$ at roughly $x = 0.008 cm$. The laser's spatial intensity profile reads $I = I_0 (1 + \cos(2\pi y/150 [\mu m]))$, with $I_0 = 5 \times 10^{14} W/cm^2$ and its temporal profile is constant (see Fig. 1.19).

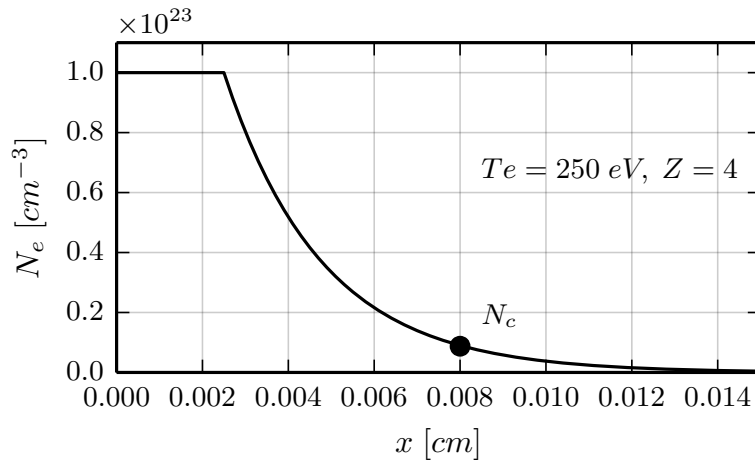


Figure 1.18: *Epperlein’s test: Density profile (cm^{-3}), uniform temperature (250 eV), fully ionized beryllium plasma ($Z = 4$).*

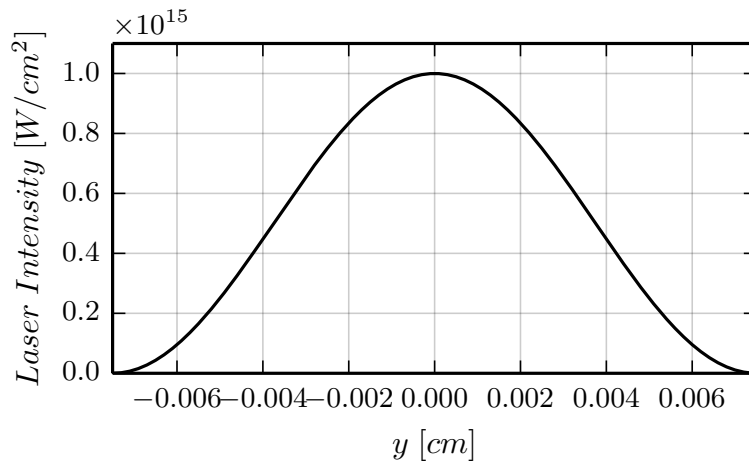


Figure 1.19: *Epperlein’s test: Laser intensity spatial profile [W/cm^2]. The laser intensity is constant over time.*

For both codes, the simulation box has been increased, compared to the one used in [63], to prevent the field from being affected by the boundaries: $450 \mu m$ wide over the “radial” direction (transverse to the laser axis) and $250 \mu m$ over the “axial” direction. It is discretized over a regular mesh of $4 \times 4 \mu m$ cells. Because ALADIN’s geometry is 2D Cartesian and FCI2’s one 2D axi-symmetrical, the simulation box of FCI2 was placed at a large distance (1 m) from the revolution axis to approximate the planar 2D geometry. Moreover, the absorbed laser power has been checked to match the one of the ALADIN simulation. The laser intensity is null for $|y| > 75 \mu m$ to match the deposited energy with [63] despite of the larger simulation box and sinusoidal intensity profile. Furthermore, ALADIN does not account for ion motion (yet), nor radiation transport. Hence, the

hydrodynamics and radiative transport modules were not activated for the comparative FCI2 simulations. In both cases, the electron distribution function was discretized in 32 velocity groups with a geometrical progression, ensuring a good description of the 10 eV – 4 keV electron energy range.

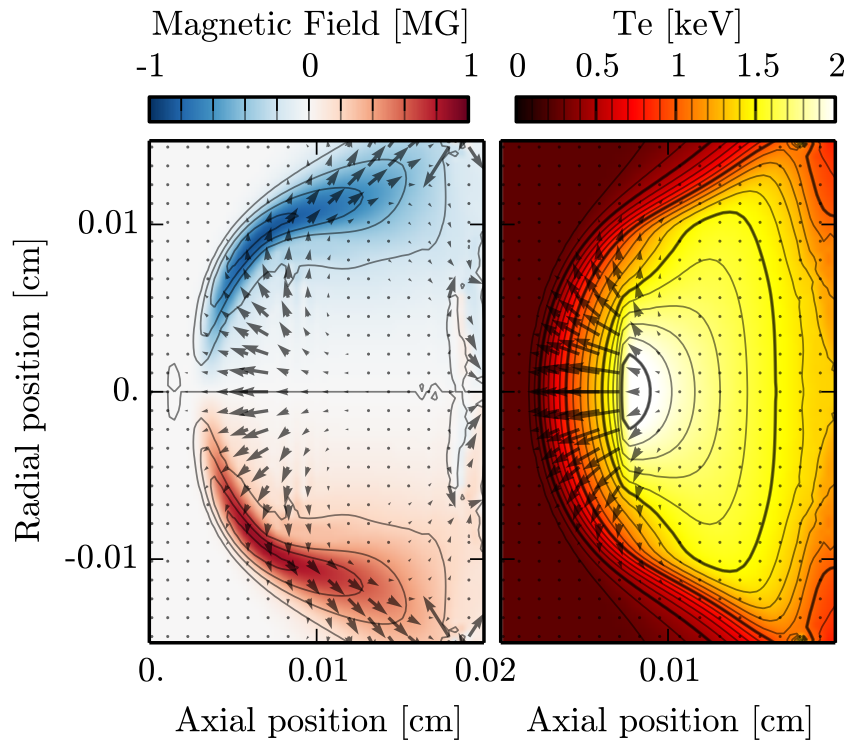


Figure 1.20: Kinetic simulation performed with the ALADIN code (snapshot at $t = 100$ ps). (a) Topology of the magnetic field with vector plots of the Nernst velocity. (b) Topology and isolines of the electron temperature (in keV) with vector plots of the heat flux.

Results

The results given by the ALADIN kinetic simulation are presented in Fig. 1.20 at $t = 100$ ps. It plots both the magnetic field map (with vector plots of the Nernst velocity overlaid) and the electron temperature map (with vector plots of the heat flux).

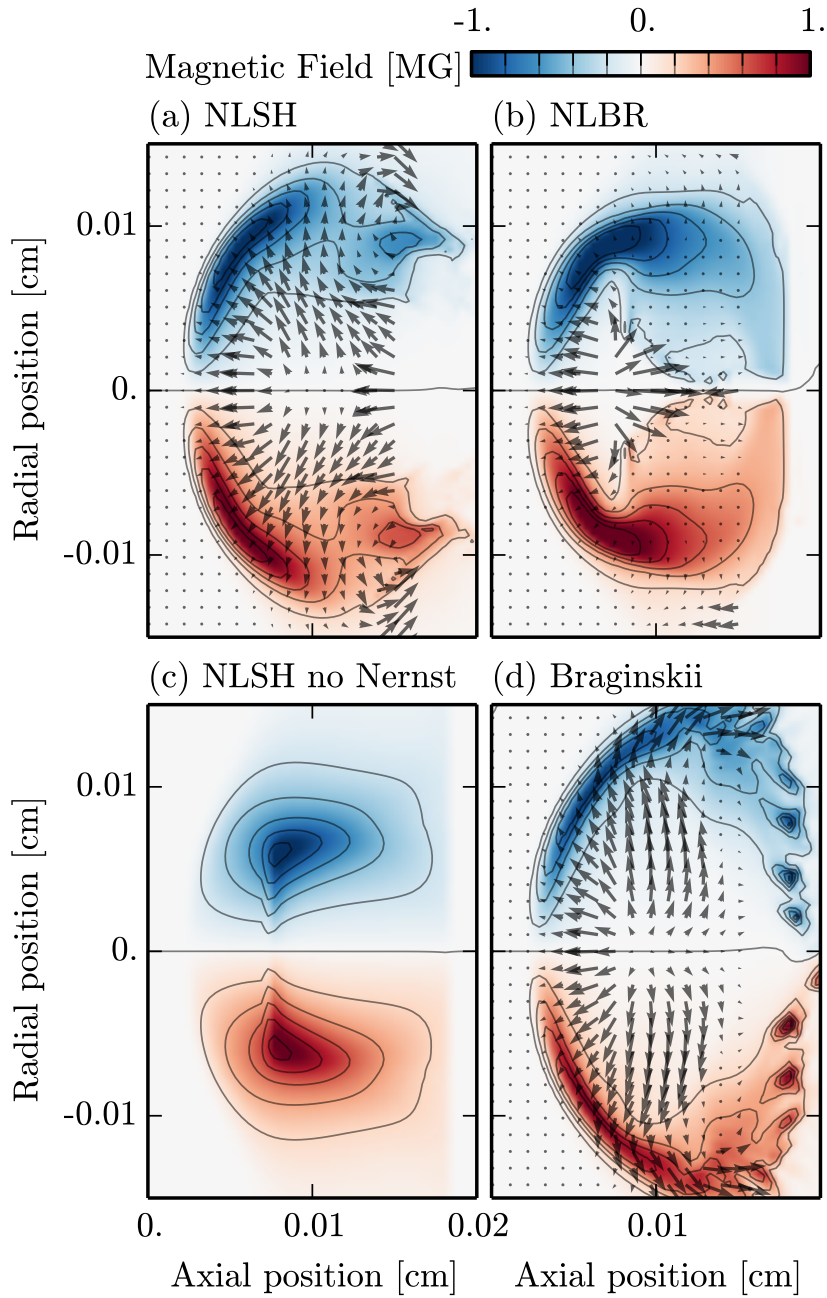


Figure 1.21: *FCI2 simulations (snapshots at $t = 100$ ps) without hydrodynamics, under the same conditions as Fig. 1.20. Topology of the magnetic field with vector plots of the Nernst velocity. (a) NLSH, (b) NLBR, (c) NLSH without Nernst effect, (d) Braginskii model.*

The simulation illustrates the fast advection of the magnetic field toward the over-dense region of the plasma ($\sim 30 \mu\text{m}$). The maximum of the electron temperature near the critical density reaches ~ 2.0 keV and exhibits a significant gradient in the corona along the Ox direction. Finally, it is important to note that due to the non-local and Righi-Leduc effects, the heat flux is no more parallel to the temperature gradient, and even “anti-natural” (*i.e.* a flux from cold to hot) in some places of the corona.

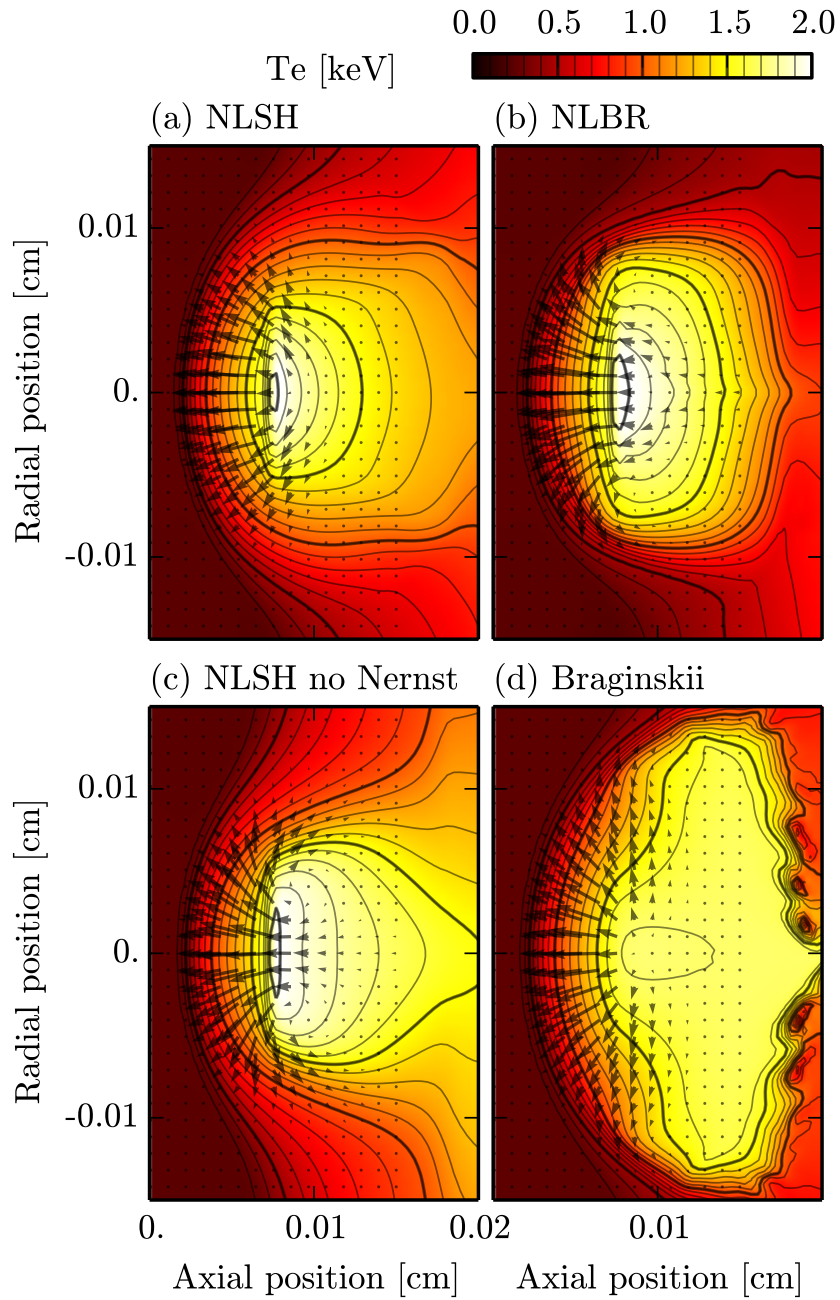


Figure 1.22: *FCI2 simulations (snapshots at $t = 100$ ps) without hydrodynamics, under the same conditions as Fig. 1.20. Topology of the electron temperature (in keV) with vector plots of the heat flux (note that the scale is 2 times smaller for (c)). (a) NLSH, (b) NLBR, (c) NLSH without Nernst effect, (d) Braginskii model.*

Using the same laser, target and mesh conditions, FCI2 simulations were run with the 4 models presented in sec. 1.5.2. Fig. 1.21 presents the resulting topology of the magnetic field, to be compared with Fig. 1.20(a), and Fig. 1.22 presents the electron temperature map to compare with Fig. 1.20(b).

Let us look at each model results:

- Without Nernst effect (**c**), the field can only diffuse in the target (as there is no hydro-motion), a mechanism which is, in this highly conductive part of the plasma, far less effective than advection. As such, the magnetic field remains roughly where it has been generated by the thermo-electric source term and is not subjected to any convective amplification beyond the critical density. Looking at the electron temperature map, it shows the typical non-isothermal corona (along the axial direction) associated with non-local heat flux models. Yet, because of the magnetic field remaining close to the laser axis ($|y| < 0$), the lateral heat conduction is efficiently inhibited, preventing the heating of the corona at larger radii. Finally, note that because of the magnetic field accumulation around the critical density, the Righi-Leduc effect is much more important there than in the kinetic result, in which the field has been swept away.
- Using the Braginskii model (**d**), the magnetic field is indeed subjected to a convective amplification, as the Nernst effect is accounted for (yet defined from a local heat flux). Nevertheless, this model suffers from the use of the linear theory, resulting in an isothermal corona opposed to the rather sharp gradient in the kinetic simulation, as well as an over-estimated lateral conduction (linked to the absence of non-local effect and/or an over-estimated Righi-Leduc rotation). As a consequence of the high heat conduction of the linear theory, the maximum of temperature is lower : $T_e \sim 1.7 \text{ keV}$, opposed to 2.0 keV .
- With the “NLBR” model (**b**), delocalized Braginskii), the strategy used to couple the magnetic field with the heat flux is obviously wrong: we can see that the field is not efficiently swept away by the heat flux, resulting in a strong, small “bubble” of magnetic field acting as a wall for the thermal conduction. This results in a confinement of the heat in a small region of the plasma, of the same size as the laser focal spot ($150 \mu\text{m}$ diameter). This leads to a vicious circle, as the strong inhibition of the heat flux is the source of strong temperature gradients, which themselves increase the thermo-electric source of magnetic field, which reduces the thermal conduction even more, *etc.* The maximum electron temperature is then naturally higher than in the local case: $T_e \sim 2.0 \text{ keV}$, closer to the kinetic simulation.
- In contrast with the previous models, the “delocalized Spitzer-Härm + B-field” coupling (“NLSH” model, **a**) is able to reproduce the results of the Fokker-Planck simulation for both the fast advection of the magnetic field toward the over-dense region of the plasma ($\sim 30 \mu\text{m}$) and the temperature map (in the conduction region). The maximum electron temperature is the same as the kinetic simulation ($T_e \sim 2.0 \text{ keV}$) and the NLSH simulation reproduces the sharp temperature gradient at the critical density, a feature typical of non-local and kinetic models. However, some magnetic field remains in the low density corona, resulting in a slightly lower lateral conduction. This illustrates the difficulty of the coupling between the heat flux and

the B-field in low collisional plasmas: a “weak” magnetic field (compared to the \sim MG field in the dense plasma) remaining in the corona can easily magnetize the electrons, because of the low collisionality, and strongly affect the heat flux.

It is of importance to note that the FCI2’s “NLSH” case matches the ALADIN simulation results only with the “thermal” definition of the Nernst velocity (Eq. 1.43), opposed to the “kinetic” Nernst velocity (Eq. 1.40). Moreover, calculating the electron-electron collision term (C_0) using the modified Young method, instead of the linear combination of High-Velocity and BGK approximations, gives a sharper temperature gradient in the corona, closer to the kinetic calculation, yet at the cost of a higher computing time [58].

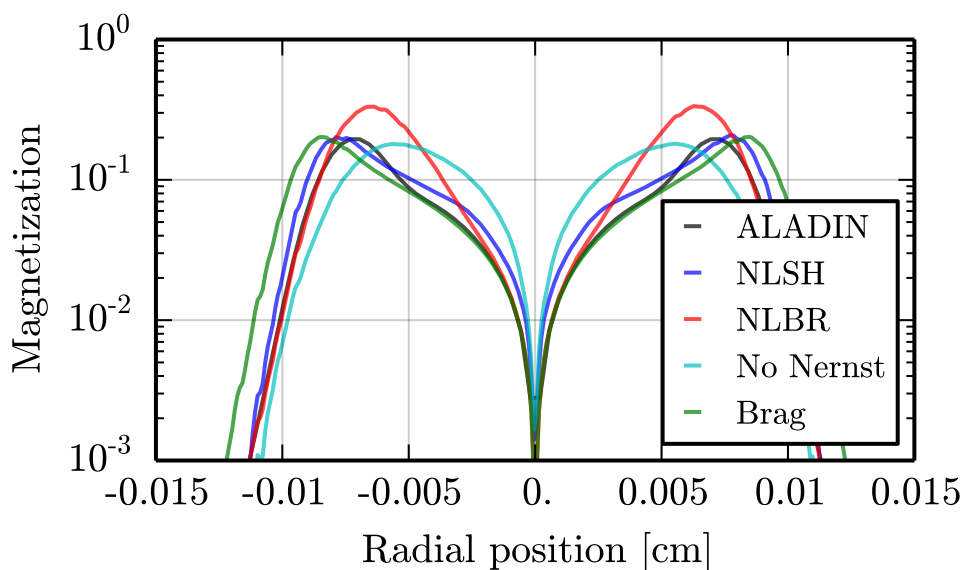


Figure 1.23: Thermal Hall parameter (electron magnetization) $\chi = \omega_{ce}/\nu_{ei}^{th}$ at $t = 100$ ps, plotted along $x = 50 \mu\text{m}$, in the thermal conduction region. The results corresponding to the various simulation cases are shown : Kinetic (black), NLSH (blue), NLBR (red), NLSH without Nernst (cyan) and Braginskii (green).

To finish the comparison between FCI2’s models and ALADIN’s results, Fig. 1.23 draws the “thermal” Hall parameter $\chi = \omega_{ce}/\nu_{ei}^{th}$ (the electron magnetization) along $x = 50 \mu\text{m}$, in the thermal conduction region. As explained earlier, magnetization is a critical parameter, as it defines the relative importance of the non-local and Righi-Leduc corrections compared to the Spitzer-Härm heat flux. In the regime of low Hall parameter $\chi \ll 1$ (*i.e.* a low magnetic field or a very collisional plasma) the heat flux is not affected by the magnetic field, and hence may impair significant non-local effects. In the regime of high Hall parameter $\chi \gg 1$, the heat flux is inhibited due to a limitation of the range of electrons at the Larmor’s radius. Finally, for $\chi \sim 1$, the electrons are weakly magnetized, resulting in a transition regime where the heat flux is progressively inhibited and rotated by the Righi-Leduc effect. Fig. 1.23 shows that in the absence of an effective transport (“No Nernst” case) or an incorrect modelization of the heat flux resulting in an accumulation

of field around the heated region (“NLBR” model), the strong magnetic field at a small distance from the laser axis results in an electron population with a magnetization closer to unity. On the opposite, for the Braginskii and “NLSH” treatments, the magnetic field is effectively transported away, resulting in a low magnetization where the laser energy is deposited. Moreover, the “NLSH” model gives slightly larger magnetization, but it reproduces better the radial “cut-off” of the magnetization than the Braginskii model. Finally, it is important to keep in mind that the Hall parameter plotted here is averaged for the whole electron population, while because $\chi_v \propto v^3$, each electron velocity group may be affected very differently by the magnetic field, hence pointing out the limitation of the “grey” Braginskii model.

Discussion

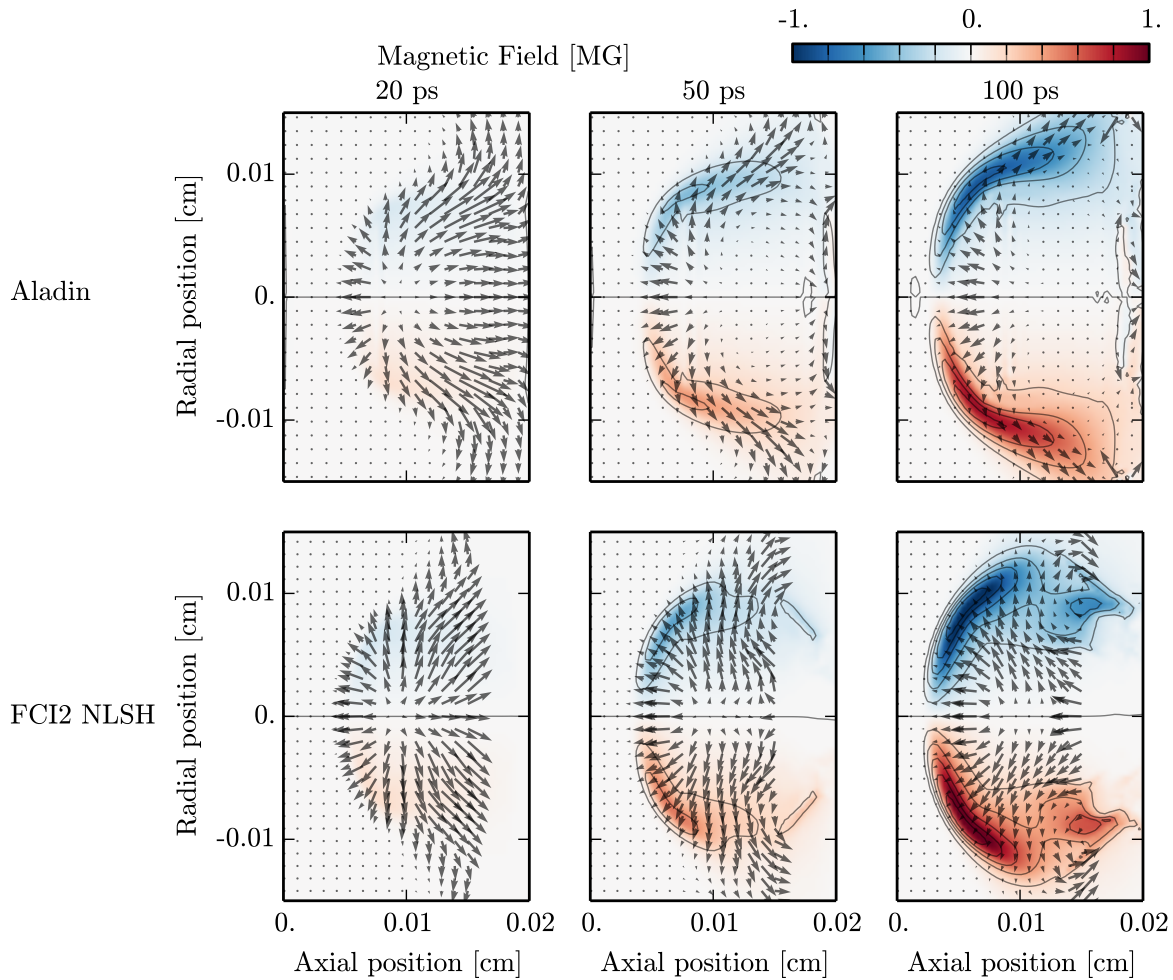


Figure 1.24: Evolution over 100 ps of the magnetic field topology, with vector plots of the Nernst velocity. **Top:** ALADIN (kinetic). **Bottom:** FCI2 (“NLSH” model).

From the previous results, it is clear that the fast advection of the field through the Nernst effect is a key mechanism as it transports away the field to the very collisional part of the

plasma, and thus directly affects the magnetization in the electron conduction region. On the opposite, without Nernst effect, the field stays at the critical density, resulting in a high magnetization and, as a consequence, induces a strong Righi-Leduc rotation as well as a reduction of the non-local effect: that leads to a higher heat flux and thus a lower maximum temperature.

With the Braginskii model, the magnetic field does impair a convective amplification toward the dense plasma through the Nernst effect, which produces a magnetization in the conduction region close to the kinetic model. The low magnetization of the corona should sharpen the electron temperature profile there, because of the non-local effects reducing the thermal conductivity. Yet, because the model relies on a linear transport theory, it cannot reproduce these effects, and then gives a quasi-isothermal corona (typical of a local heat flux), not showing a sharp temperature gradient at the critical density. While this model is an improvement of the Spitzer-Härm heat flux, it is still imperfect, especially in regions of sharp temperature gradient, free of magnetic field.

The “NLBR” and “NLSH” models, compared to the kinetic simulation, show the necessity to treat the heat flux as a perturbation of the Spitzer-Härm one, with a velocity dependent magnetization. Indeed, with the “NLBR” model derived from the Braginskii model (including the Nernst effect), the field, not correctly transported, is concentrated in a small “ball” which inhibits the heat flux.

As the “NLSH” model shows the best agreement with the Fokker-Planck simulation at 100 ps, Fig. 1.24 shows the comparison of the time evolution of the magnetic field between both of them. We observe that despite the large magnetic field, which tends to localize the electron conduction, the field’s quick advection by the heat flux out of the electron conduction region reduces its strength and thus, allows a re-emergence of the non-local mechanisms at this place, which may not be described without a consistent coupling between the non-local formalism and the Nernst and Righi-Leduc effects.

1.6 Conclusions

As we saw all along this chapter, the source and evolution of the magnetic field in laser-generated plasmas is very strongly linked to the heat flux. Indeed, on the one hand, the magnetic field arises from non-collinear gradients of electron density and temperature, which are themselves affected by the heat flux. On the other hand, the magnetic field evolves through diffusion and advection, the latest being the most efficient in the electron conduction region. Yet, within the advection term appears both the fluid and the Nernst velocities, the latter being proportional to the heat flux.

Different models of heat flux have been presented, from the most used one (Spitzer-Härm) to the latest non-local + MHD model of FCI2, as well as the widely used Braginskii heat flux. In every cases, a small anisotropy of the electron distribution function is assumed, hence allowing the use of the “P1” approximation in which the distribution function is expanded in a scalar part and a vectorial one.

For the Spitzer-Härm model, the electron population is also supposed to be at the Local Thermodynamic Equilibrium, which means that the electron distribution function is strictly a Maxwellian. This model is thus placed in the framework of the linear theory, *i.e.* the heat flux is proportional to a thermodynamic quantity, namely the electron temperature gradient. Moreover, it supposes the absence of magnetic fields and the electric field is given by a null current condition ensuring no charge accumulation. This model is the most commonly used in hydro-radiative codes due to its simplicity to implement and to calculate. Yet, it fails at reproducing experimental measurements as in laser-solid interaction, strong temperature gradients arise with a length shorter than the mean free path of the heat-carrying electrons. To correct that, this heat flux is artificially limited to a fraction f of the free streaming heat flux. This arbitrary “knob” in the simulation, despite improving the results, is constant in time, space and direction, and therefore unable to account for kinetic effects.

The Braginskii heat flux is an improvement of the Spitzer-Härm one, as it takes into account a certain magnetization of the electrons. Just as the S-H heat flux, it is derived from the linear theory, defining the heat flux as proportional to hydrodynamic quantities through the use of fitted coefficients. This means that despite accounting for the coupling of the heat flux with the magnetic field through the rotation (Righi-Leduc effect), inhibition of the heat flux and transport of the field by the heat flux (Nernst effect), it is limited by the same validity condition of small temperature gradients. Moreover, in this formalism, the magnetization χ of the electron population is an averaged parameter, function of the thermal velocity. Nonetheless, as the velocity dependent magnetization reads $\chi_v \propto v^3$, the Braginskii model can lead to results far away from the Fokker-Planck simulations.

Finally, we presented how the non-locality of the heat flux is modeled and coupled with

the magnetic field in FCI2. It is based on a perturbative development of the scalar and vectorial electron distribution functions. In the end, the non-local heat flux appears as the sum of four terms: local and non-local, in the direction of ∇T_e (or ∇h) and $\mathbf{b} \times \nabla T_e$ (or $\mathbf{b} \times \nabla h$), in which the inhibition and rotation are functions of the velocity dependent magnetization.

This non-local model (labeled as “NLSH”) as been compared to a kinetic simulation, in a simple case without hydro-motion nor radiative transport. Also presented were: a case without Nernst effect, a case with the Braginskii heat flux, and one with an alternative non-local + MHD heat flux model, based on the Braginskii model. The conclusion from this numerical study is that the “NLSH” model yields results for both the temperature and magnetic field which are the closest to the kinetic simulation. Yet, the agreement holds only if the Nernst effect is treated using the “thermal” Nernst velocity, proportional to the heat flux. Moreover, C. Boniface *et al.* have shown the need to use a lesser approximated electron-electron collision operator (modified Young method) instead of the “BGK” and high-velocity approximations.

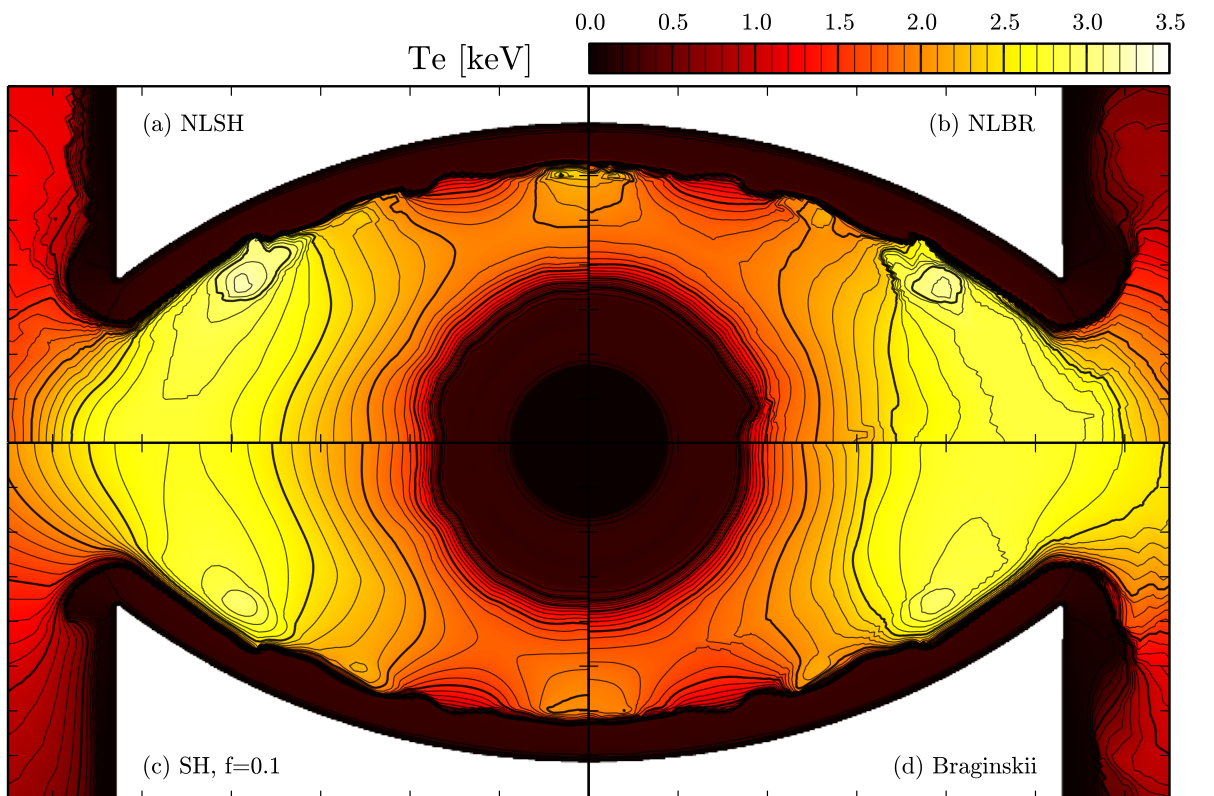


Figure 1.25: Simulations of a typical indirect drive ICF experiment : electron temperature maps deduced from **(a)** “NLSH model”; **(b)** “NLBR model”; **(c)** “sharp cut-off” limited Spitzer-Härm heat flux with $f = 0.1$; **(d)** Braginskii model.

This benchmark, while being of interest to test the models compared to a more sophis-

ticated treatment, relies on a very simplified case without hydrodynamics nor radiative transport. At the end, its validity may only be estimated when comparing experimental results with full-scale simulations, as it will be presented in the following chapter.

To conclude this chapter, we show the influence of the heat flux model, in the framework of indirect drive ICF. Fig. 1.25 presents a simulation of a rugby-shaped gold hohlraum, filled with a low density gas and driven by 1.2 MJ laser at 3rd harmonic. This simulation has been run with four different heat flux models : limited Spitzer-Härm (with $f = 0.1$ and sharp cut-off), local Braginskii, non-local “NLSH” and non-local “NLBR”. It shows that, despite the overall hydrodynamic being governed by the radiative transport, there is still a significant effect on the electron temperature, not only in the gold plasma, but also at the laser entrance hole (LEH) and in the filling gas. This variation in the electron temperature may then affect the propagation of the laser beams, near the LEH and inside the cavity, and ultimately the symmetry of the implosion.

1.6 Conclusions

Page left blank

1.7 Useful equations

Moments of the distribution function (P1 system) :

$$\begin{aligned} N_e &= \int f_0 v^2 dv & \mathcal{E} &= \frac{m_e}{2} \int f_0 v^4 dv \\ \mathbf{J} &= -e \int \mathbf{f}_1 v^3 dv & \mathbf{Q} &= \frac{m_e}{2} \int \mathbf{f}_1 v^5 dv \end{aligned}$$

Kinetic (VFPL) equations :

$$\begin{aligned} \frac{\partial f_0}{\partial t} + v \nabla_{\mathbf{x}} \cdot \mathbf{f}_1 - \frac{e\mathbf{E}}{m_e} \cdot \frac{1}{v^2} \frac{\partial}{\partial v} (v^2 \mathbf{f}_1) &= C_0 \\ \frac{\partial \mathbf{f}_1}{\partial t} + \frac{v}{3} \nabla_{\mathbf{x}} f_0 - \frac{e\mathbf{E}}{3m_e} \frac{\partial f_0}{\partial v} - \frac{e}{m_e} \frac{\mathbf{B}}{c} \times \mathbf{f}_1 &= \mathbf{C}_1 = -\nu_{ei}^* \mathbf{f}_1 \end{aligned}$$

Maxwellian distribution function (isotropic part) :

$$\begin{aligned} f_0^m &= 4\pi N_e \left(\frac{m_e}{2\pi k_b T_e} \right)^{\frac{3}{2}} e^{-(m_e v^2 / 2k_b T_e)} \\ \nabla f_0^m &= f_0^m \left[\frac{\nabla N_e}{N_e} - \frac{3}{2} \cdot \frac{\nabla T_e}{T_e} + \frac{m_e v^2}{2k_b T_e} \cdot \frac{\nabla T_e}{T_e} \right] \\ \frac{\partial f_0^m}{\partial v} &= -f_0^m \frac{m_e v}{k_b T_e} \end{aligned}$$

Spitzer-Härm electric field (null current hypothesis) :

$$\mathbf{E}_{SH} = -\frac{k_b T_e}{e} \left(\frac{\nabla N_e}{N_e} + \frac{5}{2} \frac{\nabla T_e}{T_e} \right)$$

Spitzer-Härm \mathbf{f}_1^m :

$$\mathbf{f}_1^m = -\frac{v}{3\nu_{ei}^*} \left(\frac{m_e v^2}{2k_b T_e} - 4 \right) f_0^m \frac{\nabla T_e}{T_e}$$

Spitzer-Härm's heat flux :

$$\mathbf{Q}_{SH} = -K_{SH} \nabla (k_b T_e), \quad K_{SH} = \frac{64}{Y_{ei}^*} \sqrt{\frac{2}{\pi}} \left(\frac{k_b T_e}{m_e} \right)^{\frac{5}{2}}, \quad Y_{ei}^* = \alpha \left(\frac{4\pi e^4 Z^2 \ln \Lambda_{ei}}{m_e^2} \right)$$

Braginskii's heat flux :

$$\begin{aligned}\mathbf{Q}_{Br} &= -\frac{k_b T_e \bar{\beta}}{e} \cdot \mathbf{j} + \bar{X} \cdot \mathbf{Q}_{SH} \\ &= \left(-\frac{k_b T_e}{e} \beta_{\perp} \mathbf{j} + X_{\perp} \mathbf{Q}_{SH} \right) + \mathbf{b} \times \left(-\frac{k_b T_e}{e} \beta_{\wedge} \mathbf{j} + X_{\wedge} \mathbf{Q}_{SH} \right)\end{aligned}$$

Magnetic field induction equation :

$$\frac{\partial \mathbf{B}}{\partial t} = \nabla \times \left[\frac{c}{e N_e} \nabla P_e + (u \times B) - \frac{c}{4\pi} \bar{\alpha} \nabla \times B - \frac{c (\nabla \times \mathbf{B}) \times \mathbf{B}}{4\pi e N_e} + \frac{k_b c \bar{\beta}}{e} \nabla T_e \right]$$

“Braginskii's” Nernst velocity :

$$\mathbf{u}_{Nernst} \approx -\frac{k_b c}{e} \frac{\beta_{\wedge}}{\|\mathbf{B}\|} \nabla T_e$$

“Thermal” Nernst velocity :

$$\mathbf{u}_{Nernst} \approx \mathbf{u}_T = \frac{\mathbf{Q}}{\frac{3}{2} P_e}$$

Non-local + MHD model in FCI2 :

$$f_0 = f_0^m + h$$

$$\mathbf{f}_1 = \mathbf{f}_1^m + \mathbf{y}$$

$$\frac{1}{\lambda} = \left(\frac{1}{\lambda_{ei}} + \frac{1}{d_E} \right)$$

$$a_1 = \frac{\chi_v^2}{\lambda_{ei}^2} \cdot \left(\frac{1}{\lambda^2} + \frac{\chi_v^2}{\lambda_{ei}^2} \right)^{-1} \quad a_2 = \frac{\chi_v}{\lambda \lambda_{ei}} \cdot \left(\frac{1}{\lambda^2} + \frac{\chi_v^2}{\lambda_{ei}^2} \right)^{-1}$$

$$\lambda_1 = \frac{1}{3\lambda} \cdot \left(\frac{1}{\lambda^2} + \frac{\chi_v^2}{\lambda_{ei}^2} \right)^{-1} \quad \lambda_2 = \frac{\chi_v}{3\lambda_{ei}} \cdot \left(\frac{1}{\lambda^2} + \frac{\chi_v^2}{\lambda_{ei}^2} \right)^{-1}$$

$$\frac{h}{\lambda_{ee}} - \nabla \cdot (\lambda_1 \nabla h + \lambda_2 \mathbf{b} \times \nabla h) = -\nabla \cdot [(1 - a_1) \mathbf{f}_1^m + a_2 \mathbf{b} \times \mathbf{f}_1^m]$$

$$\begin{aligned}\mathbf{Q}_{NLSH} &= \frac{1}{2} m_e \int_0^{\infty} (1 - a_1) \mathbf{f}_1^m v^5 dv && + \frac{1}{2} m_e \int_0^{\infty} a_2 \mathbf{b} \times \mathbf{f}_1^m v^5 dv \\ &- \frac{1}{2} m_e \int_0^{\infty} \lambda_1 \nabla h v^5 dv && - \frac{1}{2} m_e \int_0^{\infty} \lambda_2 \mathbf{b} \times \nabla h v^5 dv\end{aligned}$$

2 Experiments

Introduction

We have seen in chapter 1 that the magnetic field arises from the curl of the fluid pressure's gradient (which corresponds to non-collinear gradients of electron density and temperature). Next, its transport is due to advection not only with the fluid, but also with the heat flux (Nernst effect), to resistive diffusion and, for high β , to the Hall effect (neglected here). In terms of energy exchanges, it corresponds mainly to a transfer between the internal energy of the plasma and the field through the thermo-electric source and the dissipation by Joule effect. Moreover, using a Fokker-Planck code as a reference, we have compared different coupling strategies between the non-local heat flux and the magnetic field. This study has shown that our "NLSH" model is the one that matches the best the kinetic results, and that the interplay between the heat flux and the magnetic field is very strong: the B-field rotates and may even inhibit the heat flux. At the same time, the heat flux, through the Nernst effect, tends to sweep the magnetic field away from the strong electron conduction region, reducing the magnetization. Nonetheless, this study has been devoted to a very limited case: a small spatial scale ($250 \times 450 [\mu m^2]$ simulation box with $4 \times 4 \mu m^2$ cells) with a laser intensity profile of similar scale, no hydro-motion, a simplified density profile and a small duration. In order to quantify the "predictability" of our "non-local+B-field" model in more realistic cases, the only way is to compare the results to those of experiments designed such as to allow the measurement of meaningful quantities.

In the present chapter, we will first recall how the first measurements of the self generated magnetic field in laser generated plasmas, with induction coils and optical diagnostics (Faraday rotation), succeeded in showing that the field is advected deep inside the dense target. Hence, this measurement has been a major difficulty for the experimental studies of laser-solid interaction for a long time. Next, we will present two experimental campaigns which were performed in 2008 (at LULI2000) and 2011 (at JLF-Titan), *i.e.* before this thesis. Following, each diagnostic used during the JLF-Titan campaign will be detailed and we will show how these integrated measurements can be confronted to numerical results using post-processors. More specifically, proton radiography being the most important diagnostic, we will detail how the proton dose modulation pattern depends on the magnetic field topology and will study the sensitivity of the diagnostic to

laser or proton beam variations. This part will end with comparisons of such proton radiography measurements with FCI2 results, showing a good agreement for both low and high Z targets, all along their laser irradiation. Just like in the first chapter, we will conclude with a comparison of the four different heat flux models, previously described in the first chapter, with experimental results from the LULI2000 campaign, showing again a good agreement when using the “NLSH” model.

History of the measurement of self-generated magnetic fields

The presence of self-generated magnetic fields in nanosecond laser produced plasmas has been demonstrated experimentally quite early, compared to the development of the first Q-switched lasers. In 1966 in the USSR, Korobkin and Serov [64] measured a magnetic field in a plasma created by focusing a (2 J, 30 ns) ruby laser pulse in air (see Fig. 2.1). For this, they used coils placed at different locations around the spark (at a centimetric distance, the coil itself had a diameter of 10 mm). This method allows to measure the time derivative of B through the relation $V = NS \frac{\partial B}{\partial t}$, where V is the measured voltage, N the number of turns of the coil and S its surface [65].

The following year, Askar’yan *et al.* [66] measured inducted currents in a solid planar target, showing an increase when a second laser pulse interacts with the plasma generated by a first laser pulse. A few years later, Stamper *et al.* [67], still using inductance coils, probed the magnetic field at various distances from the plasma, such as to measure the gradient of the B -field. They used a (60 J, 30 ns) Nd-glass laser, focused onto either low or higher Z solid targets in an ambient gas, and were limited to measurements between 5 mm and 2 cm away from the target.

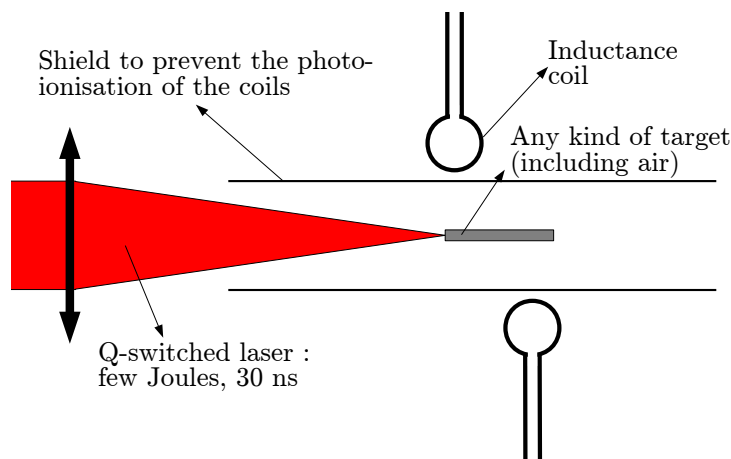


Figure 2.1: Scheme of the Korobkin and Stamper’s experiments

While allowing to experimentally prove the self-generation of magnetic field in laser plasmas (supposedly because of thermo-electric effects), the use of inductance coils is very limited, due to their large size and to the distance at which they can be placed.

The Nernst effect in laser–solid interaction

Furthermore, in 1984, Nishiguchi *et al.* [68, 69] showed that the Nernst effect results in a convective amplification of the magnetic field toward the dense part of the target (see Fig. 2.2). They used a 1D fluid particle code [70], where an initial magnetic field was artificially deposited at the critical density. As such, while the physical source of the B-field was not studied, it appeared that the advection associated with the heat flux was much more effective than the one associated with the bulk fluid motion. The magnetic field was thus compressed at the point where $u_{fluid} = -u_{Nernst}$, roughly at the ablation front, with a saturation mechanism linked to the diffusion of the field. Finally, they showed that using a higher initial magnetic field (100 kG instead of 10 kG) did not significantly change the compression ratio, as the lower thermal conductivity led to a higher temperature gradient and thus to a lower variation of the heat flux.

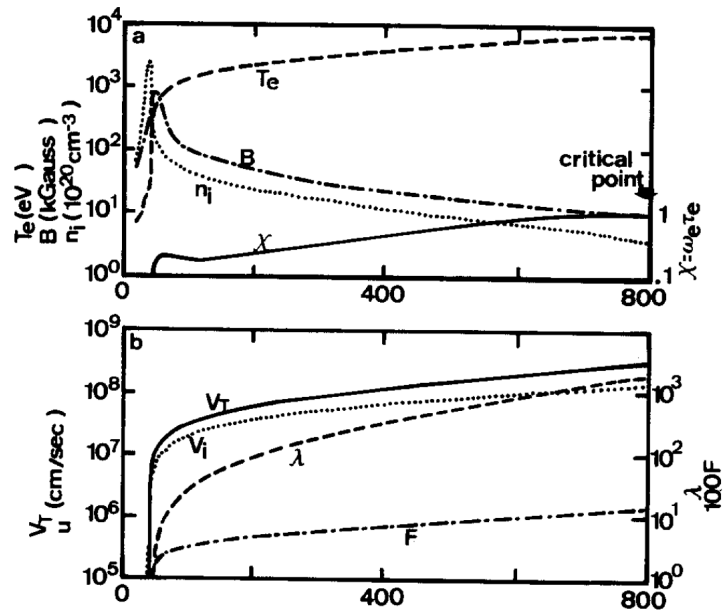


Figure 2.2: Results from Nishiguchi *et al.*'s study. V_T is the Nernst velocity, λ the ratio of the electrons' mean free path over the collisionless skin depth ω_{pe}/c and F the heat flux normalized to the free streaming flux. All quantities are plotted as a function of the axial position (in μm). From [69].

The verification of this fast convective amplification of the magnetic field toward the dense part of the target through the Nernst effect has been a major issue for experimental measurements for a long time. This, because the use of inductance coils is limited to very long range ($\sim \text{cm}$) and the polarimetry (Faraday rotation of the polarization of a probe laser beam) cannot probe the dense part of the solid target. Indeed, the probe beam cannot propagate beyond the critical density ($N_c \simeq 1.1 \times 10^{21} [\text{cm}^{-3}] / \lambda_{laser}^2 [\mu\text{m}]$, *e.g.* at best $\sim 1.8 \times 10^{22} \text{ cm}^{-3}$ for a 4th harmonic laser probe) and is in fact ineffective for much lower densities because of the strong optical index gradients close the dense

part of the target. Nonetheless, around 2001 [71, 23], it became possible to generate laminar MeV protons in laser facilities. These beams are adequate to perform point projection radiography: they have an adapted energy range to allow the protons to be significantly deviated in an integrated magnetic field of $B \cdot dl \sim 10 - 100 \text{ MG} \cdot \mu\text{m}$ [72, 73], while being fast enough to go through a solid thin foil without too much energy loss nor scattering. This new *proton radiography* diagnostic (sometimes more accurately called *proton deflectometry*) paved the way for experiments aiming at the measurement of electric and magnetic fields in dense targets, with very good spatial and temporal resolutions.

2.1 Single laser beam experiments

As discussed in the introduction, the convective amplification of the magnetic field toward the over-dense plasma (compared to the critical density of a probing laser pulse) is a major complication in view of measuring the B-field. As such, even if the presence of B-fields (in the MegaGauss range) in the dense part of the target has been extrapolated from inductance coil measurements and from simulations, time-resolved measurements of the field in the low density plasma (using the optical Faraday mechanism) could only be performed for short-pulse laser generated plasmas [74, 75]. Nonetheless, the development of laminar MeV proton sources, using laser facilities providing either a high number of laser lines (as Omega 60) or a long pulse combined with a short one (as Pico2000, JLF-Titan, Omega-EP *etc.*), allowed to give a new impulse in the experimental study of the magnetization of nanosecond laser generated plasmas. One could cite, for example, the numerous publications of the MIT group [76, 77, 78, 79, 80, 81, 82, 83] in which, using mono-energetic protons from fusion reactions in an imploding backlighter capsule, they have evidenced deflection patterns due to electro-magnetic fields in various configurations, from planar targets to *blow-off* plasmas inside a hohlraum. At the same time, proton radiographies of the electro-magnetic fields generated during nanosecond laser – foil interactions were performed, using a short-pulse laser irradiating a secondary target to produce protons through the *target normal sheath acceleration* TNSA mechanism (see page 86) [84].

Moreover, multiple experiments have shown the need for non-local corrections of the heat flux in numerical models. One could cite, for example, Glenzer *et al.* [85] who, in 1999, showed the presence of localized high electron temperature regions associated with strong temperature gradients, using 4ω Thomson scattering. Moreover, these results could be partially reproduced at “long” times, using Braginskii’s conductivities in their MHD LASNEX simulations. A year later, a CEA (3ω , $8 \times 10^{14} \text{ W/cm}^2$) laser irradiated foil experiment [39] on the Phebus laser facility [86], showed discrepancies between x-ray emission profiles and FCI2’s results. These discrepancies were reduced when accounting

2.1 Single laser beam experiments

both for non-local and B-field effects. Yet, at the time, the non-local corrections did not account for the magnetic field. Indeed, for each point in space where the heat flux was calculated, a smooth transition of the heat flux between Spitzer-Härm, Braginskii and non-local without magnetic field was used. Finally, a LIL campaign (*Ligne d'Intégration Laser* [87], a prototype of a LMJ quad) aimed at measuring the longitudinal ablation front velocity, using the time delay between the x-ray emission of two tracers (Vanadium and Titanium) buried in a CH foil [88]. The experiment has been conducted for various intensities ($0.8 - 2.0 \times 10^{15} \text{ W/cm}^2$) and simulated with CHIC (the hydro-radiative code developed at the CELIA laboratory) using various electron conduction models. The best agreement between the measurements and the results of the post-processed x-ray emission has been found when using a non-local model including the B-field effects [59], although the magnetic field itself was not measured.

2.1.1 LULI2000 (2008)

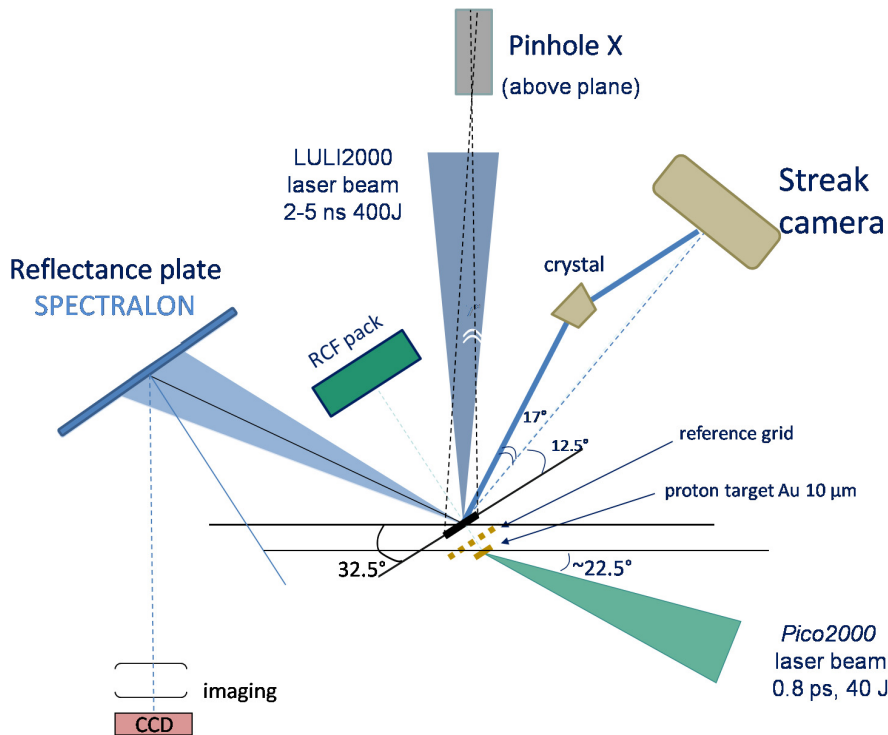


Figure 2.3: Scheme of the experimental setup of the LULI2000 campaign (2008).

From Livia Lancia, PhD thesis, École polytechnique (2010).

While, on the one hand, there were multiple experiments aiming at measuring the self-generated magnetic field, using MeV protons from either fusion product or the TNSA mechanism, on the other hand, experiments also pointed out for an effect of the B-field on the heat flux. However there were at the time no simultaneous measurements of the heat flux and B-field. This motivated an experiment which was performed at LULI2000 in

2008 [89, 90, 60] where, using the Pico2000 configuration, a (kiloJoule, nanosecond) laser line (“North” or “LULI2000 laser beam”) drove the plasma in the main target while the recompressed second line (“south” or “Pico2000 laser beam”, < 1 ps, ~ 40 J) irradiated a secondary target to generate the probing protons.

The main target was a multilayer target made by sputtering deposition. The first tracer was made of Aluminum, while the second one was made of Potassium Bromide, both of them embedded in a silicon bulk and deposited on a CH substrate. From its irradiated face to its back surface, the target was thus made of: $0.3 \mu\text{m}$ Si, $0.09 \mu\text{m}$ Al (first tracer), $1.66 \mu\text{m}$ Si, $0.2 \mu\text{m}$ KBr, $25 \mu\text{m}$ CH. This main target was then irradiated by the North arm of LULI2000 (frequency doubled at 526 nm) with either a *random phase plate* (RPP) or a *phase zone plate* (PZP) to change the focal spot shape between a $145 \mu\text{m}$ *full width at half maximum* (FWHM) Gaussian profile for the RPP and a $228 \mu\text{m}$ FWHM “flat-top” profile for the PZP. The angle of incidence was 32.5° , the pulse length varied between 2 and 5 ns (with a 100 ps rising time) and its energy between 200 and 400 J, such as to set a laser intensity between $1 - 3 \times 10^{14} \text{W}/\text{cm}^2$.

As shown in Fig. 2.3, the diagnostics for this campaign were:

- A reflectance plate (Spectralon) to measure the laser’s reflected energy.
- An x-ray pinhole for 2D, time and wavelength integrated measurements of the plasma emission.
- Proton radiography for measuring the magnetic field using the “south” re-compressed pulse (with distance proton source – main target $d = 3 \text{mm}$, main target – detector $D = 30 \text{mm}$, giving a magnification of $G = \frac{d+D}{d} = 11$).
- Two buried tracers : when the ablation front (defined as the foot of the electron temperature profile) reaches a tracer and heats it, the tracer radiates on specific lines. The time delay between the Al and KBr emissions is therefore representative of the velocity of the electron ablation front. Nonetheless, because of 2D effects, the ablation front was not planar, inducing a slower rising time of the signal, reducing the precision of the measurement. The signal was recorded in the $1.5 - 1.7 \text{keV}$ range with $\sim 2 \text{eV}$ resolution using a KAP crystal and a streak camera with a 10 ns window and $\sim 50 \text{ps}$ time resolution.

Both the time delay between the tracers’ emission and the proton radiography were first compared with post-processed CHIC simulations using a non-local+MHD heat flux model [59]. While the first diagnostic was in a reasonable agreement with the simulation [90] (the time delay in the simulation was $\sim 15\%$ lower than the measurement), the second one showed significantly smaller deflection patterns.

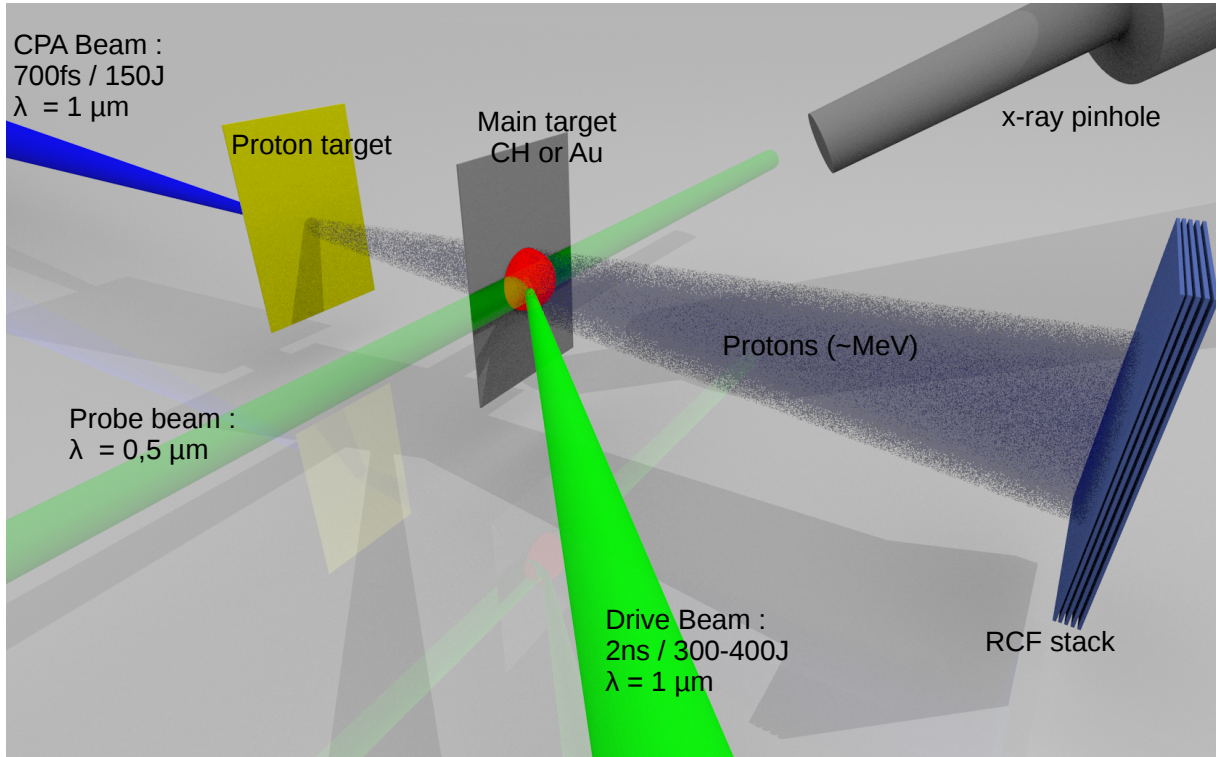


Figure 2.4: *Visualization of the JLF-Titan campaign setup (2011).*

2.1.2 JLF-Titan (2011)

Following the LULI2000 campaign, in which the magnetic field was probed at a single time (600 *ps*, after the beginning of the nanosecond laser pulse), another experimental campaign was performed in 2011 at the JLF-Titan laser facility (see Fig. 2.4), through a new collaboration between the LULI’s SPRINT team and CEA. This time, it was aiming at the measurement of the dynamics of self-generated magnetic fields through proton radiography at different times all along the plasma’s evolution, the results being compared with FCI2 simulations.

The main target was made of materials with different atomic numbers: a low Z one, and a high Z one. Its thickness being a compromise between a thick target for hydrodynamic stability and a thin one to reduce the scattering of the probing protons through the target (see Fig. 2.32, on page 97). As such, the main targets were:

- 23 μm Mylar ($Z^* = 4.5$)
- 5 μm gold ($Z = 79$)

The laser which drove the main target was the “East” beam of JLF-Titan which provided pulses of ~ 400 J at the first laser harmonic ($\lambda_L = 1053$ nm). The temporal profile was a 2 ns square pulse with a 100 ps rising time (hereafter, t_0 denotes the foot of the pulse’s rising slope) and it was focused with an $f/10$ lens. A phase plate was used, whose angular

average can be fitted by the sum of two Gaussians [91], as illustrated on Fig. 2.5 :

$$I_{exp}(r) = 0.54 \times \exp \left[- \left(\frac{r [\mu m]}{49.3} \right)^2 \right] + 1.0 \times \exp \left[- \left(\frac{r [\mu m]}{121} \right)^2 \right]$$

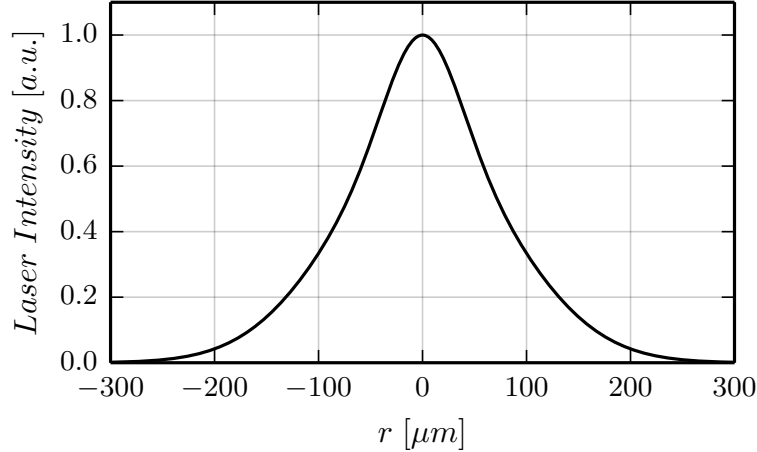


Figure 2.5: *Fit of the angular average of the JLF-Titan focal spot, as used in FCI2 simulations.*

The laminar proton beam was generated from a secondary target made of a gold foil, irradiated by the CPA (*chirped pulse amplification*) beam (called “West beam” at JLF-Titan), which is a ~ 150 J, 700 fs FWHM, focused by an $f/3$ *off axis parabola* (OAP). The proton dose variations due to the deviations by the magnetic field were then recorded on a stack of radiochromic films. A probe beam is available at JLF-Titan: it consists of a pick-off from the “west” CPA beam, frequency doubled to 2ω , $\lambda_{probe} = 526$ nm. It allows gated (700 fs) measurements with a standard CCD, *i.e.* without using micro-channel plates (MCP) which have a longer time window and a lower spatial resolution.

The interaction was characterized by different diagnostics:

- Interferometry using a Normarsky interferometer, for electron density measurements in the coronal plasma.
- Polarimetry, for the measurement of magnetic fields in the corona.
- 2D spatial, time and frequency integrated measurements of the x-ray emission, using an x-ray pinhole.
- Proton radiography (the main diagnostic) for the measurement of the magnetic field in the dense part of the target, using the “West” short pulse (with distances as follow: proton source - main target $d = 4$ mm, main target - detector $D = 37$ mm, giving a magnification $G = \frac{d + D}{d} = 10.25$).

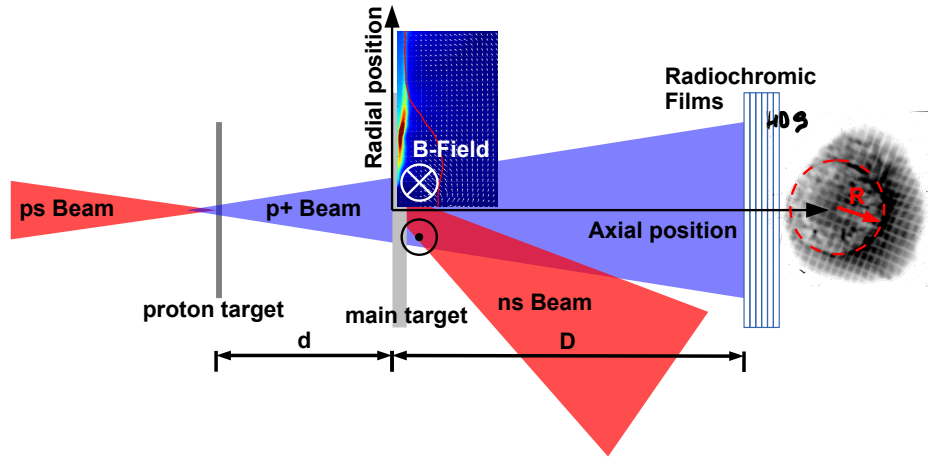


Figure 2.6: *General scheme of a proton radiography experiment with a single nanosecond beam and protons generated via a short pulse laser. The “axial position” refers to the axis normal to the target (rotation axis in 2D simulations), while the “radial position” refers to the target plane. In this configuration the magnetic field is polarized clockwise when looking at the irradiated face, so the protons are deflected to the outside.*

2.2 Comparison between integrated measurements and numerical post-processors

In this section, we will compare the integrated measurements gathered from the JLF-Titan experiment with the post-processed FCI2 results. While this kind of comparison is the basis of any study aiming at the interpretation of experimental results, the validation of numerical models or the design of experiments using simulation codes, one has to be careful and compare what is comparable.

Indeed, first of all, both the measurements and the simulations assume some hypotheses, which may delimit different validity domains. Secondly, most of the diagnostics do not measure directly a (magneto-)hydrodynamic quantity (like T_e , N_e , B etc) and are integrated over a finite time and space. On the opposite, the simulation results are the (magneto-)hydrodynamics quantities which are solution of an equation system (see Eqs. 1.1 on page 15) at discrete points in space and time. As such, it is necessary to choose where the comparison is made between the physical quantity and the integrated measurement, depending on the assumptions used to deconvolve the experimental measurement or to post-process it from simulated physical quantities.

For example, with the electron density measurement using interferometry: the experimental result consists of an interference pattern. It can be deconvolved to give a phase map, *i.e.* the optical index of the plasma, integrated along the path of the probing laser, and over a certain duration (*e.g.* the pulse’s duration of the probe beam, or the “window”

duration of a gated camera). Then, assuming cylindrical geometry of the plasma around an axis normal to the probe beam direction, one can calculate an electron density map $N_e(r, z)$ using Abel inversion and the relation between the electron density and the optical index. On the contrary, with the simulation, one has the density map $N_e(r, z)$, from which it is possible to calculate the phase map and ultimately the synthetic interference pattern. Moreover, still in the context of interferometry, the measurement is limited to the low density part of the plasma because of: *i.* the propagation of the probe beam up to $N_c(\lambda_{probe})$, *ii.* the presence of strong optical index gradients, which deflect the probe light out of the collection optics and *iii.* the limit at which the fringes of the interference pattern are too small to be resolved by the detector. On the hydro-radiative simulation's side, the low density part of the plasma may be out of the fluid hypothesis, *i.e.* where the plasma is not collisional enough. Comparisons between the measurements and simulations, for this specific diagnostic, may thus only be made for a region of the plasma with a density within a certain range.

2.2.1 Interferometry

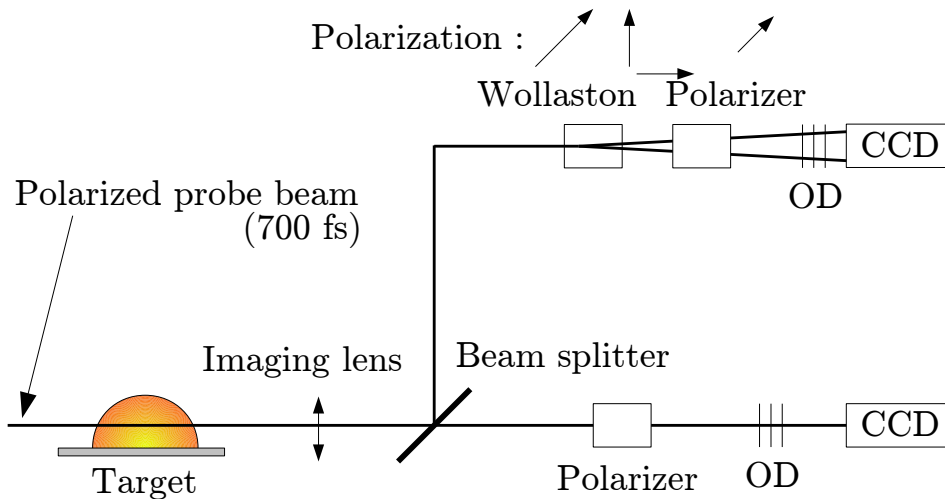


Figure 2.7: Scheme of the optical diagnostic line.

Principle

The principle of the interferometry (shown in Fig. 2.7) is to measure the electron density through the phase difference between two beams (a reference one, and a probe one which

passes through the plasma). The phase of each arm is (from the dispersion relation):

$$\phi = \int k dl = \int N \frac{\omega}{c} dl, \quad (2.1)$$

with k the wave number, $\int dl$ the path of the beam, N the optical index, ω the laser beam pulsation and c the speed of light. The phase difference between the two arms is then:

$$\Delta\phi = \int (k_{plasma} - k_0) dl = \int (N - 1) \frac{\omega}{c} dl. \quad (2.2)$$

The plasma's optical index reads:

$$N^2 = 1 - \frac{\omega_{pe}}{\omega} = 1 - \frac{N_e}{N_c}, \quad (2.3)$$

where ω_{pe} is the electron plasma pulsation, N_e the electron density and $N_c \equiv \omega^2 m \epsilon_0 / e^2 \simeq 1.1 \times 10^{21} [cm^{-3}] / \lambda_{laser}^2 [\mu m]$ the critical density for a laser with a pulsation ω . Note that if $N_e > N_c$, the optical index becomes imaginary and the electro-magnetic wave is evanescent. The phase difference between the arms, as a function of the plasma density, is finally :

$$\Delta\phi = \frac{\omega}{c} \int \left[\left(1 - \frac{N_e}{N_c} \right)^{\frac{1}{2}} - 1 \right] dl. \quad (2.4)$$

To ease the measurement of the phase difference, the two arms of the interferometer are aligned with an angle such as to form a reference interference pattern (sometimes called *carrier*) on the detector, due to a linear phase difference. Therefore, the phase difference appears as a variation of the carrier. Knowing the carrier (*i.e.* with a sufficient part without phase difference), it is then possible to unwrap a map $\Delta\phi(x, y)$. For this, we used the open-source software “Neutrino” developed at LULI and LOA (Laboratoire d’Optique Appliquée) [92].

Abel inversion

Note that this kind of diagnostic measures a physical quantity (here the electron density through the optical index) integrated along the path of the beam. Therefore, it is necessary to deconvolve the results. To do so, one can use measurements of the phase at different angles to reconstruct the density $N_e(\mathbf{r})$ with a tomography algorithm [93]. Nonetheless, this is complicated in laser-plasma experiments. Therefore, most of the time, one assumes a cylindrical geometry $N_e(\mathbf{r}) = N_e(r, z)$ to reconstruct the density with an Abel inversion [65].

Let us consider $F(y)$, a measured value which is the integration of a quantity $f(r)$ along

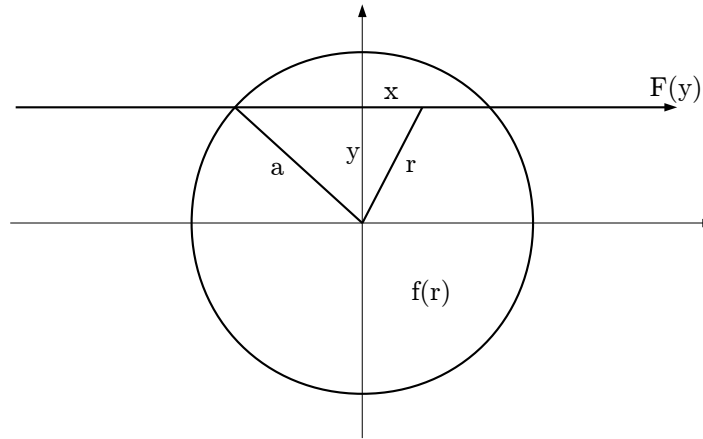


Figure 2.8: Change of coordinates for Abel transforms.

a line in a plane normal to the symmetry axis:

$$F(y) = \int_{-\sqrt{a^2-y^2}}^{+\sqrt{a^2-y^2}} f(r) dx. \quad (2.5)$$

Changing the variable, one can express the integral of r (see Fig. 2.8):

$$F(y) = 2 \int_y^a f(r) \frac{r}{\sqrt{r^2-y^2}} dr. \quad \text{Direct Abel transform} \quad (2.6)$$

The inverse transformation to obtain $f(r)$ from $F(y)$ reads:

$$f(r) = -\frac{1}{\pi} \int_r^a \frac{dF}{dy} \frac{1}{\sqrt{y^2-r^2}} dy. \quad \text{Inverse Abel Transform} \quad (2.7)$$

Despite the fact that the Abel inversion is very convenient, some precautions have to be taken. First of all, it assumes a cylindrical symmetry of the plasma. Although it is a reasonable assumption in many laser-plasma configuration, the measurement of the phase commonly shows deviations from it. Moreover, the reconstruction of the electron density depends on the gradient of phase difference in the image plane, making $f(r)$ very sensitive to any error in $F(y)$. Finally, it assumes that there is no refraction, as the integral is made over dy instead of dl , and that $f(r \rightarrow a) = 0$.

Normarski interferometer

During our experiments, the electron density of the expanding plasma was measured using a *Normarski* interferometer, which allows to save space around the targets, as every optics but the focusing lens are placed outside the target chamber. After passing through the plasma, the polarized probe beam is separated in two by a *Wollaston* prism, with equal

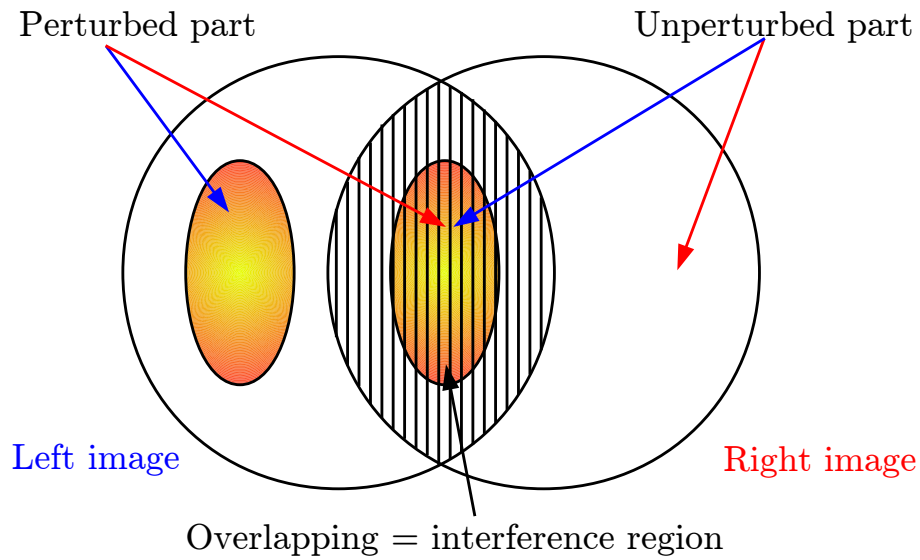


Figure 2.9: Scheme of the two interfering images in a Normarski interferometer.

energy (if the input polarization is at 45° from the ordinary and extraordinary axes of the Wollaston).

As shown in Fig. 2.7, the prism induces a slight angle in the propagation axis between the two beams having orthogonal polarization. Next, in order to have an interference pattern, they pass through a polarizer, turned by the same angle as the original probe beam’s polarization (and thus at 45° from each of the two separated beams), giving two beams with an electric field $E = E_0 \cos^2(45^\circ)$, which corresponds to an intensity $I = \frac{1}{4}I_0$. As shown in Fig. 2.9, the probe beam is usually aligned such that the plasma affects the phase of only a half of the beam, leaving the other half unperturbed. Finally, the small angle between the two beams exiting the Wollaston makes an interference pattern where they are overlapping on the image plane, placed such as the perturbed part of one image is overlapped with the unperturbed part of the other image.

Compared to a *Mach-Zehnder* interferometer, where the probe beam is separated in two before the plasma and recombined after (with 50% transmission beamsplitters), the Normarski configuration saves space in the chamber, which most of the time is not a luxury. Nonetheless, it comes at the price of a liberty of alignment, as the position of the Wollaston affects at the same time the overlapping of the two images and the size of the fringes. On the opposite, a Mach-Zehnder allows to fully overlap the images, increasing the intensity, adjust the contrast of the fringes by placing *optical densities* (OD) in the pass of the “reference” arm to compensate the absorption in the plasma for the “probe” arm, and adjust freely the size and angle of the fringes. Note that in both cases, each interfering arm contains only 25% of the original probe beam energy.

Comparison between experimental and simulated results

An example of interferometry measurement is shown in Fig. 2.10 for a shot on Mylar (420 J) measured at 1.0 ns after the beginning of the long pulse. From (a) to (d), we can see the carrier (*i.e.* reference before shot), the raw measurement (fringes pattern), the unwrapped phase difference (with the phase of the carrier removed) and the electron density from Abel inversion (eq. 2.7).

Fig. 2.11 comes from a simulation of the shot presented in Fig. 2.10. While the figures are the same, the process is inverted: starting from the simulated electron density, one can calculate a phase map with the direct Abel transform (eq. 2.6) using the probe beam wavelength. Ultimately, it is possible to calculate a simulated interference pattern using the relation : $I(x, y) = I_0 \times \cos^2\left(2\pi\frac{x}{2\lambda_{Fringes}} + \Delta\phi\right)$, where $\lambda_{Fringes}$ is the distance between two fringes in the carrier due to the angle between the two arms.

Depending on the goal of the measurement or of the simulation, one may focus on either (b), (c) or (d). Indeed, if one needs an electron density measurement of the plasma, then unwrapping the measurement up to Fig. 2.10.(d) is mandatory. Nonetheless, in order to have a reliable measurement, one needs a very clean fringe pattern, *i.e.* a good enough contrast associated with a large region without phase difference to limit the errors in the unwrapping of the phase difference, as well as a very well symmetric plasma profile with its symmetry axis normal to the probe direction. Any error in the phase unwrapping will be dramatically amplified by the Abel inversion, while asymmetries often result in aberrations after inversion. Because the inversion is done independently on each half of the phase map, one may average the two to limit this latter effect.

If one's goal is to validate the electron density calculation model in a hydro-radiative code, it may then be more pertinent to compare the experimental phase map Fig. 2.10.(c) with the one post-processed on Fig. 2.11.(c) from the calculated electron density. Indeed, the simulation has a 2D axi-symmetrical geometry, which is fully adapted to a direct Abel transform. Note that pushing the post-processing further (*i.e.* calculating an interference pattern, as seen in Fig. 2.11.(b)) is of limited interest. Yet, it is straight forward, and may be of use in the design of experiments as, for particular λ_{Probe} and $\lambda_{Fringes}$, it would allow to check which region of the plasma may be probed, and where the fringes would be so small that the interferogram could not be resolved and/or analyzed.

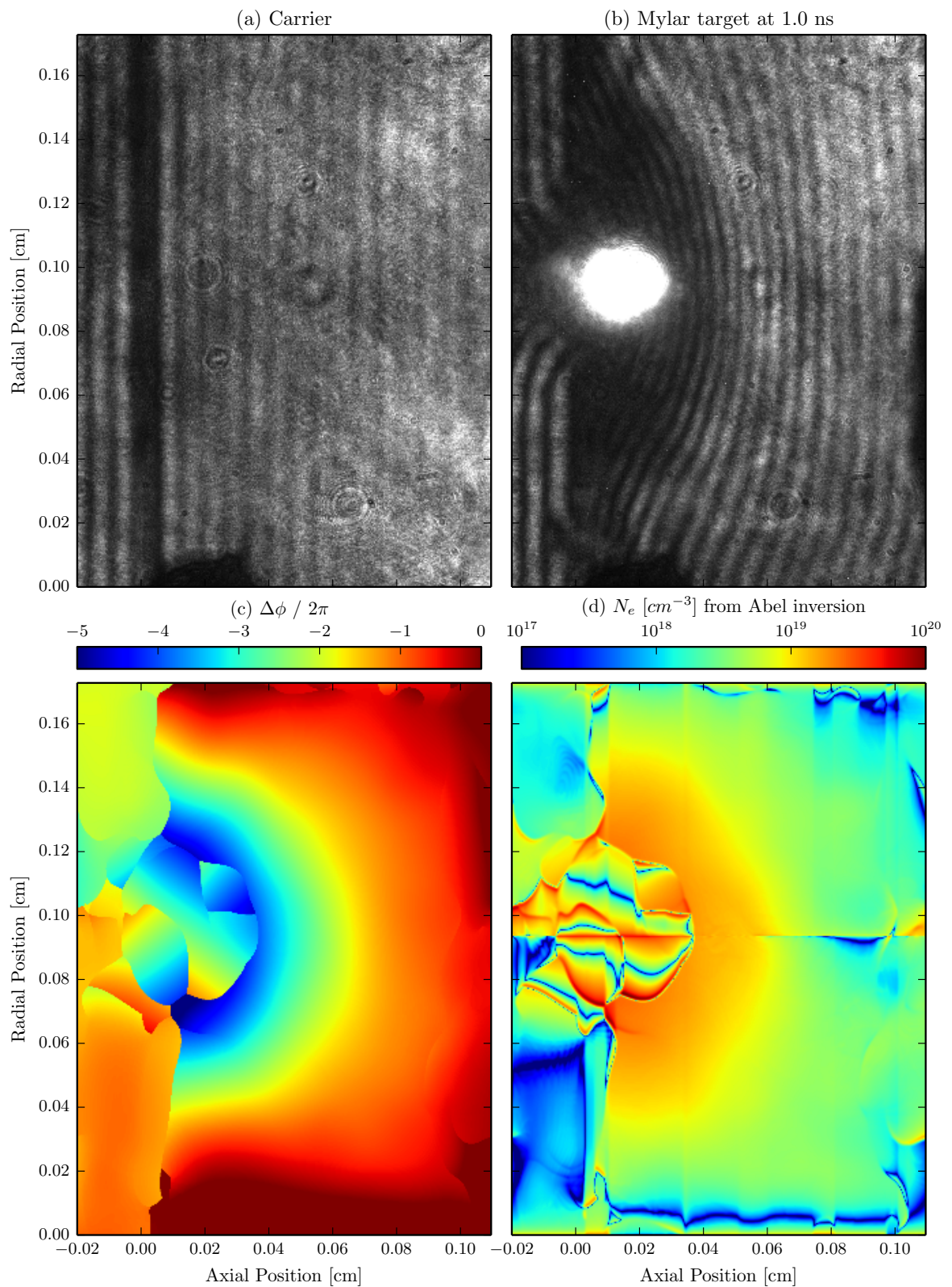


Figure 2.10: Analysis of an experimental interferometry measurement of a laser-foil experiment. (JLF-Titan, shot #38, Mylar target).

(a) Reference image before shot (carrier), i.e. linear phase difference due to the angle between the two arms.

(b) Measurement at 1.0 ns.

(c) Corresponding phase difference due to the plasma.

(d) Electron density from Abel inversion.

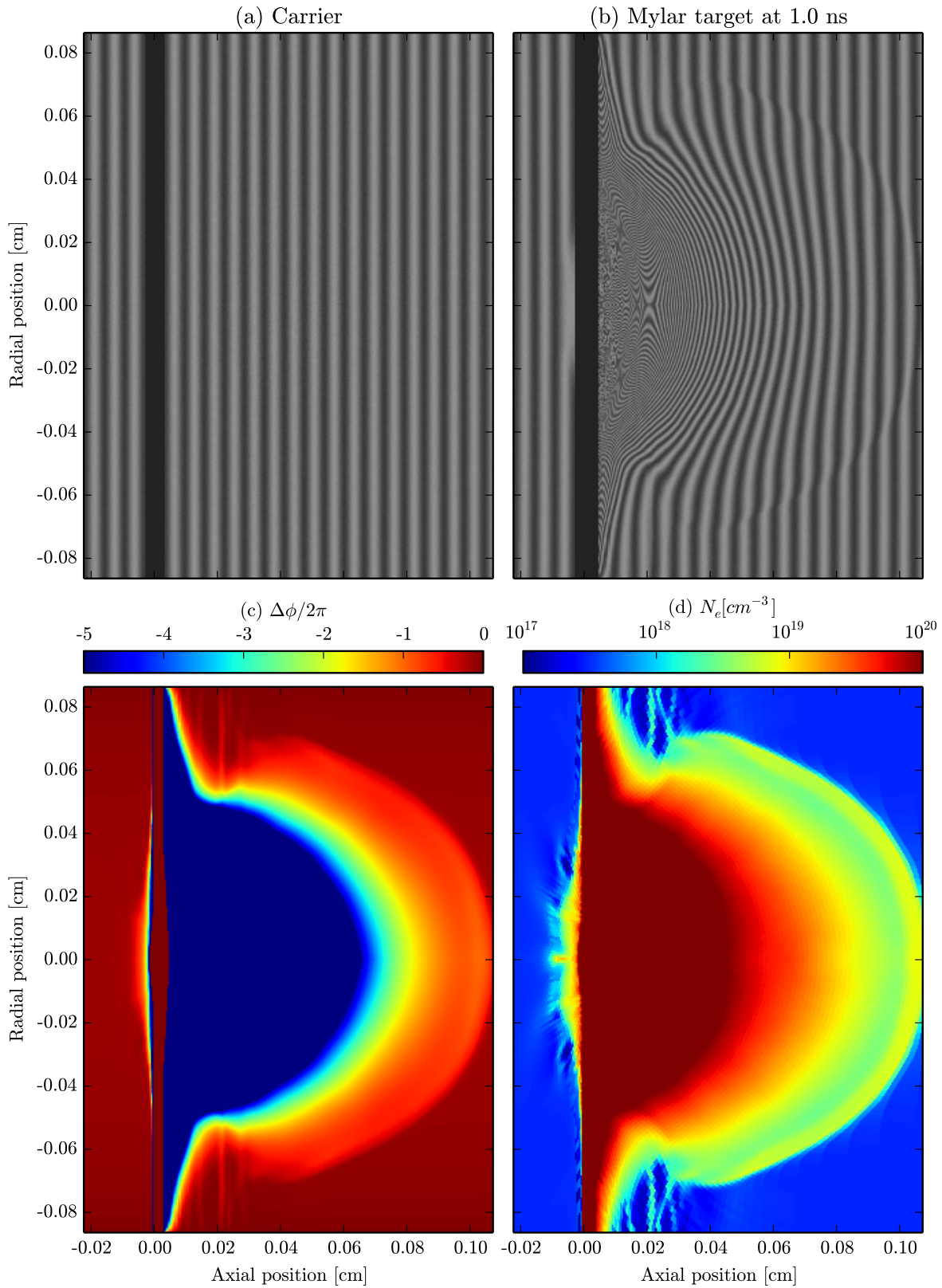


Figure 2.11: Post-processing of a FCI2 simulation (Mylar target) in the conditions corresponding to the shot presented in Fig. 2.10.

(d) Simulated electron density at 1.0 ns.

(c) Corresponding phase difference using direct Abel transform.

(b) Fringes pattern from (c) with $\lambda_{Probe} = 526 \text{ nm}$ and $\lambda_{Fringes} = 68 \mu\text{m}$.

(a) Carrier.

Validity domains

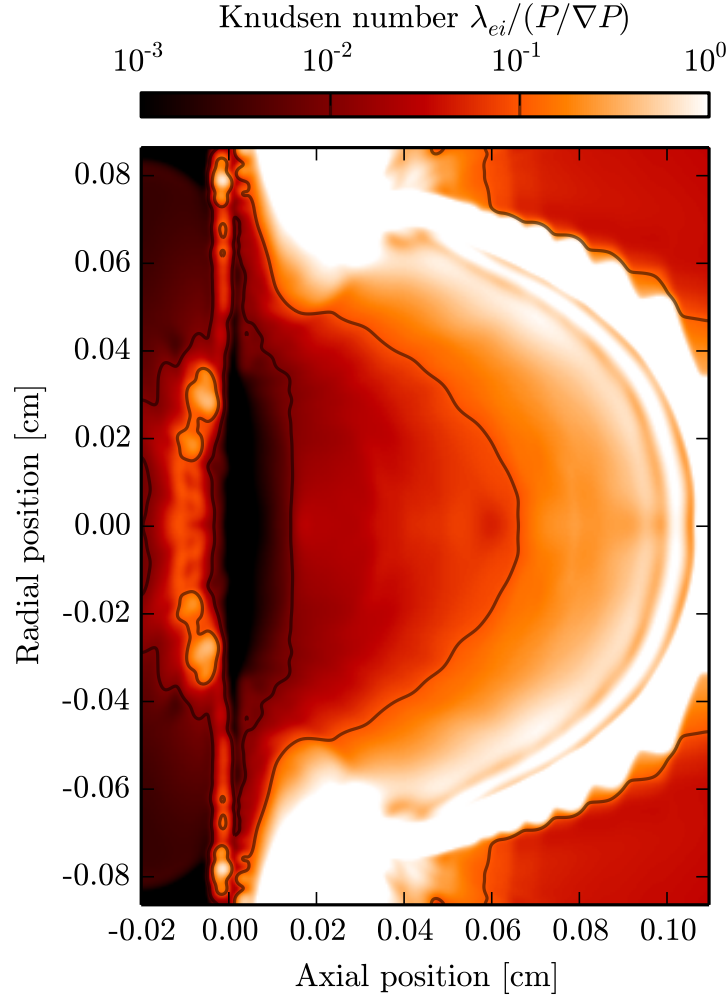


Figure 2.12: *Knudsen number at 1.0 ns for the shot on a Mylar target illustrated in Fig. 2.11.*

While Fig. 2.10 and Fig. 2.11 are evidencing large disagreements, one has to keep in mind that they both have different validity domains. The measurement is suited for the “low density part” of the plasma (10^{18} cm^{-3} to a few 10^{19} cm^{-3}) as, at higher densities, the fringes wavelength becomes too small to be resolved, and refraction becomes significant, inducing errors. On the opposite, hydro-radiative simulations are based on the assumption of a collisional plasma, which is not the case in the low density part of corona. The validity of the fluid hypothesis can be characterized by the *Knudsen* number [49]:

$$K_n \equiv \frac{M_a}{R_e} = \frac{\lambda_{mfp}}{L} \quad (2.8)$$

where $M_a \simeq \sqrt{\frac{[\text{kinetic energy}]}{[\text{internal energy}]}}$ is the Mach number (compressibility of the fluid), $R_e \simeq \frac{[\text{momentum convection}]}{[\text{momentum diffusion}]}$ is the Reynolds number (importance of the fluid's viscosity), λ_{mfp} is the mean free path of the electrons and L a characteristic length of the fluid, for which we will take $L = P / \|\nabla P\|$, as the total pressure $P = P_e + P_i$ defines the fluid's motion.

Fig. 2.12 draws the Knudsen number K_n corresponding to the simulation shown in Fig. 2.11. For $K_n > 1$, the electrons have a mean free path much higher than the fluid characteristic length and the fluid approximation falls down. This figure shows that hydro-radiative codes such as FCI2 are not suited to reproduce the evolution of the low density part of the corona in laser-foil experiments. Moreover, the simulation uses a "pseudo-vacuum". Therefore, the ablated plasma expands in a very low density gas, resulting in a weak shock at the plasma-gas interface, which should not appear because of the very low collisionality there.

To conclude, Fig. 2.12 shows that the limit $K_n = 0.1$ corresponds roughly to the limit where the probe beam has impaired a significant absorption and/or refraction (see Fig. 2.11 (b)), meaning that, in our case, the overlapping of the validity domains between the experiment and the simulation is almost null. Hence, a 2ω probe beam is not adapted for this kind of interaction, and the diagnostic would greatly benefit from a 3ω or 4ω probe beam, as the smaller the wavelength, the smaller the refraction and the phase shift, resulting in possible measurements further inside the plasma.

2.2.2 Polarimetry

Polarimetry is an optical diagnostic which allows to measure the magnetic field in a medium through the Faraday effect. When a linearly polarized electro-magnetic wave (*i.e.* our probe beam) propagates through the plasma, its polarization is rotated due to the component of the magnetic field collinear with the direction of propagation of the electro-magnetic wave. This rotation reads :

$$\alpha = \frac{e}{2m_e c} \int \frac{N_e}{N_c(1 - N_e/N_c)^{1/2}} \mathbf{B} \cdot d\mathbf{l} \quad (2.9)$$

One can understand that using this diagnostic to measure a reliable value of the magnetic field is very delicate: it is integrated along the optical path and depends on the electronic density of the plasma. Therefore, one has to measure the density through simultaneous interferometry and the axi-symmetry hypothesis is even enhanced because of the $\mathbf{B} \cdot d\mathbf{l}$ term. Finally, the linear dependence with N_e (in the limit $N_e \ll N_c$) implies that the

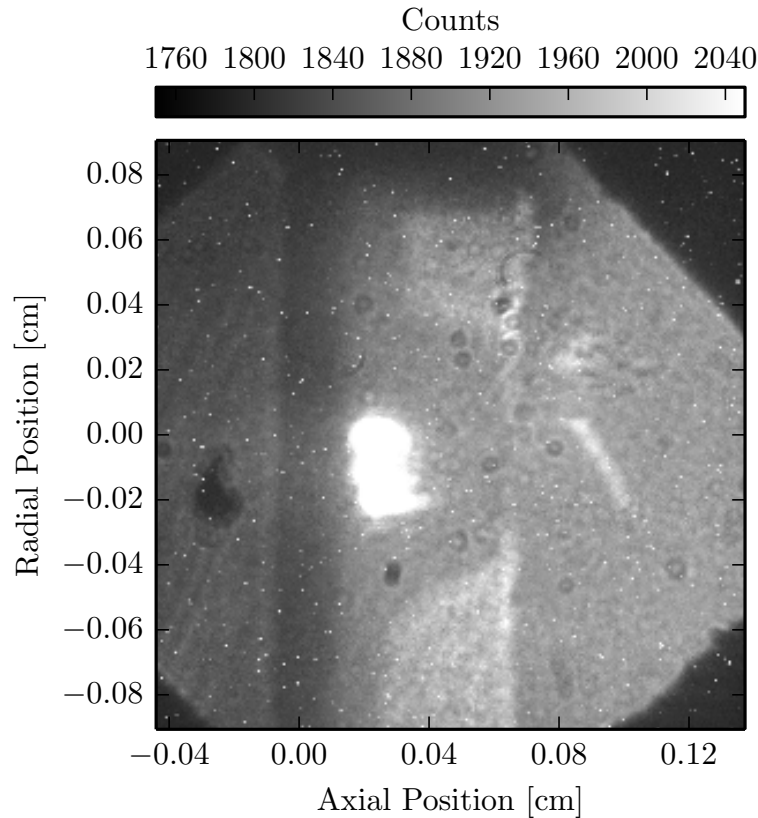


Figure 2.13: *Polarimetry measurement at 1.0 ns for a 380 J shot on a 5 μm gold target (JLF-titan, shot #51).*

most visible rotation (for an homogeneous magnetic field) will be seen in the dense part of the target, where the absorption and refraction of the probe beam are the strongest.

Experimentally, beside the need for a simultaneous electron density measurement, the polarimeter is quite compact and simple to implement. One places a polarizer (acting as an analyzer) between the plasma and the detector (a CCD camera nowadays), see Fig. 2.7. The analyzer is turned most of the time at 45° from the incident polarization, leading to symmetric intensity variations when the polarization is turned in one direction or the other. The measurement is an intensity variation of the probe beam, following the relation $I = I_0 \cos^2(\alpha_{\text{analyzer}} + \Delta\alpha_{\text{Faraday}})$, where I_0 is the intensity of the probe beam without analyzer nor plasma, α_{analyzer} is the angle of the analyzer and $\Delta\alpha_{\text{Faraday}}$ is the rotation due to the Faraday effect.

Nonetheless, if one’s goal is to show the presence of magnetic fields inducing only weak rotations, it may be preferable to place the analyzer almost at *extinction*¹ as, in this case, the ratio $I(\alpha_{\text{analyzer}} + \Delta\alpha_{\text{Faraday}}) / I(\alpha_{\text{analyzer}})$ would be much more important. More-

¹The extinction corresponds to perpendicular polarizer and analyzer directions, leading to a minimum of the transmitted light.

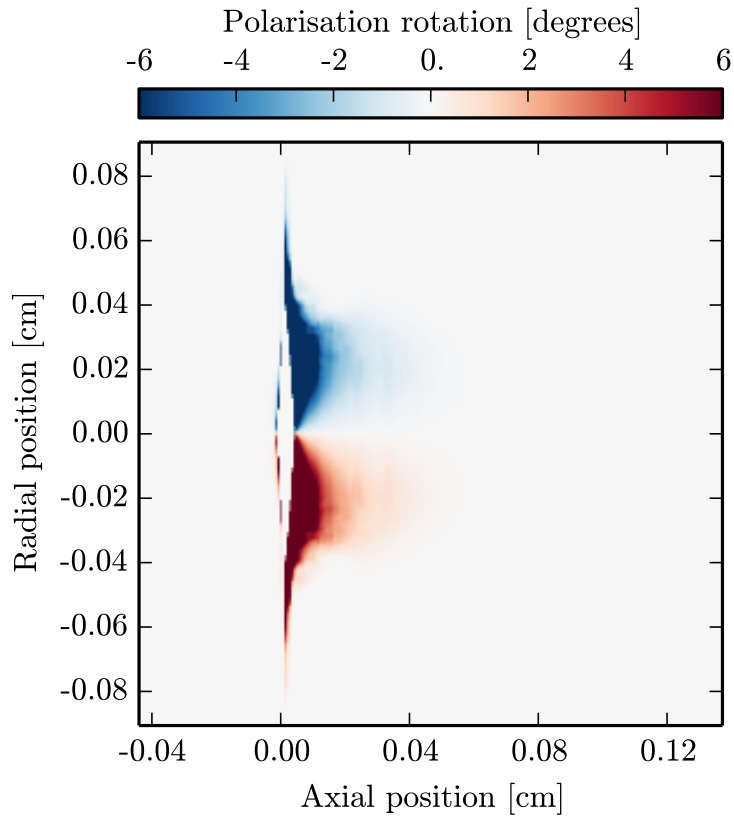


Figure 2.14: Polarization rotation post-processed from the simulation of the shot in Fig. 2.13.

over, as the measurement itself is an intensity variation, it is clear that the probe beam's intensity distribution must be as homogeneous as possible and that a CCD camera with a large dynamic range is a great asset as it would be able to differentiate smaller intensity variations. For example, assuming that the CCD would be at the limit of saturation when $(\alpha_{analyzer} + \Delta\alpha_{Faraday}) = 0^\circ$, and at 0 with $(\alpha_{analyzer} + \Delta\alpha_{Faraday}) = 90^\circ$, an 8 bit camera would have an intensity resolution of 4×10^{-3} while a 16 bit camera would have an intensity resolution of 15×10^{-6} .

Fig. 2.13 shows an example of a polarimetry measurement for a 380 J shot on a $5 \mu m$ gold target at $t_0 + 1.0$ ns, with the analyzer at approximately 3° from extinction of the 2ω probe beam. It shows significant absorption and refraction in the expanding plasma, just like interferometry, preventing any accurate measurements close to the critical density (of the 1ω laser pulse driving the plasma). Nonetheless, it appears that no significant magnetic field is present at the edges of the plasma's corona, opposed to the magnetic field topology presented using LASNEX simulations [76, 77, 79, 81]. Yet, one as to keep in mind that the density dependence of the polarization rotation may prevent any measurement of magnetic field in this part of the plasma.

The bright spot (also visible on the interferometry measurement) is due to conversion to

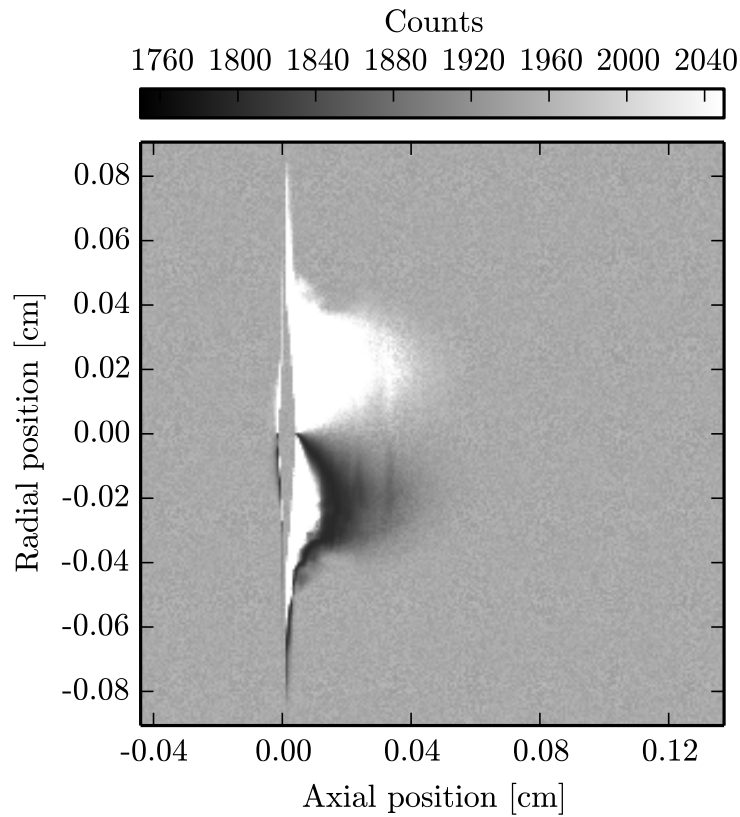


Figure 2.15: *Synthetic of Fig. 2.13 using Fig. 2.14.*

the second harmonic of the driving laser through non-linear effects in the inhomogeneous plasma. Because the probe is a pick-off from the picosecond laser line (which is amplified using the same technology than the nanosecond laser line, *i.e.* Nd-Glass amplifiers), all three laser lines share a common first harmonic. As such, it was not possible to filter the frequency doubled refraction of the nanosecond pulse from the probe beam.

Fig. 2.14 illustrates the rotation of polarization expected from the density and magnetic field topologies of the shot presented in Fig. 2.13 and simulated with FCI2. Despite the fast convective amplification of the field on the solid part of the target, it shows quite an important rotation close to the probe beam critical density which, when using Fig. 2.14 to produce a synthetic of the experimental result (see Fig. 2.15), yields very visible intensity variations.

Nevertheless, the post-processed results do not take refraction nor absorption into account and, when comparing the measurement (Fig. 2.13) with its simulated counter-part (Fig. 2.15), it appears that the intensity variations are localized in the region “obscured” by the plasma. As a consequence, while the measurement tends to agree with the idea of a magnetic field which does not expand with the corona, it does not allow to measure it around the 1ω critical density.

2.2.3 X-ray pinhole

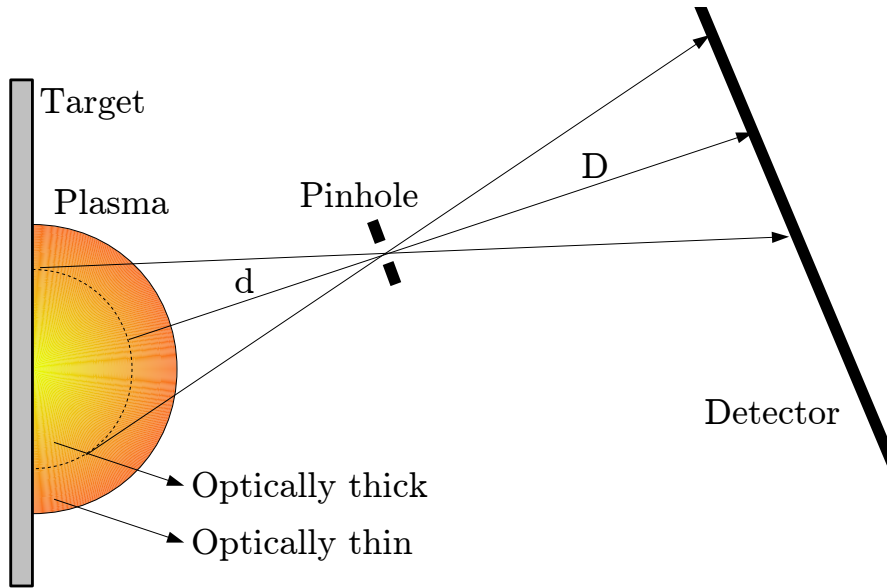


Figure 2.16: Scheme of an x-ray pinhole, for laser-foil interaction.

During the Titan experiment, an x-ray pinhole has been used in order to have an insight on the symmetry of the plasma. The principle of an x-ray pinhole is quite simple: a pinhole is placed at a given distance from the irradiated foil, and because of its small aperture, it makes an image of the plasma on the detector. By construction, a pinhole is an achromatic imaging system, and makes an image in any plane. For d the distance object – pinhole, D the distance pinhole – detector and ϕ the pinhole diameter, the magnification of the image and the resolution are then given by Thales' theorem (see scheme on Fig. 2.16: $G = \frac{D}{d}$ and $\delta x = \phi \frac{D+d}{D}$).

In the case of the Titan experiment, an array of $\phi = 10 \mu\text{m}$ pinholes has been used, each one of them making an image on an x-ray CCD (1024×1024 , $24 \mu\text{m}$ square, 16-bit pixels). The surface of the CCD's chip was covered by 4 different filters so that, combined with the multiple images from the pinhole array, one may measure different photon energy ranges for each shot. Note that the CCD was not coupled with a MCP (*micro channel plate*), and was thus triggered for a duration much longer than the interaction, resulting in time integrated measurements.

The pinhole array was at $d = 4 \text{ cm}$ from TCC (*Target Chamber Center*) and the CCD at $D = 82 \text{ cm}$ from the pinholes, giving a magnification $G = 20.5$ and a resolution of $\delta x \sim 10.5 \mu\text{m}$. The angle from the foil's normal in the equatorial plane was 45° , while the one in the vertical plane was 50° , giving a measurement with an overall angle of 62° from the target's normal.

Fig. 2.16 is a scheme of a pinhole system and shows that the system can only image

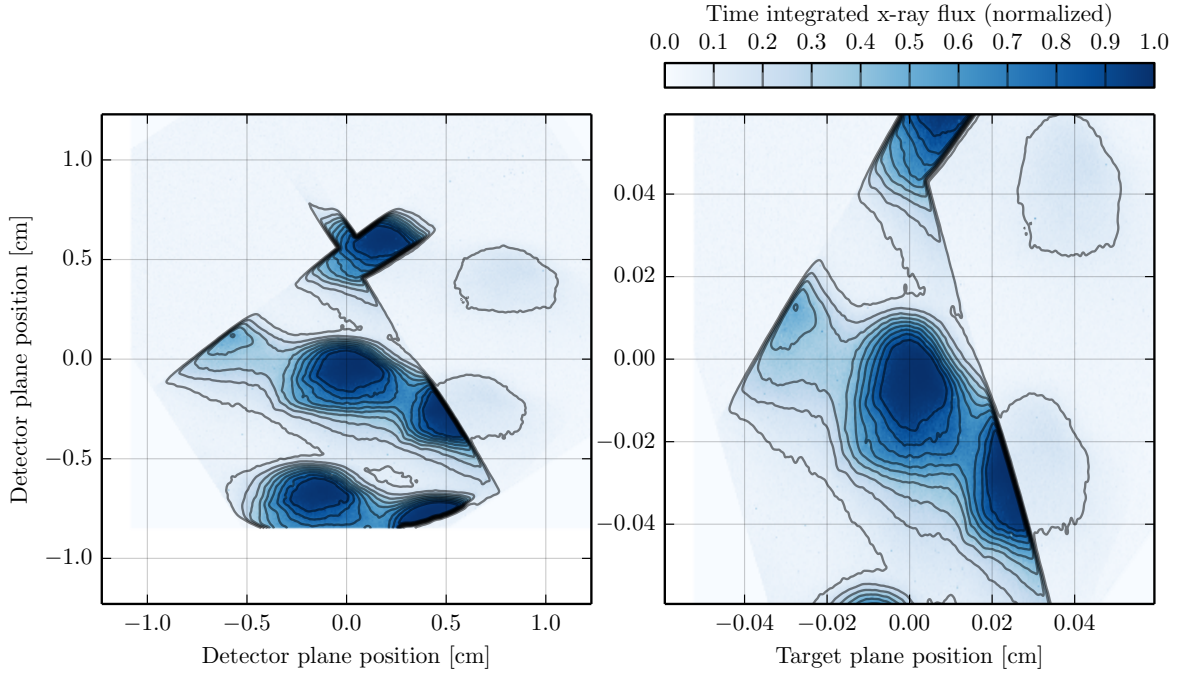


Figure 2.17: Measured time and frequency integrated x-ray image, with a 400 nm Al filter for 420 J shot on 5 μm gold target (JLF-Titan, shot #17). Left : image on the detector plane. Right : image on the target plane

the transparent part of the plasma, as the photons emitted from the opaque part of the plasma are re-absorbed before leaving the plasma. Therefore, compensating the image on the detector by the angle between the pinhole axis and the target’s normal to obtain the emission in the target plane is only valid if the limit opaque-transparent is close to the target’s surface. FCI2 includes a post-processor which allows to calculate x-ray diagnostics through spectrally resolved Monte-Carlo inverse trajectography [94]. It can account for the angle with the target’s normal, the size of the pinhole, filters and the time integration. For the later, the FCI2 simulation has been run for an extra 1 ns after the end of the laser pulse (hence, up to $t_0 + 3$ ns) to account for x-ray emission during the cooling of the plasma (yet, this correction remains very small compared to the x-ray flux integrated while the laser is still irradiating the target).

Fig. 2.17(a) presents the normalized and time integrated x-ray emission measured for a 420 J shot on a 5 μm gold target, with a 400 nm aluminum filter, while Fig. 2.18(a) is the simulated counter-part. On both figures, the (b) panel shows the image in the target’s plane, *i.e.* after magnification and angle corrections.

In both the measurement and the post-processed images, one can see a bright emission in a 400–600 μm FWHM diameter region (in the target’s plane), corresponding to the laser-heated region of the target (see Fig. 3.5(right) for an example of electron temperature).

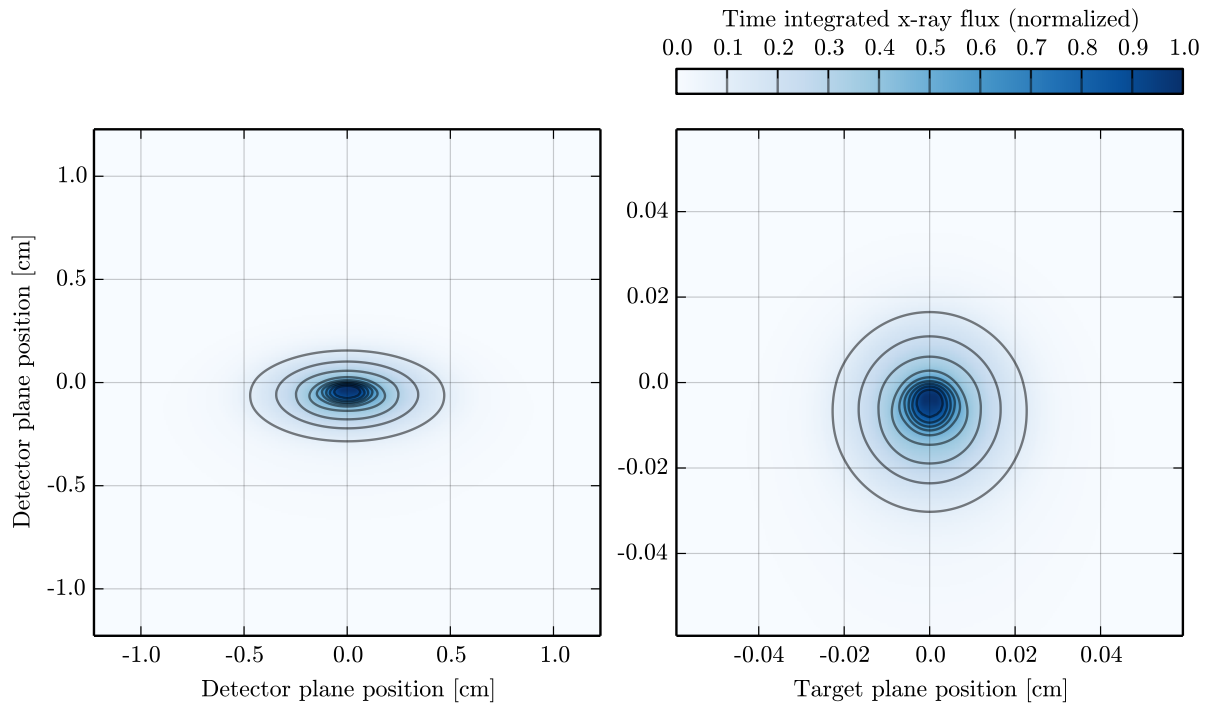


Figure 2.18: Simulated time and frequency integrated x-ray image, with a 400 nm Al filter for a 420 J shot on 5 μm gold target, corresponding to the JLF-titan shot shown in Fig. 2.17. Left : image on the detector plane. Right : image on the target plane

Also, note the slight asymmetry due to the emission further away from the target’s surface, and the difference in the spatial profile: the measurement is much more “flat-top” like than the post-processed result. Therefore, it appears that the measurement suffers from the spectral integration and the too large magnification, for which the images from different pinholes overlap. Finally, Fig. 2.18 shows an integrated flux (*i.e.* in erg/cm^2) and, as such, does not account for the response function of the x-ray CCD, which may vary with the photons’ energy.

2.2.4 Proton-Radiography

As we saw earlier, the fast advection of the magnetic field towards the dense part of the target prevented any measurement of the field in the electron conduction region, where the effects on the heat flux are the most important. Indeed, induction coils are limited to measurements at a few millimeters, and optical Faraday rotation to tenths of the critical density for the probe beam wavelength, due to refraction effects. Nonetheless, the development of MeV protons sources using lasers in the mid 2000 decade [95, 96, 97, 98] allowed to probe the field throughout micrometer thick solid targets. As a matter of fact, these MeV protons have enough energy to cross a few micron thick solid target without significantly losing energy (note that the ions lose most of their energy at the end of

their range, showing a well known “Bragg peak” [99] in their energy deposition profile). Yet, their velocity is low enough to be sensitive to electromagnetic fields in laser generated HED plasmas.

Backlighter imploded capsule

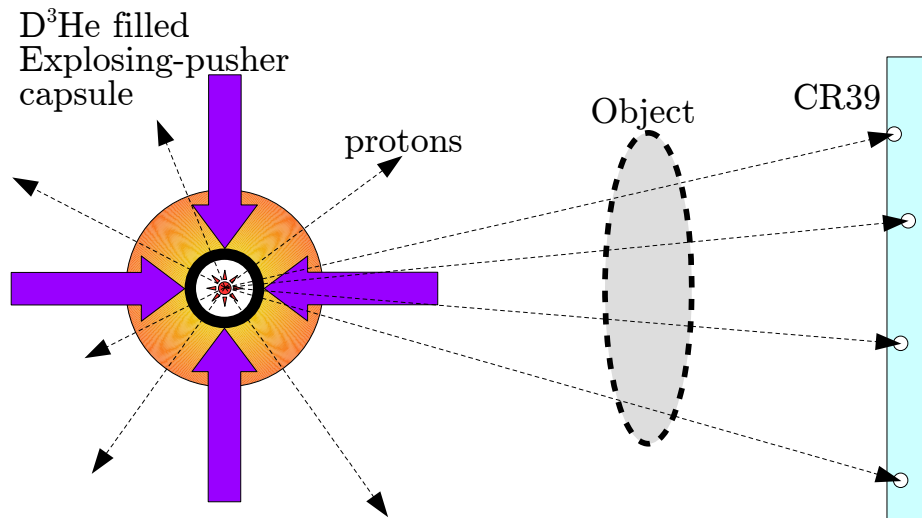


Figure 2.19: *Scheme of an exploding-pusher capsule proton source.*

Before presenting the method used to generate the protons in our case, it is worth mentioning the one using imploding backlighters [72]. In this last method, as shown in Fig. 2.19, an “exploding-pusher” capsule filled with Deuterium and Helium 3 is imploded using direct laser irradiation, producing mono-energetic protons at the peak of the implosion (also called “bang time”) through the fusion reactions $D + {}^3\text{He} \rightarrow \alpha (3.6 \text{ MeV}) + p (14.7 \text{ MeV})$ and $D + D \rightarrow T (1 \text{ MeV}) + p (3 \text{ MeV})$. This produces a source of protons whose characteristic duration is 130 ps FWHM, with a size of $40 \mu\text{m}$ FWHM. Moreover, the protons are emitted isotropically, ensuring very good homogeneity of the dose on the detector. Nonetheless, because the proton fluence is very low, one has to use CR39 as detectors [100, 101], consisting of a plastic slab, in which each proton leaves a track. The CR39 are then etched in a NaOH solution to increase the size of the tracks, up to a size visible using a microscope or a scanner.

Because CR39 are able to record the impact of each single proton, it makes it a very well suited detector for backlighter proton sources. Especially, if one places a mesh between the source and the object to radiograph, one would obtain well defined beamlets of a few thousand protons. This allows to directly track the lateral displacement of the protons due to electromagnetic fields, at the cost of a reduced spatial resolution (typically 10×10 beamlets).

Finally, due to the isotropy of this kind of proton source, it allows to probe multiple objects simultaneously, hence allowing to maximize the number of experimental results per shot.

Short pulse laser generated protons beams

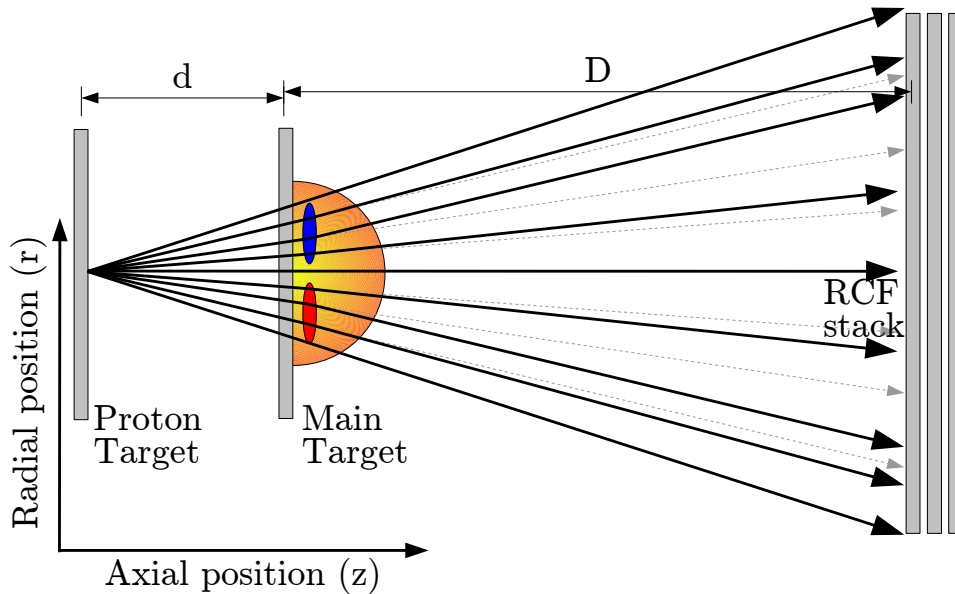


Figure 2.20: Scheme of the deflections imparted by the proton beam by an azimuthal B -field, leading to a dose modulation.

While the imploded backlighter proton source has the great advantage of giving a homogeneous fluence with a quasi mono-energetic spectrum, it requires a facility able to implode the capsule, with enough remaining laser beams to drive the object to radiograph. Hence, the number of laser facilities allowing this kind of experiment is very limited: Omega and NIF (as well as LMJ when fully operational). This explains why proton radiography is most of the time performed with the other method, *i.e.* short pulse laser accelerated protons, as most of the HED laser facilities nowadays include at least one short pulse laser (Omega EP, ARC at NIF, Petal at LMJ, Orion in UK, Pico2000 at LULI2000 *etc.*).

This last method has been used in the experiments presented in this thesis. In our case (and as in almost every other experiments performing proton radiography), the mechanism responsible for the acceleration of the protons is the *Target Normal Sheath Acceleration* (TNSA):

A picosecond CPA (*Chirped Pulse Amplification* [102]) beam is focused onto a solid thin foil (micrometric thickness) with a laser intensity $I > 10^{19} \text{ W/cm}^2$. This leads to a volumetric heating of the target and yields a population of suprathermal electrons [103], which are energetic enough to leave the solid foil and produce a sheath of electrons in

front of the non-irradiated face of the foil [104]. This sheath may be assimilated to the negative electrode of a capacitor and the foil to the positive one (charged due to the lack of electrons). This yields an electrostatic field in the order of TV/m , high enough to ionize the ions at the back of the foil, mainly the hydrogen contaminants (from water and carbohydrates), and accelerate them as they have the highest charge over mass ratio. Upon reaching a stationary state, the electric field has accelerated the protons and slowed down the electrons, such that they both travel at the same velocity. Because of their mass ratio, most of the electrons' energy has been transferred to the protons.

This results in a spectrally broad proton beam (in facilities such as Pico2000 and JLF-Titan, typically up to 20 MeV), with a number of protons exponentially decreasing for increasing energy, typically from 10^{13} to $10^{10} MeV^{-1}sr^{-1}$. The protons are emitted in a laminar beam, whose half angle decreases with the protons' energy with a maximum of 20° for $E_p/E_{max} \sim 0.3$ [105].

It is possible with TNSA proton beams to use a grid to imprint fiducials on the proton image, just like with imploded backlighters. But, in the case of TNSA proton beams, the proton dose is much less homogeneous, therefore significantly reducing the precision of this method. Indeed, the homogeneity of the proton dose is affected by the flatness and the surface roughness of the irradiated foil, as it acts as the electrode of a capacitor. Hence, defects on the surface of the foil will affect the electrostatic field and the laminarity of the proton beam.

Moreover, because of the broadband spectrum and high proton flux, the detector used is a stack of *RadioChromic Films* (RCF) [106]. Each film consists of an active layer embedded in a polyester substrate. When irradiated, the active layer darkens through polymerization as a function of the absorbed dose of ionizing radiations. The films are then scanned and, after a calibration, one can retrieve the absorbed dose from the optical transmission. Because ions have a much higher stopping power (energy loss per distance unit) at the end of their range (in cold matter) [99], each of the films measures mostly the dose for the protons whose range corresponds to its position in the stack. For a given energy, the protons of higher energy also contribute to the dose deposited in the associated film. Yet, the higher is the energy, the lower is the number of protons (exponential decrease): their contribution becomes negligible after $\sim E_p + 1$ MeV.

Finally, because of this spectrally resolved aspect and of the time of flight of the protons, the diagnostic is also time resolved: the films at the back of the stack measure the dose from fast protons, probing the object at early time, while the films at the front record the dose from low velocity protons, probing the object at later time. The duration of the “gated” measurement is therefore dependent on the distance between the proton source target and the object, and on the highest and lowest measurable protons doses. Indeed, as RCF films are also sensitive to x-rays and electrons and in order to prevent damages

by target debris, the RCF stack is packed in a $12.5\ \mu\text{m}$ thick aluminum foil (kitchen foil aluminum). Hence the first RCF records 1.1 MeV protons, yet the dose is most of the time too high and the film saturates, which gives a minimum measurable energy of 3.2 MeV (second film). This results in a time window of 240 ps/cm between the 3.2 and 20 MeV protons. Thus, in our case, with a 4 mm separation between the two targets and because of the evolution of the probed system over nanosecond time scale, the diagnostic cannot provide time resolved measurements. It means that one has to vary the delay of the picosecond laser beam with respect to the nanosecond laser pulse to probe the magnetic field at different times.

Analytical study of the proton modulation pattern

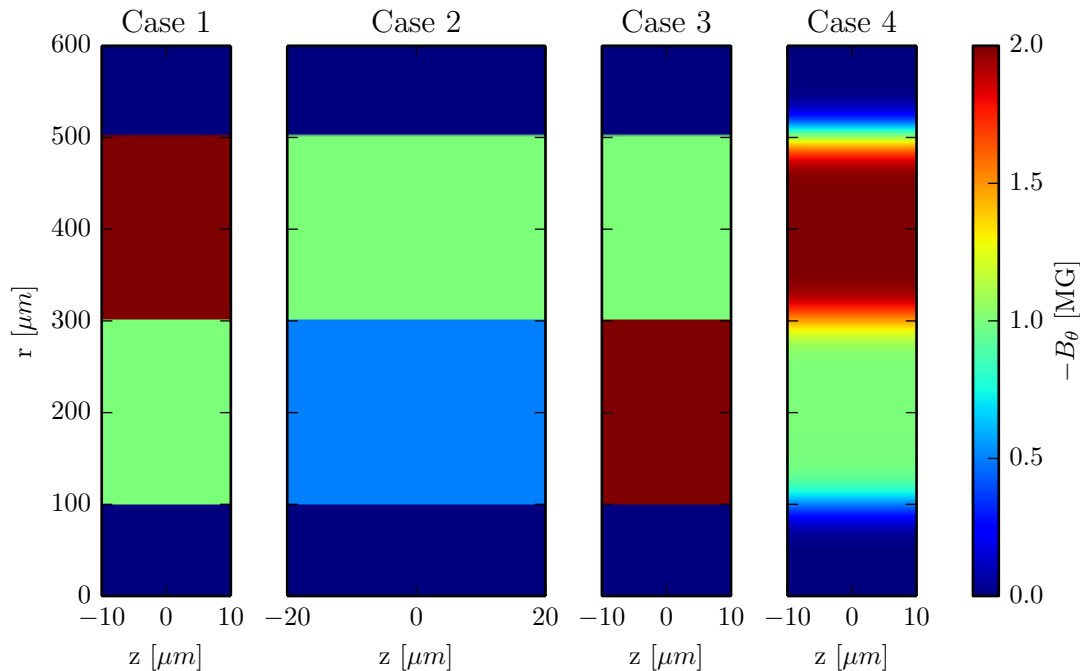


Figure 2.21: Illustration of the azimuthal magnetic field topologies for the tests cases 1 to 4. Note that the spatial scale is different between the z and r axis for an easier visibility.

As said previously, using a mesh allows to directly measure the lateral displacement of the proton beamlets which depends on $\int B \cdot dl$ (the magnetic field integrated along the trajectory of protons). From there, one can estimate the order of magnitude of the field, using a hypothesis on the thickness of the field. Yet, if the protons' energy is not high enough, the resolution of the grid's image on the detector will be strongly affected by proton scattering through the solid target. Therefore, in our case, we performed proton radiography without mesh, which means that the measurement is a variation of the proton dose on the RCF due to the variations of the integrated magnetic field $\int B \cdot dl$.

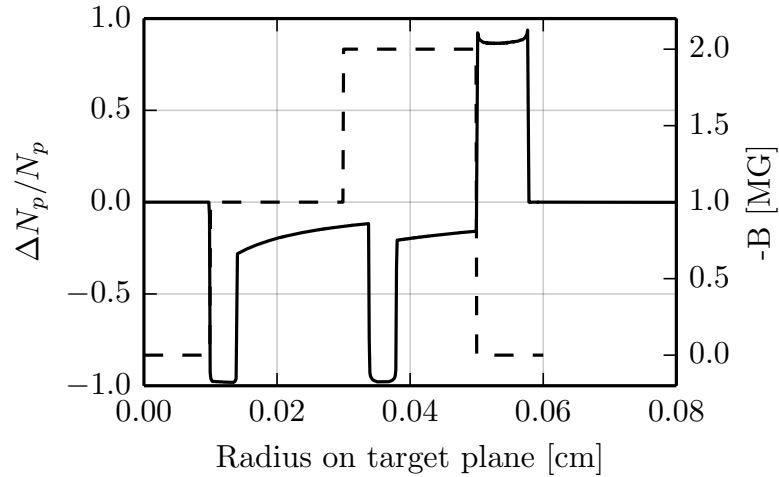


Figure 2.22: *Case 1: Azimuthal magnetic field, invariant along the proton propagation axis, $\Delta z = 20 \mu\text{m}$. Dashed line: magnetic field profile, solid line: proton dose variation.*

As depicted on Fig. 2.20, protons passing through a region empty of magnetic field do not suffer deflections and the dose on the film will not be affected. On the opposite, the deflection of protons passing through an azimuthal magnetic field will induce a lack of proton dose in the profile, close to a proton dose accumulation.

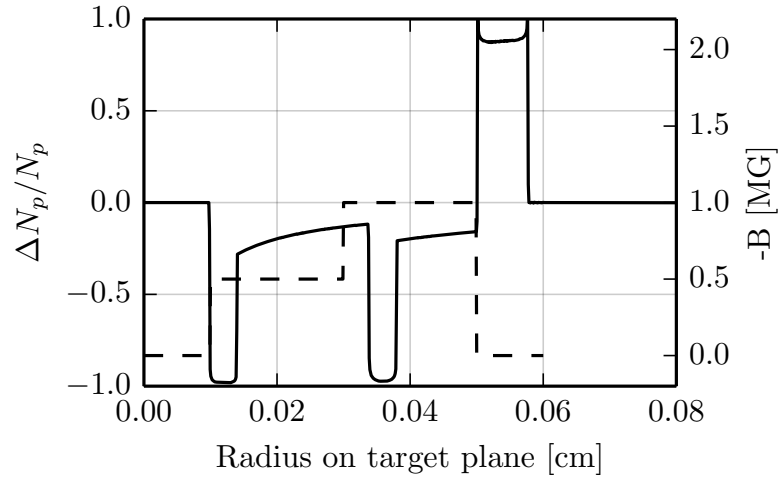


Figure 2.23: *Case 2: Azimuthal magnetic field, invariant along the proton propagation axis, $\Delta z = 40 \mu\text{m}$. Dashed line: magnetic field profile, solid line: proton dose variation.*

In the following, we will study into more details these patterns using ILZ, a code developed by the author, which simulates the behavior of any isotropic charged ion beam, propagating through any electro-magnetic field map (regular, Cartesian, either axi-symmetric 2D, planar 2D with invariance over a given thickness, or 3D). All ions are supposed independent and are emitted simultaneously from a common point source. The electromagnetic

field is interpolated continuously at either 0th order (*Nearest Grid Point*) or 1st order (*Particle In Cell*). The transport equation is solved using the Boris “leap-frog” algorithm [107, 108]. Note that this code does not calculate the scattering through the foil, nor the energy loss. Moreover, all ions have the same initial energy, and it is assumed that the energy change due to electric field is low enough so that they are all recorded by the same RCF film (which is fully valid in our case, where only a magnetic field is present).

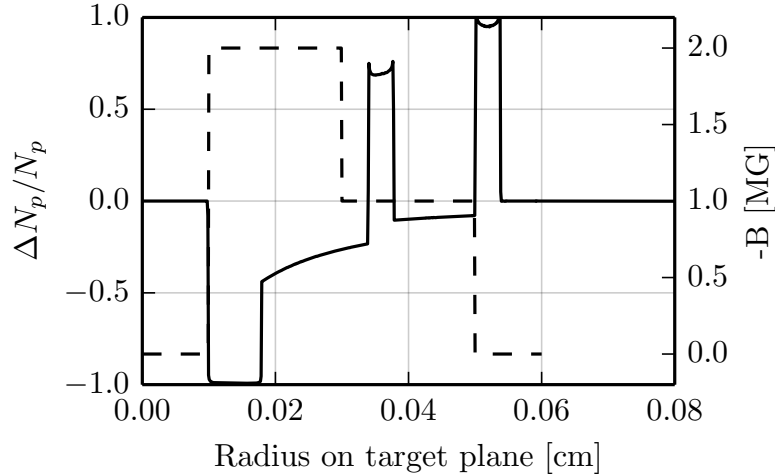


Figure 2.24: *Case 3: Azimuthal magnetic field, invariant along the proton propagation axis, $\Delta z = 20 \mu\text{m}$. Dashed line: magnetic field profile, solid line: proton dose variation.*

Fig. 2.22 to Fig. 2.25 show the dose modulation pattern using ILZ for different axi-symmetric magnetic field topologies. For all cases, a 10 MeV proton source is placed at $z = -1 \text{ cm}$, the field map is centered on $z = 0$, and the detector at $z = 9 \text{ cm}$, giving a magnification $G = 10$. As shown in Fig. 2.21, in case 1 (corresponding to Fig. 2.22) the magnetic field is invariant over $\Delta z = 20 \mu\text{m}$ while, in case 2 (Fig. 2.23), the field is two times lower than in case 1 but invariant over $\Delta z = 40 \mu\text{m}$. Case 3 (Fig. 2.24) is similar to case 1, but the 1 MG and 2 MG regions are switched. Finally, case 4 (Fig. 2.25) uses the magnetic field of case 1, but convolved by a Gaussian to remove the sharp variations of the B-field over the radial direction. On each figure, the proton dose modulation $\Delta N_p/N_p$ is plotted as a function of the radial position on the target’s plane, instead of the film’s one, by using the magnification factor: $r_{\text{target}} = r_{\text{film}}/G$.

First, it shows that cases 1 and 2 give the same dose modulation, meaning that for a thin enough magnetic field, the dose modulation can be assumed to be due to $\int B \cdot dz$ instead of $\int B \cdot dl$. Moreover, it appears that deficits or accumulations of protons on the detector are due to variations of $\int B \cdot dz(r)$. In this geometry (clockwise magnetic field when looking from the detector), an increase of the magnetic field will result in a deficit of protons (they are swept away to larger radii), while for a decreasing magnetic field, the proton dose is increasing (due to protons coming from lower radii).

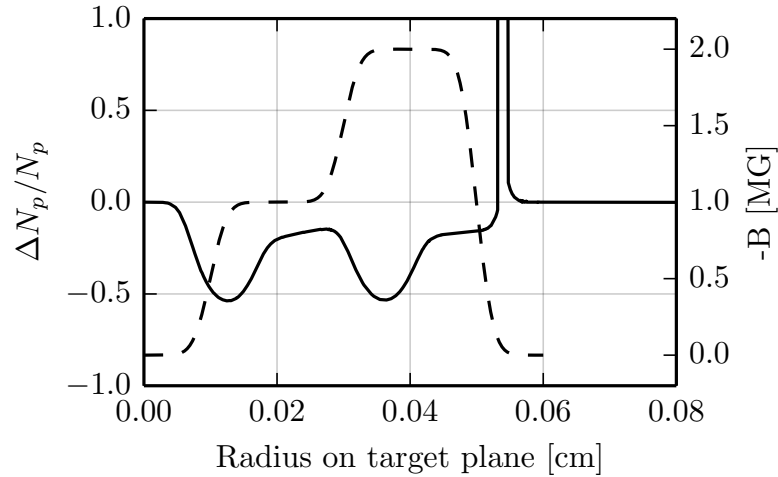


Figure 2.25: *Case 4: Azimuthal magnetic field, invariant along the proton propagation axis, $\Delta z = 20 \mu\text{m}$. Dashed line: magnetic field profile, solid line: proton dose variation.*

The small dose variations in regions of constant magnetic field are due to the cylindrical geometry because as the surface $S = 2\pi r.dr$ increases with r , the dose due to protons deflected from r to $r + \delta r$ is reduced. Case 4 shows something closer to what can be found in reality: it illustrates that in some cases, a caustic (divergence) may appear in the proton dose on the detector [109].

Finally, as shown in Fig. 2.26, it is once again possible to simulate the detector from the post-processed results. In this case, the transmission of the RCF is calculated using the calibrated response of the film, assuming an homogeneous proton dose of 400 Gy (with a random noise, just for “realism”). Yet, in the case of a single irradiation spot on the main target, the simulation is axi-symmetric: we will then compare azimuthally averaged dose modulations with the simulated $\Delta N_p/N_p(r)$, as color maps do not allow to compare them precisely [76, 110].

Sensitivity study of proton radiography

In this subsection, before comparing experimental proton radiography measurements and post-processed results, we will study the sensitivity of the proton radiography diagnostic. In order to point out what is the main source of error in the measurement, we will use FCI2 and its proton-radiography post-processor. To do so, we will refer to a reference case typical of the JLF-Titan experiment: the targets are the same as described in sec. 2.1.2, the focal spot is the one shown on Fig. 2.5, the laser power law is a 2 ns square pulse with a 100 ps rising time and the energy is 400 J . The proton source is located at $z = -0.4 \text{ cm}$ and the detector at $z = 3.7 \text{ cm}$. For this reference case, the protons’ energy is 10 MeV . For all the results presented in this subsection, the proton radiography is simulated at

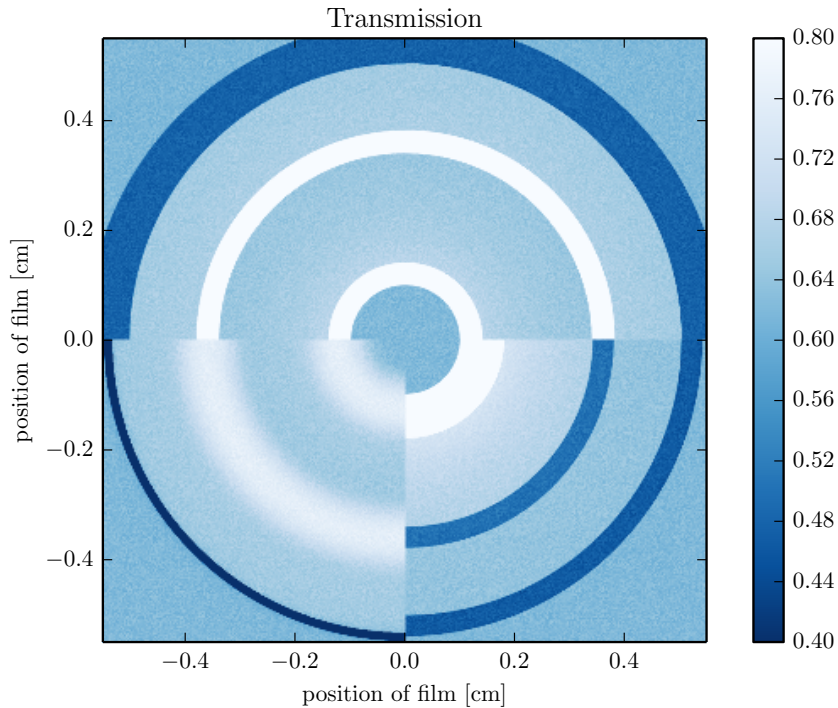


Figure 2.26: *Synthetic optical transmission of an EBT type RCF for a proton dose of 400 ± 50 Gy. Top left: case 1; top right: case 2, bottom left: case 3, bottom right: case 4.*

$t = 1.0$ ns.

In order to simulate a proton-radiography measurement, a Monte-Carlo module of FCI2, solving the Boltzmann-Fokker-Plank equation for neutral particles, has been adapted to incorporate the low angle collisions due to electromagnetic fields [111]. It is therefore able to calculate the propagation of MeV protons through the MegaGauss magnetic fields produced in laser irradiated solid targets where, on top of the deflections due to the B-field, the scattering (large angle collisions) are far from being negligible.

Firstly, the effect of the scattering is presented in Fig. 2.27, where the reference cases have been run with and without scattering. For the mylar target, despite its greater thickness ($23 \mu\text{m}$), the low density results in a quite low scattering: the overall dose modulation is not strongly affected by the large angle collisions. On the opposite, for the gold target, the much higher areal density ($\int \rho \cdot dz$) and mean charge state induce a very strong scattering of the probing protons: while without scattering the dose modulation is very complex, once accounting for the scattering, the pattern becomes very simple. In this case, a large region corresponding to a deficit of dose is surrounded by a single smooth ring a proton accumulation. Finally, note that in the gold case without scattering, the limit of the proton dose modulation is well-marked at $r_{film} = 0.6$ cm, while once accounting for the scattering the unperturbed region is at a larger radius ($r_{film} = 0.8$ cm).

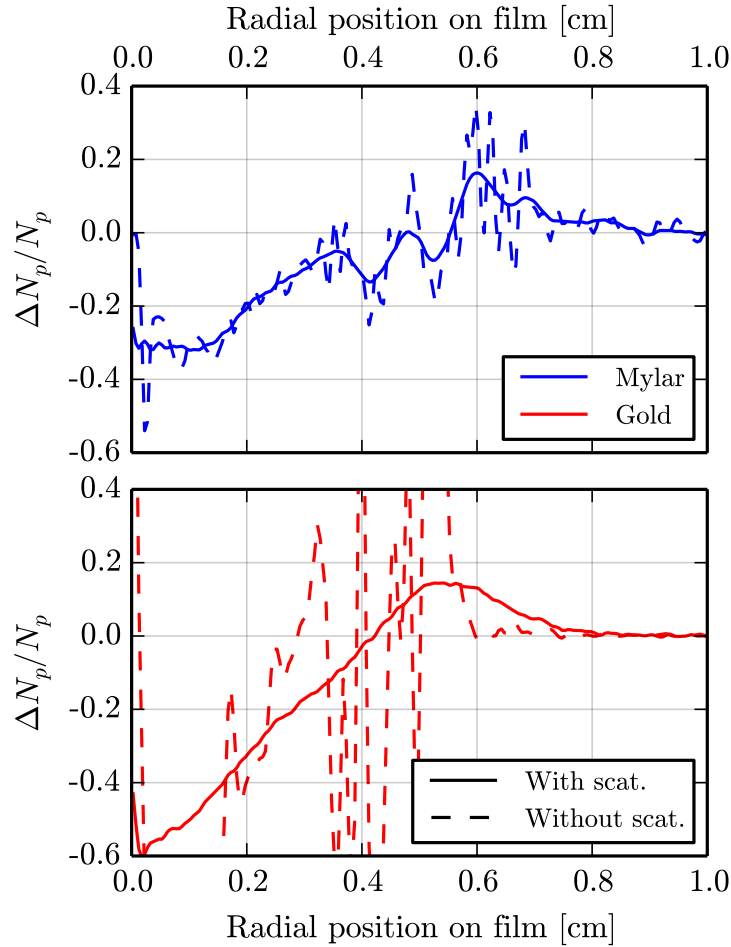


Figure 2.27: Sensitivity study of the proton radiography: effect of the scattering.

Secondly, Fig. 2.28 shows the effect of varying the probing protons' energy on the dose modulation pattern. For this, the post-processor has been run with 3 MeV , 10 MeV and 20 MeV protons. The most important result is that the energy is too low for the 3 MeV protons (roughly corresponding to the 2^{nd} RCF of the stack), resulting in a very high influence of the scattering: in the low Z case, the dose modulation pattern is similar to the one described for gold at 10 MeV , while for the high Z target, the dose modulation from the field is almost completely nullified at 3 MeV by the scattering, presumably preventing any discrimination of the effect of the magnetic field. For the high proton energy (20 MeV), in the Mylar case, no significant effect appears despite the sharper dose modulation. Nonetheless, the radial positions of the local minima and maxima are not affected. On the opposite, for the gold target, another local maximum becomes visible and the main one is slightly shifted toward a lower radius. The increased stiffness of the protons allows some of the complex deflection patterns seen in Fig. 2.27(bottom) to re-appear.

Next, Fig. 2.29 presents how the laser power impacts the dose modulation. For this, the dose modulations associated with 300 and 500 J laser pulses are plotted concomitantly

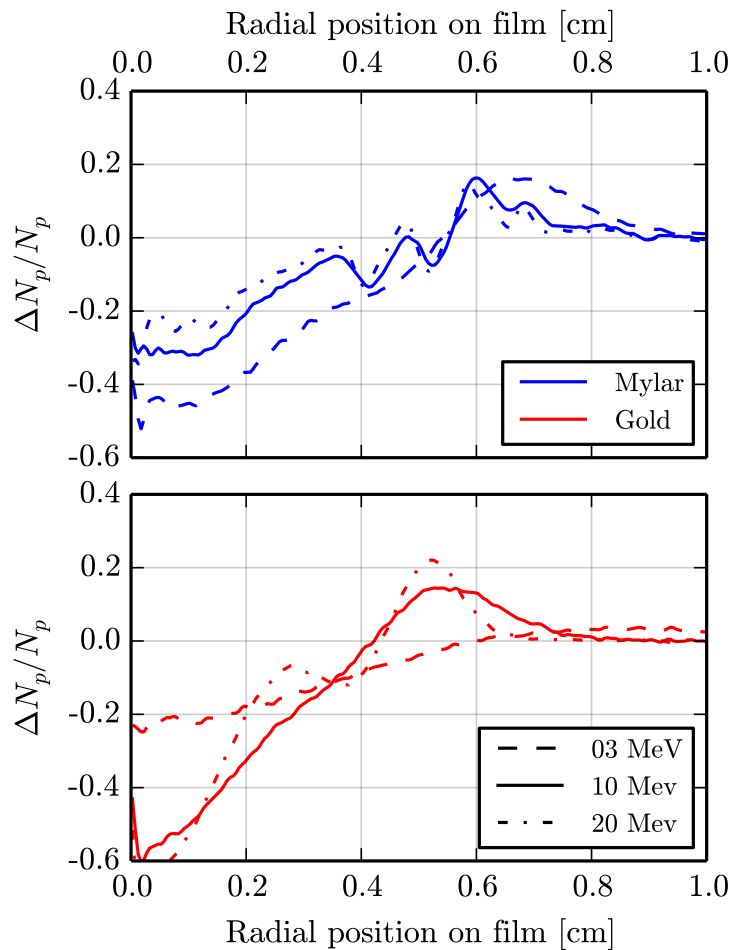


Figure 2.28: Sensitivity study of the proton radiography: effect of the protons' energy.

with the $400 J$ reference case. The high Z target plots are very insensitive to the laser's energy: the dose modulation pattern is almost the same, both for the trend and the amplitude. Yet, for the low Z target, the low laser energy case gives a slightly different pattern with a very sharp proton accumulation ring which radial position is shifted by $\sim 10\%$. For a higher energy, the dose modulation is almost the same.

Finally, in Fig. 2.30 we look at the influence of the laser's focal spot (with the same power law) over the dose modulation pattern. For this, FCI2 simulations were run with a "flat-top" focal spot ($300 \mu m$ FWHM, 16^{th} order super Gaussian) or one close to a case without phase plate ($50 \mu m$ FWHM Gaussian). Examples of magnetic field topologies associated to these cases can be seen at $1.5 ns$ in sec. 3.2.2, on page 117. The plastic target plots show quite similar dose modulations with local maxima and minima at the same positions, but with different amplitudes. For the gold target, the "flat-top" focal spot case results in a central region of constant proton dose (yet lower than without any field), with a sharp increase of the dose up to a maximum located at a smaller radius than the reference case. For the high intensity case (small focal spot, *i.e.* without RPP) the depletion of protons in the central region is much more important (the same goes for the Mylar target) and

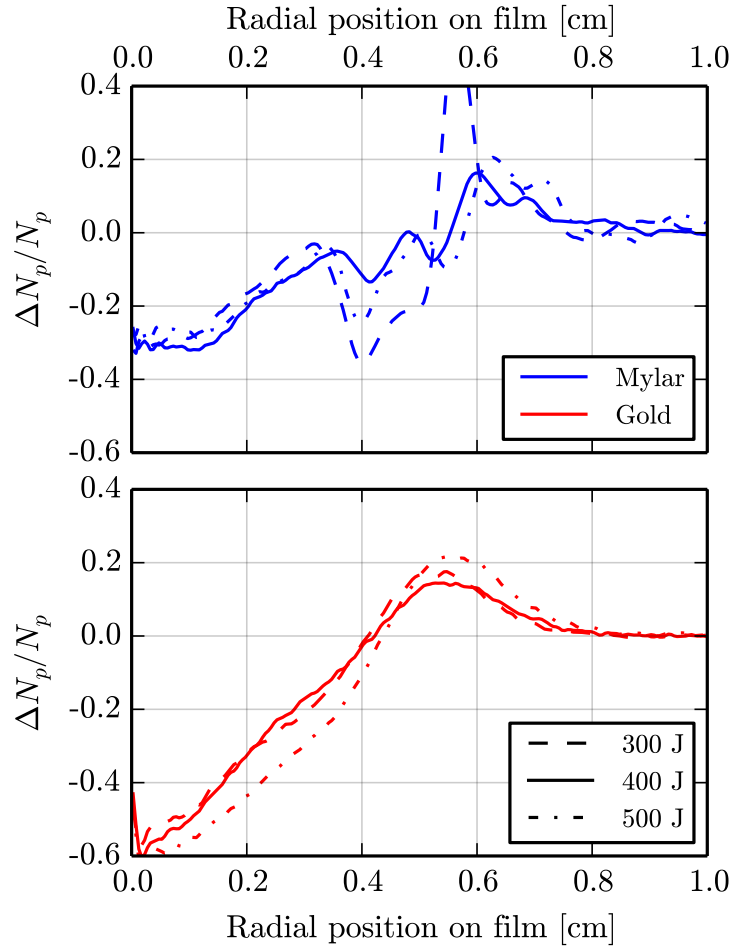


Figure 2.29: *Sensitivity study of the proton radiography: effect of the laser power.*

the maximum of dose is higher and again at a smaller radius.

The conclusions of this study are the following:

1. The dose modulation was affected by the laser energy only in the plastic case at 300 J . Therefore one may assume that the laser energy variations from shot to shot (in the worst case $400 \pm 50\text{ J}$) do not significantly affect the results of the proton radiography.
2. In the case of the plastic target, unless using low energy protons (too strongly affected by the scattering), the dose modulation is insensitive to the probing protons' energy. Yet, it is not the case with the gold target. Hence, for plastic, one is free to use either film of the RCF pack to compare with other shots, while for gold, one should use the same film.
3. We saw that despite using very different focal spots, the dose modulation patterns were not significantly different, as shown experimentally in [89]. As such, one can assume that the error due to the azimuthal average of the experimental focal spot is not an important source of error for the diagnostic.

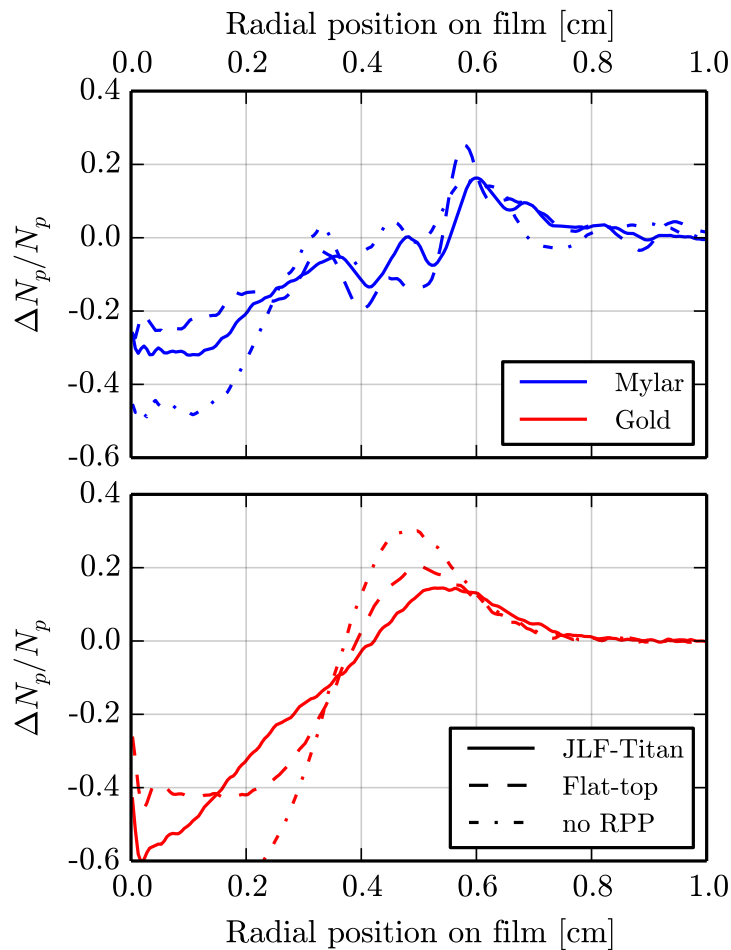


Figure 2.30: Sensitivity study of the proton radiography: effect of the laser's focal spot.

4. Finally, it appeared that the most important effect on the dose modulation pattern is the scattering of the protons through large angle collisions in the solid target. Therefore, in the following, we will define the uncertainty on the proton radiography measurements from the scattering, as a function of the target and the protons' energy. For this, the FCI2's proton radiography post-processor has been run for various proton energies at $t = 0$, with and without scattering. We used an isotropic source within a given solid angle and nullified the proton emission for angles $\alpha > \alpha_{cut-off}$ (see Fig. 2.31). The error bar of the proton radiography is then defined as the half width at $1/e$ for the Gaussian which, once convolving the dose profile without scattering, reproduces the one with scattering as illustrated in Fig. 2.32.

Experimental results

As already said, our hydro-radiative code FCI2 is 2D axi-symmetrical and the experimental dose modulations recorded of the RadioChromic Films do not exhibit significant azimuthal variations (see Fig. 2.33). In order to be compared with the numerical results,

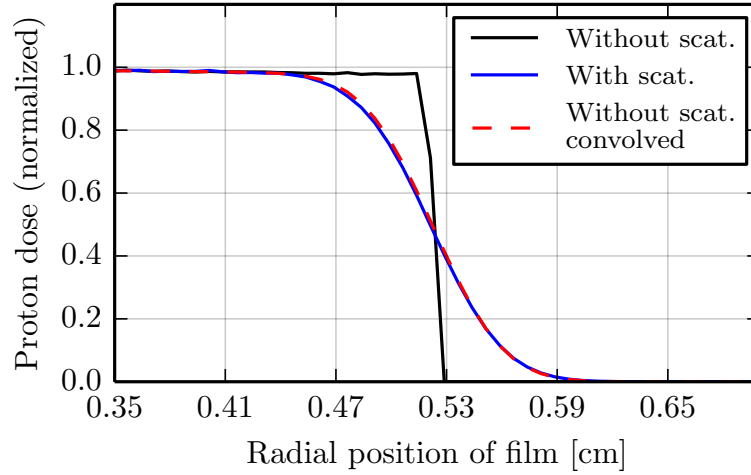


Figure 2.31: Example of the method used to estimate the error due to the scattering.

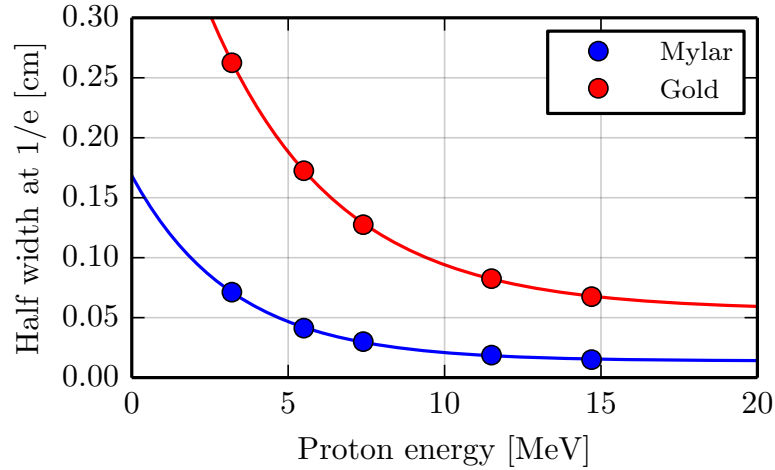


Figure 2.32: Half width at $1/e$ of the convolving Gaussian used to reproduce the scattering, as a function of the protons' energy.

the experimental dose modulation is thus angularly averaged around an axis of symmetry. Hence, we will compare experimental and simulated dose variations as a function of the radial position, $\frac{\Delta N_p}{N_{p0}}(r)$, where ΔN_p is the difference between the recorded (modulated) proton dose and the supposed reference dose N_{p0} (non modulated).

Typical angularly averaged dose modulations, corresponding to the RCF shown in Fig. 2.33, are presented in Fig. 2.34 for both Mylar (top, blue) and gold (bottom, red). As one can see, the averaged modulations are characterized by a ring of proton accumulation (*i.e.* a maximum of the proton dose in 1D). Therefore, in order to illustrate the dynamics of the magnetic field during the irradiation of the solid target by the nanosecond laser pulse, we have plotted in Fig. 2.35 the mean radius of this accumulation proton ring as a function of time, for both the measurement and the corresponding post-processed simulations. It

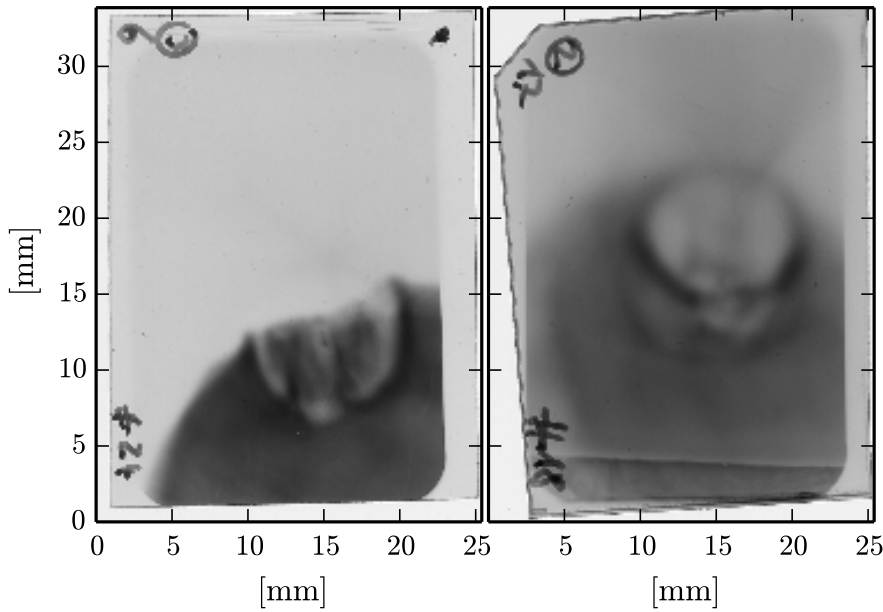


Figure 2.33: Radiochromic films used for Fig. 2.34 (JLF-Titan campaign, 1.1 ns). Left: Mylar (shot #24), right: gold (shot #18).

is important to note that, as discussed earlier, the time window of the broadband proton spectrum due to the time of flight is in the order of 0.1 ns. Hence, each different point in time corresponds to a particular shot.

Furthermore, for the shots on the low Z target, we did not observe any correlation between the protons' energy and the radius of the proton dose accumulation ring. On the contrary, for the shots on the high Z target, the energy of the probing protons has an influence on the radius of the proton accumulation ring, as seen in the sensitivity study of the diagnostic (Fig. 2.28). This means that the integrated magnetic field $\int B \cdot dz$ is sufficiently small in the first case to assume that the deflections imparted by the protons are small in comparison with the dimensions of the detector. As a consequence, the modulations of the proton dose are linked to a geometric image of the integrated magnetic field on the detector. For high Z targets, this is not the case anymore, meaning that the integrated magnetic field is higher and that the modulations on the detector are no more related to a projection of the magnetic field on the detector.

Hence, for the Mylar (Fig. 2.35, top) different proton energies were used depending on the highest energy film exploitable for each shot, while for gold (Fig. 2.35, bottom) only the 7.4 MeV RCF was used. For the latter, a compromise had to be done: high energy protons are less affected by the scattering, but the high energy cut-off of the proton spectrum [112] is varying from shot to shot, due to experimental variations (alignment of the targets, picosecond pulse contrast, energy and focal spot *etc...*).

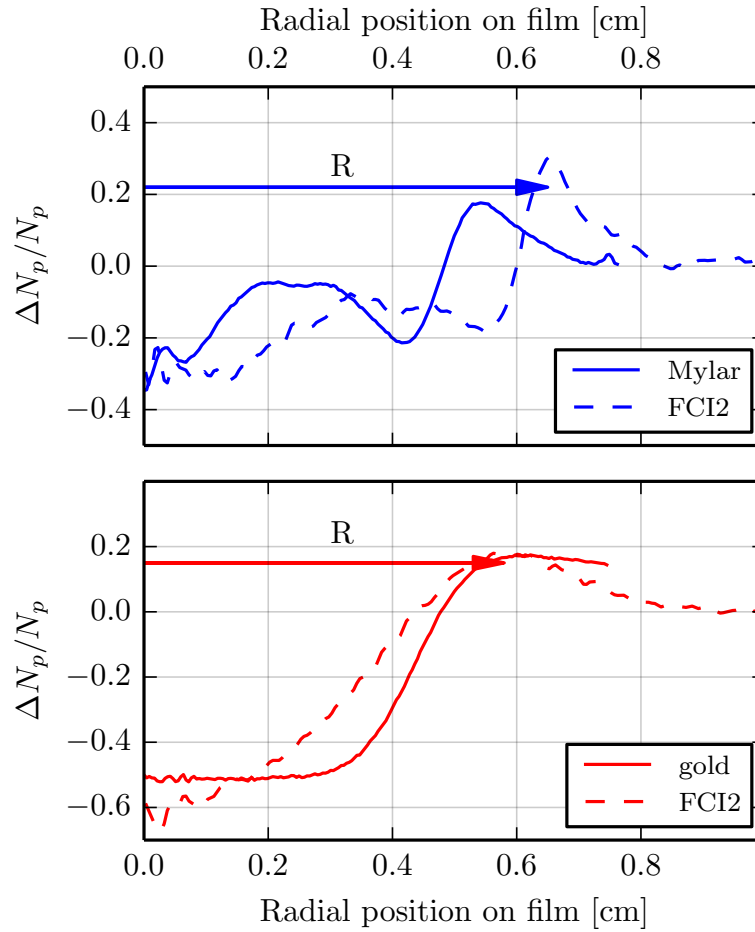


Figure 2.34: Modulation of the proton dose, as a function of the radius for Mylar (top, blue) and gold (bottom, red), at 1.1 ns.

Conclusions

These results show that the magnetic field topology given by FCI2, using our non-local heat flux – MHD coupled “NLSH” model, gives very similar proton radiography patterns that the ones measured during the JLF-Titan experiment, for both a low Z target (Mylar) and a high Z one (gold), and this, all along the nanosecond laser pulse. Nonetheless, one has to keep in mind the limits of this diagnostic. As presented earlier, large variations of the laser’s energy or focal spot did not affect the proton dose modulations as much as one may expect. Hence, the validation of numerical models cannot be performed only from comparisons with proton radiography measurements, and the use of a detailed reference code (such as ALADIN) is mandatory (but not sufficient).

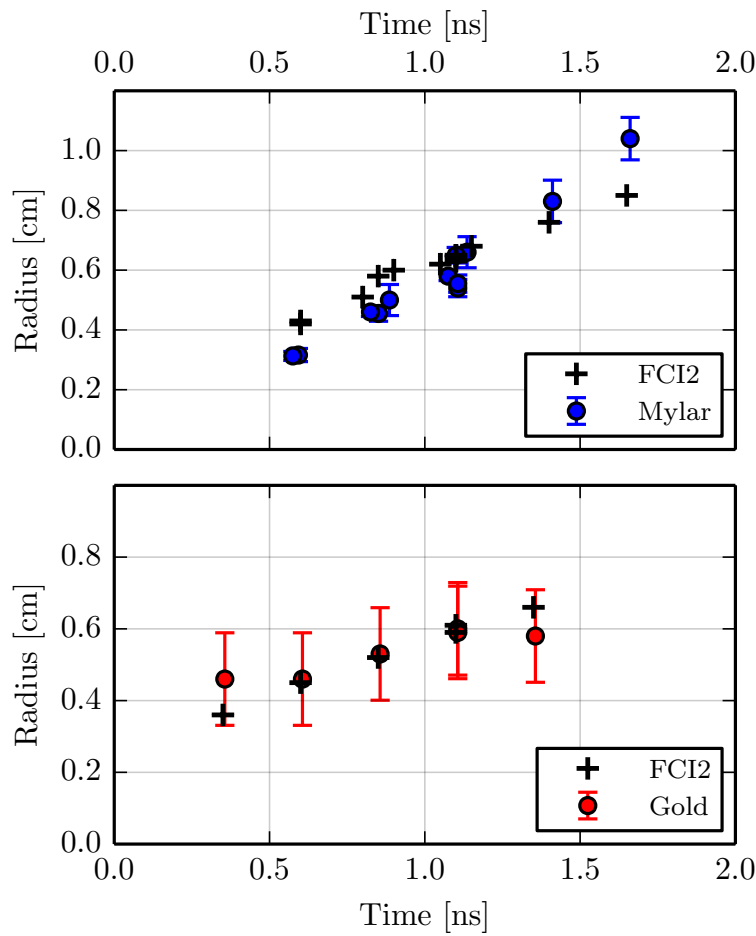


Figure 2.35: Evolution of the radial position of the maximum of the proton dose modulation, as a function of time. Error bars are given by the scattering through the target (see Fig. 2.32).

2.3 Comparison of the heat flux models with the LULI2000 experiment.

Now that the proton radiography diagnostic has been presented, and before concluding this chapter dedicated to experimental results, we will come back to the LULI2000 experiment which was performed in 2008 (hence before the 2011 JLF-Titan campaign). During this experiment, proton radiography measurements were performed at early times in the interaction (600 ps), in order to validate the numerical treatment of the coupling between the non-local heat flux and the magneto-hydrodynamics. Therefore, following the comparison of the different models, through a simplified case without hydrodynamics (see chapter 1), we will now present simulations of the LULI2000 campaign using the same models:

- NLSH: our standard model, with “thermal” Nernst velocity

- NLBR: non-local correction on the Braginskii heat flux, with “kinetic” Nernst velocity
- Braginskii: the classical Braginskii transport model
- No Nernst: NLSH model, without Nernst effect.

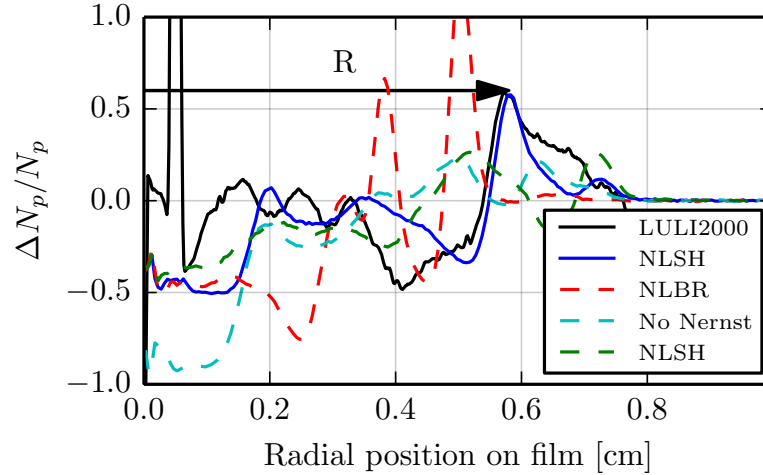


Figure 2.36: Proton dose modulation from the LULI2000 experiment at $t = 0.6$ ns, with the post-processed FCI2 simulations using various models.

Fig. 2.36 shows an example of proton dose modulation obtained from the LULI2000 experiment, compared to the post-processed results from the FCI2 simulations performed with these four models. It shows that only the NLSH model allows to obtain a single, well defined peak of proton accumulation, at the same radius as in the experiment. Both the Braginskii and NLSH without Nernst give two proton dose accumulation rings whose radii are too small for one of the rings, and too large for the other. The delocalized Braginskii model (NLBR) gives also two proton dose accumulation rings whose sizes are too small and the proton dose much too high (more than twice the reference dose). Finally, the amplitude of the measured dose modulation $\Delta N_p/N_{p0}$ shown in Fig. 2.36 (solid black line) has been increased by a factor 2 for visibility. One has to keep in mind that the RCF are also sensitive to x-rays and electrons, which could lead to an overestimation of the non-perturbed dose N_{p0} , and then an underestimation of the dose modulation $\Delta N_p/N_{p0}$.

Fig. 2.37 presents the magnetic field topologies at $t = 0.6$ ns issued from FCI2 simulations using the four models presented before. Without the Nernst effect, the magnetic field is clearly expelled outward by the fluid’s motion and “diluted” in the coronal plasma (see Fig. 2.37(c)). It results in a weak deflection of protons, in disagreement with the experimental observation. With the NLSH model (see Fig. 2.37(a)), we can distinguish three main areas splitting the magnetic field distribution. Firstly, the B-field is strongly convected toward the target center (in the region of radius $r < 0.01$ cm, in the order of the focal spot size), deep in the over-dense plasma: the magnetic field can reach several

MegaGauss there. Then, a part of the magnetic field extends radially (from ~ 0.01 to 0.03 cm) between N_c and $\sim 10 N_c$ with an amplitude of $0.5\text{--}1$ MG. Finally, a small part of the less compressed ~ 1 MG magnetic field is located in the under-dense ($N_e < N_c$) plasma, at the edge of the plasma “plume”.

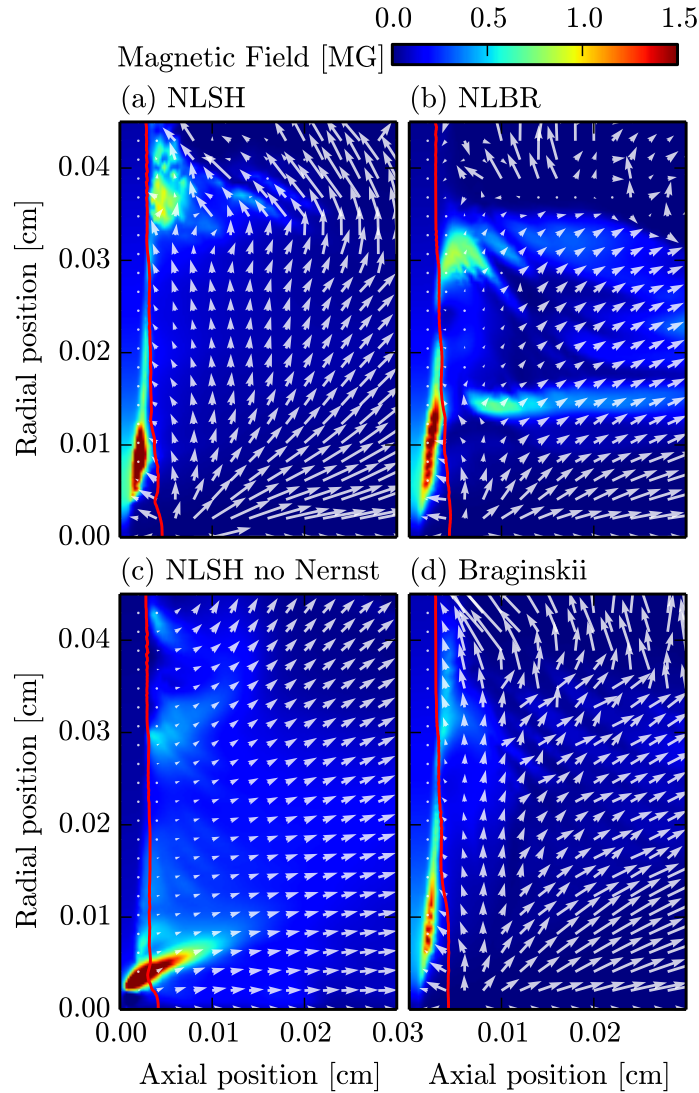


Figure 2.37: FCI2 simulations of the LULI2000 experiment at $t = 0.6$ ns. Color maps of the magnetic field (in MG), with vector plots of the advection velocity $\mathbf{U} = \mathbf{u}_{Fluid} + \mathbf{u}_{Nernst}$ and red iso-line of the critical density at the second laser harmonic. **(a)** NLSH model, **(b)** NLBR model, **(c)** NLSH without Nernst effect and **(d)** Braginskii model.

As presented in the first chapter, the magnetic field is convected at a velocity \mathbf{U} , linked both to the “frozen-in-flow” velocity \mathbf{u}_{Fluid} , directed by the plasma expansion outward of the target, but also to the Nernst velocity \mathbf{u}_{Nernst} which direction depends on the heat flux. Consequently, the convective transport of the magnetic field alternates between the radial and axial directions and through the under- and over-dense regions of the plasma. Neither the Braginskii model nor the delocalized Braginskii (NLBR) model were able to reproduce

the experimental observations. Although the magnetic field is partially compressed on the target for the latter, the radial extension of the outer “blob” of magnetic field is lower, and some field appears in the corona at $r \sim 0.015$ cm. The Braginskii model reproduces roughly the same topology of magnetic field as the NLSH case, yet by definition does not account for the non-locality of the heat flux.

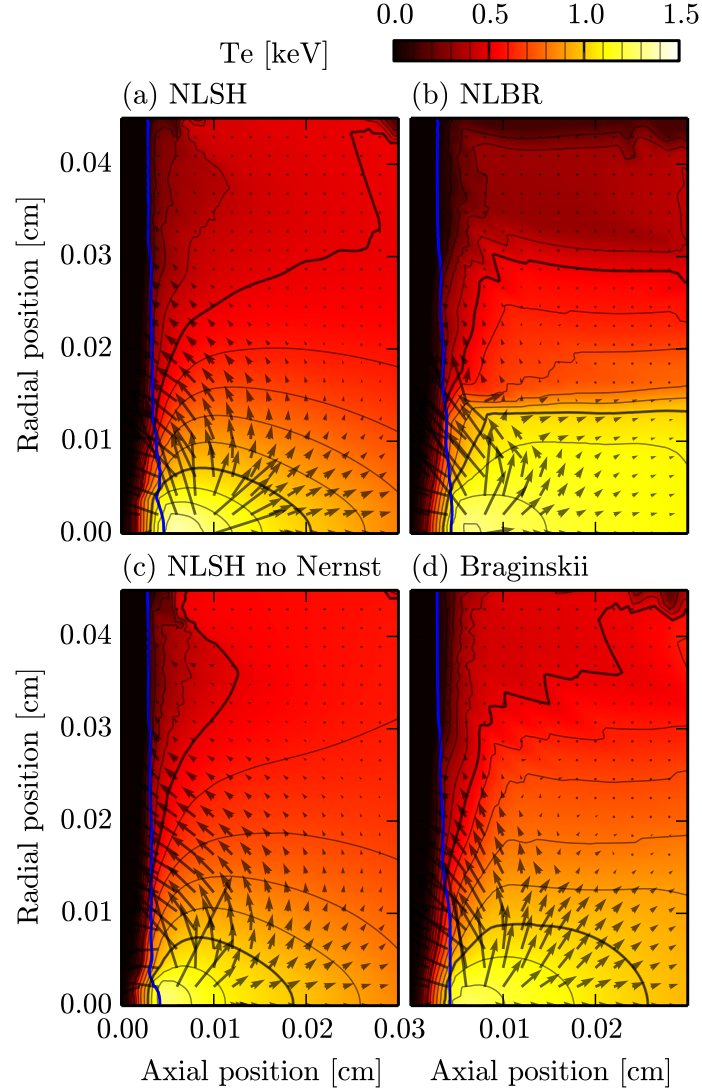


Figure 2.38: *FCI2* simulations of the LULI2000 experiment at $t = 0.6$ ns. Color maps of the electron temperature (in keV), with vector plots of the heat flux and blue iso-line of the critical density at the second laser harmonic. (a) NLSH model, (b) NLBR model, (c) NLSH without Nernst effect and (d) Braginskii model.

These simulations allow us to illustrate the fact that a precise modeling of the magnetic field transport is crucial, as it will affect the electron thermal conduction and hence impact the plasma temperature, as can be seen in Fig. 2.38. It shows that both Braginskii models (even the delocalized one) exhibit an almost isothermal corona, typical of heat fluxes based on the linear theory. Moreover, for the NLBR model, a sharp lateral gradient is present

at $r \sim 0.015$ cm, which is, at the same time, due to the inhibition of the heat flux and the source of the magnetic field at this location. On the opposite, both “NLSH” models induce a significant electron temperature gradient in the corona, commonly associated with a non-local thermal conduction.

In conclusion, while using the Braginskii thermal conduction model gives in overall a topology of magnetic field in a “disk-like” shape, it does not reproduce the experimental measurement, nor does it account for the effect of non-locality, which is troublesome for high power generated plasmas. Delocalizing the Braginskii model, such as done in the NLBR model, leads to an obviously wrong coupling between the heat flux and the B-field, as illustrated by the peculiar phenomenon at the radial limit of the laser heated region. Finally, the NLSH without Nernst effect is just presented here as an illustration and has no physical meaning.

2.4 Conclusions

In this chapter, devoted to the comparisons with experimental results, after a short history of the measurement of the self-generated magnetic field, we have presented two experiments: the first one has been performed at LULI2000 in 2008 and presented in details in [89], while the second, performed at JLF-Titan in 2010, has been presented in [91]. However, in the present thesis, the results from this JLF-Titan campaign have been compared in details with post-processed FCI2 simulations.

First of all, the optical diagnostics have been discussed, starting with the interferometry measurement. It has been performed using a Normarskii interferometer, producing interferograms which have been deconvolved such as to obtain a phase map (\sim integrated density). Following, assuming a cylindrical symmetry, one may obtain a density profile using an Abel inversion. We showed that the opposite process may be performed for the simulation results: starting from the electron density profile, one may calculate a phase map and, eventually, a synthetic interferogram. As FCI2's results did not match the measurement, neither for the phase map nor the electron density profile, we recalled that both the interferometry diagnostic and the hydro-radiative simulation have their own validity domains. The first is limited to the low density part of the plasma's corona, where the probe beam can propagate without significant refraction. On the opposite, the simulation, being based on the hydrodynamic reduction, is only valid for the collisional part of the plasma, quantified by the Knudsen number. In other words, FCI2 is not suited to simulate the expansion of the corona in vacuum, where the fluid hypothesis are no more verified.

The second optical diagnostic presented was the polarimetry. It allows to measure a rotation of the probe beam's polarization, due to the integrated electron density and the magnetic field's component along the probe beam's propagation direction. The measurements did not show any variation of the polarization within the diagnostic sensitivity range. Hence, it is in agreement with FCI2's post-processed results, showing a rotation of the polarization only deep within the dense plasma, where the measurement clearly showed strong absorption and refraction of the probe beam. This is in contradiction with the results presented by the MIT group, showing a shell-like shaped topology of magnetic field, from LASNEX simulations.

Next, results from the x-ray pinhole (on gold target) have been presented. From the magnification of system and the angle with the target's normal it is possible to transform the image on the detector plane into one on the target plane, assuming that the x-ray emission was mostly localized onto the target plane. While the results from FCI2 did show a smaller emission size, they reproduced the shape of the emission region. Therefore, because FCI2 is axi-symmetric, one could conclude that despite the angle between the target and its driving laser, as well as the inhomogeneous focal spot, the heated region

was quite round.

The last diagnostic presented was the proton radiography. We presented at first the two methods used to accelerate the MeV protons: the imploding backlighter capsule, suited for experiments on Omega, and the TNSA mechanism, adapted for a large number of laser facilities. Before presenting the results, a study of the diagnostic has been performed. Using a simplified post-processor without scattering to analyze analytical magnetic field topologies, we firstly showed how the proton dose on the detector is modulated by the variations of magnetic field. Then, using FCI2's proton radiography post-processor, we performed a sensitivity study, showing the importance of accounting for scattering of the protons through the solid target. As a consequence, the error on the proton radiography measurement has been defined based on this scattering, as a function of the target's material and thickness and the protons' energy. Lastly, because both the experimental and simulated proton dose variations exhibit a ring of proton accumulation, the radius of this proton dose accumulation has been used as a mean to compare FCI2's results with the measurements. It showed that FCI2 was able to reproduce the evolution of this radius all along the laser irradiation, both for the mylar and the gold targets.

The chapter has been concluded with comparisons of the different heat flux models presented in the first chapter, but this time against a LULI2000 measurement, following the study published in [60]. It showed that only the "NLSH" model was able to reproduce the size of the proton accumulation ring measured during the experiment.

3 Analysis using FCI2

As it was seen in the first chapter, the presence of magnetic fields in laser generated plasmas may strongly affect the plasma's dynamics and evolution, depending on their strength. The Hall parameter (*i.e.* the magnetization of the electrons $\chi = \omega_{ce}\nu_{ei}$) allows us to define if the electron conduction is modified. For $\chi \ll 1$ the conduction is not affected. For $\chi \gg 1$, the conduction is first re-localized and then inhibited as the Larmor radius $R_L = \frac{m_e v}{eB}$ becomes smaller than the thermal gradient length or the mean free path of the electrons, meaning that the electrons are trapped by the magnetic field as they are not subject to enough collisions during a gyro-period to be transported. For intermediate χ , the electron transport is still effective, yet rotated in the $\mathbf{b} \times \nabla T_e$ direction (Righi-Leduc effect). In the case of laser-solid interactions the longitudinal heat flux is reduced in the electron conduction region (*i.e.* between the critical density and the electronic ablation front), while the radial heat flux is increased.

The effect of the magnetic field on the fluid's motion is defined by the β parameters: $\beta_{th} = \frac{P_{th}}{P_{mag}}$ and $\beta_{kin} = \frac{P_{kin}}{P_{mag}}$, where $P_{mag} = \frac{B^2}{8\pi}$ is the magnetic pressure (in *cgs*), $P_{th}(\rho, T)$ is the thermal pressure according to the equation of state and $P_{kin} = \frac{1}{2}\rho u^2$ is the kinetic pressure, also called *ram pressure*. These parameters, which are basically the ratios of the fluid internal or kinetic energy density over the magnetic field's energy density, define which of the fluid or the field is dominant during the evolution of the magneto-hydrodynamics system. For example, if $\beta_{kin} \ll 1$, the fluid motion is confined by the magnetic field, such as in plasma jets [113, 114], or if $\beta_{th} \ll 1$, the plasma expansion due to its pressure is limited by the field (like in tokamaks). Hence, these parameters define the master/slave relationship between the field and the fluid. Finally, the magnetic Reynolds number is defined as the ratio of the advection velocity over the diffusion velocity, $R_m \equiv U_{conv}/U_{diff} = \frac{4\pi}{c^2}\sigma V L$, with $V = U_{conv} = \|\mathbf{u}_{fluid} + \mathbf{u}_{Nernst}\|$, and L is a characteristic length of the system, chosen here as the magnetic field gradient length $L \equiv B/\nabla B$ (see the advection and diffusion terms in eq. 1.38). It characterizes the dominant term between the advection and the diffusion.

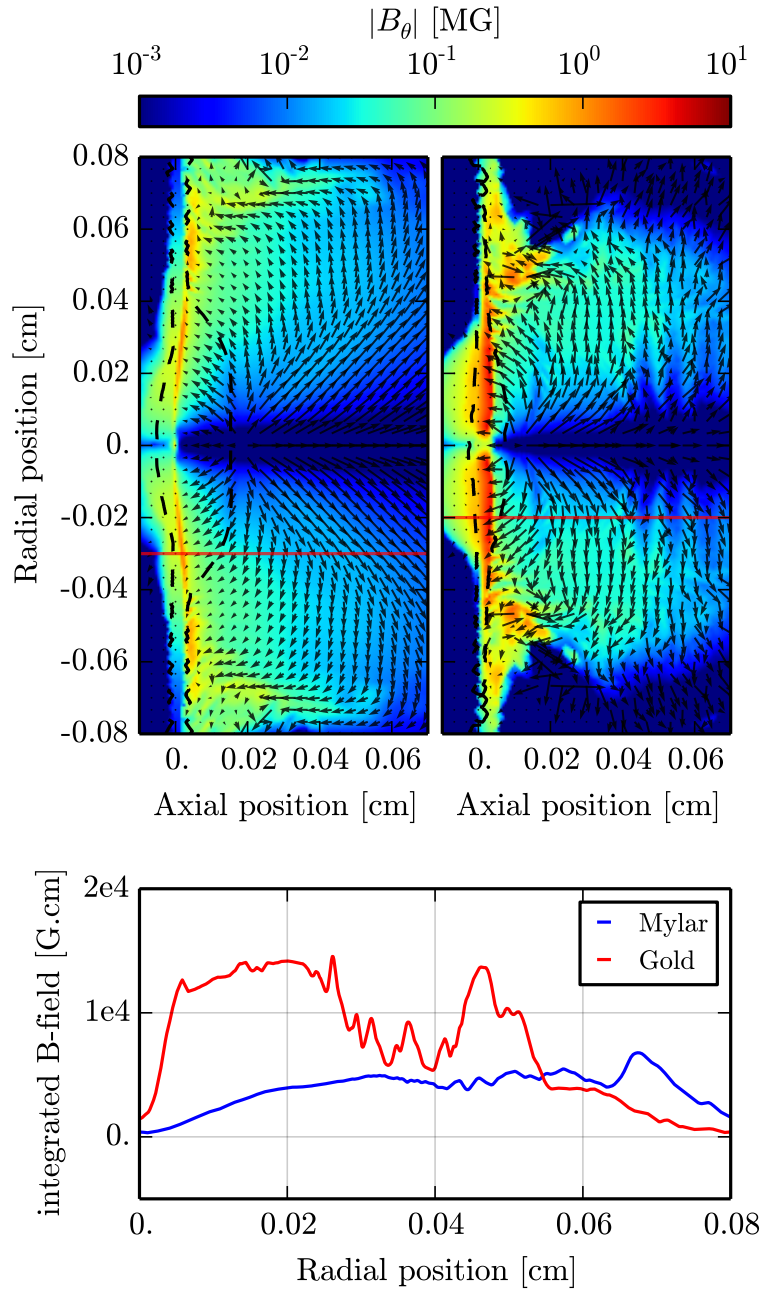


Figure 3.1: *Experimental case (JLF-Titan) at 1.5 ns. Top: color map of the magnetic field in log scale, with the iso-line of the critical density at first laser laser harmonic and vector plots of the advection velocity $\mathbf{U} = \mathbf{u}_{Fluid} + \mathbf{u}_{Nernst}$ for mylar (left) and gold (right). Bottom: integrated magnetic field $\int \mathbf{B}.dz$ as a function of the radial position for mylar (blue) and gold (red)*

As we saw at the end of the first and second chapters, our “NLSH” model coupling the non-local thermal conduction with the MHD in FCI2 is able to reproduce the results of both the kinetic simulation and the proton radiography measurements for the LULI2000 and the JLF-Titan experiments, giving us confidence that the physics included in the model is more accurate than the one assumed in the other models, at least within the

range of parameters explored here. As such, in this chapter, we will use FCI2 simulations to get an insight on:

1. why the magnetic field exhibits such a disk-like topology (see Fig. 3.1),
2. the differences between the mylar and gold targets,
3. how the resulting topology depends on the laser parameters,
4. how the magnetic field affects the overall interaction, from the point of view of the electron conduction, hydrodynamics and overall energy balance.

While in the previous chapter we aimed at showing the compressed topology of the magnetic field in contrast with previously published results [76, 77, 79, 81], in this section we will focus more on the different regimes of magnetization and will therefore present the magnetic field maps in log scale, for an easier interpretation of the dimensionless quantities. Indeed, for example, a 10 kG magnetic field in the corona may have a more important effect on the heat flux or hydro motion than a 1 MG field in the dense part of the target.

Note that in the following figures, the origin of the axial direction corresponds to the back of the foil (the front being the irradiated face). Results for mylar and gold targets will always be shown side by side for comparison. On colormap figures, the mylar target will be on the left and the gold one on the right. For lineouts, the blue curve will represent the mylar while the red one will correspond to the gold target. Finally, for a more intuitive visualization of the results, most of the time the $r < 0$ plane will be displayed, despite of the cylindrical symmetry of the simulations around the $r = 0$ axis. Therefore, in the case of magnetic field color map figures, the quantity shown is $|B_\theta|$ because of the logarithmic color scale.

3.1 Magnetic field topology

3.1.1 Topology of the magnetic field

First of all, on Fig. 3.1 the magnetic field maps are drawn for simulations at $t = 1.5 ns$ of shots on mylar and gold targets with laser parameters typical of the JLF-Titan experiment (as presented in sec. 2.1.2, page 67). It shows that for both targets, the magnetic field exhibits a similar topology. Indeed, one can see that the magnetic field is efficiently swept out of the heated region by the Nernst effect and accumulates onto the solid foil in a plate-like shape. The magnetic field is strongly compressed at the foot of the electronic ablation front and less compressed when trapped in the “waist” of the expanding plasma plume (around the heated region, where the plasma ablated at a large radial distance

meets the one ablated in the laser irradiation region, see the scheme in Fig. 3.2) where the Nernst effect is not strong enough to compress the field (see Fig. 3.1(top)).

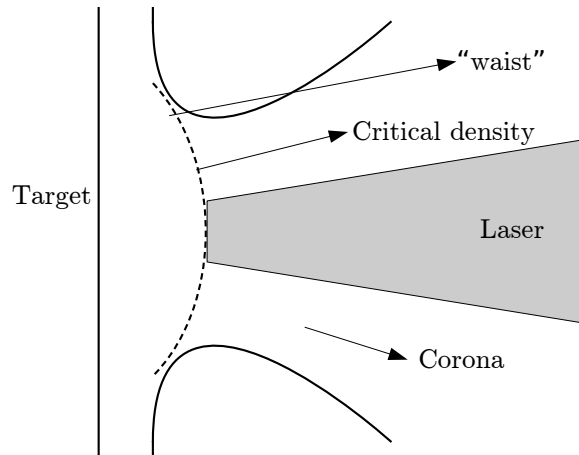


Figure 3.2: Scheme of the “waist” of the plasma plume.

Overall, only a weak (10-100 kG) magnetic field remains in the laser heated corona. This B-field topology is similar to what was recently obtained by L. Gao et al. [110] using a Braginskii treatment in DRACO, but quite different from the shell-like shape around the expanding plasma, presented in other publications using LASNEX [76, 77, 79, 81].

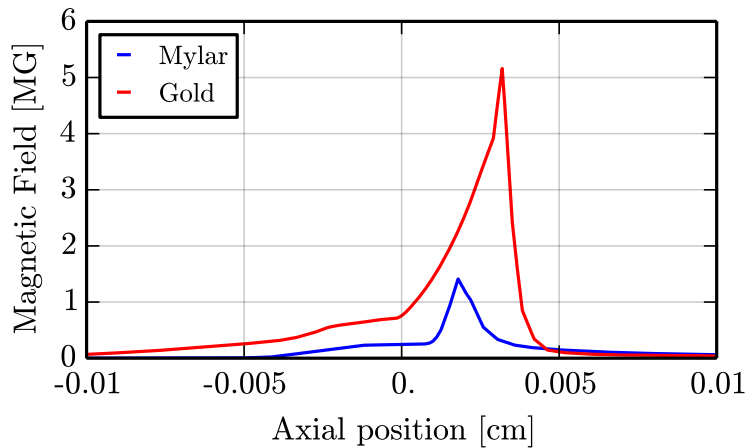


Figure 3.3: Experimental case (JLF-Titan) at 1.5 ns. Lineouts of the magnetic field over the axial position (i.e. normal to the target surface), through the ablation front ($r = 0.03$ cm for mylar and $r = 0.02$ cm for gold, see solid red lines in Fig. 3.1).

Nonetheless, two differences clearly appear between the low and high Z materials: for the gold target, the magnetic field is stronger and extends longitudinally over a greater distance. In order to have a better insight on this, we have plotted in Fig. 3.3 the magnetic field along the longitudinal axis at a radius of interest (approximately where the magnetic field is maximum: $300 \mu\text{m}$ for Mylar, $200 \mu\text{m}$ for gold, see solid red lines in Fig. 3.1). This figure shows different things. First of all, the gradient of magnetic field is very strong

on the electron conduction side, leaving almost no field in the low density plasma: this is consistent with the fast advection of the field by the hot electron population, namely the Nernst effect. Secondly, the field extends over $\sim 40 \mu\text{m}$ in the case of the gold target, compared to the $\sim 20 \mu\text{m}$ with the mylar target: this would mean that the advection velocity drops further away from the solid foil for high Z targets. Finally, one can see a $\sim 100 \text{ kG}$ magnetic field behind the target: this is an evidence of the transport of the field through the dense and cold target, where there is no heat flux and thus no advection of the field. As such, the only remaining process is the diffusion of the field through the target, due to the high resistivity of the plasma at this location, coupled with the strong magnetic field gradient, source of a high electron current through Ampere's law $\mathbf{j} = \frac{c}{4\pi} \nabla \times \mathbf{B}$.

3.1.2 Source and confinement of the magnetic field

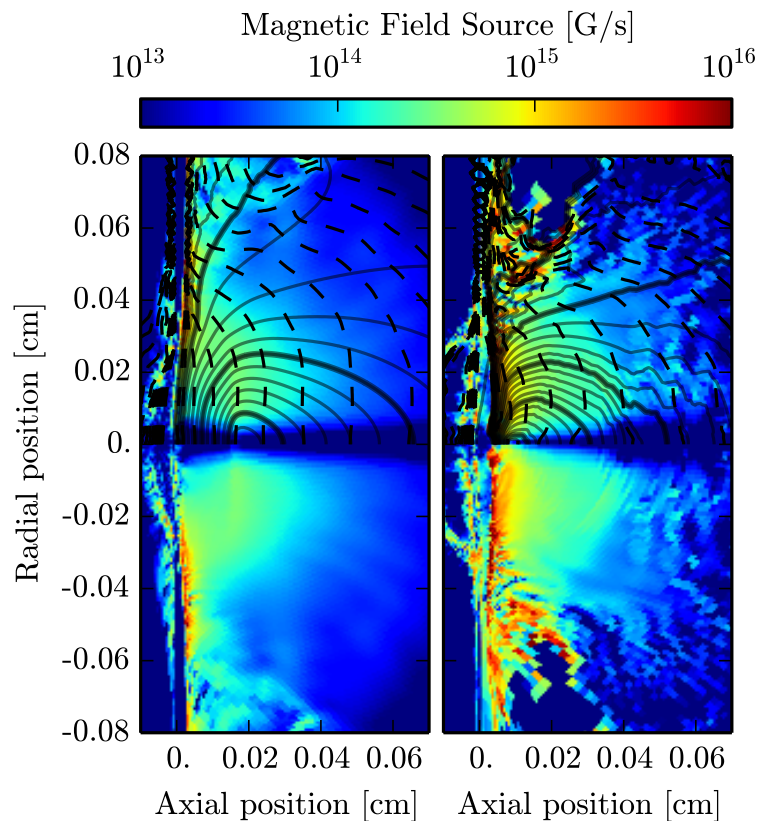


Figure 3.4: *Experimental Case (JLF-Titan) at 1.5 ns. Color maps of the magnetic field source, with iso-lines of the electron temperature (solid, 100 eV step) and iso-lines of the electron density with logarithmic steps (dashed)*

To understand why the magnetic field exhibits those topologies, one needs to answer two questions: “*where does the magnetic field come from?*” and “*how is it transported?*”. For

the first, let us recall the expression of the source term of the magnetic field, which in our case is due exclusively to the thermo-electric effect and thus to the crossed electron temperature and density gradients:

$$\left. \frac{\partial B}{\partial t} \right|_{source} = \frac{k_b c}{e} \frac{\nabla T_e \times \nabla N_e}{N_e} \quad (3.1)$$

Fig. 3.4 illustrates the maps of magnetic field source (in G/s) for the experimental case at 1.5 ns, with isolines of the electron temperature (linear steps) and density (logarithmic steps) in the upper half to visualize the strength and direction of the gradients. It shows that the magnetic field is mainly produced at the electronic ablation front, while the source in the corona is two orders of magnitude lower. This is consistent with the dependence with respect to the density gradient, as it is maximum in the ablation front, where it suddenly drops from the compressed solid to the low density, expanding hot plasma. Moreover, it shows the stronger dependence with the gradient strength than with their collinearity, *i.e.* from the critical density to the ablation front, $\|\nabla T_e\| \times \|\nabla N_e\|$ increases faster than $\frac{\sin(\theta)}{N_e}$ decreases.

Nonetheless, one can see some differences between plastic and gold targets. For the first, the source is mostly located around the laser energy deposition region, while for gold, the source is almost radially continuous from the symmetry axis. These differences can be explained when looking at the temperature profiles (see Fig. 3.5): for the plastic target case, both the temperature and density gradients are perpendicular to the target in a large area around the symmetry axis, while for the gold target the temperature presents a radial gradient up to the symmetry axis.

Finally, some magnetic field is generated in the “waist” of the plasma plume, where the low density and almost perpendicular gradients compensate for the smoothness of the gradients. Yet, one has to be careful when studying this region, as the low collisionality implies a deviation from the hydrodynamics regime (see Fig. 2.12 in sec. 2.2.1).

Once generated, the magnetic field is then transported through the Nernst effect. Looking at both the source map (Fig. 3.4) and the magnetic field map with the vector plots of the advection velocity (Fig. 3.1), one easily understands that the 0.1 – 1 MG/ns magnetic field, generated in the whole corona except on the axis, is quickly convected away from the heated region and redirected toward the “waist” of the plasma. Note that the Nernst velocity has the same order of magnitude in most of the plasma, as the lower heat flux in the corona is compensated by a lower electron pressure. This explains why in our case the magnetic field presents a plate or crater like topology, in contrast with the shell-like topology which can be found in previous publications [76, 77, 79, 81].

To conclude this study on the topology of the magnetic field, we stress out that the magnetic field is transported up to a point where it will be trapped between two “walls”

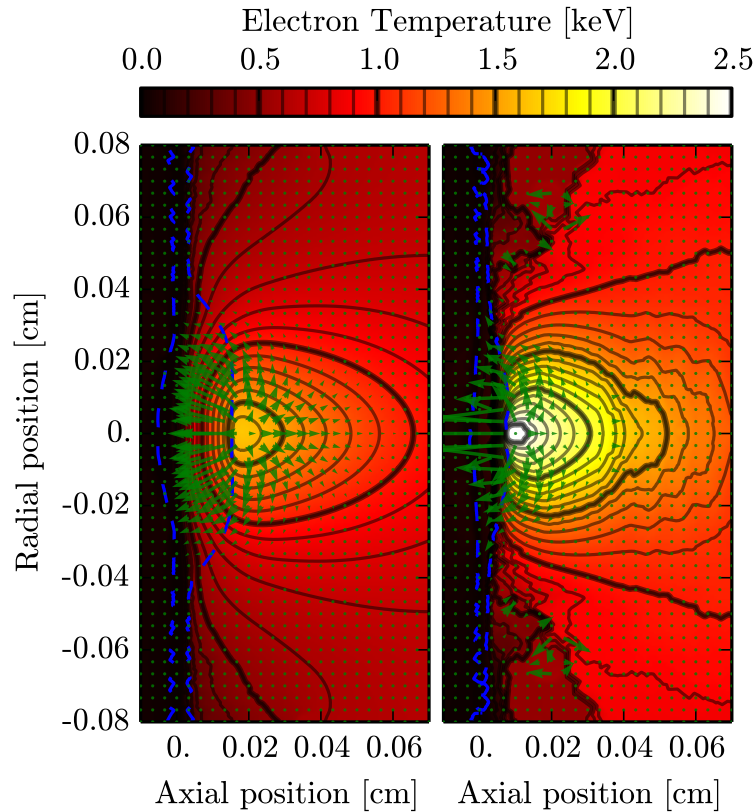


Figure 3.5: *Experimental Case (JLF-Titan) at 1.5 ns. Color maps of the electron temperature with vector plots of the Non-Local heat flux. Dashed iso-lines of the critical density (N_c) at first laser harmonic.*

(see Fig. 3.6 and Fig. 3.7): on the one hand the fast advection with the heat flux and, on the other hand, the remaining solid foil. This explains the most striking difference between the two materials: in the case of high Z materials, a radiative ablation front forms ahead of the electronic one. This phenomenon, called *double ablation fronts* [32], implies a typical constant temperature and density region between these two fronts, as illustrated on Fig. 3.6. As such, in the case of the plastic target, the magnetic field is compressed in a very small thickness onto the solid foil, while for the gold case, the thickness of the accumulated magnetic field increases along the separation between the two ablation fronts.

We want to highlight here the difficulty of getting an intuition on the resulting magnetic topology. Indeed, one could think that because the density ranges on much many orders of magnitude compared to the temperature, the first one would dominate the strength of the source while the later would determine the topology. We saw that in reality the maximum of the field source is not that different between the two cases despite a very different hydrodynamics behavior. When looking into more details at the source term (Eq. 3.1), it appears that it depends on these two gradients, but also on the angle between them

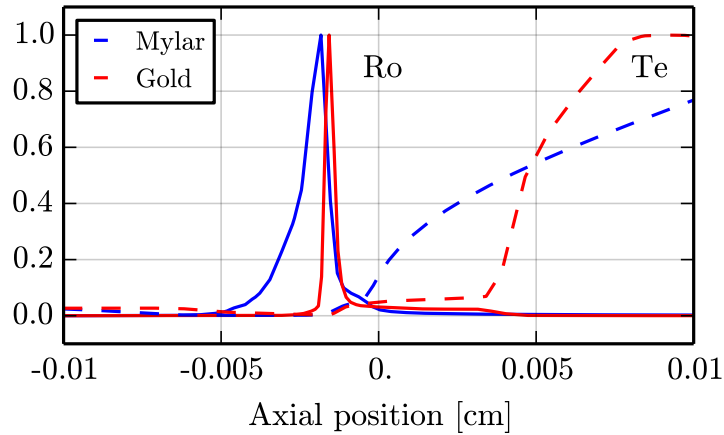


Figure 3.6: *Experimental Case (JLF-Titan) at 1.5 ns. Lineouts along the symmetry axis of the density and electron temperature (normalized).*

(i.e. 2D effects) and on the electron density. Hence, it depends on the hydrodynamics which itself depends on a lot of effects: laser parameters, target material, heat flux (and so on the magnetic field) and radiative transport. In a nutshell, the magnetic field source and transport is strongly coupled to the hydrodynamics, preventing any estimate of the magnetic field topology without accurate simulations.

3.1.3 Transport regimes

To emphasize on the complexity of the physics at play during high power laser – solid interactions, Fig. 3.8 plots lineouts along the target’s normal direction of the β parameter and the magnetic Reynolds number R_m (see definitions in the introduction of this chapter, on page 107), at the same radii as before ($300 \mu m$ for the mylar target and $200 \mu m$ for the gold one), still at 1.5 ns.

It is commonly admitted that for laser generated plasmas $\beta \gg 1$ and $R_m \gg 1$, *i.e.* the magnetic field is “slave” to the plasma and follows the fluid motion through advection. However, Fig. 3.8 shows that depending on the region of the plasma, different transport regimes may be at play. From the corona to the rear of the target (the front being the irradiated face):

- (a) $\beta > 1$ and $R_m > 1 \rightarrow$ in the electron conduction region, the magnetic field is convected by the plasma (in fact by the heat flux) up to the electron ablation front, where it is accumulated.
- (b) $\beta > 1$ and $R_m < 1 \rightarrow$ at the ablation front, the ablated plasma is free to diffuse through the accumulated magnetic field, because of the high plasma pressure (the ablation pressure which drives the shock and accelerates the foil) and low conductivity (the plasma is “cold”).

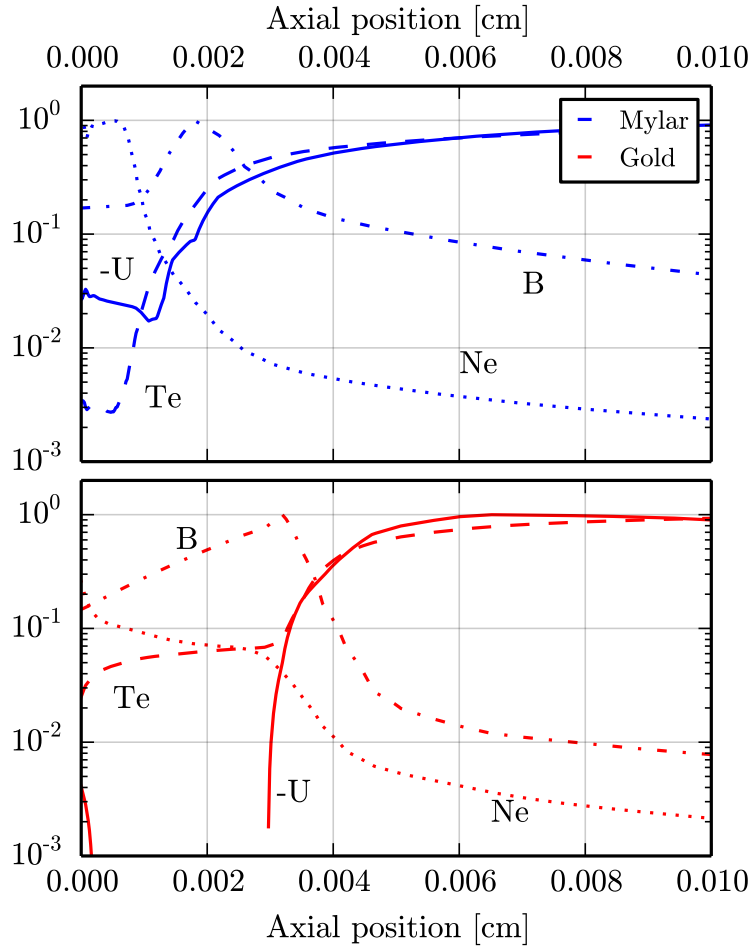


Figure 3.7: *Experimental Case (JLF-Titan) at 1.5 ns: Lineouts along the axial direction, at $r = 0.03$ cm (mylar) and $r = 0.02$ cm (gold) of the advection velocity $-U$ (solid), electron temperature (dashed), electron density (dotted) and magnetic field (dashed-dotted). All quantities are normalized to their maximum.*

- (c) $\beta < 1$ and $R_m < 1 \rightarrow$ in the very thin remaining solid foil, the magnetic field can diffuse through the dense and cold plasma (low conductivity and minimum plasma pressure).
- ($\beta < 1$ and $R_m < 1 \rightarrow$) in the hypothetic presence of a low pressure plasma at the back of the target (for example because of a rarefaction wave after a first shock), this plasma would be convected by the magnetic field motion.

This illustrates that in order to accurately simulate the evolution of the magnetic field in this context, one needs a radiative-hydrodynamic code integrating a non-local electron conduction model correctly coupled with a *resistive* MHD package. Indeed, it deviates significantly from the simple “magnetic field frozen in flow” vision of laser-generated plasmas. Moreover, the presence of a ~ 100 kG magnetic field behind the solid target (see Fig. 3.3) is now explained by the diffusion of the field through the solid target.

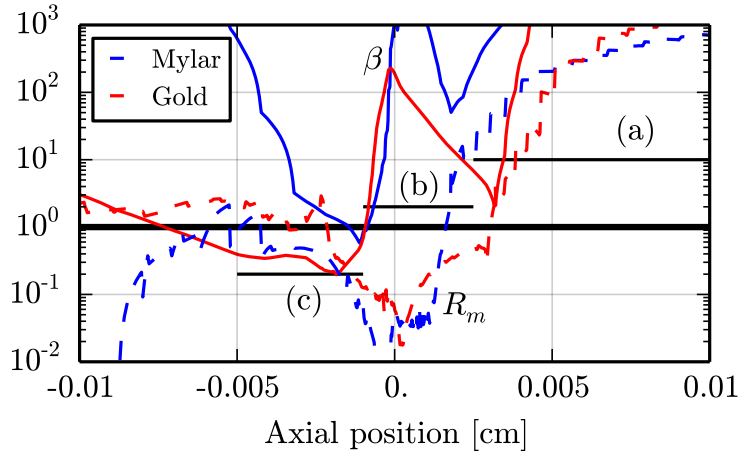


Figure 3.8: *Experimental Case (JLF-Titan) at 1.5 ns. Lineouts along the axial direction, at $r = 0.03$ cm (mylar) and $r = 0.02$ cm (gold) of beta parameter β (solid) and magnetic Reynolds number R_m (dashed).*

3.2 Parametric study of the laser parameters

As seen in the previous section, the topology of the magnetic field is strongly related to the hydrodynamics of the interaction. Thus, in this section, we will see how the topology of the magnetic field varies with the parameters of the laser driving the plasma.

3.2.1 Reference (Fig. 3.9) and high energy (Fig. 3.10) cases

We will start with a reference case (shown in Fig. 3.9) close to the experimental one, but with a simpler laser focal spot. The laser is at first harmonic ($\lambda_0 = 1057$ nm), 400 J with the same power law than the experimental case (constant 0.2 TW over 2 ns, after a 100 ps linear rising time). The focal spot is a 4th order super Gaussian with a full width at half maximum (FWHM) of 300 μ m, giving an intensity $I \sim 3 \times 10^{14}$ W/cm². Targets are still made of Mylar for the low Z case and gold for the high Z case.

As expected, changing the focal spot for another one close to the experimental case does not drastically change the topology of the magnetic field, as the heating of the target is almost similar. One may just observe a magnetic field in the waist extending slightly more normal to the target than in the experimental case (Fig. 3.1) where the magnetic field at this position seems more compressed onto the foil. This could be due to higher intensity gradients compared to the Gaussian experimental focal spot.

Fig. 3.10 shows results from simulations performed with the same parameters as in the reference case, but with a 4 kJ laser pulse (2 TW). We can see an increase of the magnetic field by approximately a factor 3, coherent with the steeper temperature gradient associated with the higher laser power. This confirms the obvious: as the magnetic field depends

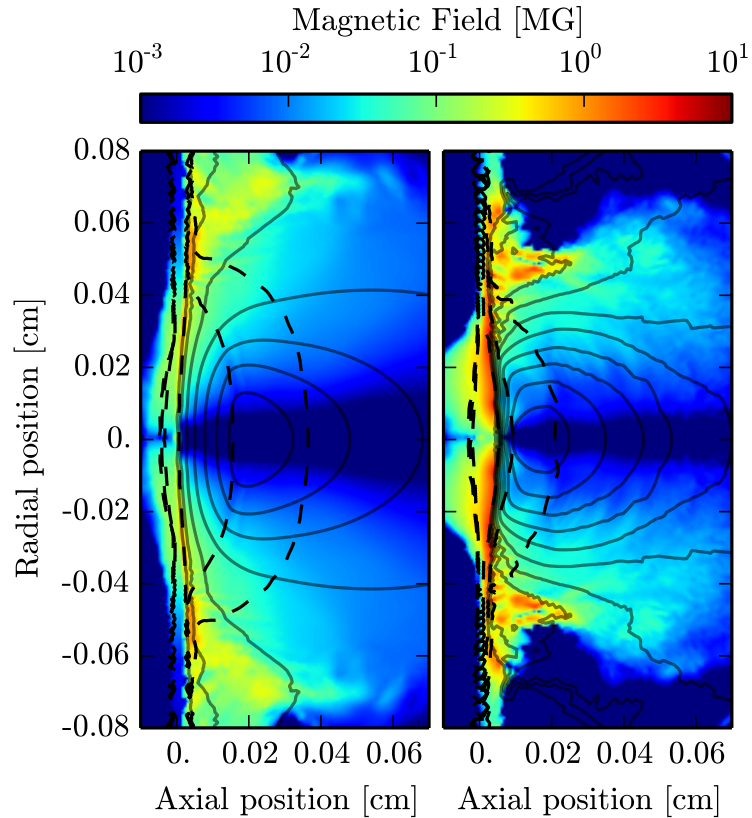


Figure 3.9: Reference case at 1.5 ns: 400 J, 2 ns square pulse, 1st laser harmonic and 4th order super-Gaussian focal spot having a 300 μm FWHM ($I \sim 3 \times 10^{14} \text{ W/cm}^2$). Color maps of the magnetic field, with solid iso-lines of the electron temperature (200 eV steps) and dashed iso-lines of 10 Nc, 1 Nc and 1/4 Nc. Left: Mylar, right: gold.

on the hydrodynamics of the plasma, the dependence of the magnetic field strength to the laser intensity has no reason to be linear. In addition to the higher electron temperature, because of the higher laser power, the hydrodynamics is faster, which implies a more developed plasma at a given time. Hence the magnetic field extends over a larger radius (beware of the different spatial scale on Fig. 3.10). Yet, overall, the topology of the magnetic field remains similar to the one of the reference case.

3.2.2 Focal spot : Flat-top (Fig. 3.11) and high intensity cases (Fig. 3.12)

We then investigated the effect of the shape of the focal spot: in Fig. 3.11 it is a 16th order super Gaussian (still with 300 μm FWHM) representing a well marked flat-top profile, *i.e.* a large region with homogeneous intensity and a sharp decrease of the intensity. One may then expect that it would result in a different temperature profile. Yet, because of both refraction of the laser in the plasma and thermal conductivity, the effects on the

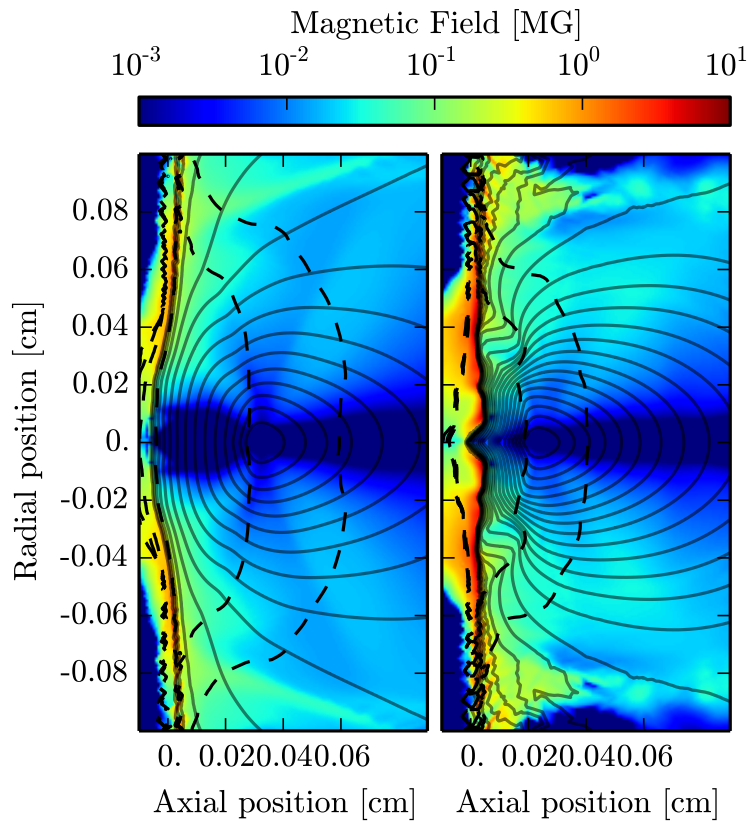


Figure 3.10: *High energy case at 1.5 ns: 4 kJ, 2 ns square pulse, 1st laser harmonic and 4th order super-Gaussian focal spot having a 300 μm FWHM ($I \sim 3 \times 10^{15} \text{ W/cm}^2$). Color maps of the magnetic field, with solid iso-lines of the electron temperature (200 eV steps) and dashed iso-lines of 10 Nc, 1 Nc and 1/4 Nc. Left: Mylar, right: gold.*

hydrodynamics and therefore on the magnetic field profile is extremely small.

On the opposite, Fig. 3.12 displays the B-field from simulations performed with a very small focal spot (50 μm FWHM Gaussian), mimicking a laser beam without phase plate and similar to the one used in [115, 116, 73], giving a very high intensity ($I \sim 1 \times 10^{16} \text{ W/cm}^2$). In this case the laser energy is deposited in a very localized region. As such, the electronic ablation front has a smaller radial extent and is localized deeper in the target compared to the reference case at the same time. The radial thermal conduction seems smaller and, in the case of gold, the magnetic field presents a concave topology, directly linked to the form of the electron ablation front. Nevertheless, once again, the magnetic field still exhibits a “plate-like” topology with a similar strength.

3.2.3 Laser wavelength : 3ω case (Fig. 3.13)

Finally, Fig. 3.13 depicts the influence of the laser wavelength on the interaction. For this, we have run simulations with a laser pulse at the 3rd harmonic (351 nm). This leads

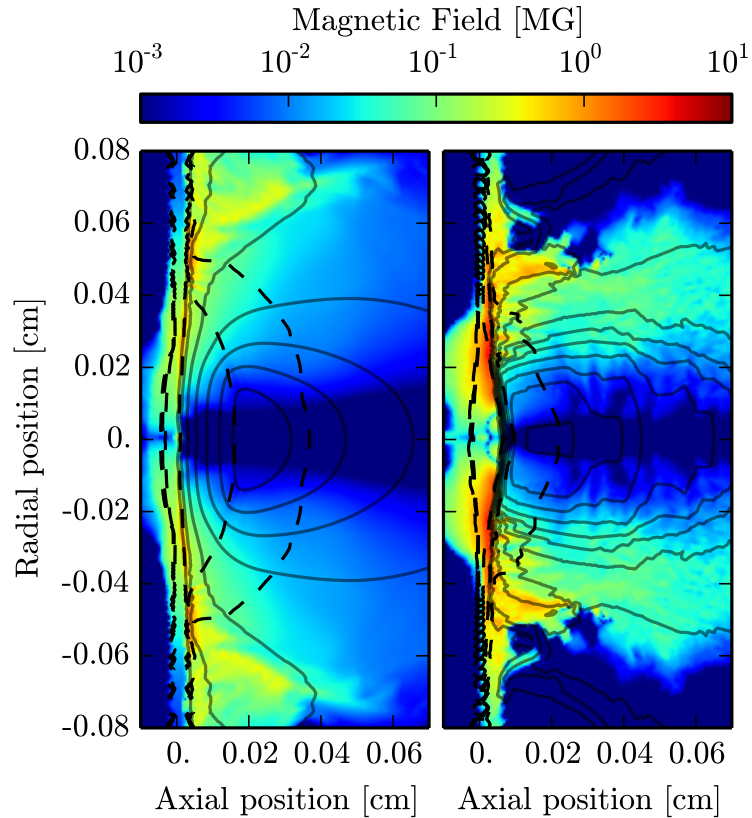


Figure 3.11: *Flat-top case at 1.5 ns: 400 J, 2 ns square pulse, 1st laser harmonic and 16th order super-Gaussian focal spot having a 300 μm FWHM ($I \sim 3 \times 10^{14} \text{ W/cm}^2$). Color maps of the magnetic field, with solid iso-lines of the electron temperature (200 eV steps) and dashed iso-lines of 10 Nc, 1 Nc and 1/4 Nc. Left: Mylar, right: gold.*

to a high acceleration of the foil and thus to significant variations in the magnetic field topology. Indeed, while some magnetic field is still present onto the accelerated part of the foil, we can observe the formation of a strong magnetic field at the limit between the accelerated part of the foil and the one at rest. This is consistent with the presence of strong electron density and temperature gradients in the ablation front, which, in this particular region, are close to being perpendicular.

Moreover, because of the deep laser energy deposition, the electron conduction region has a much smaller radial extent. It is thus surrounded by the magnetic field in the non-accelerated part of the foil. Hence the lateral electron conduction seems significantly reduced compared with other cases, as can be seen by looking at the electron temperature iso-lines in Fig. 3.13.

After all those laser parameter variations, we can conclude that, overall, the magnetic field does not radically change: its intensity remains of the same order of magnitude and it remains compressed onto the target with a less compressed part in the waist of the plasma bubble. With higher laser power, the magnetic field strength increases, in accordance with

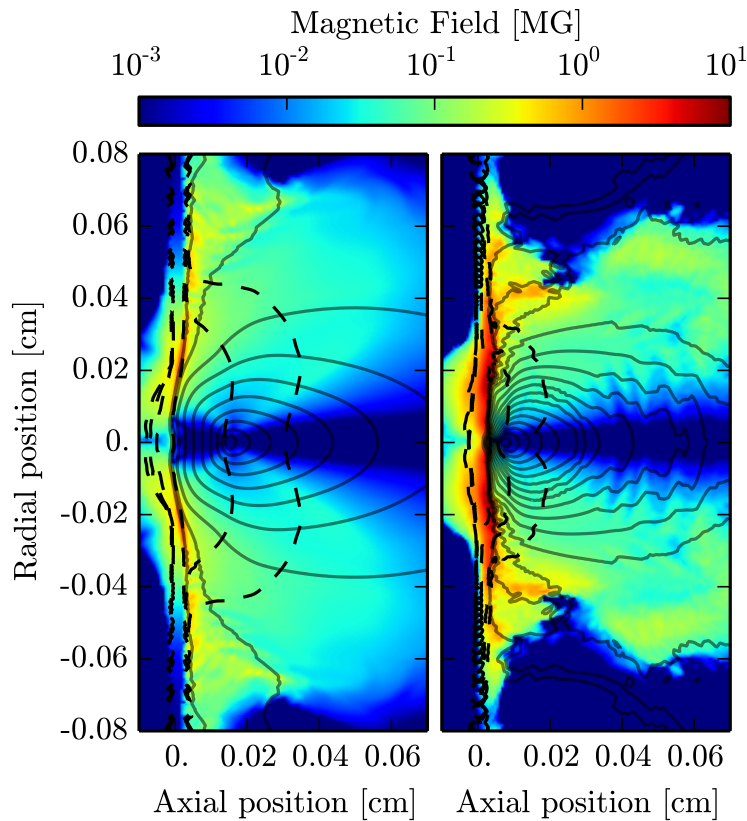


Figure 3.12: *High intensity case at 1.5 ns: 400 J, 2 ns square pulse, 1st laser harmonic, Gaussian focal spot having a 50 μm FWHM ($I \sim 1 \times 10^{16} \text{ W/cm}^2$). Color maps of the magnetic field, with solid iso-lines of the electron temperature (200 eV steps) and dashed iso-lines of 10 Nc, 1 Nc and 1/4 Nc. Left: Mylar, right: gold.*

the stronger temperature gradients and faster hydrodynamics evolution. Moreover, the magnetic field's topology seems quite insensitive to the profile of the laser focal spot, as the refraction in the plasma will anyhow smooth the laser energy deposition. Yet, one has to keep in mind that for the three different focal spots presented here, the profile of the laser intensity was continuous. Thus we cannot extrapolate our results to more realistic focal spots, *i.e.* to 2D laser spots having a non-uniform speckle pattern, which could induce much more complicated magnetic field topologies. Finally, the most significant difference appears at higher laser harmonics, for which the more effective acceleration of the foil induces a deformation of the electron ablation front, and as a consequence, a deformation of the magnetic field compressed behind it.

3.3 Effects of the magnetic field on the interaction

Now that we have a better understanding on the source and transport of the magnetic field, which both determine its resulting topology, one may question the importance of

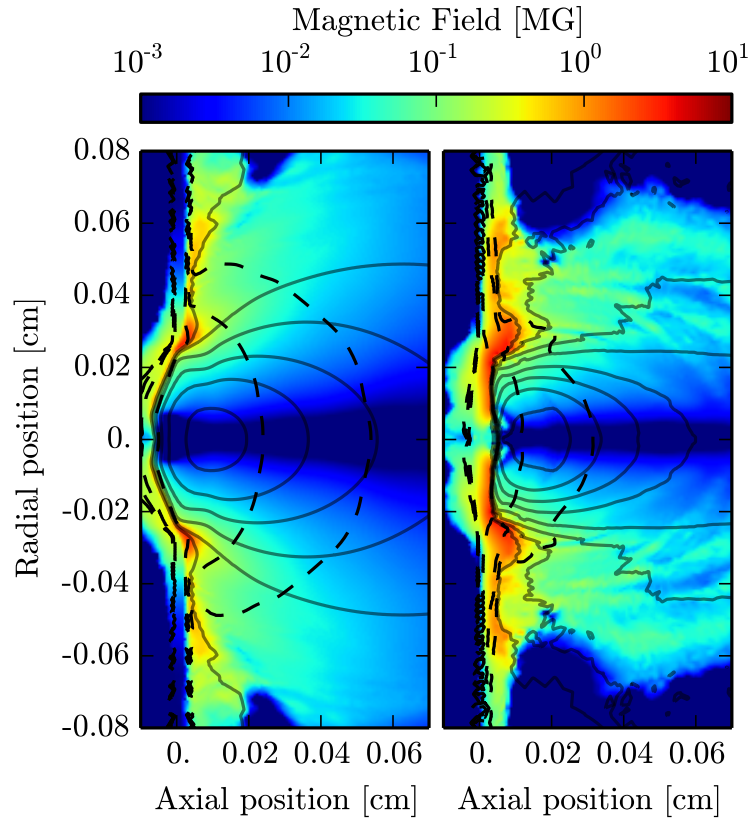


Figure 3.13: 3ω case at 1.5 ns: 400 J, 2 ns square pulse, 3rd laser harmonic and 4th order super-Gaussian focal spot having a 300 μm FWHM ($I \sim 3 \times 10^{14} \text{ W/cm}^2$). Color maps of the magnetic field, with solid iso-lines of the electron temperature (200 eV steps) and dashed iso-lines of 10 Nc, 1 Nc and 1/4 Nc (for a laser a first harmonic). Left: Mylar, right: gold.

the B-field in laser–solid interaction. The effect of the magnetic field can be analyzed according to three points of view:

1. its effects on the electrons, *i.e.* on the heat flux,
2. its effects on the ions, *i.e.* on the hydrodynamics,
3. its effects on the energy balance of the system.

In this subsection, unless specified otherwise, all figures come from the reference case shown on Fig. 3.9 (400 J, 2 ns, 1st laser harmonic, 300 μm FWHM 4th order super-Gaussian focal spot).

3.3.1 Effects on the heat flux

As we saw in the first chapter, the heat flux in laser generated plasmas is a challenge to model as, due to the presence of strong temperature gradients, the linear (Spitzer–Härm

and Braginskii) approximation breaks down. Therefore, the heat flux at a given point in space does not depend anymore on the local thermodynamic characteristics (∇T_e , *etc.*), but is rather determined by the entire electron population carrying the heat flux. This can be seen in our model in the diffusion equation (eq. 1.56) of h (the correction to the scalar part of the electron distribution function). Moreover, the heat flux in a given direction does not depend anymore only on the electron conductivity in this direction. Indeed, for example, in the case of a strong gradient along the longitudinal axis, the lateral component of the non-local heat flux would be reduced, even if the linear approximation along the lateral direction is still valid [22].

Plasma magnetization

Looking at our magnetized non-local heat flux model (see eq. 1.58, 1.54 and Fig. 1.17), it appears that the magnetization of the electrons (characterized by the Hall parameter $\chi_v = \omega_{ce}\tau_{ei} \propto v^3$) is a critical parameter, as it affects every term in the expression of the heat flux. Basically, the more χ increases, the more the heat flux is rotated and inhibited. Yet, as we saw in sec. 1.5, the heat flux takes the form of a local component coupled to a non-local one. The first is directed along the ∇T_e direction (and $\mathbf{b} \times \nabla T_e$ for its Righi-Leduc component), while the second is directed along the ∇h direction (and $\mathbf{b} \times \nabla h$ for the non-local Righi-Leduc component). Hence, we can see that trying to guess how the heat flux will be affected by the magnetization is very delicate.

- Each velocity group is affected by its own magnetization χ_v which varies quickly from one group to another due to the v^3 dependence.
- The non-locality is ensured by a diffusion term involving h , the correction to the scalar Maxwellian electron distribution function. This means that any intuition on the form of h (and thus of \mathbf{y}) is complicated. On the opposite, in the framework of the linear theory, the knowledge of the local electron temperature and “thermal” magnetization ($\chi = \omega_{ce}\tau_{ei}^{th} \propto v_{th}^3$) allows to get an idea on: which is the heat flux direction, where it is stronger or inhibited, *etc.*
- The diffusion of h also means that the non-local correction terms are not collinear to ∇T_e and may thus either reduce or amplify the local heat flux depending on the direction of ∇h , as illustrated previously in chapter 1 (see Fig. 1.12). Therefore the inhibition of the non-local terms due to the magnetization can either amplify or reduce the total heat flux. Yet, because these terms eventually vanish with increasing χ , one can expect a relocalization of the heat flux.

Nonetheless, because the fast electron population responsible for the non-local effects are more effectively magnetized (due to a longer collision time), one can expect a relocalization of the heat flux, before its complete inhibition. Fig. 3.14 represents the “thermal”

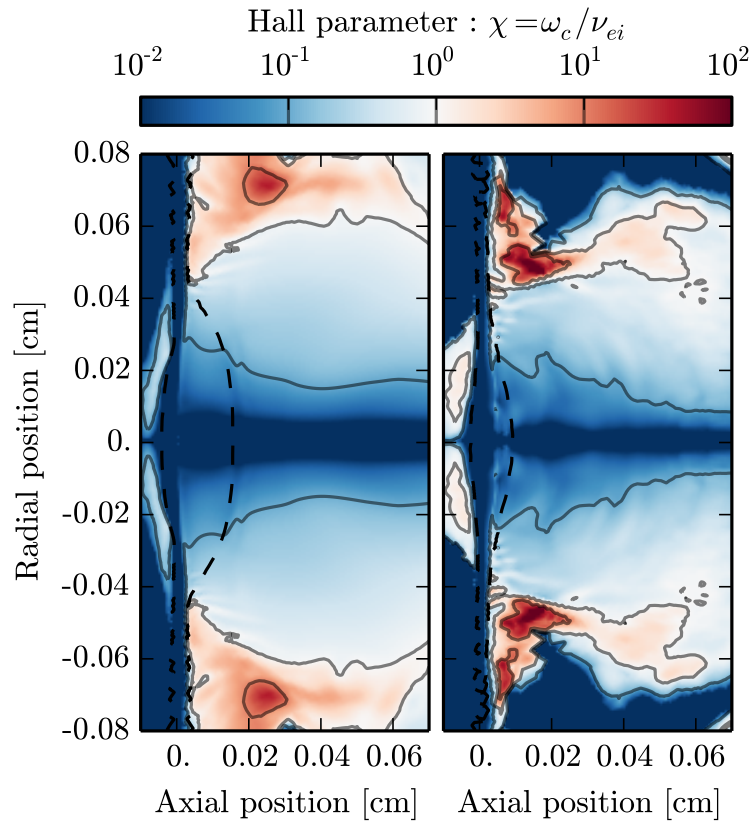


Figure 3.14: Reference case at 1.5 ns: Color map of the “thermal” Hall parameter $\chi = \omega_{ce} \nu_{ei}^{th}$ (magnetization), with dashed iso-line of the critical density at first laser harmonic. Left: mylar, right: gold.

magnetization for the reference case (corresponding to Fig. 3.9) at 1.5 ns. A striking result is that despite the fast advection of the magnetic field with the Nernst effect, the continuous generation of magnetic field in the corona (yet a few order of magnitude lower than the field generated around the ablation front, as seen in Fig. 3.4) is enough to keep a 10–100 kG magnetic field in the corona. There, associated with the longer collision time, it results in a weak magnetization ($0.1 < \chi < 1$) of a major part of the expanding plasma. Finally, note that the accumulation of magnetic field in the low density “waist” of the plasma bubble¹ implies a higher magnetization which could be responsible for an inhibition of the heat flux.

Comparison of the heat fluxes, with and without magnetic field

In order to have a better insight on the B-field effects on the non-local heat flux, the reference simulations (Fig. 3.9, 400 J at 1ω over 2 ns, within a $300 \mu\text{m}$ FWHM 4th order super-Gaussian focal spot) have been post-processed to calculate the heat flux using

¹The region close to $z \sim 0.02$ cm, $r > 0.06$ cm for the Mylar target and $0.04 < r < 0.06$ cm for the gold one.

different models, from the same temperature and magnetic field profiles (at 1.5 ns). The heat flux models which will be compared are:

- Spitzer-Härm → local, no B-field effects.
- Braginskii → local, B-field effects.
- “NLSH” with $\mathbf{B} = 0$ → non-local, no B-field effects.
- “NLSH” → non-local, B-field effects

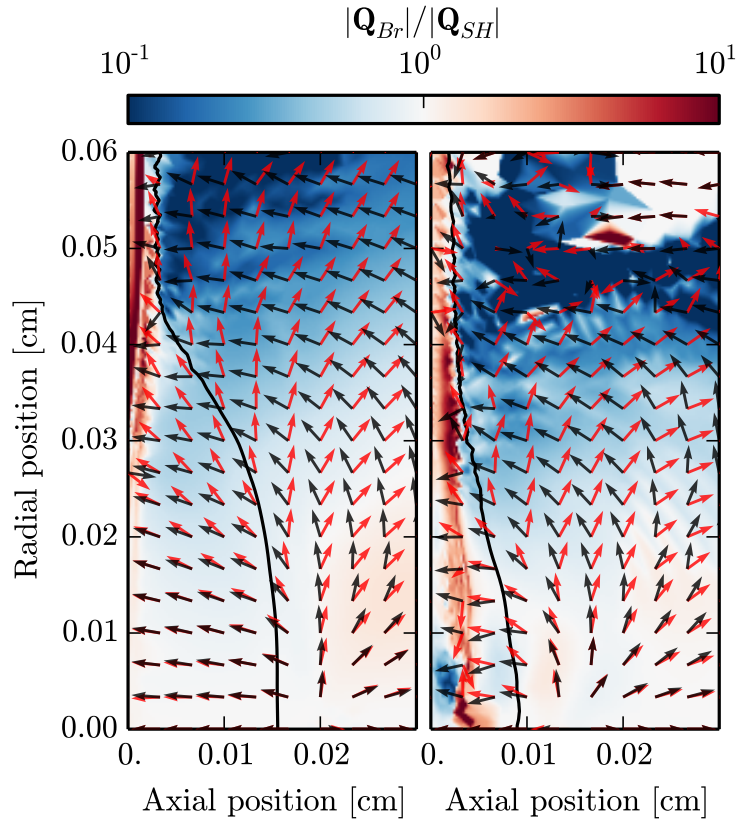


Figure 3.15: Reference case at 1.5 ns, local comparison. Color maps of the ratio of the Braginskii heat flux module over the Spitzer-Härm one. Vector plots of the heat flux directions (red for Braginskii, black for S-H). Iso-lines of the critical density at first laser harmonic. Left: Mylar, right: gold.

This will therefore allow us to see how taking into account the magnetic field affects the heat flux depending on the formalism used (local or non-local). Fig. 3.15 compares the Braginskii heat flux with the Spitzer-Härm one. For that, the color maps represent the ratio of the modules $\|\mathbf{Q}_{Br}\| / \|\mathbf{Q}_{SH}\|$, *i.e.* the inhibition of the heat flux, and the normalized vector plots represent its direction, allowing us to visualize the rotation due to the Righi-Leduc effect. Fig. 3.16 is similar, yet using the non-local (“NLSH”) with B-field model instead of the Braginskii one, and the non-local without B-field model instead of the Spitzer-Härm one. Note that for an easier visualization of the electron conduction

region, the symmetric domain $r < 0$ is not shown and the extents of the frame are smaller than in previous figures.

First of all, for the local case (Fig. 3.15), one can see that the effect of the magnetic field follows what we would expect considering the thermal magnetization (Fig. 3.14) and how the components of the thermal conductivity X_{\perp} (inhibition) and X_{\wedge} (Righi-Leduc) vary (see Fig. 1.9, on page 29). Where the magnetization increases, $\sqrt{X_{\perp}^2 + X_{\wedge}^2}$ decreases and so does $\|\mathbf{Q}_{Br}\| / \|\mathbf{Q}_{SH}\|$ (blue region in Fig. 3.15), while X_{\wedge}/X_{\perp} increases due to the R-L effect (see the increasing angle of the red arrows compared to the black ones)². In the present case magnetization increases with the radial position, which results in a heat flux that is more and more rotated and eventually inhibited.

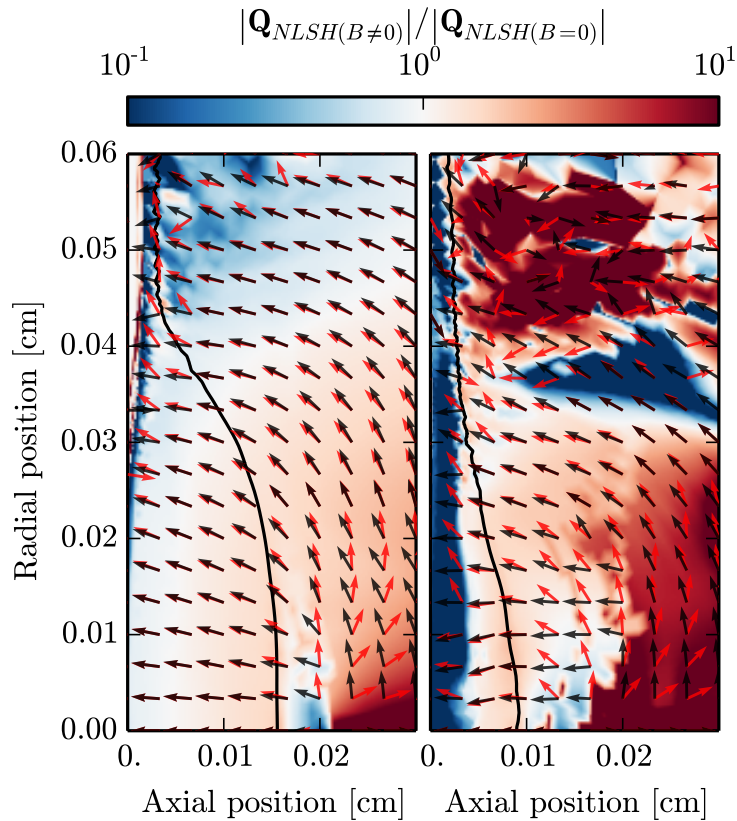


Figure 3.16: Reference case at 1.5 ns, non-local comparison. Color maps of the ratio of N-L heat flux module with B-field over the one without B-field. Vector plots of the heat flux directions (red with B-field, black without). Iso-lines of the critical density at first laser harmonic. Left: Mylar, right: gold.

Before going further, it is of importance to note that our non-local model (and every other “SNB” non-local models) relies on a multi-group diffusion. This means that the integral expression of the heat flux (Eq. 1.57, on page 40) is discretized according to a finite number of electron velocity groups (32 for the FCI2 simulations presented in this thesis).

²We recall that without current, the Braginskii’s heat flux reads $\mathbf{Q}_{Br} = X_{\perp} \mathbf{Q}_{SH} + X_{\wedge} \mathbf{b} \times \mathbf{Q}_{SH}$.

Therefore, the reading of the non-local case (pictured in Fig. 3.16) is less intuitive than with the “grey” local case. It illustrates the need of accurate simulations of $\mathbf{f}_1^{\mathbf{m}}(v_g) + \mathbf{y}(v_g)$, where v_g is the discretized electron velocity, validated through comparisons with kinetic simulations and experiments. While looking at the ratio of the heat flux modules, it appears that contrary to the local case, the heat flux may be increased (see the red regions in Fig. 3.16). It corresponds to a relocalization of the heat flux in regions where the non-local correction acts as a flux limiter. Then, further away from the electron conduction region, where the non-local effects are less important, the magnetization acts on the local components of the heat flux and inhibits it (blue regions). Understanding the influence of the magnetic field on the direction of the heat flux is even more difficult as, for each discretized electron velocity group v_g , it would require to represent³:

- the magnetization χ_v for the corresponding electron velocity v_g ,
- the contribution to the local terms of the heat flux ($(1 - a_1) \mathbf{f}_1^{\mathbf{m}} v_g^5$ and $a_2 \mathbf{b} \times \mathbf{f}_1^{\mathbf{m}} v_g^5$),
- the contribution to the non-local terms ($\lambda_1 \nabla h v_g^5$ and $\lambda_2 \mathbf{b} \times \nabla h v_g^5$).

Nonetheless, in the electron conduction region, the magnetic field does not seem to significantly change the direction of the heat flux. Finally, one has to keep in mind that in our non-local formalism, the expressions of λ_1 and λ_2 (which depend on χ) mean that the heat flux at a given point may also depend on the magnetic field at a larger distance (see the diffusion equation of h , eq. 1.56 on page 40).

Yet, a striking result from this figure is that the heat flux is strongly inhibited at the ablation front, where the magnetic field has been accumulated (see the deep blue area on the left of Fig. 3.16). Therefore, the well known pre-heat at the foot of the ablation front, usually illustrating the effects of the non-local models, tends to be nullified when taking into account the effects of the magnetic field. This is in agreement with the ablation front velocity measurements performed on the *Ligne d'Integration Laser*⁴ [88] and LULI2000 [89, 90], where non-local calculations without magnetic field over-estimated the ablation front velocity. Note that this is well consistent with the fact that flux limited calculations required to adjust the f parameter *a posteriori* to fit their measurements, depending on the laser intensity.

3.3.2 Effects on the hydrodynamics

Considering that the magnetic field is subject to a convective amplification and may thus reach several MegaGauss, one may point out to the possibility of a feedback of the field on the hydrodynamics. The extent of this feedback can be described through two “ β ” parameters:

³ $\mathbf{f}_1^{\mathbf{m}}$, \mathbf{y} , ∇h and χ_v are all function of the electron velocity, while a_1 , a_2 , λ_1 and λ_2 are function of χ_v .

⁴The *Ligne d'Integration Laser* (LIL) was a prototype of a LMJ quad, operating from 2005 to 2015 [87]

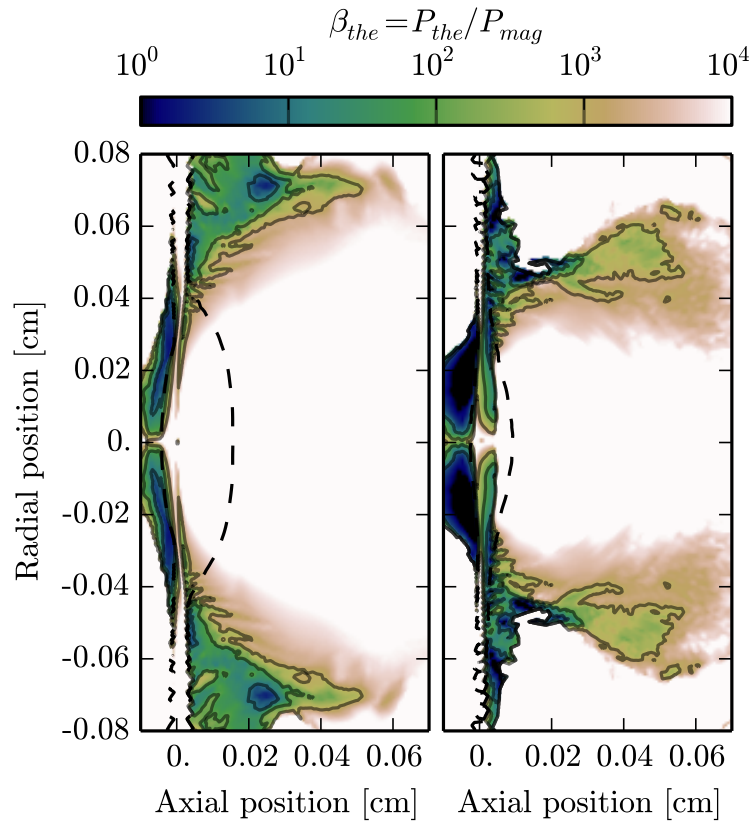


Figure 3.17: Reference case at 1.5 ns. Color maps of the thermal beta parameter $\beta_{th} = P/P_{mag}$. Dashed iso-line of the critical density at first laser harmonic. Left: Mylar, right: gold.

- $\beta_{th} \equiv P/P_{mag}$, the ratio of the plasma's pressure over the magnetic one, characterizes the ability of the magnetic field to overcome the expansion of the plasma due to its pressure. See the momentum equation (eq.1.32) in the first chapter.
- $\beta_{kin} \equiv \rho \cdot \mathbf{u}_{flow}^2 / P_{mag}$, the ratio of the kinetic energy density (sometimes called *ram pressure*) over the magnetic pressure, which characterizes the ability of the magnetic field to oppose to the moving plasma.

Fig. 3.17 presents the color maps of the thermal β_{th} parameter at 1.5 ns. As expected when the magnetic field is swept away from the corona, the plasma's pressure greatly overcomes the magnetic pressure there. Nonetheless, as opposed to the classic view of high beta laser generated plasmas, we can see that in the regions where the magnetic field has been convected and compressed, the magnetic field's pressure starts to be close to the fluid's pressure. Yet, β_{th} stays over unity, hence the Laplace (Lorentz) force should not affect significantly the dynamics of the plasma.

Fig. 3.18 draws the color maps of the kinetic β_{kin} parameter at 1.5 ns. Once again, it is greater than unity everywhere, at the exception of the ablation front, which marks the limit between the solid foil accelerated toward $z < 0$ and the ablated plasma accelerated

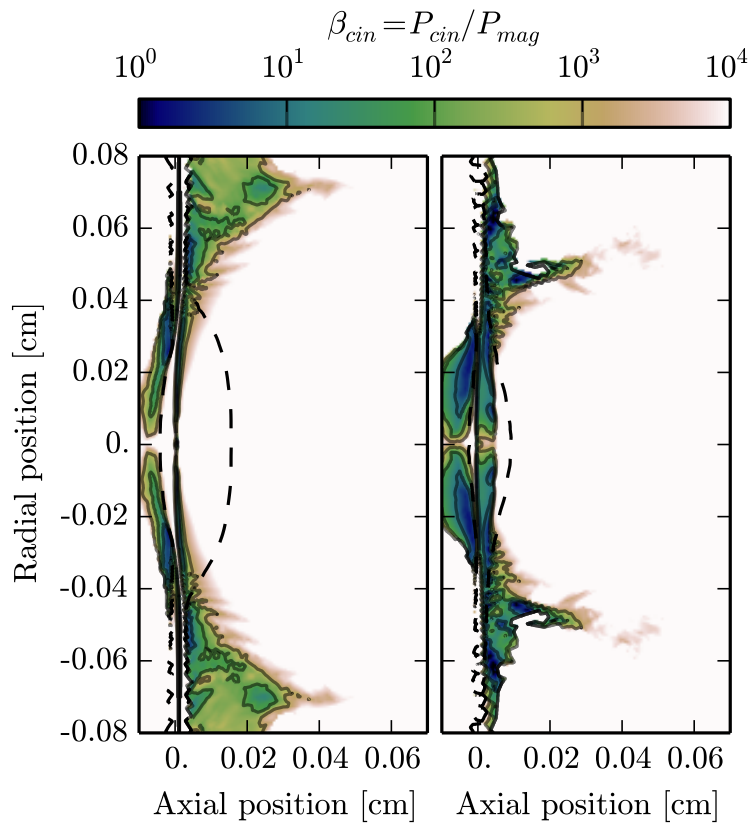


Figure 3.18: Reference case at 1.5 ns. Color maps of the kinetic beta parameter $\beta_{cin} = \rho \mathbf{u}_{flow}^2 / P_{mag}$. Dashed iso-line of the critical density at first laser harmonic. Left: Mylar, right: gold.

toward $z > 0$, and therefore presents a minimum of kinetic energy. As it clearly appears in the mylar case, the accelerated foil contains a major part of the system energy (see Fig. 1.3, on page 19). Associated to the low magnetic field which has diffused into it, this leads to a foil dynamics fully free from magnetic constrain (yet, the modified heat flux affects the way the foil is driven).

As expected from these β larger than unity, the density color maps shown on Fig. 3.19 do not present any confinement of the plasma by the magnetic field. In summary, the field is mostly generated at the ablation front or, in a smaller extent, in the corona and quickly convected and trapped at the ablation front. There, despite the high values of magnetic field, the high ablation pressure prevents the field from constraining the plasma motion.

As this picture depends on the effective advection of the field toward the target, in the case of a magnetic field in a coronal region without significant heat fluxes, the B-field may increase in time and finally overcome the fluid's pressure. This is illustrated in Fig. 3.20 which comes from simulations of a recent reconnection experiment (see chapter 4): a single laser beam irradiates either a 25 μm Aluminum or a 5 μm gold target with 180 J over 4 ns with a $\sim 90 \mu m$ FWHM focal spot. The combination of a smaller heated region

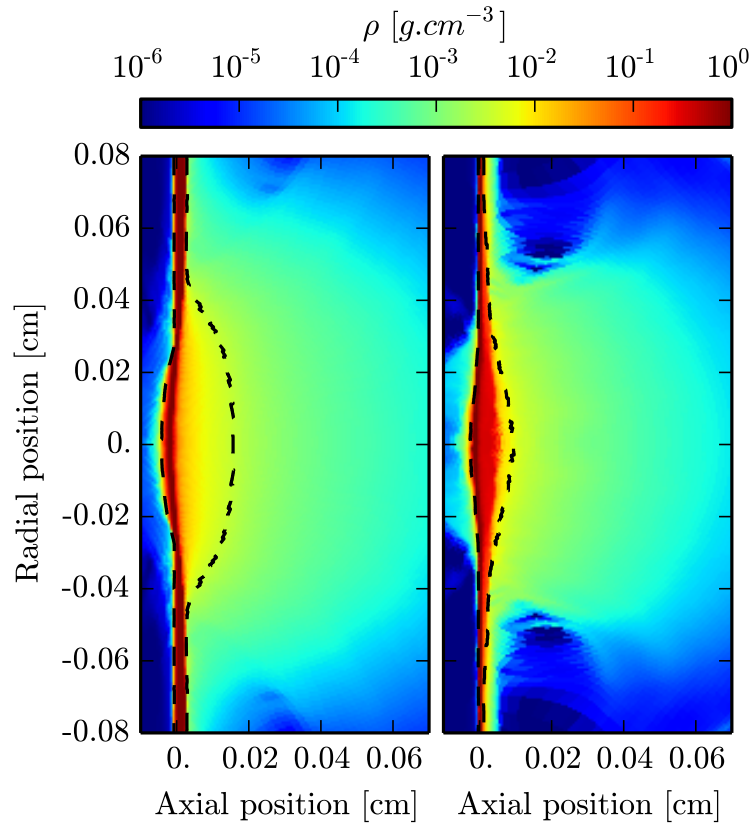


Figure 3.19: Reference case at 1.5 ns. Color maps of the density [g/cm^3]. Dashed iso-line of the critical density at first laser harmonic. Left: Mylar, right: gold.

and of a long duration for the laser irradiation leads (mostly for gold) to the development of a magnetic field around the focal spot which is not efficiently transported on the target through the Nernst effect. As a consequence, a region of $\beta_{th} \lesssim 1$ appears (see the solid iso-line) and, within it, a drop of plasma density. While it may look like an obvious effect of the Laplace force, it appeared that this feature is still present if the simulations are run without the Laplace term in the momentum equation.

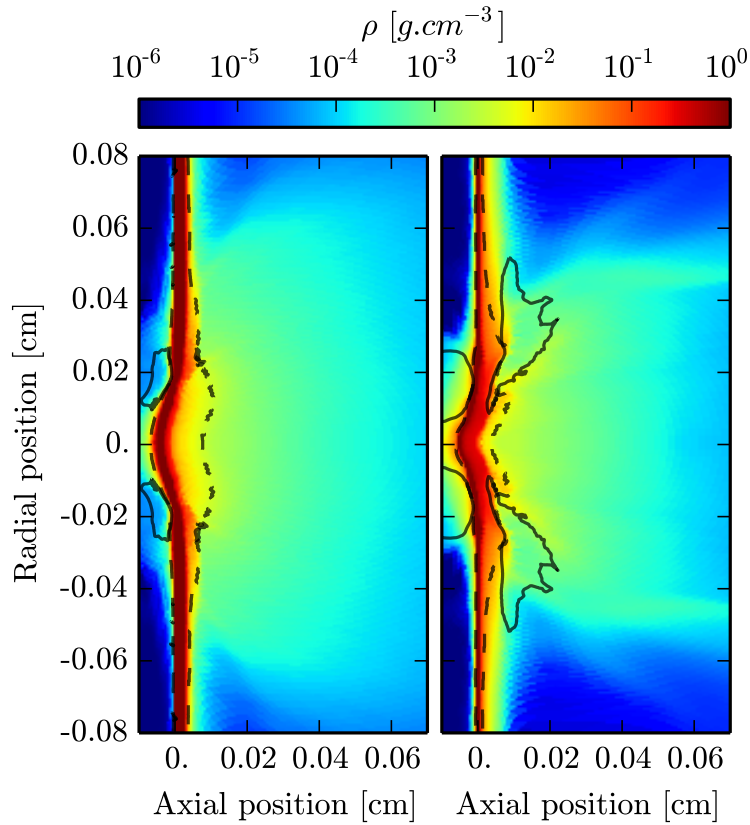


Figure 3.20: LULI2000 2015 campaign, 3.0 ns. Color maps of the density [g/cm^3]. Dashed iso-line of the critical density at first laser harmonic and solid iso-line for $\beta_{th} = 1$. Left: Aluminum, right: gold.

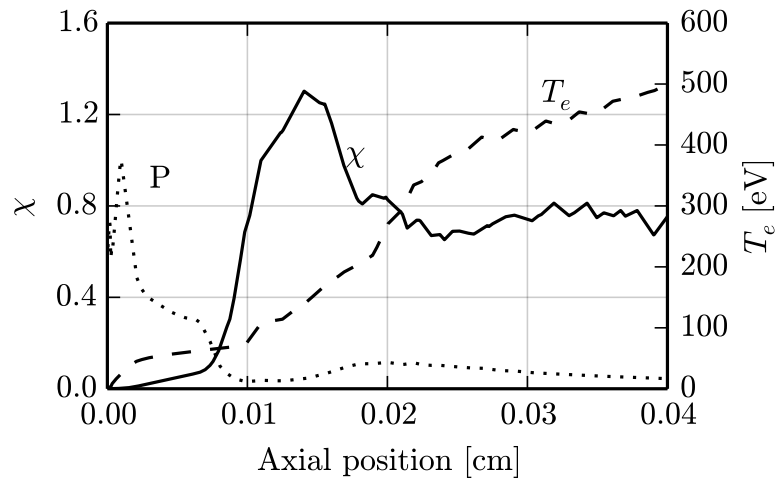


Figure 3.21: LULI2000 2015 campaign, 3.0 ns, gold target. Lineouts along the axial direction, at $r = 0.025$ cm, of the thermal magnetization (solid), the electron temperature (dashed) and the thermal pressure (dotted, normalized).

One possible explanation for this feature is that the inhibition of the heat flux in the magnetized region leads to a kind of double electron ablation front: the sharp increase of heat flux, where the magnetization decreases, causes an increase of the ablation pressure at a larger distance from the “natural” electron ablation front.

Fig. 3.21 draws lineouts along the axial direction (z), at $r = 0.025\text{ cm}$, of the thermal electron magnetization χ , the electron temperature and the thermal pressure, for the gold target in the condition of the LULI2000 2015 campaign (at $t = 3.0\text{ ns}$). It shows the radiative ablation front close to $z = 0$, where the electron temperature drops to the “cold” target temperature. The electron ablation front is around $z = 0.009\text{ cm}$, where the electron temperature becomes higher than the radiative temperature (not shown), and where the pressure suddenly increases. Nonetheless, it appears that, around $z = 0.02\text{ cm}$, the pressure presents a local maximum while the electron temperature decreases significantly. This is consistent with the idea of an increasing magnetization which induces a “pseudo-ablation front” and its associated ablation pressure. Because of this pressure, the matter ablated at the radiative and electron ablation fronts is slowed down, forming a localized increase of density.

3.3.3 Energy balance

As discussed above, the MegaGauss magnetic field which is generated in laser driven plasmas may have a significant effect on the non-local heat flux, but has a negligible effect on the hydro-motion. Yet, in the framework of indirect drive ICF, because the pellet is driven by radiation, it is of interest to know the effect of the self-generated magnetic field on the energy balance of the system.

In other words, even if the magnetic field does not affect the hydrodynamics, how do the transfers of energy (see the energy equations: eq.1.33 to 1.35 in the first chapter) reduce the energy available to accelerate and heat the foil, or is the release of magnetic energy (through resistive heating) enough to pre-heat the plasma?

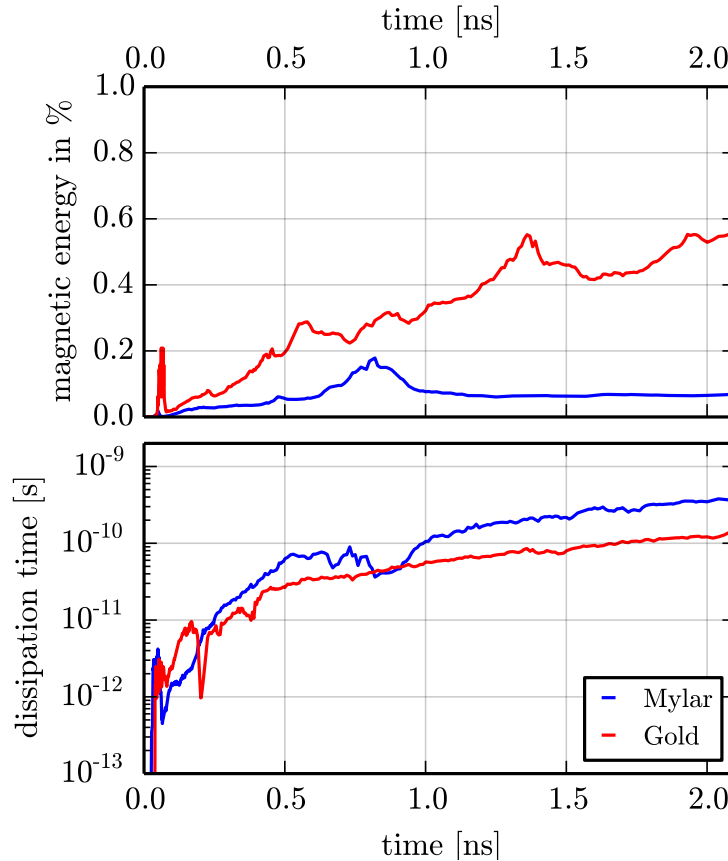


Figure 3.22: Reference case. Top: fraction of the system's energy as magnetic field, in %. Bottom: characteristic dissipation time of the magnetic field through Joule effect, in seconds.

Looking at Fig. 3.22(top), one can easily answer the first question. It represents over time the fraction of the system's energy stored as magnetic field (the total system's energy being the sum of internal, kinetic, magnetic and radiative energy). In the case of a low Z target, all along the interaction, approximately 0.1% of the system energy is used to build up the magnetic field, which is completely negligible. Note the roughly stationary trend. For the case of high Z target, there are two differences: first, overall, there is a higher fraction of the system's energy used to build up the field. Secondly, it represents an increasing fraction over time (but still very low, even at the end of the laser pulse).

The reason for this discrepancy between low and high Z targets is simple: because of the open geometry of a laser-foil interaction experiment, the gold target loses most of its energy through radiation. The total remaining energy of the system being smaller, associated to the higher magnetic field generation, this leads to a higher fraction of the energy in the magnetic field. Moreover, in the case of an ICF cavity, because the geometry is closed, one may expect this ratio to be smaller, yet of the same order of magnitude, around a few tenth of percent.

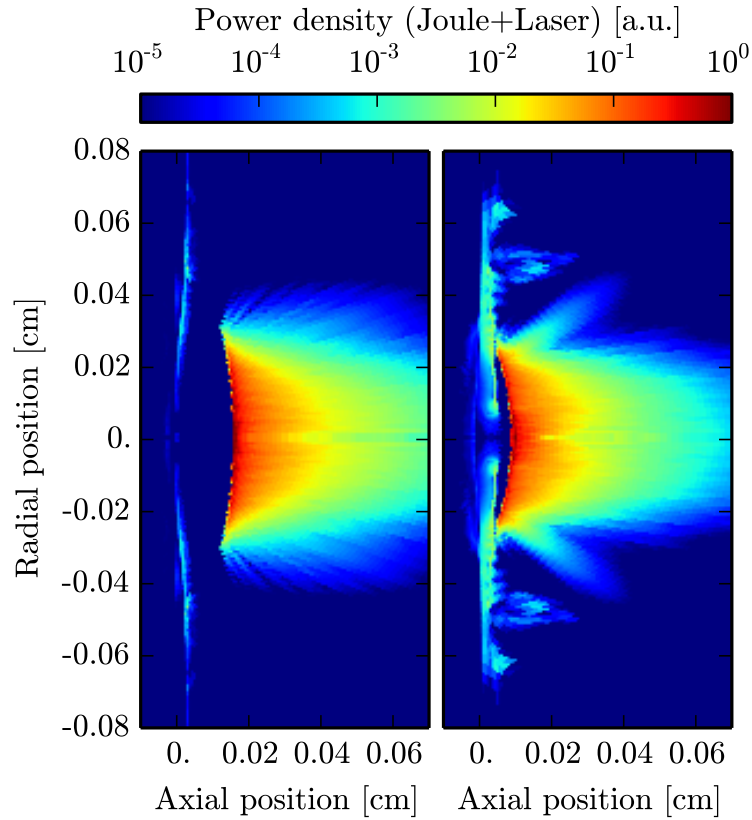


Figure 3.23: *Reference Case. Sum of the power density of the laser and resistive heating, normalized to the maximum value. The $\sim 10^{-3}$ [a.u.] localized onto the solid target ($z \sim 0$) corresponds to the Joule heating, behind the critical density. Left: mylar, right: gold.*

The bottom part of Fig. 3.22 plots over time the characteristic dissipation time of the magnetic field through resistive heating (Joule effect), defined as $\tau_{Joule} \equiv E_{mag}/P_{Joule}$. It shows that the Joule effect is a very efficient mechanism, as without magnetic field sources it would dissipate the magnetic field in less than a few hundreds of picoseconds. This means that there is a strong competition between the thermo-electric source and Joule losses. Indeed, because of the Nernst effect compressing the field, it exhibits a strong gradient of B-field at the electron ablation front (see Fig. 3.3), where the plasma conductivity is small (“cold” plasma). Therefore, it leads to a strong Joule effect ($\frac{j^2}{\sigma}$, with $\mathbf{j} = \nabla \times \mathbf{B}$). As a consequence of the very short lifetime of the field at the beginning of the interaction (tens of picoseconds), any incorrect modeling of the field at early times, despite affecting the heat flux, would not affect the topology of the magnetic field at later times. Finally, once the laser pulse is over, we saw that the magnetic field becomes less compressed, strongly reducing the Ohmic losses.

Nonetheless, while the power dissipated through the Joule effect is important compared to magnetic energy, it is very low compared with the internal energy of the system. Hence,

as it can be seen in Fig. 3.23, the energy transferred from magnetic to internal by ohmic heating is negligible compared to the laser heating (see the $\sim 10^{-3}$ region onto the solid foil, behind the critical density, compared to the large energy deposition of the laser in the corona). One may thus expect no pre-heat of the plasma by the magnetic field.

3.4 Extrapolation to ICF conditions

In this section we will extrapolate our results to conditions relevant to large scale facilities such as Omega, NIF or LMJ, *i.e.* either a foil driven by a $\sim 10^{15} \text{ W/cm}^2$, 3ω and $\sim \text{TW}$ laser pulse, or a full scale ignition experiment with a rugby cavity.

3.4.1 Driving laser : LMJ or NIF quad

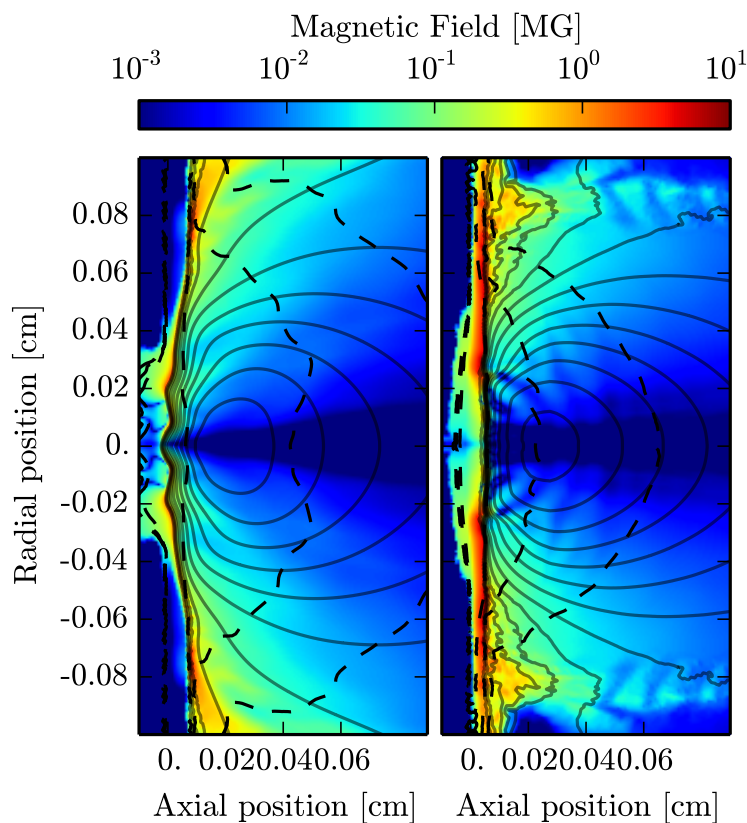


Figure 3.24: LMJ case at 1.5 ns. 15 kJ, 5 ns square pulse, 3rd laser harmonic and 4th order super-Gaussian with 940 μm full width at 3% focal spot ($I \sim 1 \times 10^{15} \text{ W/cm}^2$). Color maps of the magnetic field, with solid iso-lines of the electron temperature (200 eV steps) and dashed iso-lines of 10 Nc, 1 Nc and 1/4 Nc (for a laser a first harmonic). left: Mylar, right: gold.

Fig. 3.24 illustrates FCI2 simulations of Mylar and gold foils irradiated by a LMJ quad (here with an energy reduced to 15 kJ) at 1.5 ns. The laser pulse is at the third laser harmonic (351 nm). Its temporal profile is a 5 ns square with a 100 ps rising time, while its focal spot is a 4th order super-Gaussian with a 940 μm full width at 3%. Note that due to the higher delivered energy, the foils are thicker for a better hydrodynamic stability. Therefore, it corresponds in overall to the laser variations of Fig. 3.10 and Fig. 3.13, but with a larger focal spot. As such, the results are very close to what one could expect: a slightly lower temperature than in Fig. 3.10 because of the lower intensity, a very flat magnetic field profile due to the large focal spot, with a maximum value around 10 MG. The foils are less accelerated than in Fig. 3.13 because they are thicker. Finally, note the relatively large region around the symmetry axis without magnetic field (especially for the gold case) because of the large focal spot inducing a “flat” temperature profile.

3.4.2 Full scale ICF experiment

Because FCI2 is mainly used to design and analyze ICF experiments, we present in Fig. 3.25 a simulation of a 1.2 MJ experiment, using the “NLSH” model. Shown are the magnetic field (in log scale, therefore not showing the sign) with vector plots of the advection velocity $\mathbf{U} = \mathbf{u}_{\text{Fluid}} + \mathbf{u}_{\text{Nernst}}$, the magnetization of the thermal electrons with vector plots of the fluid velocity, the Nernst number $N_N \equiv \|\mathbf{u}_{\text{Nernst}}\| / \|\mathbf{u}_{\text{Fluid}}\|$ and the electron temperature color map. It shows that our conclusions drawn from the laser-foil study hold in the case of a closed geometry: a MegaGauss scale magnetic field appears at the electron ablation front and is trapped there by the Nernst effect, leaving a very weak magnetic field in the low density filling gas of the cavity. Nonetheless, this $\sim 10 \text{ kG}$ magnetic field is enough to induce a weak magnetization of the plasma within the cavity, justifying the need to account for magnetic field in the non-local model, and resulting in high electron temperature in the region irradiated by the outer beams. The Nernst number shows quite interesting results, as it naturally illustrates the region of low fluid or Nernst velocity (*e.g.* in the blue regions the field is transported only with the fluid’s motion). One could cite for example the area where the capsule’s ablator plasma meets the expanding gold plasma, or the region of maximum electron temperature, separating the heat flux directed toward the laser entrance hole and the one directed toward the inside of the cavity. Finally, we can associate the electron ablation front to the surface where N_N suddenly drops below unity (white).

Looking at the capsule, it appears that because it is driven by the x-ray flux instead of laser beams, the electron ablation front is at a large distance from the radiative one, resulting in a very efficient isolation of the imploding capsule from the large magnetic fields generated in the rest of the cavity. Moreover, the weak heat flux prevents the field from being compressed on the capsule’s electron ablation front.

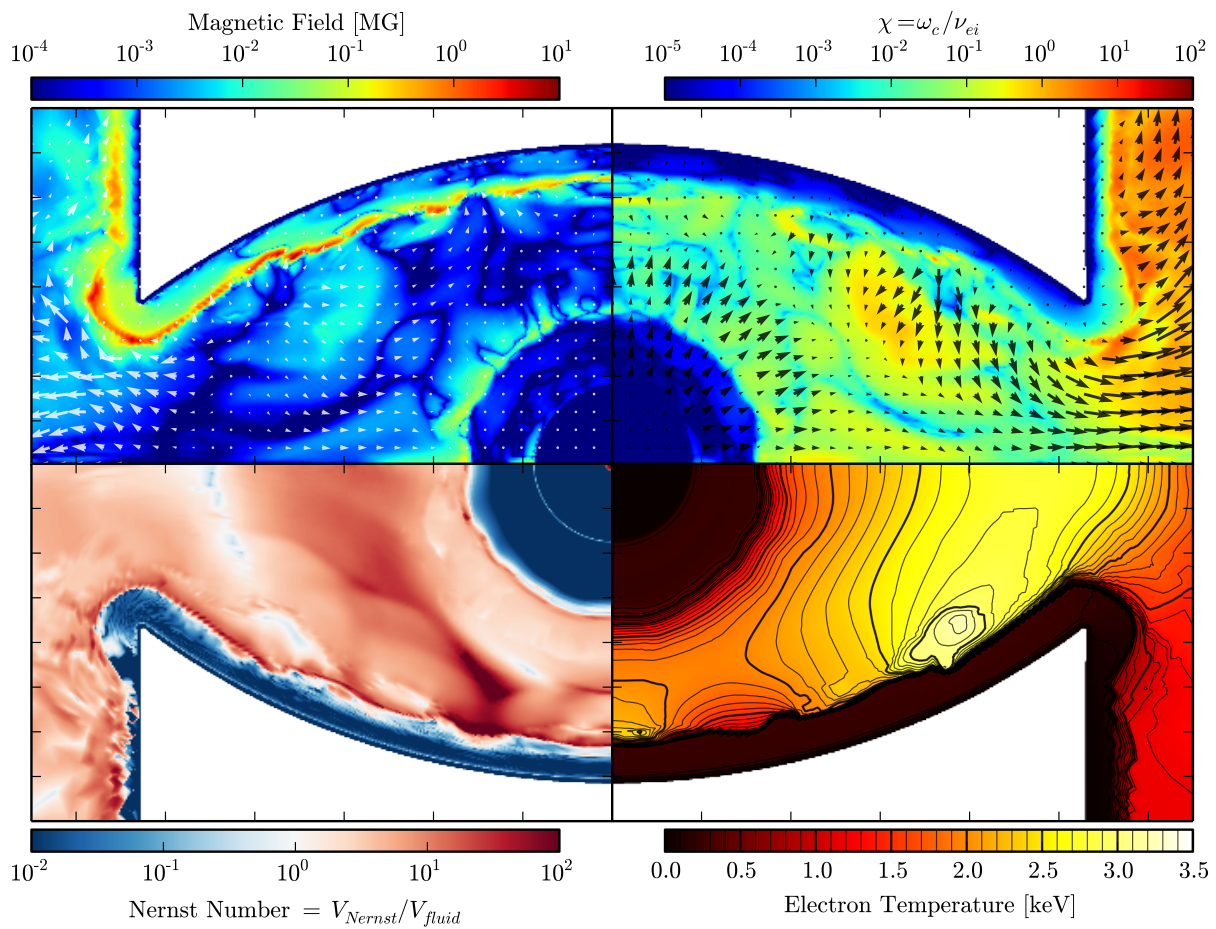


Figure 3.25: Full scale ICF experiment using the “NLSH” non-local heat flux with MHD model.

Top left : magnetic field (log scale) with vector plots of the advection velocity $\mathbf{U} = \mathbf{u}_{Fluid} + \mathbf{u}_{Nernst}$.

Top right : electron magnetization (for thermal velocity), with fluid velocity.

Lower left : Nernst number $\|\mathbf{u}_{Nernst}\| / \|\mathbf{u}_{Fluid}\|$.

Lower right : electron temperature.

3.5 Conclusions

In this chapter, we used FCI2 to analyze the mechanisms at the source of the magnetic field, its different transport regimes, its dependence with the driving laser and its effects on the interaction.

We have shown that the magnetic field is mostly generated at the electron ablation front, where the density gradients are large, despite the small angle between the temperature and density gradients. Nonetheless, some B-field is generated in the corona, with a strength that is lower by roughly two orders of magnitude. There, the large angle between the gradients and the low electron density compensate for the weaker density and temperature gradients. The magnetic field is then transported behind the electron ablation front with the heat flux, through the Nernst effect. The ablated plasma is then able to diffuse through the accumulated magnetic field because of the small conductivity of the dense cold plasma. This results in a thickness of the magnetic field (over the axial direction) which depends on the atomic number of the target, as the field will be trapped between the remaining solid target and the fast advection back onto the target at the electron ablation front. This is why for a high Z target such as gold, the magnetic field extends over a large thickness, as the target is ablated by radiation, deep behind the electron ablation front.

Following, we have shown that the topology of magnetic field is rather insensitive to the laser parameters as, in each case, the magnetic field remained compressed behind the ablation front and did not present any large variation such as a shell-like topology.

Next, we looked at the effect of the magnetic field on the interaction. It appeared that it significantly affects the electron transport, depending on the magnetization of the electrons. Yet, for a transport model using a grey diffusion the effects are easily readable: the higher the magnetization, the higher the rotation (Righi-Leduc effect) and the inhibition. In the case of a non-local (multi-group diffusion) model it is much less straightforward. Indeed, the heat flux takes the form of a sum of a local component and a non-local correction. Hence, on top of the magnetization, dependent of the velocity group, the heat flux may even be increased if the non-local correction is inhibited more than the local part. Nonetheless, a striking feature is the complete inhibition of the heat flux at the ablation front, where the magnetic field is accumulated, nullifying the well-known pre-heat at the foot of the electron temperature profile, which is one of the main effect highlighted by non-magnetized non-local models.

Moreover, we showed that because of the transport of the magnetic field in the dense part of the target, the magnetic field energy density remains small compared to the kinetic and internal energy densities. As such, the effect of the field on the fluid's motion through the Laplace (Lorentz) force remains very small. The same conclusion holds from the

point of view of the energy balance of the system: the magnetic field represents only a few tenths of percents of the total energy. Nonetheless, we showed that the losses of magnetic field through the Joule effect are important, resulting in a competition between the thermo-electric sources and the resistive losses.

Finally, we looked at the physical quantities relevant to the study of the B-field in an indirect-drive ICF simulation. It showed that, just like in the case of laser irradiated foils, the magnetic field is compressed onto the cavity's wall. Yet, because of the low collisionality in the filling gas of the cavity, the remaining kiloGauss magnetic field is enough to weakly magnetize the electrons. Accounting for the magnetic field with a non-local electron conduction model is thus of importance if one requires a more precise electron temperature topology. Moreover, the electron ablation front of the capsule is at a large distance from the radiation ablation front. Hence, the capsule is isolated from the strong magnetic field generated on the walls.

4 Reconnection of the magnetic field in high energy density plasmas

As we saw in the previous chapters, the irradiation of a solid target by a $\sim 10^{14} \text{ W/cm}^2$ laser produces an expanding plasma in which the electron temperature and density gradients are not collinear. This is the source of an azimuthal magnetic field around the heated region which is then advected by the heat flux onto the target and whose spatial extent increases with the growing plasma bubble. For experiments involving a hohlraum (indirect drive ICF experiments, radiation ablation or heating *etc.*), the laser irradiation of the inner wall of the high Z enclosure has to be as homogeneous as possible in order to obtain an isotropic x-ray irradiation of the driven object. This is achieved through numerous close-by irradiation spots, as illustrated in Fig. 4.1 (showing the irradiation of a hohlraum at the Nova laser facility). For each irradiation spot, a magnetic field loop is self-generated and, at some point, it is clear that because of their growth the magnetic field loops will be compressed onto each other. Because they all share the same polarization (clockwise when looking from the laser direction), there will be a region of compressed anti-parallel field lines between the magnetic field loops, which is the setup for the reconnection of the magnetic field [117].

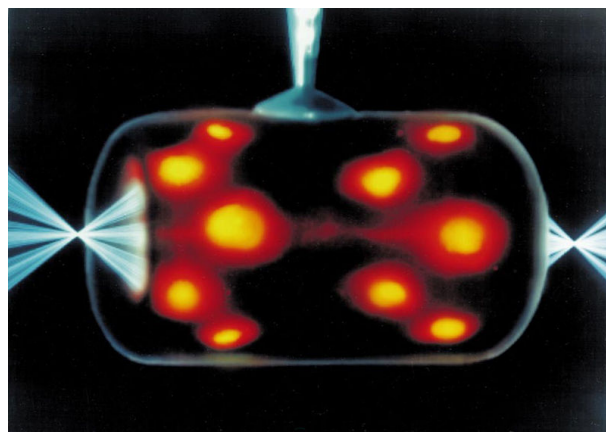


Figure 4.1: *Illustration of the laser irradiation of a hohlraum at the Nova laser facility.*

A schematic view of the reconnection of two magnetic field loops is presented in Fig. 4.2: for each of the two near-by plasma plumes, a magnetic field loop “private” to its own

plasma plume, is self-generated and its size increases as the plasma plume grows. At some point, private fields lines of different plasma plumes will touch each other, but cannot merge in the ideal MHD framework. There, a reconnection of the field lines may occur, *i.e.* two private field lines break and reconnect, forming a single “public” magnetic field line around both plasma plumes.

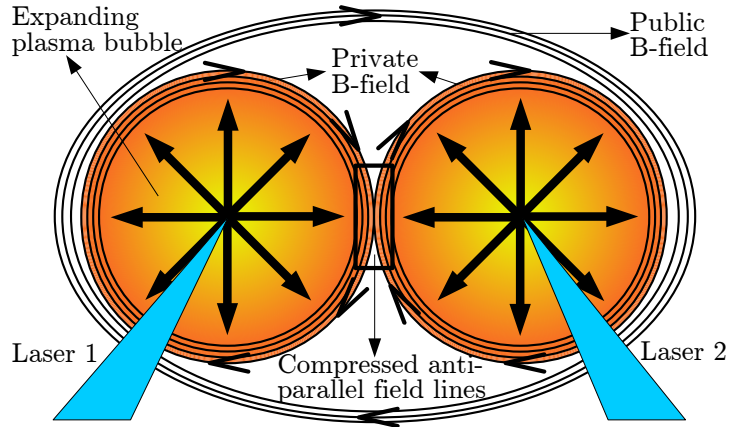


Figure 4.2: Scheme of two near-by irradiation spots on a solid target.

In this chapter, we will first present the Alfvén theorems, allowing to define the concept of magnetic field lines and “frozen in flow” magnetic field in ideal MHD. Then, in the first section we will review the state of the art of magnetic reconnection: what is the Sweet-Parker model, what is the context, in which fields of plasma physics it is of interest, what are the different experimental platforms allowing its study, *etc.*

Following, we will discuss the specificities of magnetic reconnection in high energy density laser generated plasmas and how it can be simulated (either fluid, PIC, hybrid or Fokker-Planck codes). This will lead us to the hybrid code HECKLE from LPP (Laboratoire de Physique des Plasmas, at École Polytechnique) and how its simulations are initialized with simple profiles, relevant for laser plasmas. Next, we will present the numerical study which was performed at LPP and thus show that the reconnection may be inhibited if the magnetic field loops are not co-planar such as to produce an “anti-Hall” quadrupolar out-of-plane component of the magnetic field. Finally, we will present experimental results from campaigns at the Phelix laser facility (GSI, Darmstadt) and the LULI2000 laser facility (LULI, Palaiseau), and ultimately describe the design of a LMJ-Petal experiment that is planned to be performed in 2017.

Magnetic field lines and Alfvén theorems

Before giving more details about the reconnection of the magnetic field, let us introduce the notion of magnetic field line and of “frozen” magnetic field. For this, we place ourselves

in the framework of ideal MHD, *i.e.* an perfectly conductive plasma, for which Ohm's law reduces to:

$$\mathbf{E} + \mathbf{u} \times \mathbf{B} = 0 \quad (4.1)$$

Within this context, the first Alfvén theorem (also called flux theorem) [49], which we will not demonstrate here, states that the flux of magnetic induction through a surface formed by a closed curved C bounded to the fluid, is constant over time:

$$\frac{d}{dt} \Phi [\mathbf{B}(\mathbf{r}, t), C(\mathbf{r}, t)] = 0 \quad (4.2)$$

Hence, it means that the fluid and the field are strongly coupled: any increase (respectively decrease) of the surface, *i.e.* compression (*resp.* relaxation) of the fluid, is linked to an increase (*resp.* decrease) of the magnetic field, such that the flux through the surface remains constant.

The second Alfvén theorem shows that in ideal MHD, a “magnetic field line” is frozen in the plasma, *i.e.* fluid “particles” placed on a field line stay on this same field line all along the evolution of the system. Let us consider an infinitely conductive plasma with a velocity field $\mathbf{u}(\mathbf{r}, t)$: the fluid convects the magnetic field following the relation $\nabla \times (\mathbf{u} \times \mathbf{B}) = \partial \mathbf{B} / \partial t$, and the field carries the fluid through the Laplace force (see momentum equation, sec. 1.4.1, on page 29): $\rho D_t \mathbf{u} = -\nabla P + \frac{1}{4\pi} (\nabla \times \mathbf{B}) \times \mathbf{B}$.

Let us consider a “magnetic field line”, defined as a line tangent to \mathbf{B} in each point, containing M_1 and M_2 , two infinitely close points of the fluid on this line and define the vector $\mathbf{L} = \overrightarrow{M_1 M_2}$. As such, we have $\mathbf{L}(t_0) \times \mathbf{B}(\mathbf{r}, t_0) = \mathbf{0}$. The evolution of \mathbf{L} and \mathbf{B} follows (in an Eulerian system):

$$\begin{aligned} \frac{d\mathbf{L}}{dt} &= \mathbf{u}(M_2) - \mathbf{u}(M_1) = (\mathbf{L} \cdot \nabla) \mathbf{u}, \\ \frac{d\mathbf{B}}{dt} &= \nabla \times (\mathbf{u} \times \mathbf{B}) + (\mathbf{u} \cdot \nabla) \mathbf{B} = (\mathbf{B} \cdot \nabla) \mathbf{u} - \mathbf{B} (\nabla \cdot \mathbf{u}). \end{aligned} \quad (4.3)$$

Therefore, the evolution of $\mathbf{L} \times \mathbf{B}$ follows:

$$\frac{d(\mathbf{L} \times \mathbf{B})}{dt} = \mathbf{L} \times (\mathbf{B} \cdot \nabla) \mathbf{u} - \mathbf{L} \times \mathbf{B} (\nabla \cdot \mathbf{u}) - \mathbf{B} \times (\mathbf{L} \cdot \nabla) \mathbf{u}. \quad (4.4)$$

The first and last terms of the right hand side of the equation are equal but have a

different sign, while the second term is null at t_0 . Hence, $\left. \frac{d(\mathbf{L} \times \mathbf{B})}{dt} \right|_{t_0} = 0$ and because $\mathbf{L}(t_0) \times \mathbf{B}(\mathbf{r}, t_0) = \mathbf{0}$, \mathbf{L} remains at all time tangent to \mathbf{B} .

Consequently, still in the framework of ideal MHD, one can consider the magnetic field lines as “strings” with a physical identity, which cannot break and which have a pressure term $-\nabla \frac{\|\mathbf{B}\|^2}{8\pi}$ and a tension term $\frac{1}{4\pi} (\mathbf{B} \cdot \nabla) \times \mathbf{B}$, from the Laplace force.

We can thus associate the reconnection to a process where two anti-parallel sets of magnetic field lines moving toward each other, meet, “break” through non-ideal MHD phenomena and finally reconnect, in a configuration of lower magnetic energy after transport of some energy from the field to the plasma.

4.1 State of the art of magnetic reconnection

The concept of the reconnection of the magnetic field comes from the studies of the solar corona, in which the high temperature and the large amount of energy released during solar flares could not be explained solely by resistive dissipation. The associated characteristic time of the latter process is in the order of 10^6 years, to be compared with x-ray observations showing magnetic field’s topology modifications over minutes to hours [118].

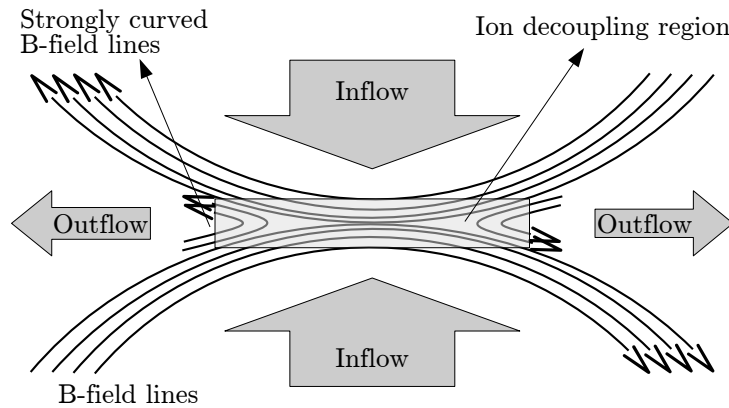


Figure 4.3: *Scheme of the reconnection region.*

Models were thus proposed where anti-parallel field lines driven toward each other would be the source of a strong current layer (due to the strong rotational of \mathbf{B}) [119] which could increase the dissipation rate because of the j^2 dependence of the Joule heating. In fact, the strong current could allow the field lines to break and reconnect, and despite the small amount of energy released during the process, the reconnected field lines will be strongly curved, as sketched in Fig. 4.3. Thus, because of the Laplace (Lorentz) force, the

plasma will be accelerated out of the reconnection region, unfolding the field lines frozen within. It is during this process, and not during the reconnection itself, that the plasma's kinetic energy increases and the magnetic energy reduces [18].

Note that the scheme drawn in Fig. 4.3 depicts a “double Y” shaped current sheet, i.e. reconnection on a single point. Depending on the plasma conditions [120], the current sheet may “break” into an “O” shaped (two reconnection points), or even in multiple magnetic islands [121, 122].

4.1.1 The Sweet-Parker model

In this subsection, we will present the well-known Sweet-Parker model [123, 124]. Despite strong assumptions, preventing it to correctly reproduce astrophysics measurements, it allows to get an insight on the physics of magnetic reconnection (due to its simplicity).

Let us suppose two sets of “private” magnetic field lines in a plane, frozen in counter propagating plasmas as depicted in Fig. 4.3. The field lines will then be compressed toward each other, forming a thin out-of-plane electric current layer according to Ampere's law $\mathbf{j} = \frac{c}{4\pi} \nabla \times \mathbf{B}$. As long as the resistive term $\eta \mathbf{j}$ ($\eta = 1/\sigma$ being the electrical resistivity) is negligible in Ohm's law

$$\mathbf{E} + \frac{\mathbf{u}}{c} \times \mathbf{B} = \eta \mathbf{j}, \quad (4.5)$$

the magnetic field lines will keep their identity (as shown by the second Alfvén theorem), preventing them to “break” and continuing to be compressed. Eventually, the current density will become so large that the resistive term will no longer be negligible, despite of the low (yet non-zero) resistivity.

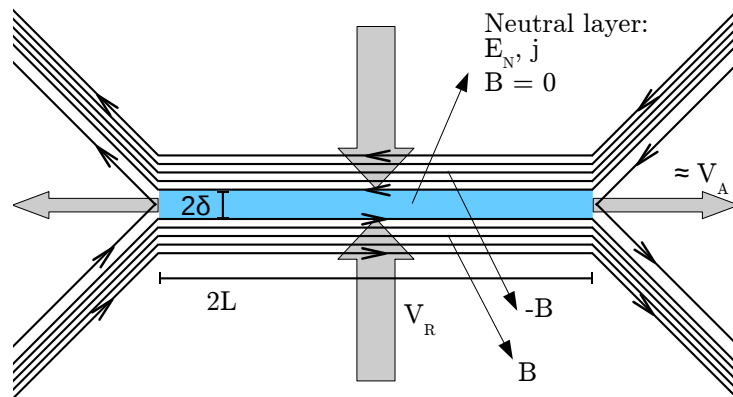


Figure 4.4: Scheme of the Sweet-Parker model.

Indeed, in the neutral layer between the anti-parallel magnetic fields, $\mathbf{B} = \mathbf{0}$. Yet, due to the induction law, the electric field E_N in the neutral layer, perpendicular to the plane, is

proportional to the rate at which the private lines reconnect into public ones. Therefore, if E_N is non-zero such as to allow rearrangements of the field lines, a null resistivity would result in an infinite current density.

Hence, in the neutral layer, we have $E_N = \eta j$, with j inversely proportional to δ , the thickness of the layer: $j \simeq \frac{c}{4\pi} B/\delta$. This gives the following reconnection rate

$$\frac{d\psi}{dt} = \frac{\eta c}{4\pi} B/\delta, \quad (4.6)$$

which could seem to be associated with any speed given a sufficiently small δ . Yet, as the magnetic field lines flow inside the neutral layer and flow out after reconnection, they also carry the plasma with them, because of the *flux freezing*. Moreover, the velocity of the flow exiting from the neutral layer can be approximated by the Alfvén velocity $V_A = B/\sqrt{4\pi\rho}$, corresponding to the velocity at which a plasma is expelled by a magnetic pressure $\frac{\|\mathbf{B}\|^2}{8\pi}$. Consequently, to conserve the mass, the velocity V_R at which the field lines and their associated plasma enter in the neutral layer must verify:

$$V_R = (\delta/L) V_A. \quad (4.7)$$

Eqs 4.6 and 4.7 show that the smaller is δ , the higher is the reconnection rate, but also the smaller is the inflow velocity. Taking $\frac{d\psi}{dt} = V_R B$ gives the system:

$$\begin{cases} \frac{\eta c}{4\pi} B/\delta = V_R B \\ (\delta/L) V_A = V_R \end{cases} \quad (4.8)$$

and thus δ and V_R :

$$\begin{cases} \delta = \sqrt{\frac{\eta c}{4\pi} \frac{L}{V_A}} = \frac{L}{\sqrt{S}} \\ V_R = \sqrt{\frac{\eta c}{4\pi} \frac{V_A}{L}} = \frac{V_A}{\sqrt{S}} \end{cases} \quad (4.9)$$

where S is the Lundquist number $4\pi L V_A/\eta c$, ratio of the Alfvén velocity over the diffusion velocity. It is equivalent to the magnetic Reynolds number with the Alfvén velocity instead of the convection one.

Finally, one can define the characteristic reconnection time

$$t_R \simeq L/V_R = L \frac{\sqrt{S}}{V_A}, \quad (4.10)$$

to be compared with the characteristic resistive dissipation time

$$t_{\Omega} \simeq \frac{4\pi L^2}{\eta c} = \frac{LS}{V_A} = \sqrt{S}t_R. \quad (4.11)$$

In the case of a laser generated HED plasmas, with $L = 0.01 \text{ cm}$ and, from FCI2 simulations, $S \sim 100$ and $V_A \sim 10^8 \text{ cm/s}$, we obtain $t_R \sim 1 \text{ ns}$, a time similar to the hydrodynamics time scale.

In the context of solar flares, while significantly decreasing the time required to break the magnetic field lines (due to the large Lundquist number $S \sim 10^{12}$ in the solar corona) compared to the resistive dissipation time, the Sweet-Parker model still gives a reconnection time much longer than observations : $10^6 - 10^7 \text{ s}$, compared to $10^3 - 10^4 \text{ s}$. This pinpoints out the numerous assumptions which were made, yet not necessarily justified: steady state, incompressibility of the plasma, uniform pressure outside of the reconnection region ($P_{up} = P_{down}$), use of the classical Spitzer resistivity (*i.e.* MHD framework) and outflow at the Alfvén velocity, while magnetic reconnection is most of the time studied in plasmas for which the electron mean free path is longer than δ , the thickness of the current sheet.

Therefore, to conclude this presentation of the Sweet-Parker model, it is worth mentioning the generalization of the model presented in [125] which allowed to reproduce the reconnection velocity V_R measured on the MRX machine [126] for relatively low Lundquist number $S \lesssim 10^3$. For this, they defined an effective Lundquist number:

$$S_{eff} = \frac{4\pi LV_A}{\eta_{eff} c} \cdot \frac{1}{1 + L\dot{n}/nV_{down}} \cdot \frac{V_{down}}{V_A}, \quad (4.12)$$

where n is the electron density and \dot{n} the associated time derivative, and

$$V_{down}^2 = V_A^2 (1 + \kappa) - 2 \frac{P_{down} - P_{up}}{\rho} \quad (4.13)$$

is the downstream velocity with $\kappa (B_{up}, B_{down})$ ranging from 0.2 to 0.3. To account for the low collisionality, the classical resistivity is replaced by the measured resistivity $\eta_{eff} = E_N/j$.

Finally, despite the good reproductivity of the MRX measurements using this effective Lundquist number, the Sweet-Parker model remains only valid for collisional plasmas (*i.e.* moderate S). Indeed the Sweet-Parker model uses the MHD framework, in which the plasma is treated as a single fluid where the electrons and ions are moving together, even with the presence of electrical currents. Yet, in many fields of research involving magnetic reconnection, the reconnection layer has a thickness comparable or smaller than the ion skin depth c/ω_{pi} . This results in a demagnetization of the ions in the current sheet,

while the electrons remain magnetized, leading to strong two fluid effects (most notably the Hall effect, see the generalized Ohm's law Eq. 1.38 on page 31). Hence, in most cases, the Sweet-Parker model cannot apply and one needs to use complex simulations with more physics than a one fluid MHD code such as FCI2.

4.1.2 The magnetic field reconnection in various plasma physics contexts

Solar physics

As said earlier, the magnetic reconnection was conceptualized in an attempt to explain the physics of the solar corona, in which the electron temperature is anomalously high (typically 100 eV) compared to the solar surface, and where fast events such as *coronal mass ejections* (CME) and solar flares could not be explained by pure Ohmic heating.

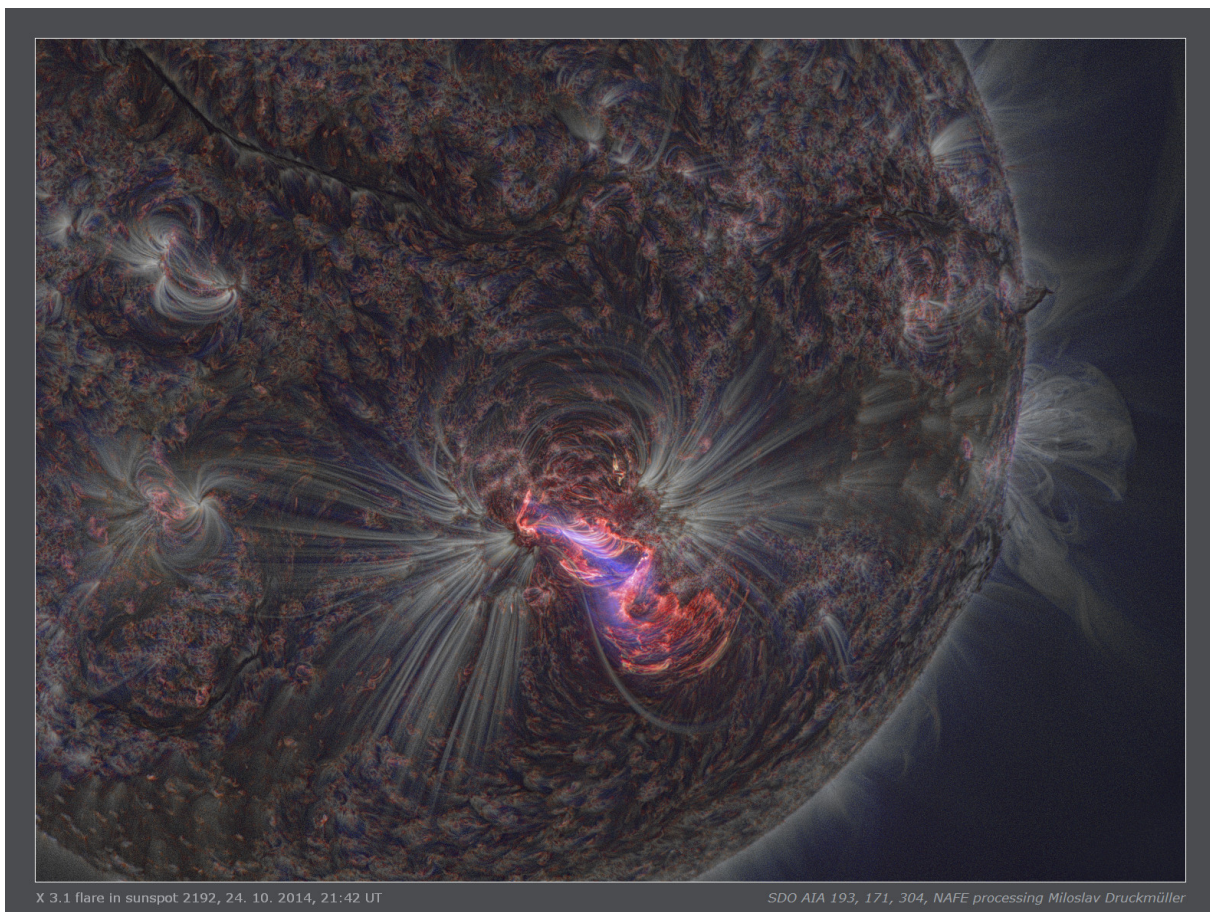


Figure 4.5: Composite image of the Sun from three different wavelengths (19.3 nm in blue, 17.1 nm in white and 30.4 nm in red), measured by the Solar Dynamics Observatory. These emissions trace the magnetic field lines looping through the hot plasma of the Sun's outer chromosphere and corona. From apod.nasa.gov

For the temperature, it has been shown [127] that the continuous movement of the numerous small-scale magnetic flux accumulations (see Fig. 4.5), associated with the continual appearance and disappearance of oppositely polarized pairs of fluxes, could be a seed for a continuous large number of small scale reconnection events. It would remap the magnetic flux in the corona in only 1.4 h and, therefore, be a very effective source of energy to heat the solar corona.

Magnetic reconnection has also been supposed to play a significant role in the generation of various solar flares, such as the *coronal mass ejections* (CME), which are large scale arcade loops associated with filament eruptions. Fig. 4.6 shows the CME model proposed by Shibata *et al.* [128], based on observations from the *Yohkoh* satellite, which has shown that in impulsive compact-loop flares, a loop of hard x-rays (HXR) source appeared above the bright soft x-rays (SXR) loop during the impulsion phase [129]. This source of hard x-rays has been supposed to be linked to reconnection events occurring above the loop and sending a high-velocity plasma jet which eventually collides with the bottom loop.

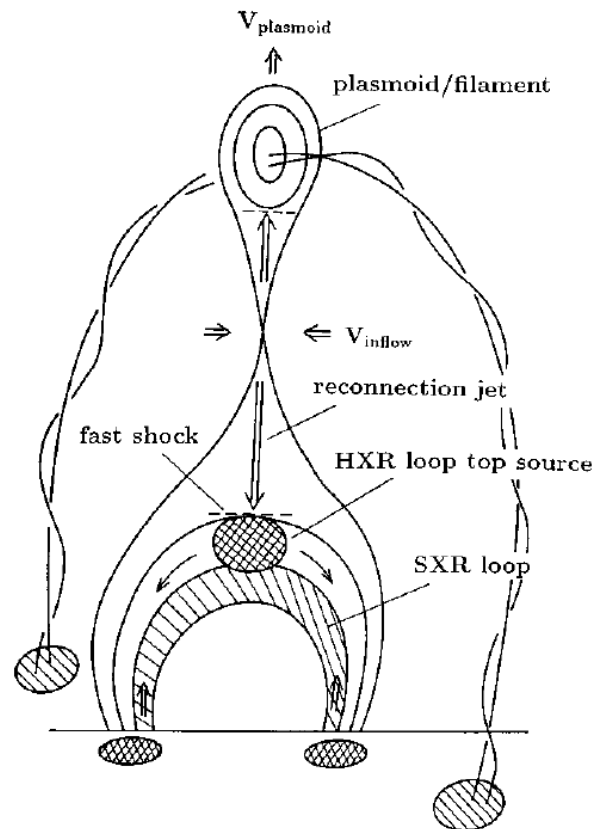


Figure 4.6: Scheme of the coronal mass ejection model. From [128].

Initially, an arcade of magnetic flux in the solar corona is in equilibrium, supporting a high-density (compared to the rest of the corona) filament, called *prominence* (see top of Fig. 4.6). Once the prominence's magnetic field breaks, a CME occurs, ejecting a plasmoid¹ away from the Sun and therefore pulling field lines, such as to drive a reconnection of the magnetic field between the plasmoid and the arcade of magnetic flux below it. This reconnection of the B-field then sends particles down the magnetic field lines which, upon reaching the bottom loop, emit hard x-ray radiations.

¹A plasmoid is a plasma confined by a closed field (in two dimensions), or by a helically twisted flux tube (in three dimension).

Space physics

In the framework of space physics, magnetic reconnection has been studied extensively, due to the possibility to probe the magnetic field itself using orbiting satellites. The solar wind travels through the solar system, carrying a magnetic field called *interplanetary magnetic field* (IMF). Upon reaching an oppositely polarized planetary magnetic field (in the following we will consider the Earth), a current sheet (neutral layer) will develop between the anti-parallel field lines. Such sheets are found both on the dayside (*magnetopause*) and nightside (*magnetotail*) and allow the Earth dipole magnetic field to reconnect with the IMF [130, 131] (see Fig. 4.7).

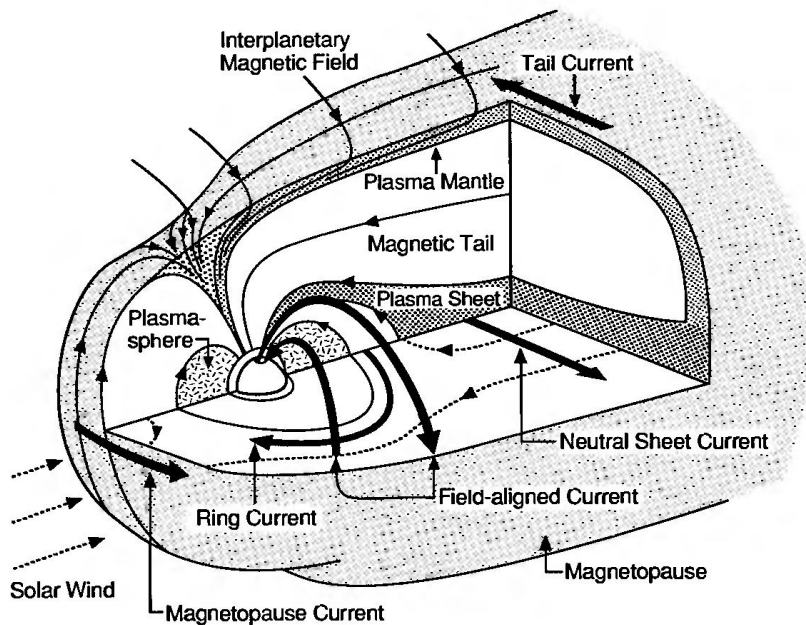


Figure 4.7: Scheme of the magnetosphere.

Because of the solar wind, the magnetotail presents a very elongated shape, with a magnetic field almost directed in the Earth-Sun axis. It is divided into a northern and a southern lobe of very low density ($\sim 0.1 \text{ cm}^{-3}$, among the lowest densities in the solar system). Between these two lobes is a current sheet (with a much higher density than the lobes, therefore called plasma sheet), where the magnetic field's direction inverts. There, the magnetic field lines linking the Earth to the IMF can reconnect and return to the closed dipole magnetic field lines. During this intermittent process, energy and plasma are released into the inner *magnetosphere* (the region enclosed by the magnetopause), which is called a *magnetic substorm*. Finally, the open magnetic field lines coming from the Earth poles and connected to the IMF allow the solar wind to penetrate the Earth atmosphere and produce aurora through collisional ionization.

4.1.3 Experimental platforms for the study of reconnection

The pioneering experiments dedicated to the study of magnetic reconnection were performed in the late 70's, using pinch plasmas and “high” density pulsed (microsecond) plasma discharges. These experiments were then in a regime of collision-dominated MHD with low Lundquist number ($S \approx 1 - 10$), and despite the lack of high resolution diagnostics, reconnection rates larger than the classical Sweet-Parker value were measured. One could cite the experiment carried by Frank *et al.* [132] who used a Z pinch to produce a reconnection-relevant topology of the magnetic field. Using magnetic probes, they were able to measure the profile of the magnetic field across the neutral layer at different times. They showed that the current sheet that forms on the neutral layer presented a final thickness determined by the balance between the pressure of the reconnecting magnetic field and the kinetic pressure of the plasma.

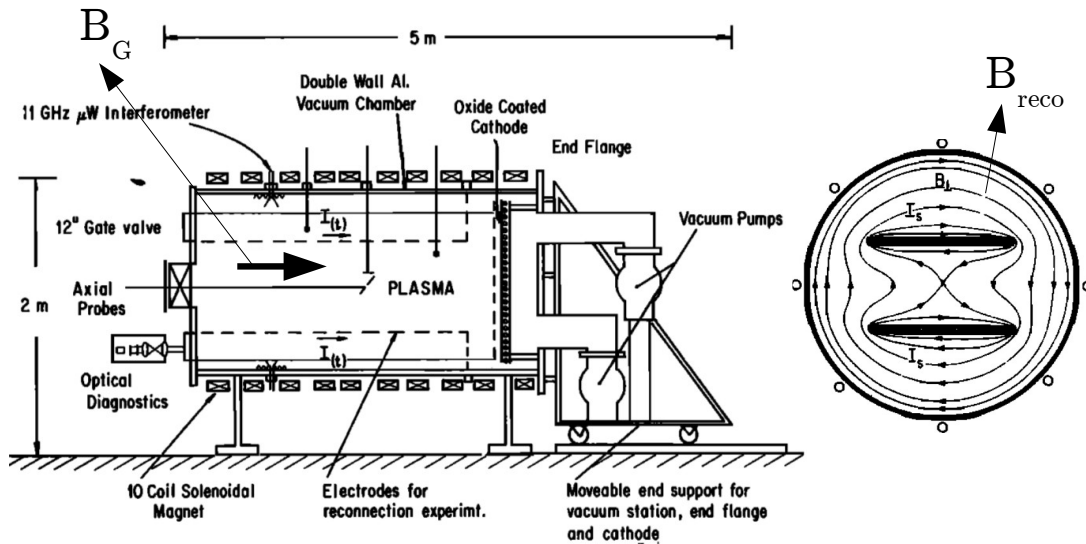


Figure 4.8: Stenzel and Gekelman's experiment. Left: side view, right: front view of the reconnecting fields. From [133]

It is also worth mentioning the experiment performed by Stenzel and Gekelman [133, 134], whose setup is illustrated in Fig. 4.8. Within a discharge plasma, a strong guide field ($\|B_G\| \gg \|B_{reco}\|$, $B_G \cdot B_{reco} = 0$) is applied using solenoid coils. Then, a current is run within two parallel conductive plates, such as to generate reconnecting magnetic fields. The discharge plasma generated was once again in the *electron MHD* regime (EMHD) where only the electrons are magnetized, with a relatively low Lundquist number ($S \approx 1 - 10$). The electron and magnetic pressures were recorded, along with the ion velocity vectors, showing the formation of a typical “double-Y” shaped neutral layer in

less than two characteristic Alfvén times $\tau_A \equiv L/V_A$. After a few τ_A , the ion flow pattern showed characteristic jets from the current sheet, with a velocity close to the Alfvén one. Moreover, by increasing the strength of the guide field from 20 to 100 G, they saw a shear of the double-Y shaped neutral layer into a O shaped magnetic island.

Spheromaks: plasma merging

Following these pioneering works, numerous studies of magnetic field reconnection were also performed with plasma merging into double spheromak facilities. A spheromak produces a toroidally shaped plasma designed such that the force-free currents ($\mathbf{j} \times \mathbf{B} = 0$) are allowed to get an equilibrium configuration, without external fields, resulting in microsecond confinement times. Depending on whether the two spheromaks have parallel or counter-parallel toroidal B-field, one can study the reconnection of magnetic fields with either co-helicity or counter-helicity.

With this kind of facility, the produced plasma presents higher Lundquist numbers ($S > 100$) and is entirely representative of the MHD regime. Experiments at the TS-3 facility [135, 136] showed that the merging of counter-helicity spheromaks occurs faster than for co-helicity ones, supposedly because in the first case the toroidal field reduces quickly to zero, resulting in an attractive force accelerating the reconnection. This is a good illustration of the strong dependence of the reconnection speed on the velocity at which the two plasmas merge. In other words, it shows the importance of the external forces driving the two plasmas toward each other to determine the reconnection rate.

MRX: a controlled driven reconnection device

On top of the various spheromak devices, a series of devices is dedicated to performing controlled driven reconnection experiments. Among them is the *magnetic reconnection experiment* (MRX) device built at PPPL (Princeton Plasma Physics Laboratory) [126]. In an axi-symmetrical geometry, two flux cores generate a plasma by inductive discharges. The flux cores contain both a poloidal and a toroidal field coil, to which is added a steady-state equilibrium field. The operating cycle is the following: first, a quadrupolar magnetic field is generated through the poloidal field coils. Then, using the toroidal field coils, toroidal plasmas are generated around each flux core by inductive discharge. These plasmas have a typical electron density $N_e \sim 10^{14} \text{ cm}^{-3}$, electron temperature $T_e \sim 10 \text{ eV}$ and magnetic field $\|B\| \sim 0.2 - 1 \text{ kG}$, giving a Lundquist number $S > 500$.

The topology of the magnetic field was measured in the reconnection region using a two-dimensional magnetic probe array, showing once again that the shape of the neutral layer depended on the directions of the toroidal fields. For null-helicity (no toroidal field)

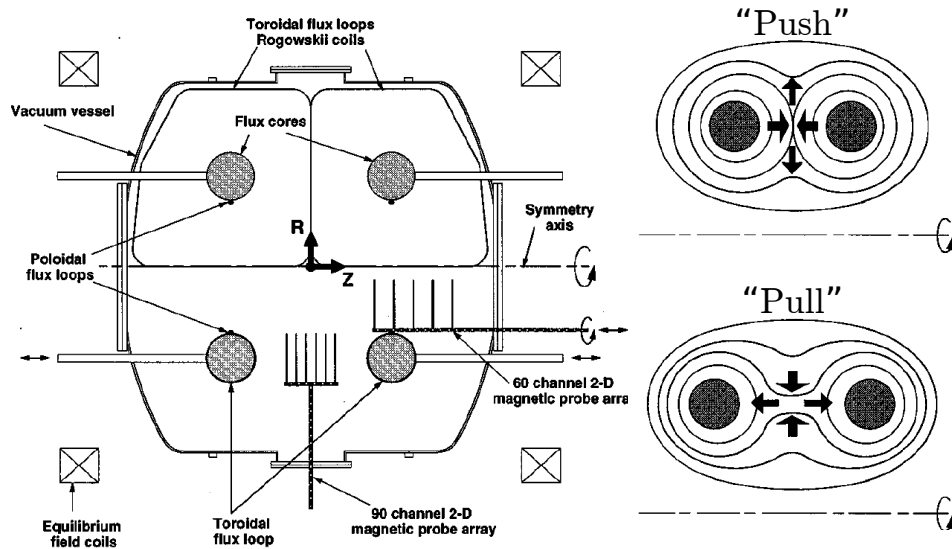


Figure 4.9: *Left: Cross section of the MRX device, based on two flux cores in an axis-symmetrical geometry. Right: increasing (reducing) the poloidal field allows to study a push (pull) configuration.*

or counter-helicity (anti-parallel toroidal field), it exhibits a double-Y shape, while for co-helicity (parallel toroidal field), an O-shaped neutral layer formed.

Satellites

Complementary to the numerous laboratory experiments dedicated to the study of magnetic reconnection, a number of satellites have been launched, in order to measure and observe magnetic reconnection in Nature. Among them, some are dedicated to the study of solar flares through the use of optical and x-ray diagnostics. In this category, we find Yohkoh (Japanese for sunlight), operational from 1991 to 2001 for almost a full solar activity cycle, Soho (*solar and heliospheric observatory*) launched in 1995, Trace (*transit region and coronal explorer*) and Hinode (sunrise in Japanese), launched in 2006. Another type of satellites is equipped with diagnostics such as to measure *in-situ* the magnetic field and particle velocity distribution of the magnetosphere. One could cite the *international Sun-Earth explorers* (ISEE 1 & 2), Geotail which as its name suggests, aims at studying the magnetotail, WIND, POLAR for the study of the polar magnetosphere through the multi-wavelength imaging of aurora, CLUSTER which is an ESA mission using four identical satellites flying in a tetrahedral formation, like the THEMIS mission made of a constellation of five satellites.

Laser plasmas

As said in the introduction of this chapter, the reconnection of the magnetic field may play a significant role in indirectly driven ICF experiments, and more generally in laser-generated high energy density plasmas. Following the first proton radiography experiments [72, 73], which, as we said previously, allowed to probe the MegaGauss magnetic field generated deep within the target, experiments were performed with two or more nanosecond lasers irradiating simultaneously a solid target, with a slight spatial separation between the focal spots.

Among the firsts, an experiment has been conducted on the Vulcan laser facility at the Rutherford Appleton Laboratory, in the UK [115, 116]. Two 200 J, 1 ns Nd:glass laser pulses were focused on a 30 – 50 μm FWHM focal spot, giving a laser intensity $I \sim 1 \times 10^{15} \text{ W/cm}^2$. The lasers were at the first harmonic ($\lambda = 1.054 \mu\text{m}$), the separation between the two laser spots was varied during the experiment, and the target was made of either aluminum or gold. The interaction was probed using several diagnostics, including an optical probe (for shadowgraphy and interferometry) at the 4th laser harmonic ($\lambda = 263 \text{ nm}$), allowing to observe a deeper part of the plasma than allowed by a probe beam at the 1st or 2nd harmonic. It showed, for some laser spot separations, the presence of two plasma jets in the mid plane where the plasmas collide, with an angle of $\sim 40^\circ$ with the target plane. Moreover, proton radiography was performed using a proton beam generated by the TNSA mechanism, showing a strong proton dose accumulation in the mid-plane between the two irradiated spot. Finally, the electron temperature in the mid-plane (at 100 μm from the target's surface) was measured using Thomson scattering with a 1 ns, 10 J and 263 nm wavelength probe beam, showing a strong increase of the electron temperature, even after the heating lasers were turned off.

Later on, numerous experiments have been conducted on the Omega and Omega-EP facilities by a team from MIT. In each of them, the main target was a 5 μm thick CH target, driven by 1 ns square, 500 J laser pulses at the 3rd harmonic (351 nm), focused in a 800 μm diameter spot, ensuring similar plasma conditions during the different experiments.

In the first one [137], they showed a “proof of concept” of their setup, showing an annihilation of the field after a given time. Yet, because of the low spatial resolution² of the proton radiography (imploded backlighter with grid), it is possible that the ion dissipation region could not be resolved. During the same experiment [138], electron and ion temperatures were measured using Thomson scattering, at different locations of a single plasma bubble or in the mid plane of two colliding plasma bubbles. In the first case, the electron temperature at late times ($> 2 \text{ ns}$) was higher than LASNEX predictions,

²While performing proton radiography with an imploded backlighter and a grid, the diagnostic consists in the measurement of the displacement of an array of $\sim 10 \times 10$ beamlets of protons. The information is thus a map of $\int B \cdot dl$ over $\sim 10 \times 10$ points.

possibly due to a heating from the Thomson scattering beam (not accounted for in the 2D hydro-radiative simulations). Finally, in the case of colliding bubbles, they did not measure a significant increase in temperature compared to the measurement on the edge of a single plasma plume. This agrees with the conclusions of chapter 3, in which we showed that the fraction of energy stored as magnetic field is very low, thus unable to affect the plasma temperature within the resolution range of the diagnostic.

In a following publication [139] they reported measurements of reconnection rates, particularly for asymmetric reconnection (*i.e.* with a time delay between the two driving lasers). From this experiment, they concluded that the rate of magnetic flux annihilation is dictated by the relative flow velocities of the opposing plasmas and is insensitive to initial asymmetries. In another experiment [140], they measured the flux pile up in the case of parallel magnetic fields, using two face-to-face targets, separated by $\delta_z = 1 \text{ mm}$. Yet, this setup is valid only in the hypothesis of a magnetic field in a shell like shape, *i.e.* with a large extension in the direction normal to the targets. In the case of a “disk-like” shape magnetic, such as in FCI2 simulations, the magnetic fields from each target would not meet, considering the large separation between them. Finally, they performed high resolution proton radiography at the Omega-EP facility [141] and showed patterns in the proton dose modulation, that they identified as fast and transitory electron jets.

While these results are of interest, their interpretations are based on the assumption of colliding magnetic field “shells” such as predicted using LASNEX simulations. Hence, these conclusions may be wrong if the magnetic field is compressed onto the target, such as predicted from DRACO [110] and FCI2 simulations. This is what motivated our team to perform the experiments presented below.

Finally, it is worth mentioning an experiment performed by G. Fiksel *et al.* [142] on Omega EP. As opposed to the previously mentioned experiments, they studied the reconnection of externally generated magnetic field. The setup was as follow: a 100 J, 1 ns laser irradiated a plastic target, such as to generate a tenuous background plasma. This plasma was then magnetized using a current discharge in two parallel conductive plates, producing 8 T magnetic field loops. Each plates were coated with CH and irradiated by a 1.8 kJ, 2 ns laser pulse. Hence, the two counter-propagative plasma plumes compressed the magnetic field loops from each plate onto each others, through advection with the flow, triggering a reconnection of the field. Using proton radiography in this plasma of lower density (compared to the irradiated foils) and PIC simulations, they showed the formation and collision of magnetic ribbons, pileup of the magnetic flux and a fast reconnection, with a transient reconnection rate comparable to the Alfvén reconnection rate.

4.2 Motivation for the experiments : study using Heckle

In high power laser generated plasmas, various studies has been performed by the means of numerical codes. They can be classified in four different types:

- Vlasov-Fokker-Planck codes, solving the kinetic equation in the phase space.
- Fluid codes, using the MHD framework.
- Particle codes (called PIC codes by metonymy from the most common interpolation order), where the plasma is described by macro particles.
- Hybrid codes, for which either the electrons or the ions are described by macro particles, while the other species is described as a fluid.

After a brief description of each type, we will present the study which has been performed with the hybrid code HECKLE and motivated the experiments presented hereafter.

4.2.1 Different methods to simulate the reconnection

Vlasov-Fokker-Planck

A kinetic code is a type of code seldom used, because of its computational cost. Indeed, as they solve the kinetic equation in the phase space, they require to discretize a distribution function over both space and velocity. As such, a simulation in two space dimensions requires four dimensions in total. Nonetheless, it is worth mentioning the work of Joglekar *et al.* [143]. Using the electron Vlasov-Fokker-Planck code IMPACTA [61, 144], they performed 2D (in space) simulations in conditions relevant for high power laser driven reconnection. Indeed, as we saw in the previous chapter, the magnetic field may be mostly advected with the heat flux (Nernst effect). Looking at the different terms of Ohm's law, they showed that the reconnecting electric field was mostly due to the Nernst term. As such, they concluded that for high power laser driven magnetic reconnection, the reconnection rate may be due to an inflow at the Nernst velocity.

PIC

Using a particle in cell code (PIC) allows to account for both the electron and ion kinetic effects at a reduced CPU cost, depending on the number of macro-particles. As such, PIC codes are well suited for the study of magnetic reconnection in collisionless plasmas, for which the fluid reduction is not valid. Moreover, they naturally allow to account for the decoupling between the electrons and the ions in the neutral layer. Nevertheless, because the electron plasma oscillation time and the Debye length are much smaller than the spatial and temporal scales of the reconnection, PIC simulations still remain very

expensive to calculate in term of CPU time. Hence, most of the PIC simulations of magnetic reconnection are bounded by a very small box size, with periodic boundary conditions. Additionally, most of the time, the electron-ion mass ratio m_e/m_i is increased artificially, such as to remove the fast electron plasma oscillations.

Using the PSC PIC code, Fox *et al.* performed simulations in the conditions of the Rutherford and of the Omega experiments [145, 146], using the plasma parameters given in [116] and [137]. Doing so, they showed substantial flux-pileup effects, increasing the upstream magnetic field and thus boosting the reconnection rate. Moreover, with the larger system size of the Omega experiment, the PSC simulation showed the formation of plasmoids, while for the small system size of the experiment conducted on Vulcan (at the Rutherford Appleton Laboratory), a single X-line current sheet is formed.

Resistive MHD

Because of their highly reduced computational cost compared to kinetic or particles codes, the magneto-hydrodynamic codes have been widely used in space and astrophysics. Indeed, they allow to simulate over wider domains, such as 3D volumes of the Earth magnetosphere, while kinetic and particle codes are most of the time limited to two dimensions. The complexity of the physics included in MHD codes relies in the different terms of the Ohm's law.

Obviously, a simple ideal MHD formalism does not allow the reconnection of the magnetic field, as it will be frozen in the plasma. The least sophisticated MHD model able to study the reconnection has to account for an homogeneous resistivity of the plasma. Yet, it appeared that an anomalous resistivity has to be used in the current sheet to reproduce fast reconnection events. In fact the GEM challenge [147] showed that in order to obtain a reconnection rate similar to PIC or hybrid simulation with a MHD code, one has to account for the peculiar physics in the ion decoupling region where the ions are no more magnetized while the electrons still are. This is done either by accounting for the Hall term in the Ohm's law (the $\mathbf{j} \times \mathbf{B}$ term in 1.25, on page 26), or by using a two fluid (electrons and ions) code. To our knowledge, no study of magnetic reconnection in high power laser generated plasmas has been performed with Hall-MHD nor two fluid MHD codes.

Hybrid

Hybrid codes are a kind of compromise between particles and fluids: in the case of the study of magnetic reconnection, the ions are treated as macro-particles, while the electrons as a fluid. This allows to model the decoupling between the two species, while neglecting the small spatial and temporal scales due to the electron oscillations. In this chapter, we

will present results from HECKLE, a 3D (here used in 2D) hybrid code parallelized using domain decomposition. The ions are treated as macro particles whose dynamics is solved using a first order interpolation of the electromagnetic field. The electrons are treated as a massless fluid, with an isothermal closure, hence without heat flux and therefore no Nernst effect. The quasineutrality of the plasma is assumed and the electric field comes from the Ohm's law including the Hall, Joule and thermo-electric effects:

$$\mathbf{E} = -\mathbf{u}_p \times \mathbf{B} + \frac{1}{N_e} (\mathbf{j} \times \mathbf{B} - \nabla P_e) + \eta \mathbf{j}, \quad (4.14)$$

where \mathbf{u}_p is the ion bulk velocity (*i.e.* the “fluid” velocity), N_e the electron density, \mathbf{j} the current density (through $\nabla \times \mathbf{B}$), P_e the scalar electron pressure and η the resistivity. The code uses normalized units from arbitrary B_0 and N_0 : lengths are normalized to the proton inertial length $d_p \equiv c/\omega_p = \sqrt{m_p/(\mu_0 N_0 e^2)}$, times are normalized to the inverse of the proton's gyrofrequency $\omega_c^{-1} = m_p/eB_0$, velocities are normalized to the Alfvén velocity $V_A = B_0/\sqrt{\mu_0 N_0 m_p}$ and the electric field to $E_0 = V_A B_0$.

4.2.2 Hall component of the magnetic field

As said above, in order to reproduce kinetic results of collisionless reconnection in fluid codes, it is necessary to account for the decoupling between electrons and ions, especially in the ion decoupling region (see Fig. 4.3) where the ions are no more bound to the field lines, but the electrons remain magnetized. This is the so-called Hall effect, which can be accounted for with two fluid codes or Hall-MHD codes (with the Hall $\mathbf{j} \times \mathbf{B}$ term in the Ohm's law).

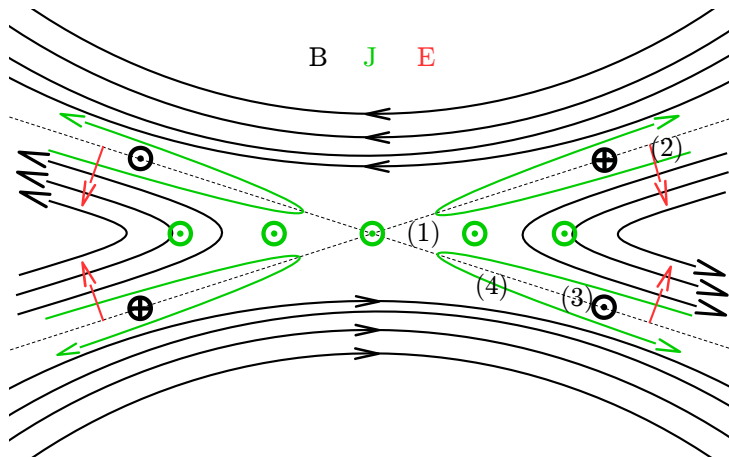


Figure 4.10: Scheme of the electro-magnetic fields and currents in the reconnection region. (1) Ampère, (2) Ohm (Hall term), (3) Faraday, (4) Ampère.

This electron-ion decoupling is associated, in 2D geometries, with the formation of a quadrupolar out-of-plane magnetic field. As shown in Fig. 4.10, this is due to the formation

of the thin current sheet:

1. The anti-parallel magnetic fields (black lines) pinched onto each other are the source of a current sheet (green “dots”) through Ampère’s law $\mathbf{j} = \nabla \times \mathbf{B}$.
2. This current sheet generates an in-plane electric field (red arrows) from the $\mathbf{E}_{Hall} = \mathbf{j} \times \mathbf{B}$ term in Ohm’s law.
3. The in-plane Hall electric field generates the quadrupolar Hall magnetic field (black “dots”) from Faraday’s law $\frac{\partial \mathbf{B}}{\partial t} = -\nabla \times \mathbf{E}$.
4. Because of the out-of-plane magnetic field, an in-plane current (green lines) forms through $\mathbf{j} = \nabla \times \mathbf{B}$.

Note that, from kinetic simulations performed during the “GEM challenge” [147], the formation of this Hall out-of-plane magnetic field was viewed as a consequence of the collisionless magnetic reconnection: the out-of-plane B-field is formed by the current carried by the electrons traveling along the separatrix toward the X point and then down stream [148]. Because the electron dynamics is a consequence of the fast reconnection, the quadrupolar magnetic field was also viewed as such.

Yet, as we saw from the Hall-MHD formalism, the out-of-plane magnetic field may form from the pinching of the anti-parallel in-plane B-field and its associated current sheet. The reconnection of the field is not necessary for the Hall component of the magnetic field to form.

4.2.3 Effects of an angle between the irradiation spots

In order to study the effect on the reconnection of the out-of-plane quadrupolar magnetic field component, 2D HECKLE simulations have been run [24], for which the magnetic field loops had an angle Ψ with the reconnection plane. Doing so, depending on the sign of this angle, a “pro-Hall” (same polarization as the Hall magnetic field that will form later on) or “anti-Hall” out-of-plane component of the field was present in the reconnection region, prior to the reconnection.

The initial conditions of the HECKLE simulations were similar to those of the PSC simulations of Fox *et al.* in [145, 146]: the simulations have been run in the Oxy plane, and invariance has been assumed along the Oz axis. The current sheet is built up by the encounter of two magnetic field tubes, driven toward each other by the expanding plasma cylinders (because of the planar 2D geometry). Fig. 4.11 shows a cartoon of the geometry of the HECKLE simulations. The periodicity is allowed by using in a single simulation two reconnection points: one with an initial “pro-Hall” out-of-plane B-field, and one with an “anti-Hall” magnetic field.

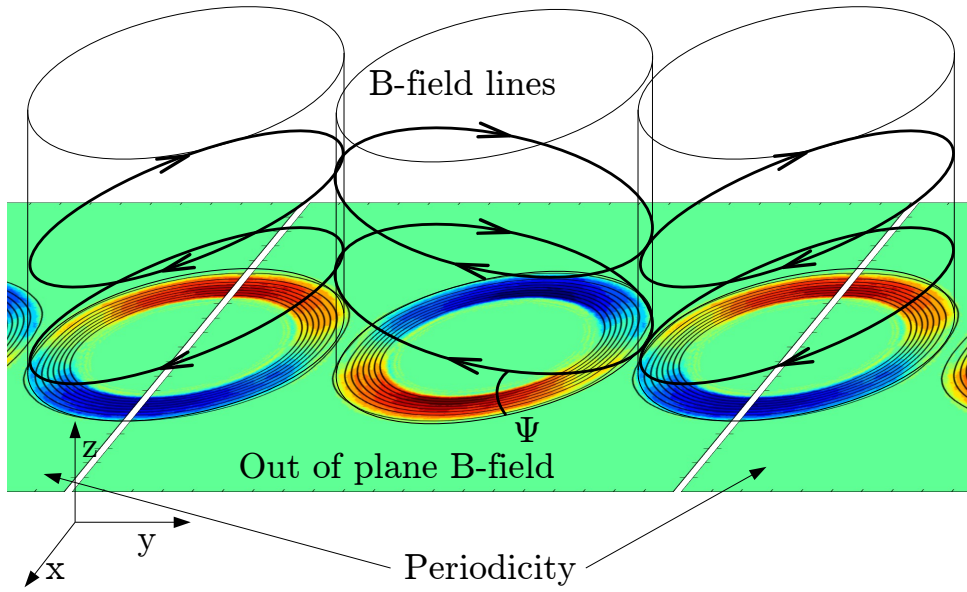


Figure 4.11: *Cartoon of the Heckle simulations' geometry, at $t = 0$. The color map is the out-of-plane magnetic field, red is positive, blue is negative.*

At $t = 0$, each plasma has a cylindrical shape. The initial density, velocity and magnetic field profiles were defined using the fifth order polynomial

$$P(u) = -6|u|^5 + 15|u|^4 - 10|u|^3 + 1, \quad (4.15)$$

which gives $+1$ for $u = 0$, 0 for $u = 1$ and its first derivative is null for $u = 0$ and $u = 1$. P is set to 0 for $|u| > 1$.

Let (x, y) be the coordinates in the simulation plane. After a rotation by an angle Ψ in the Oyz plane, we have $y' = y/\cos\Psi$ and $r' = \sqrt{x^2 + y'^2}$ the radius vector. Let L_R be the mean radius of the magnetic field tube and L_w its half width.

Fig. 4.12 shows the initial profiles of the density, bulk velocity and magnetic field as a function of r' . The density was defined as

$$N = N_0 P(r'/L_R), \quad (4.16)$$

with a background proton density $N_b = 0.2N_0$. The initial “fluid” velocity was set as

$$\mathbf{u}' = u_0 P((2r' - L_R)/L_R) \mathbf{e}_{r'}, \quad (4.17)$$

with $u_0 = 1V_A$ in the HECKLE normalized unit system. Finally, the magnetic field profile read:

$$\mathbf{B}' = B_0 P((L_R - r')/L_w) \mathbf{e}_{r'} \times \mathbf{e}_z.$$

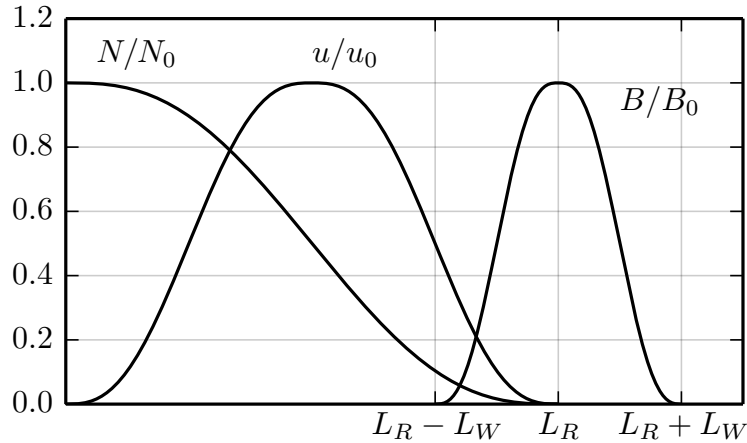


Figure 4.12: Profiles of the initial density, bulk velocity and magnetic field as a function of the radius, in the Heckle simulations.

These quantities (functions of r') have then been projected into the Oxy plane. The electron and ion temperatures were homogeneous and set such as to have a beta parameter (relative to B_0) equal to $\beta_p = 1.0$ for the protons, $\beta_e = 0.2$ for the electrons and $\beta_b = 0.2$ for the background protons. Note that the electron temperature remained always homogeneous due to the isothermal closure. Finally, L_R was set to $16 d_p$ (the proton inertial length, which is HECKLE's normalized length unit) and L_W to $4 d_p$.

The size of the simulation box was $80 \times 80 d_p^2$, the cells' size was $0.2 \times 0.2 d_p^2$ and the time step was fixed to $0.001 \omega_c^{-1}$. The simulation used 32×10^6 macro-particles to simulate the proton population, corresponding to an average of 200 per cell.

Fig. 4.13 plots the reconnected magnetic flux as a function of time for the co-planar case ($\Psi = 0^\circ$), showing the start and the end of the reconnection, as well as its rate. Below are plotted $\|\mathbf{B}_z\|$, $\|\mathbf{E}_{xy}\|$ and j_z in

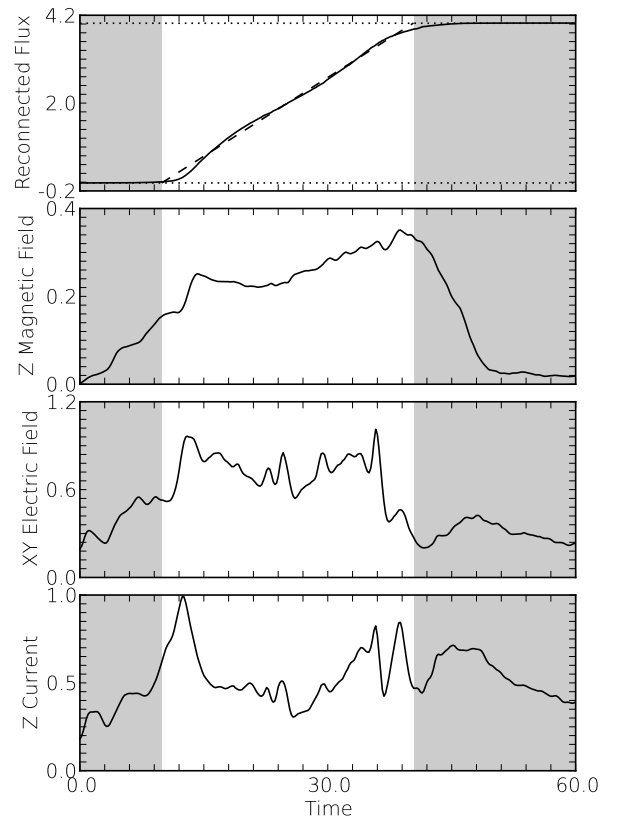


Figure 4.13: Co-planar case. From top to bottom, as a function of time (in ω_c^{-1} units): reconnected magnetic flux, $\|\mathbf{B}_z\|$, $\|\mathbf{E}_{xy}\|$ and j_z in the reconnection region. The shaded region marks the periods before and after the reconnection of the field. From [24]

the reconnection region. It shows that a current sheet forms, associated to an in-plane electric field and an out-of-plane magnetic field, before the start of the reconnection process. The Hall component of the B-field appearing before the magnetic field reconnects, one may thus conclude that this is not a cause of the reconnection process. Hence, it disproves the idea that the electron flow generates the in-plane current and the associated Hall field because of the reconnection. In other words, in order for the quadrupolar magnetic field to grow, one needs a thin and pinched (non-flat) current sheet, which happens to be the initial condition of the GEM challenge simulations (Harris-like topology) and the setup for magnetic reconnection.

Finally, as the Hall magnetic field forms prior to the reconnection, it has been investigated if the presence of this out-of-plane magnetic field is a requirement for the reconnection to trigger. For this, simulations were run with various angles Ψ , up to 28° , inducing an artificial quadrupolar out-of-plane magnetic field in the reconnection region.

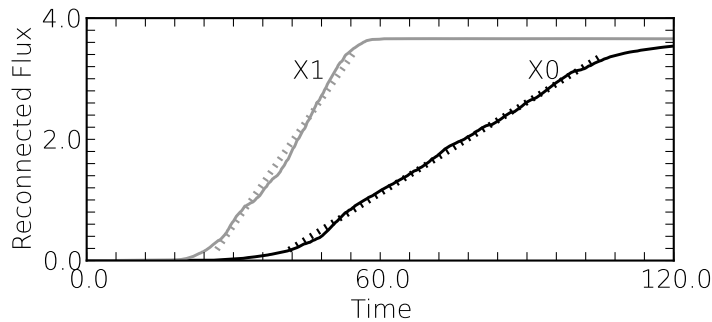


Figure 4.14: *Reconnected magnetic flux given by the HECKLE simulation with an angle $\Psi = 24^\circ$. X1 is the reconnection region with an initial “pro-Hall” out-of-plane B-field and X0 the region with an “anti-Hall” B-field. From [24]*

It appeared that with an angle $\Psi \neq 0$, the reconnection at the “pro-Hall” location remains unaffected. On the opposite, for increasing Ψ angles, the reconnection at the “anti-Hall” location starts later on and has a lower rate. This is illustrated in Fig. 4.14, showing the reconnected flux at the two locations (X0 corresponds to the anti-Hall while X1 is the pro-Hall) for the run with an angle $\Psi = 24^\circ$. For the $\Psi = 28^\circ$ simulation, the magnetic field did not reconnect at all at the anti-Hall location. From this, one may conclude that some time is required to “reverse” the B_z field when an initial anti-Hall field is present. Moreover, the magnetic field could not reconnect as long as the out-of-plane magnetic field remained in an anti-Hall configuration.

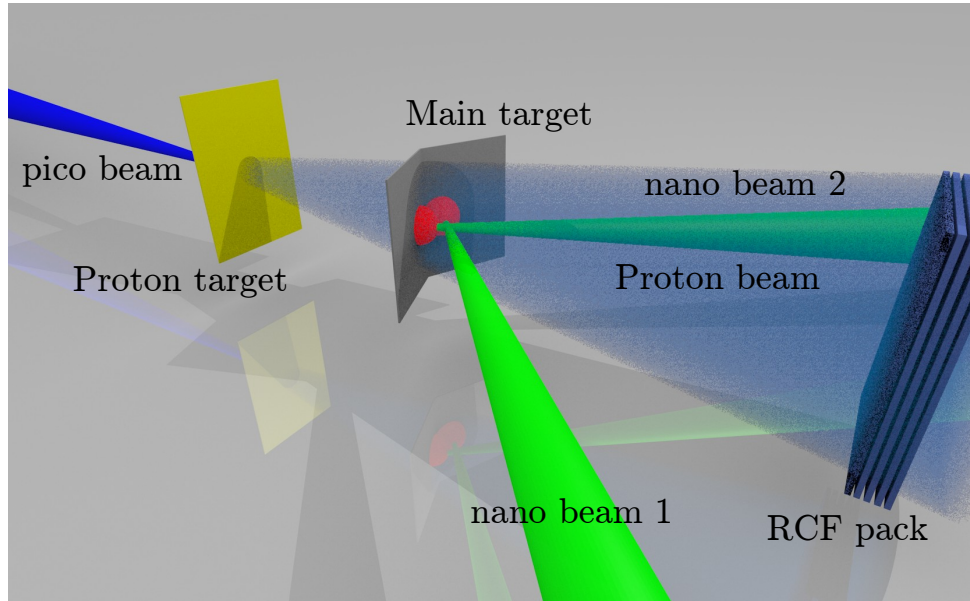


Figure 4.15: *Visualization of the reconnection experiments.*

4.3 Reconnection experiments using laser driven plasmas

Following this numerical study, we proceeded to conduct experiments in order to evidence the effect of an initial anti-Hall magnetic field. For this, a first experiment was performed in 2014 at the Phelix laser facility at GSI (Gesellschaft für Schwerionenforschung, Darmstadt, Germany), for which the target was a Mylar flat foil (for comparison with the single laser beam experiment on JLF-Titan). A second experiment was then performed in 2015 at LULI2000, this time with flat and bended aluminum and gold targets, such as to study the effect of the pro- or anti-Hall initial out-of-plane magnetic field on the reconnection process.

Fig. 4.15 shows a scheme of the reconnection experiments. The setup remains the same as for the single beam “LULI2000 2008” and “JLF-Titan 2011” campaigns, the difference being that this time two nanosecond laser beams drive two near-by plasmas and their associated magnetic field loops. Note that in the case of the LULI2000 reconnection experiment, the foil was bended such that each magnetic field loop was in a plane tilted compared to the other one.

4.3.1 Phelix

The first experiment was conducted at GSI, on the Phelix laser system, for which one week of shots had been attributed. Therefore, due to the limited number of shots available during this campaign, the experiment served as a test of the setup and we used only flat $23\ \mu\text{m}$ Mylar targets, just like during the JLF-Titan experiment. While Phelix is mostly

used in the “PetaWatt” configuration (up to 250 J in a 0.4 ps pulse), the facility also provides a nanosecond plus picosecond beams configuration that we used during our experiment.

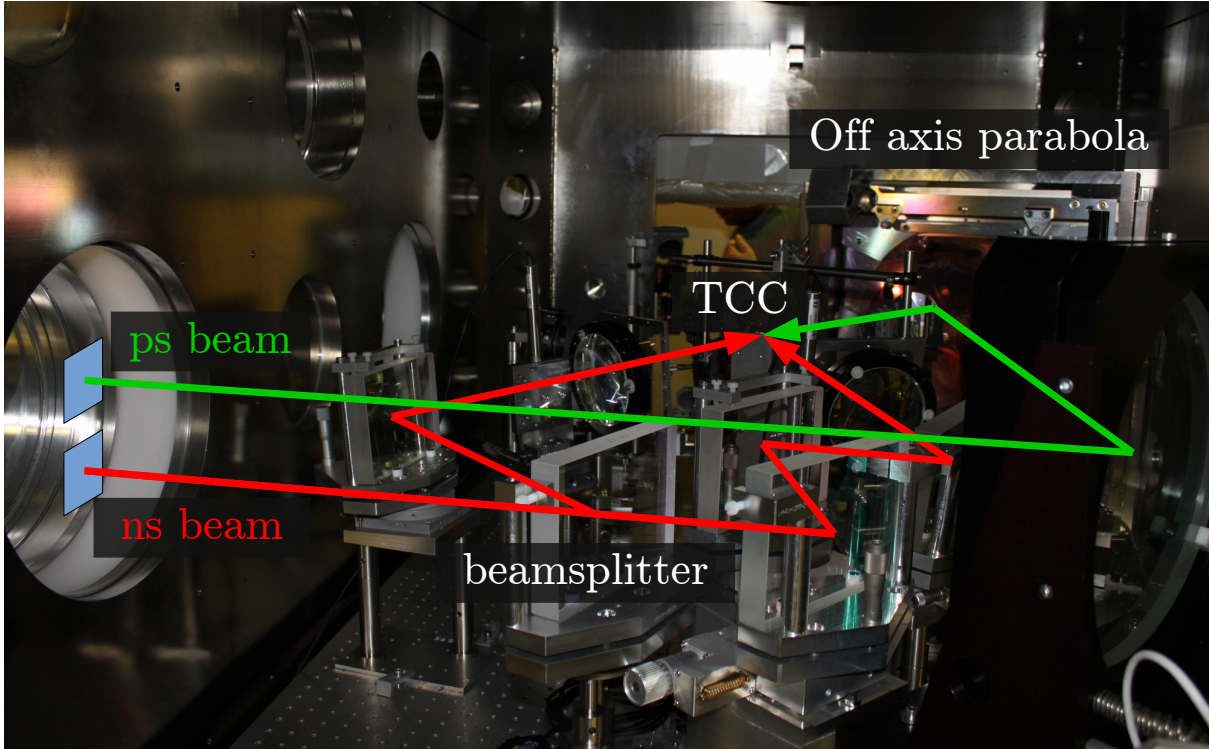


Figure 4.16: Photograph of the Phelix interaction chamber.

As illustrated in the photograph in Fig. 4.16, in this configuration, the two 90×90 mm beams arrive in the experimental chamber on top of each other. The picosecond beam is a ~ 50 J over 0.5 ps pulse, at the first laser harmonic. Due to the configuration of the experimental room, the nanosecond beam was split in two within the interaction chamber using a 50% reflectivity beamsplitter. The two resulting beams were then transported up to the “Target Chamber Center” (TCC) along optical paths of the same length such as to ensure the synchronization of the two plasmas.

The two nanosecond beams consisted each in 25 J, 1.8 ns full width at $1/e^2$ Gaussian pulses at the first laser harmonic ($\lambda_L = 1.053 \mu\text{m}$). They were focused onto the main target using $f = 300$ mm lenses with Random Phase Plates (RPP), giving focal spots whose angular average could be fitted by a Gaussian with a $86 \mu\text{m}$ Full Width at Half Maximum and an intensity $I \sim 2 \times 10^{14} \text{ W/cm}^2$.

During this first experiment, we performed proton radiography of the main target at different times and for different separations δ (200, 400, 600 and $1400 \mu\text{m}$) between the two focal spots. The distance “main target – films” was $D = 55 \text{ mm}$ and the distance “proton target – main target” was at first $d = 6 \text{ mm}$ (giving a magnification $G = 10.2$) and then increased to $d = 10 \text{ mm}$ ($G = 6.1$) such as to *i*) have a more homogeneous

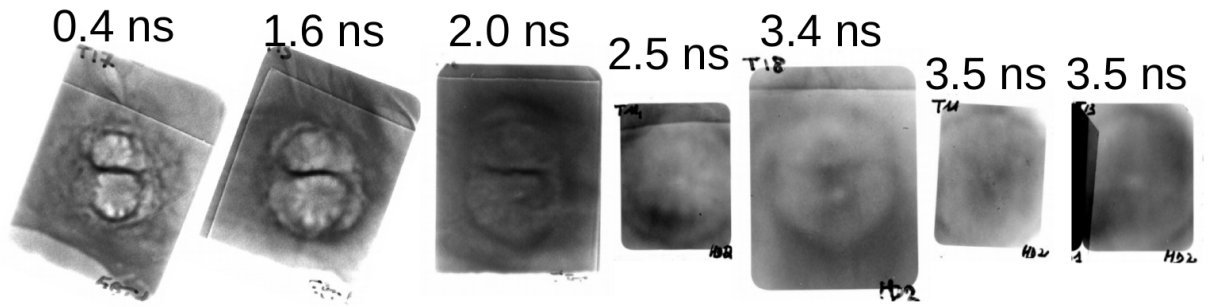


Figure 4.17: Results of the proton radiography performed on Phelix at different times, for a laser spot separation $\delta = 600 \mu\text{m}$. Note that the laser is off at $t = 1.8 \text{ ns}$.

proton dose on the object to radiograph, and *ii*) decrease the size of the image on the radiochromic films, whose dimensions were fixed by their cassette.

Fig. 4.17 shows the results of the proton radiography measurements at different times (during and after the laser irradiation) for a separation $\delta = 600 \mu\text{m}$ between the two focal spots. It shows that a strong line of proton accumulation forms early on, and persists all along the time during which the target is irradiated by the two laser pulses. On the opposite, as soon as the lasers are off, the proton dose modulation becomes smoother and the strong proton accumulation in the mid plane between the two plasmas vanish.

Fig. 4.18 presents the results of a FCI2 simulation of the interaction of a single laser pulse, at 1, 2, 3 and 4 ns. The top panel shows the absolute value of the azimuthal magnetic field (in linear scale) while the bottom panel shows the thermal *beta parameter*. The dotted line represents the mid-plane between the two plasma bubbles, for a separation $\delta = 600 \mu\text{m}$. From this, one can see that *i*) the two magnetic field loops meet before $t = 1.0 \text{ ns}$, as seen on the proton-radiography at 0.4 ns, and *ii*) as soon as the laser is “turned off”, the plasma temperature homogenizes and the magnetic field is no more compressed onto the solid foil by the Nernst effect. Therefore after $t \sim 1.8 \text{ ns}$, the magnetic field starts to expand with the fluid (only remaining advection effect), and vanishes through resistive effect.

From this first experiment, because we did not see significant changes in the proton radiography while the field was still compressed onto the target, we concluded that one needs longer laser pulses. Doing so would allow to keep the magnetic field loops onto the targets plane for a longer duration, giving the time to observe changes in the magnetic field topology. Finally, it showed the need for numerical tools, such as to understand if this line of proton dose accumulation is a signature of ongoing reconnection, or is due to anti-parallel magnetic field fluxes, compressed onto each other without reconnecting.

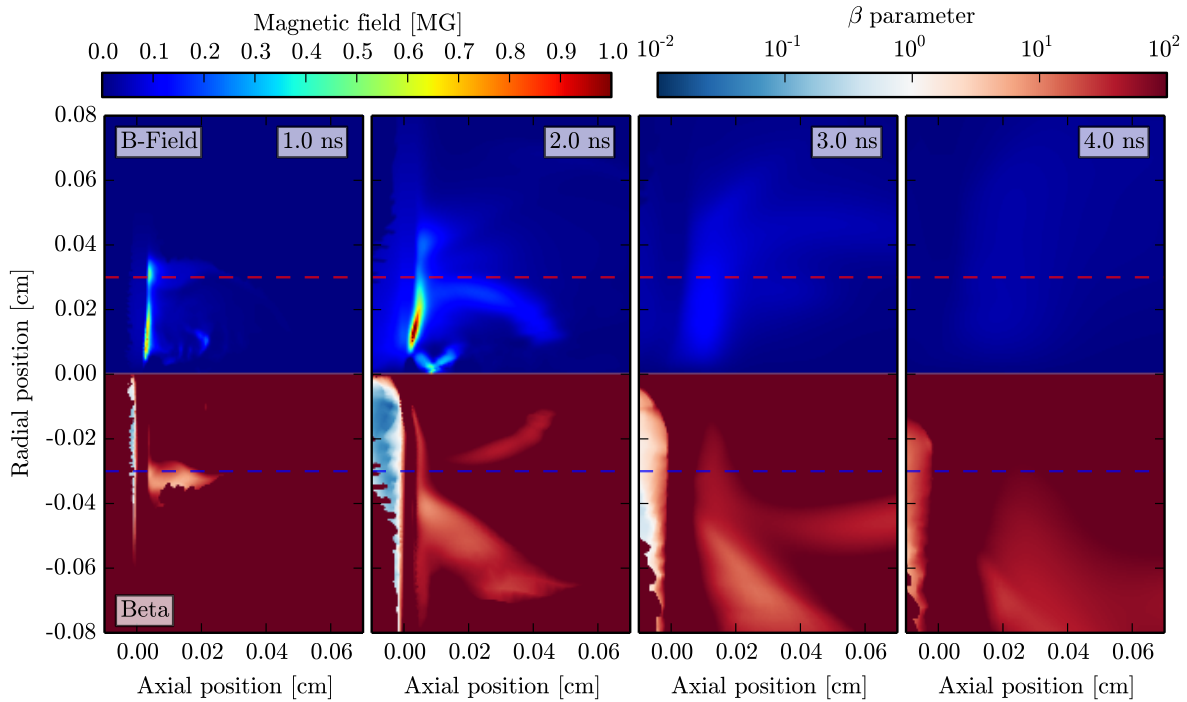


Figure 4.18: FCI2 simulation of the irradiation of a single pulse for the Phelix experiment (Mylar target): 25 J, 1.8 ns full width at $1/e^2$ Gaussian temporal profile, focused at $\lambda_L = 1.053 \mu\text{m}$ in a $86 \mu\text{m}$ FWHM focal spot. Color maps at 1, 2, 3 and 4 ns of $|B_\theta|$ (top) and β_{th} (bottom). The dotted lines at $r = 0.03 \text{ cm}$ represent the mid plane with the other plasma for the separation $\delta = 0.06 \text{ cm}$, shown in Fig. 4.17.

4.3.2 LULI2000

The following year a second reconnection experiment has been performed, at the LULI2000 laser facility. This facility provides two kiloJoule beamlines (called North and South) to the “room 2” and offers the possibility for “room 1” to compress the South line, giving a kJ beamline alongside a picosecond one.

Because of the need of a picosecond pulse for proton radiography, our experiment was conducted in room 1, and the north beamline was split in two (called North and North-bis) to drive the two plasmas on the main target. Because the beams are much larger on LULI2000 (200 mm diameter), we could not use a beamsplitter like during the Phelix experiment. The solution, illustrated in Fig. 4.19, was to take a “pick-off” from the “ $\Phi 200 \text{ mm}$ ” full beam using an elliptical mirror, whose projection on the beam direction is a 100 mm diameter section. Then, $\Phi 100 \text{ mm}$ apodizers were placed after the pick-off mirror, in both the North and North-bis paths. Therefore, it resulted in two beams, each containing 1/4 of the original beam’s energy, the rest being blocked by the apodizers. Of course, the repartition of energy between the two beams depends on the homogeneity of the intensity in the original “full North” beam. Finally, the North-bis line was send into

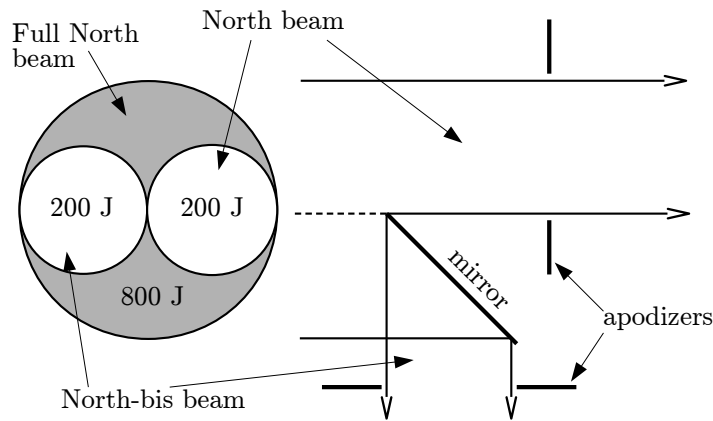


Figure 4.19: Scheme of the North + North-bis configuration on the LULI2000.

a delay line, such as to set the synchronization with the North line

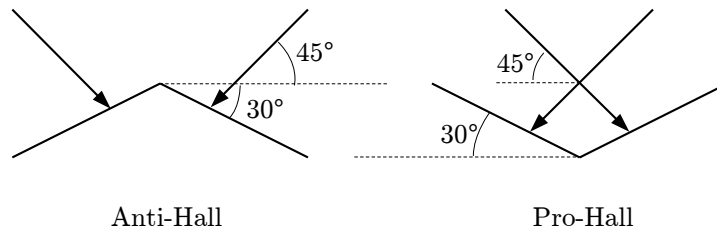


Figure 4.20: Geometry of the pro- and anti-Hall targets during the LULI2000 campaign.

The original North pulse delivered by the facility was 800 J (hence 200 J in each sub-pulses) at $\lambda_L = 1.053 \mu\text{m}$, over a squared 4 ns with 100 ps rising time temporal profile. They were focused onto the target by the same $f = 300 \text{ mm}$ lenses and random phase plates as in the Phelix experiment, giving an intensity $I \sim 8 \times 10^{14} \text{ W/cm}^2$.

As three weeks of shots were allocated for this experimental campaign, we could perform measurements at different times, for our three target's geometries (co-planar, anti-Hall and pro-Hall) and two target's material ($5 \mu\text{m}$ thick gold for high atomic number and $25 \mu\text{m}$ thick aluminum for low Z). Note that we switched from Mylar to aluminum target for the low Z, such a to have a pure material target, in an attempt to have simulations with more accurate opacities and equation of state tables.

As illustrated in Fig. 4.20, the North and North-bis beams were at 90° from each other and, for the anti- and pro-Hall configurations, each half plane of the target was bended by $\Psi = 30^\circ$. Switching the position of the beams focalization allowed to have irradiation with a small angle compared to the normal of each “half-targets”.

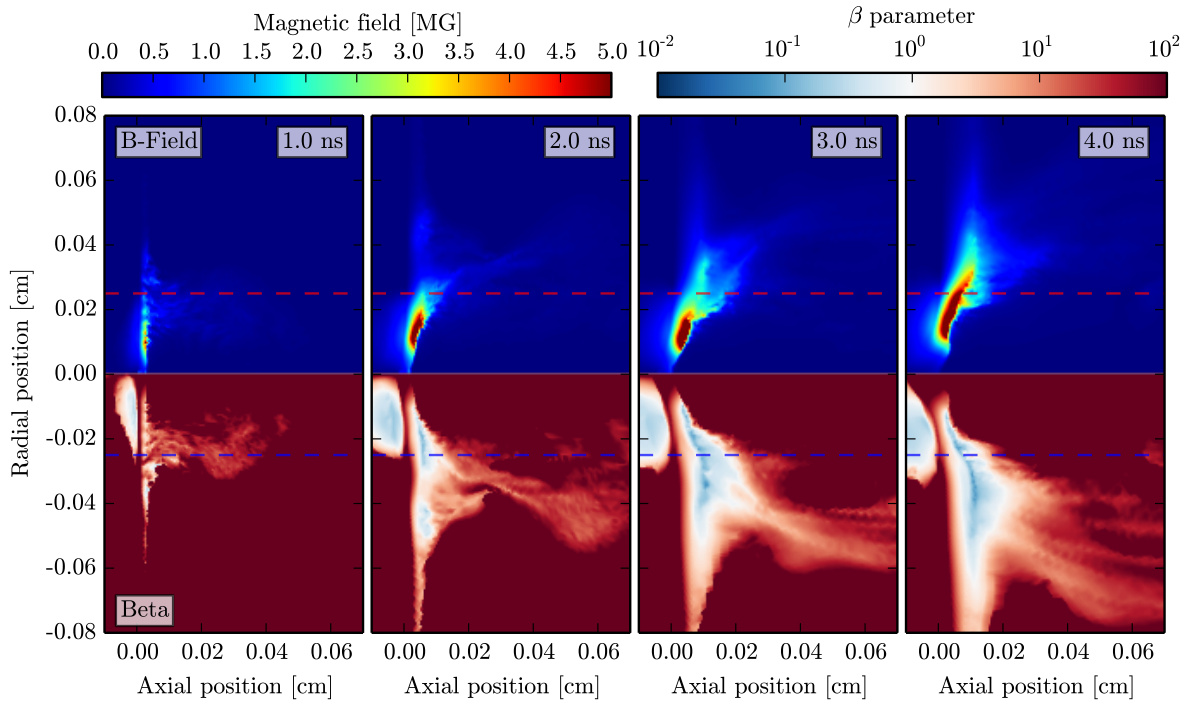


Figure 4.21: FCI2 simulation of the irradiation of a single pulse for the LULI2000 experiment (gold target): 200 J, 4.0 ns square temporal profile, focused at $\lambda_L = 1.053 \mu\text{m}$ in a $86 \mu\text{m}$ FWHM focal spot. Color maps at 1, 2, 3 and 4 ns of $|B_\theta|$ (top) and β_{th} (bottom). The dotted lines at $r = 0.025 \text{ cm}$ represent the mid plane with the other plasma for the separation $\delta = 0.05 \text{ cm}$, shown in Fig. 4.23.

During all the experiment, the separation between the two focal spots has been set to $\delta = 500 \mu\text{m}$, based on the results of the Phelix experiment and of the FCI2 simulations of a single laser pulse, shown in Fig. 4.21 and Fig. 4.22. Indeed, they show that it corresponds both to a position at which the magnetic field is important and, therefore, where the β_{th} parameter is small. Moreover, it is just a little larger than the size of the hot plasma heated by the laser pulse, marked by the sharp decrease of magnetic field (and thus increase of the β_{th}). Hence, once the $\sim 400 \mu\text{m}$ diameter central part of the foil is accelerated, the critical density moves inward and the magnetic field around is quickly advected radially through the Nernst effect. The distance “main target – films” was $D = 50 \text{ mm}$ and the distance “proton target – main target” was $d = 10 \text{ mm}$ (giving a magnification $G = 6$).

The results from the proton radiography are shown in Fig. 4.23 (gold) and Fig. 4.24 (aluminum). They show, for both materials, the proton dose modulation due to the magnetic field at different times during the laser irradiation of the target (1, 2, 3 and 3.8 ns plus a 0.19 ns time of flight for the 14.3 MeV protons). The RCF shown here are of the EBT3 type, which are more sensitive than the HD type (allowing to look at more energetic protons), but also have a kind of grain.

As we saw in the second chapter, due to the important scattering of the probing protons

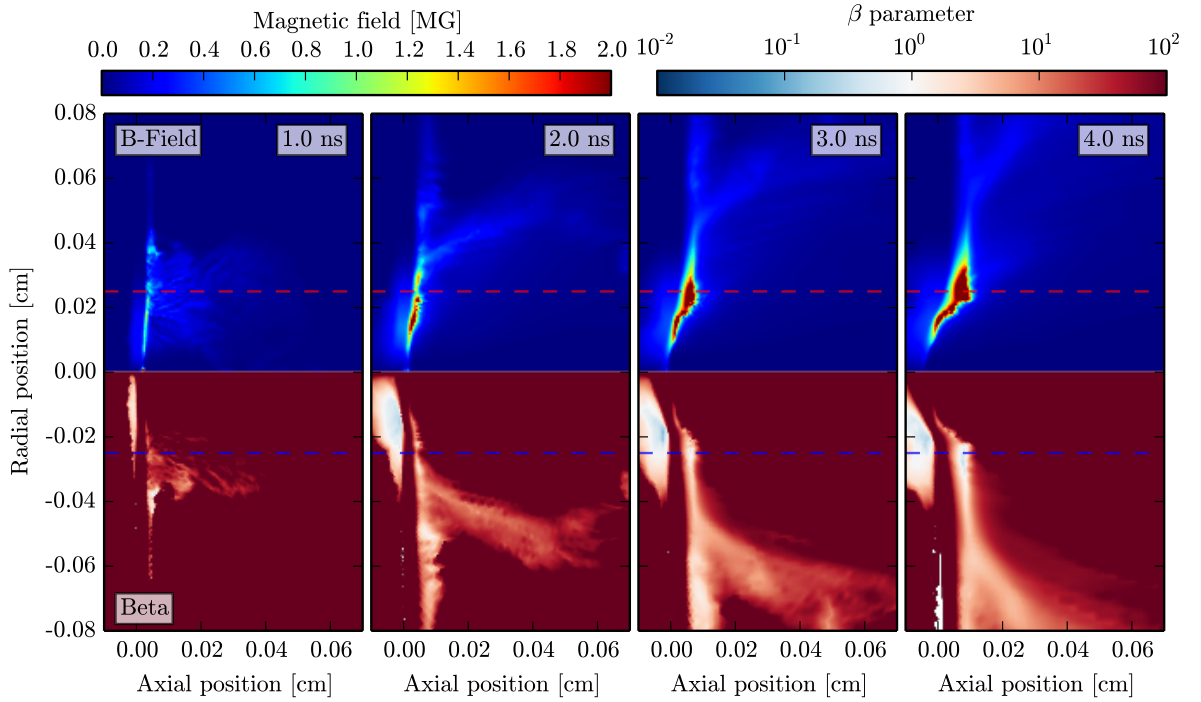


Figure 4.22: FCI2 simulation of the irradiation of a single pulse for the LULI2000 experiment (Aluminum target): 200 J, 4.0 ns square temporal profile, focused at $\lambda_L = 1.053 \mu\text{m}$ in a $86 \mu\text{m}$ FWHM focal spot. Color maps at 1, 2, 3 and 4 ns of $|B_\theta|$ (top) and β_{th} (bottom). The dotted lines at $r = 0.025 \text{ cm}$ represent the mid plane with the other plasma for the separation $\delta = 0.05 \text{ cm}$, shown in Fig. 4.24.

through the gold target, only large scale proton dose modulations are visible, while for the aluminum target, one can see a turbulent pattern, extending over a large distance beside of the accumulation rings around the two focal spots. Note that as this is our first experiment using aluminum, further studies would be required to understand these large scale turbulent dose modulations.

- Looking at the co-planar gold results, it appears that just like in the Phelix experiment, a line of proton accumulation forms early on, and remains all along the laser irradiation. Note that because of the method used to split the full North beam into the North + North-bis, it happened for some shots that one of the two pulses carried less energy than the other, due to the inhomogeneous intensity repartition in the full beam. For the results relative to the aluminum targets, the proton dose line is present at 1 and 2 ns, but at 3 and 4 ns it is much less clear if this line is still present.
- For the anti-Hall configuration, in the gold case the proton line is visible at 1 ns, but at longer times the results are different from the co-planar case. Instead of a strong accumulation of protons within the reconnection region, we now have a rather homogeneous dose, with two “V” of higher dose in the “outflow” regions. For

the aluminum target, the results are much less easy to see because of the turbulent behavior of the proton dose, yet it presents some similarities with the gold target. At 1 ns there is also the line of proton dose, and afterward, one can see a kind of double “Y” shape of proton dose in the reconnection region.

- The results in the pro-Hall configuration are even less readable. This is because of the collision of the two plasma bubbles occurring in the mid plane between the two targets, on top of the reconnection region. Yet, at 4 ns, when the oval shaped proton deflection due to the collision becomes large enough, one can see that a line of proton accumulation is still there, just like in the co-planar case.

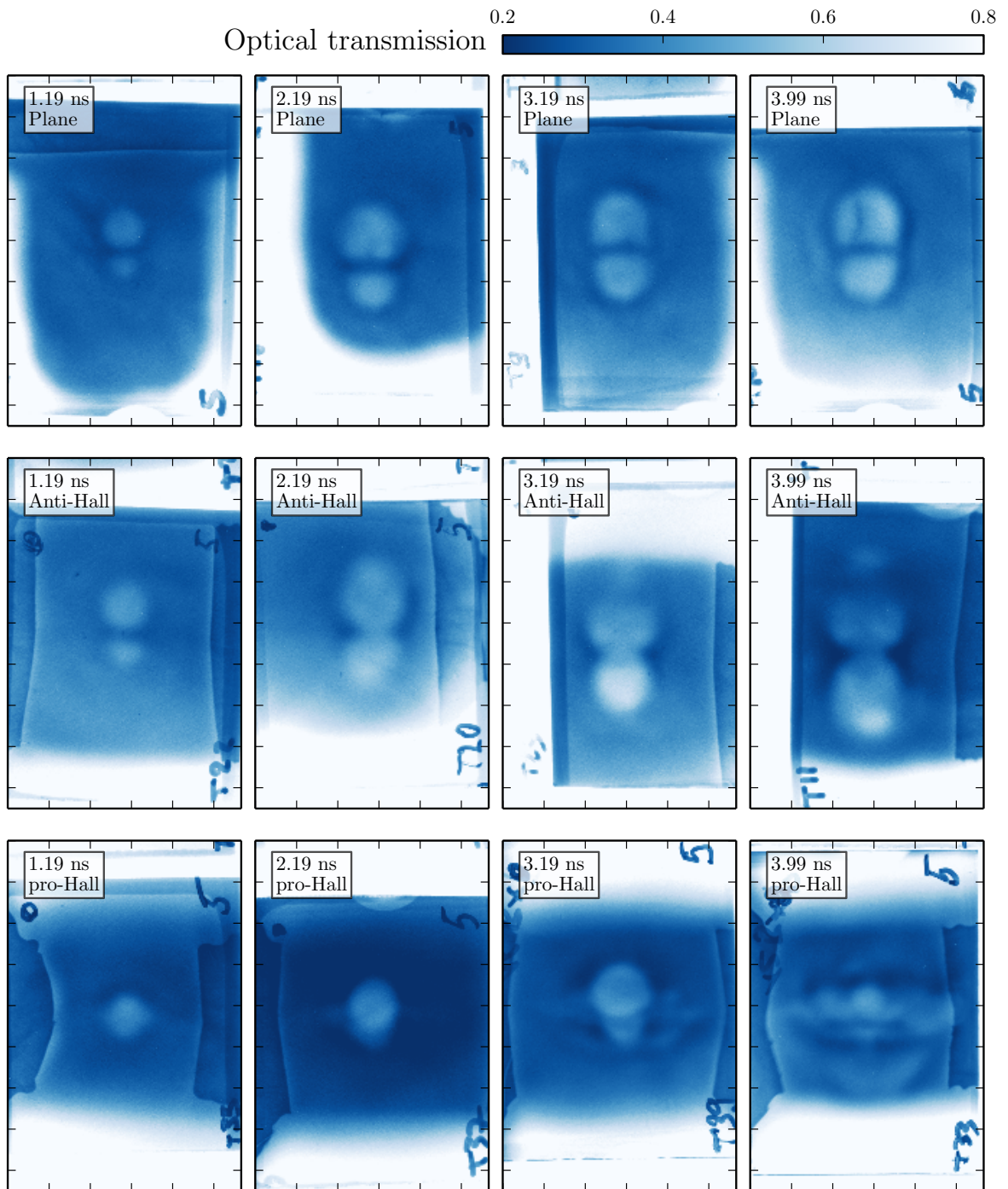


Figure 4.23: Results of the proton radiography performed on LULI2000 at different times with 14.3 MeV protons, for a laser spot separation $\delta = 500 \mu\text{m}$ (gold target). From left to right: time of probing. From top to bottom: target geometry (co-planar, anti-Hall and pro-Hall). Each box is $24 \times 36 \text{ mm}$ in the detector plane, i.e. $4 \times 6 \text{ mm}$ in the target's plane.

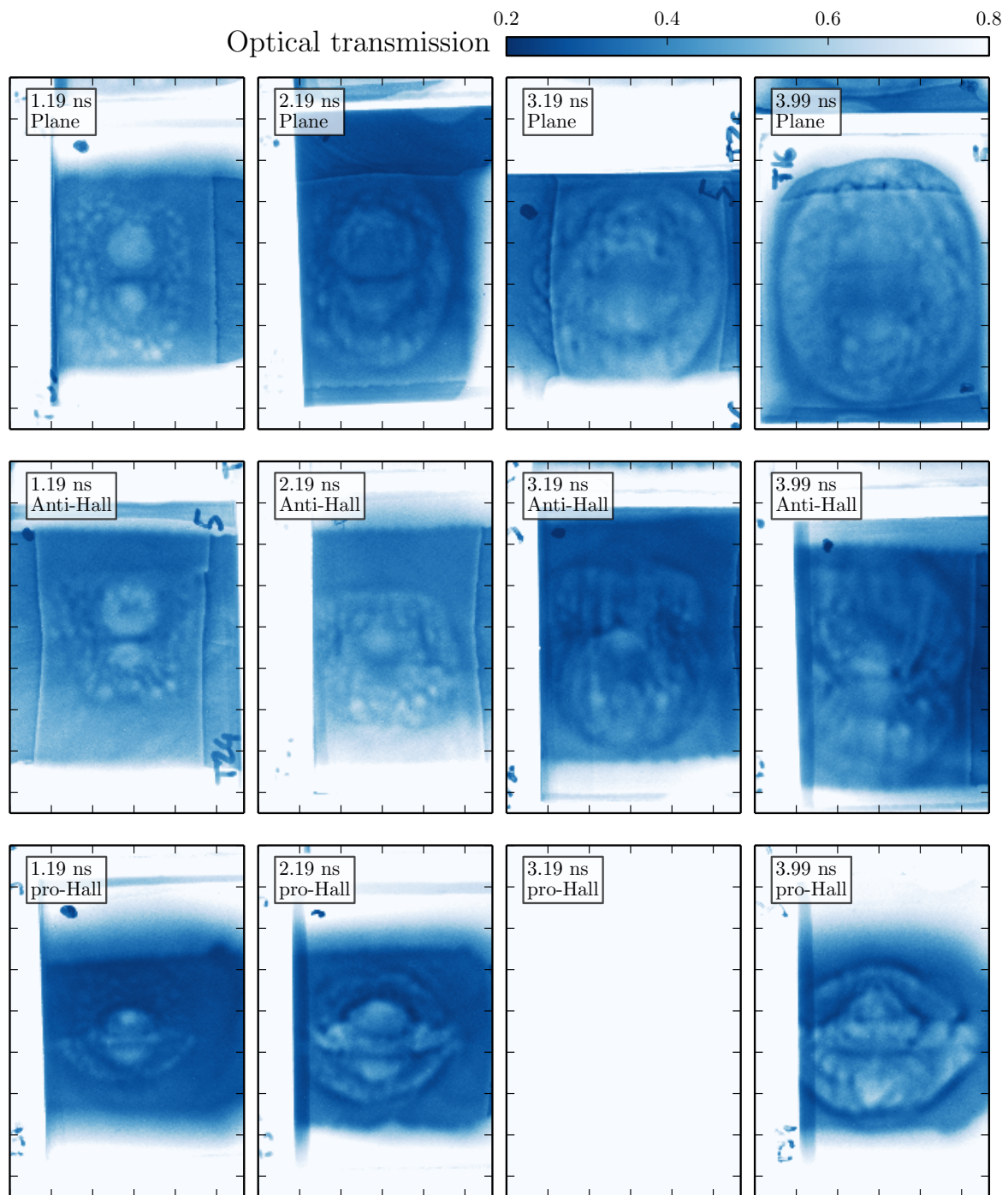


Figure 4.24: Results of the proton radiography performed on LULI2000 at different times with 14.3 MeV protons, for a laser spot separation $\delta = 500 \mu\text{m}$ (aluminum target). From left to right: time of probing. From top to bottom: target geometry (co-planar, anti-Hall and pro-Hall).

Each box is $24 \times 36 \text{ mm}$ in the detector plane, i.e. $4 \times 6 \text{ mm}$ in the target's plane.

4.3.3 Interpretation of the results

While in the case of the irradiation of a foil by a single laser pulse, the results could be directly compared with post-processed simulations of the interaction, in the case of a reconnection experiment, the results are much more complicated to interpret, because of the 3D nature of the problem and of the complex physics to account for (both the hydrodynamics of the irradiated foil and the reconnection of the magnetic field occurring at the same time). Nonetheless, using the HECKLE simulations and the ILZ proton radiography post-processor, we will try to get an insight on what happened during the experiments.

Fig. 4.25 shows proton radiographies calculated by the ILZ code from HECKLE simulated B-field topologies. The HECKLE simulation used for this figure is a co-planar case, with the same parameters as described in sec. 4.2.3. The simulation box was large enough to enclose two full magnetic field loops and keep distant the boundaries, thus without effects from the periodic boundary condition. The color maps of the in-plane and out-of-plane simulated magnetic fields are shown in Fig. 4.27.

Because the HECKLE simulations use quantities normalized to arbitrary B_0 and N_0 , one has to choose values for them in order to have physical units. For the proton radiography, these values were set as 2 MG and 10^{20} cm^{-3} (giving a millimetric simulation box), typical values from FCI2 simulations. The HECKLE simulation assumes an invariance along the z axis (*i.e.* the protons' axis), hence we had to choose a typical thickness. Here it has been assumed in ILZ that the field is constant over a thickness $\delta_z = 50 \mu\text{m}$ (see the lineouts of the B-field along the axial direction Oz in Fig. 3.3, on page 110 from FCI2). Therefore, because the integrated magnetic field $\int B \cdot dz$ is a rough estimate (yet representative of FCI2 simulations), the energy of the probing protons corresponding to the experimental results displayed here may not be accurate in the simulation. Hence, Fig. 4.25 shows post-processed proton radiography for three different proton energies (5, 10 and 20 MeV).

Fig. 4.25 and Fig. 4.27 display results at four characteristic times:

1. the initial time of the simulation: “initial time”.
2. The beginning of the reconnection: “start of reconnection”.
3. When half of the magnetic flux has reconnected: “during reconnection”.
4. When all of the magnetic flux has reconnected: “end of reconnection”.

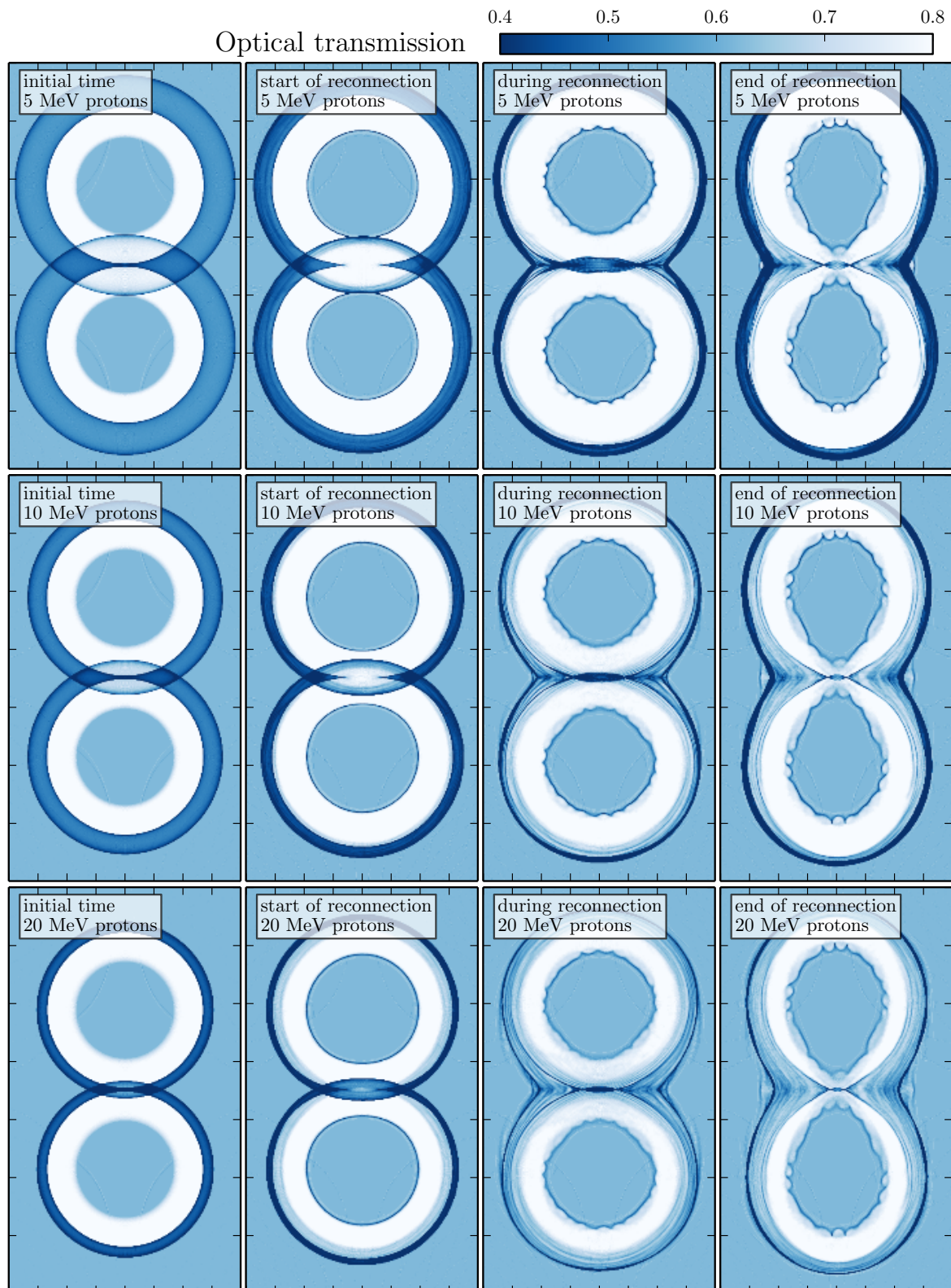


Figure 4.25: Post-processing of the non-periodic, co-planar, Heckle simulation using the code ILZ. B_0 is set to 2 MG and the field is supposed constant over a thickness $\delta_z = 50 \mu\text{m}$. From left to right: different times during the Heckle simulation. From top to bottom: different probing proton energies.

The physical times are: 0.0 ns, 0.4 ns, 1.5 ns and 2.3 ns



Figure 4.26: Post-processing of the non-periodic, co-planar, Heckle simulation using the code ILZ. B_0 is set to 2 MG and the field is supposed constant over a thickness $\delta_z = 50 \mu\text{m}$. From left to right: different times during the Heckle simulation. From top to bottom: different probing proton energies.

The physical times are: 0.0 ns, 0.4 ns, 1.5 ns and 2.3 ns

Note that the results have been convolved by a Gaussian in order to mimic the effects of the scattering.

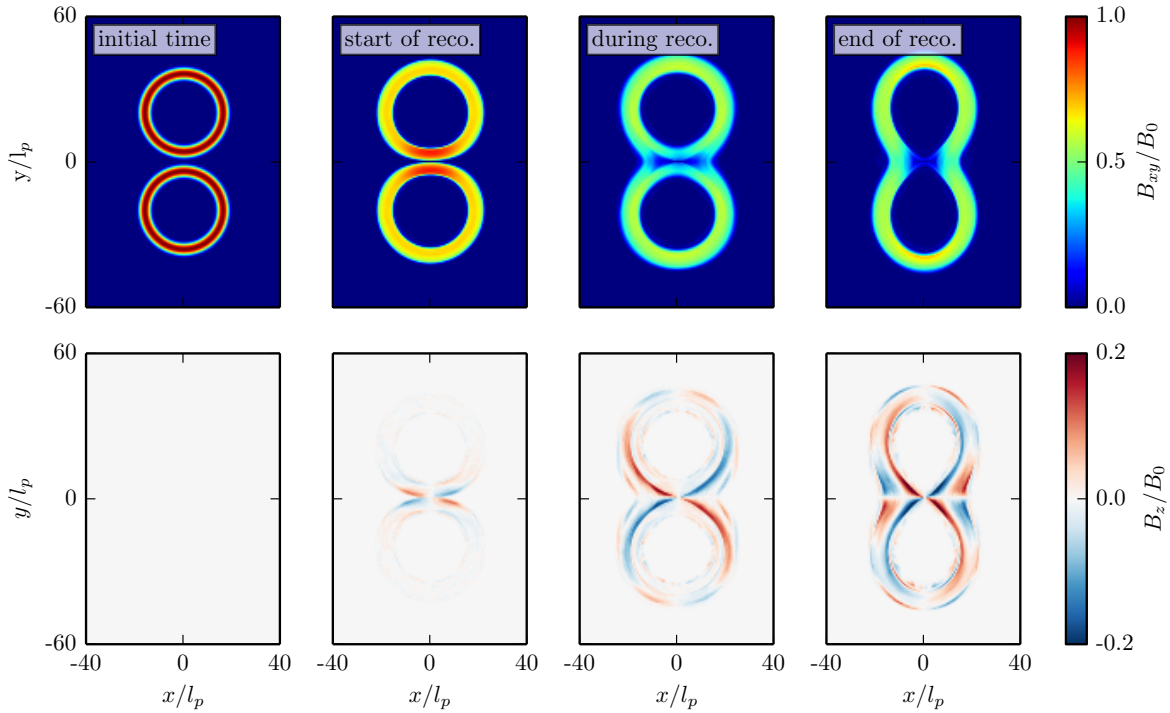


Figure 4.27: Color maps of the normalized magnetic field in the Heckle simulation corresponding to Fig. 4.25. Top row: in-plane magnetic field B_{xy}/B_0 (polarized clockwise). Bottom row: out-of-plane magnetic field B_z/B_0 .

Let us look at the patterns of the simulated proton radiographies and how they can be linked to the measurements, while keeping in mind that the ILZ results do not account for the scattering of the protons.

- At the initial time of the simulation, we have two independent circular loops of magnetic field next to each other. Hence, the proton radiography shows just a superposition of two rings of proton accumulation. The energy of the probing protons makes the diameter and thickness of these dose accumulation rings vary. Depending on the distance between the two loops and the distance at which the protons are deflected, we can see that the superposition of the accumulation ring may look like a more or less intense line of high proton dose (*e.g.* see “initial time”, 10 and 20 MeV in Fig. 4.25). This would explain while with certain experimental measurements, a line of high proton dose is visible at 1 ns both for the co-planar and the anti-Hall geometries. This can be seen at 1 ns for both the co-planar and anti-Hall cases, and for both targets.
- At the start of the reconnection process, the magnetic field loops have been compressed onto each other by the plasma pressure, leading to a flux pile-up. The Hall quadrupolar out-of-plane magnetic field starts to grow, but no magnetic flux is reconnected yet. Because the magnetic fields are compressed on each other, in op-

position to the “initial time”, we can see that: *i*) the dose modulations do not have a ring shape anymore, they are “flattened” at the reconnection point, *ii*) there is still a superposition of two independent patterns, but the dose at the center of the overall structure is very low, the protons being compressed near the ‘outflow’ regions. This can be quite well seen in the anti-Hall case of the gold target, throughout the evolution from 2 to 4 ns.

- During the reconnection, the magnetic field lines are bent toward the dense part of the target due to the Hall effect (see the out-of-plane component in Fig. 4.27). Moreover, as the magnetic field lines “unfold” themselves there is an increase of the section of the flux tubes. The conjunction of these two effects results in a reduced in-plane magnetic field in the reconnection region, and hence a double "Y" shaped proton dose accumulation structure appears. This structure exhibits the significant difference, compared to the one characteristic of the start of the reconnection, that there is here an accumulation of protons at the center. This characteristic structure can be observed in the co-planar case of the gold target from 2 to 4 ns, as well as 2 ns for the co-planar case of the Al target and throughout the temporal evolution of the anti-Hall case of the same target. This notably implies that for the gold target, in the co-planar case, the reconnection starts very quickly, while it is strongly slowed down in the anti-Hall case (compare the top two rows of Fig. 4.23). It also implies that the reconnection is clearly not as delayed for Al compared to gold.
- At the end of the reconnection, some of the field lines are still unfolding. This leads to a pattern of proton dose showing a strong accumulation around both plasma plumes, and a small, weaker double “Y” shaped accumulation in the mid-plane compared to what can be observed during the reconnection. There is still an accumulation of protons at the center of the structure, but it is much weaker than during the reconnection. Such structure is consistent with what can be observed at 3 and 4 ns in the co-planar case of the Al target. Again, when compared to the measurements recorded for the gold target, it implies that the reconnection takes place faster in the case of the Al target.

To summarize this interpretation, based on a simulation with simplified conditions (simple initial density, velocity and magnetic field profiles, no laser deposition and isothermal electrons, hence no Nernst effect, no continuous source of field), our preliminary conclusions are the following.

For the gold co-planar case, the reconnection started at an unidentified time and is still ongoing at the end of the laser pulses: at 4 ns, the observed structure is still consistent with what is simulated during the reconnection; the processus seems therefore here quite slow. For the gold anti-Hall, the structures bear a strong similarity with the ones observed in the simulation at the start of the reconnection; it seems therefore that the process has

been considerably slowed down compared to the co-planar case. For the aluminum case, whether in co-planar or anti-Hall configurations, the process seems much faster than in gold. In the co-planar case, at 3 and 4 ns, the structures tend toward the one observed at the end of the reconnection in the simulation, and in the anti-Hall case some reconnection seems to take place, while it was strongly slowed down for the gold target. One can also note that the structures seen in the pro-Hall configurations are also, although less clearly, consistent with the above stated picture: at 4 ns, in the gold case, one can observe a central accumulation of protons, and in the Al case a wide zone separating the two bubble-like structures, similarly the co-planar case at the same time.

Hence, the conclusions are that: *i)* the reconnection rate is higher with the low Z target compared to the high Z one. *ii)* The anti-Hall geometry of the target does delay the reconnection or reduces its rate for the aluminum target, while for gold it prevents the reconnection.

4.3.4 LMJ-Petal

Before concluding this last chapter, we present here the design of a reconnection experiment planned to be conducted by our LPP-CEA-LULI collaboration at the LMJ-Petal laser facility in 2017, when four quads (*i.e.* nanosecond laser beams) will be available. The geometry of the planned experiment is illustrated in Fig. 4.28. Following the previous experiments, the main target will consist of a low or high Z foil, in either co-planar, anti-Hall or pro-Hall geometry.

In order to reduce the risks of damage to the optics, the available energy for the quads is limited. Fig. 3.24 on page 134 showed example of a Mylar and a gold target irradiated by a 15 kJ over 5 ns frequency tripled ($\lambda_L = 0.351 \mu m$) laser pulse representative of what is available for academic access. Note that one major advantages of such a large laser facility is that the focal spots are much smoother than the one employed for the experiments presented in this thesis, thanks to a larger number of speckles in the focal spots, associated with temporal smoothing methods such as SSD [149]. The proton radiography will be performed using the Petal laser (a kJ, PetaWatt class laser) and CRACC, its RCF pack diagnostic.

Using the capability of the facility to electronically delay each quad individually will allow to maximize the results per shots. For example it is planned to use the first shot to reproduce the results of the JLF-Titan with higher energy and large focal spot. For this, two quads will irradiate a low Z target with different timing and a large enough separation to ensure the independence of the two plasmas. The same goes with the two remaining quads on a high Z target. Placing the proton target far enough from the main one, such as to have all four interaction regions within the proton beam, will then allow

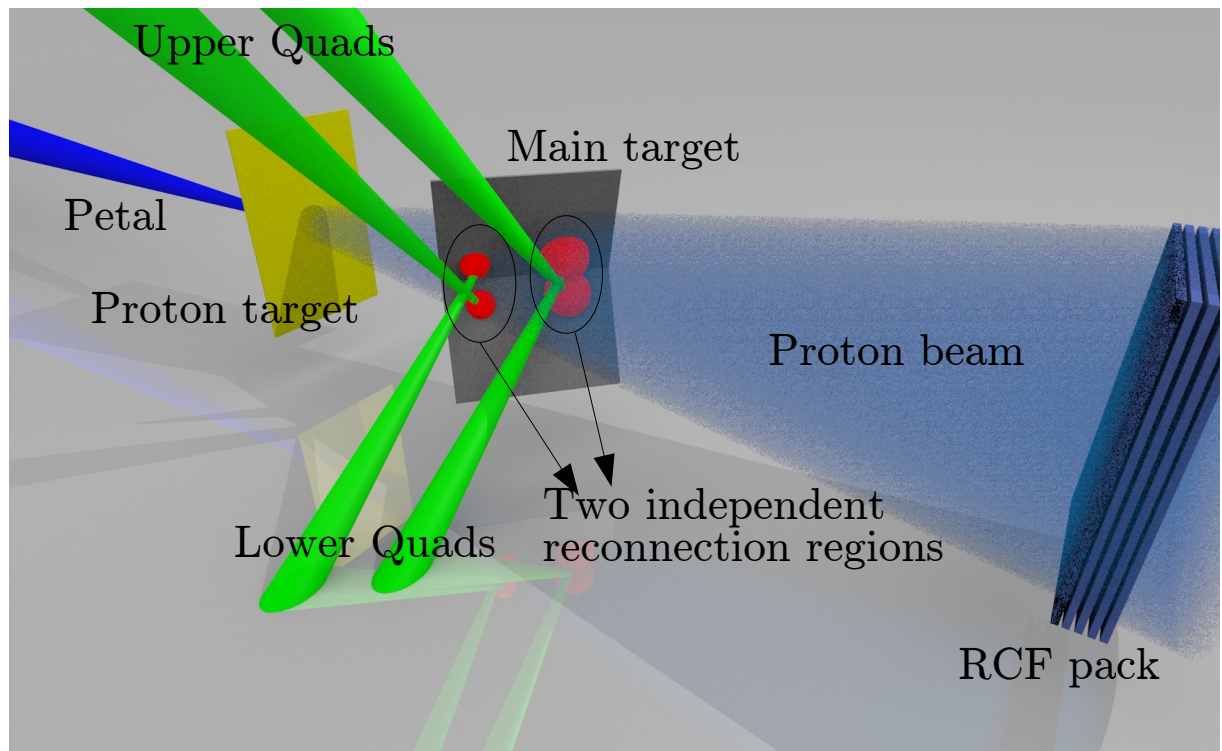


Figure 4.28: *Visualization of the LMJ-Petal experiment.*

to perform proton radiography at two times for both low and high Z targets in a single shot. For reconnection measurements, having two separated interaction regions will allow to perform measurements at two times in the plasmas' evolution per shot.

4.4 Conclusions

In the previous chapters, the magnetic field influence over the hydrodynamics was mostly limited to the electron transport through their magnetization, with minimal effect on the fluid from the overall energy balance and momentum equation. Yet, in this last chapter aiming at the study of the reconnection of the magnetic field, the coupling between the field and the fluid is much more important and the study of the reconnection uses most of the time a magneto-hydrodynamic (MHD) formalism.

Therefore, after briefly explaining why the reconnection of the magnetic field is of importance in the framework of inertial confinement fusion, we recalled the consequences of the ideal MHD, *i.e.* an infinitely conductive plasma. These are the Alfvén theorems: the *conservation of the magnetic flux* and the *field frozen in fluid*, allowing to introduce the concept of *magnetic field lines*.

Following, a state of the art of magnetic reconnection has been presented. First, the mechanism of the reconnection has been explained, as well as the transfer of energy from the field to the plasma through the strong Laplace (Lorentz) force due to the highly bent reconnecting magnetic field lines. Next, a simple analytical model of the reconnection has been detailed: the Sweet-Parker model. It relies on the hypothesis of ideal-MHD and homogeneous anti-parallel magnetic fluxes, advected toward each other by the fluid at a characteristic velocity. By conservation of the mass between the inflow and the outflow at the Alfvén velocity, one can estimate a reconnection time, function of the Lundquist number and a characteristic scale length. In our laser-generated plasmas, the reconnection would then be a nanosecond process.

In the rest of this state of the art, we presented different contexts in which the reconnection has been extensively studied: solar physics (heating of the corona and coronal mass ejections) and space physics (reconnection of the Earth magneto-sphere with the interplanetary magnetic field). In the continuity, different methods to study the reconnection have been listed: x-ray observations of the sun, orbiting satellites from the magneto-sphere, plasma merging in spheromaks and the MRX, a device dedicated to the study of the driven reconnection in a discharge plasma. This part ended with a short review of the reconnection experiments in high-power laser generated plasmas and their associated azimuthal magnetic field.

The second section was dedicated to the numerical method used to interpret these kind of laser plasma reconnection experiments. It started with a list of the different types of code used and their main results. Using a kinetic code (IMPACTA) Joglekar *et al.* [143] showed the importance of the Nernst effect, as a drive to the reconnection, while Fox *et al.* [145, 146, 142] used a PIC code (PSC) to interpret the Rutherford and Omega experiments. This lead us to the hybrid code HECKLE, that was used to design and interpret our experiments.

In specifics, we presented the study that motivated our non-planar experiments. Indeed, the out-of-plane “Hall” magnetic field was traditionally viewed as a consequence of the reconnection, based on PIC simulations, while in a MHD framework it may be explained by the formation of a current sheet, this latter being also the cause of the reconnection process. Indeed, the hybrid simulations showed that adding an angle between the magnetic loops such as to form an “anti-Hall” out-of-plane field, prior to the reconnection, delays the beginning of the reconnection and reduces its rate.

In the last section, the experiments performed during this thesis were presented, followed by a preliminary interpretation using a post-processed HECKLE simulation. The first experiment has been conducted on Phelix, at GSI with planar Mylar foil and laser pulses of moderate energy and duration. The proton radiography showed no variation in the dose pattern, all along the time the field remained compressed onto the foil by the laser driven heat-flux. Hence, for the second experiment, on LULI2000, the laser pulse duration has been increased. Moreover, more energy was available and non planar aluminum and gold foils were used. Proton radiography measurements have been performed for both materials at different times, for planar, “anti-Hall” and “pro-Hall” geometry. In order to interpret the results, a Heckle simulation has been post-processed with ILZ such as to simulate the proton radiography. This allowed to link each moment of the reconnection with a different pattern of proton dose modulation. From this, we concluded that: *i)* the reconnection is faster with the aluminum target than with the gold one, *ii)* in the “anti-Hall” geometry, the reconnection rate is indeed smaller.

Finally, we presented an accepted LMJ-Petal experiment, in which we will benefit from long laser pulse to drive the plasma and keep the field compressed and smooth focal spots which should minimize the turbulent pattern seen in the proton dose for low Z shots on LULI2000.

Conclusion

In this thesis, we performed a study of the mechanisms of self-generation, transport and reconnection of the magnetic field during a high-power laser ($I \sim 10^{14} \text{ W/cm}^2$) – foil interaction. To do so, we both performed and/or analyzed experiments and used numerical tools to interpret these results.

We started by presenting the framework of this study, namely the motivation to better understand the interaction of the multiple high-power lasers with the inner wall of the hohlraum in indirect drive inertial confinement fusion. This is the method for ICF studied at CEA-DAM (in France with LMJ) and at the Lawrence Livermore National Laboratory (in the United-States with the NIF).

Because the magnetic field may significantly affect the heat-flux, the first chapter was dedicated to the description of different models of electron transport. We started by a brief presentation of the physics of laser – foil interaction and introduced FCI2, the hydro-radiative code used at CEA to design and interpret laser experiments, including ICF. Then, in order to introduce the non-local with magnetic field electron transport model of FCI2, we presented the different simpler models. First, the Spitzer-Härm one, which allows to treat the diffusion of heat for a non-magnetized “equilibrated” electron (or ion) population. Nonetheless, as any diffusive process, this model requires a limitation. Even more for the simulation of high power laser experiments, for which it has to be limited to a fraction of the “free streaming” flux. Next was the Braginskii model which, just like the linear Spitzer-Härm model, is based on the calculation of diffusion coefficients, yet this time accounting for a magnetization of the electron population. Hence while including more physics, it suffers from the same limitation as all the “grey” diffusion models: it assumes an equilibrated population. To overcome this need for an arbitrary “knob” in the simulation (namely the value of flux limiter), a “non-local” electron transport model, based on a multi-group diffusion, was previously developed at CEA. We thus described it, and how it accounts for the effects of the magnetic field. Nonetheless, as shown in this thesis, this coupling may be done through different methods. Hence, we performed comparisons of two methods (“NLSH” and “NLBR”) with a kinetic code (ALADIN), using a simplified test case, without hydrodynamics (Epperlein’s test). From this, it appeared that the NLSH model was the best at reproducing the kinetic code’s results.

Because these comparisons have been performed in a simple case, experiments still remain

of first importance to validate our model. In order to do so, we presented the results of an experiment performed at JLF-Titan, before this thesis, side by side with the post-processed results of FCI2 simulations corresponding to each shot. The comparison of electron density measurements remained unfruitful. Yet, it has been reminded that both the diagnostic and the simulation have different validity domains, whose overlap was very limited. The polarimetry measurement showed that no magnetic field could be measured within the low density part of the plasma, in agreements with the post-processed result, showing a significant rotation of the polarization only in the dense part of the plasma.

Much attention was spent on the proton radiography diagnostic. After presenting the two methods used to generate the MeV protons (imploded backlighter on Omega, and the TNSA with short pulse laser in our case), we performed a sensitivity study of the diagnostic using ILZ, an ion trajectography code, and simple magnetic field topologies. It showed that the variations of proton dose depend on the radial variations of the magnetic field, and that for a thin enough disk of magnetic field, the dose modulations are function of the magnetic field integrated along the proton direction, $\int B.dz$. Following, we continued this study by comparing the results of different post-processed FCI2 simulations. It showed that for protons' energies higher than 10 MeV, the results do not vary significantly, including the case where the laser energy is varied. We showed that while changing the shape of the focal may affect the result, the diagnostic may not be able to discriminate too small variations (such as flat-top or super-Gaussian). Finally, this study showed the importance of the scattering when using proton radiography to probe solid targets. As such, we defined the uncertainty on the measurement as a function of the scattering. Finally, the results of proton radiography exhibit a pattern of dose variation showing a ring of accumulation. Hence, in order to compare the post-processed and measured results as a function of time, we plotted the radius of the accumulation ring as a function of time, for both targets (low and high Z) and both the measurements and the simulations. It showed that the post-processed FCI2 simulations, using the NLSH model, were able to reproduce the measurement, all along the laser irradiation of the target.

The second chapter concluded with the comparison of a proton radiography result from a previous LULI2000 experiments, with post-processed FCI2 simulations with the different models presented before. It showed an excellent agreement when using the NLSH model, giving us confidence in the choice of this model for further interpretations.

From this we used, in the third chapter, FCI2 simulations with the NLSH electron conduction model to explain the mechanisms at play in the source and transport of the magnetic field, along with the effect of the field on the interaction. Firstly, we showed that our FCI2 simulation gave topologies of magnetic field very different from those from Lasnex, that have been previously published. While in these publications, the Lasnex simulations presented a shell-like shape of magnetic field around the plasma bubble, FCI2 presents a disk-like shape of magnetic field, compressed onto the target.

In order to explain it, we showed that the magnetic field is mostly generated near the electron ablation front, where the gradients of electron density and temperature are the strongest. Next, because of the heat flux, the field becomes trapped between two walls: the solid target and the electron ablation front. Hence, the thicker field for a high Z target is naturally explained by the double ablation fronts due to the radiation ablation. Moreover, we showed that in this kind of interaction, different transport regimes are present: advection of the field by the electron population, diffusion of the ablated plasma through the accumulated field and, ultimately, diffusion of the field through the dense part of the plasma. This pinpointed the need for a code accounting for the diffusion of the field, and with an accurate heat flux model, for a correct advection of the magnetic field.

Following, in order to make sure that the discrepancies between our topology and Lasnex's one were not due to peculiar conditions in which each code is run, we performed a study in which the laser parameters were changed. We showed that, for both low and high Z targets, changing the energy, the focal spot or the laser wavelength did not change the overall disk-like shape of the magnetic field. This conclusion holds for simulations of the irradiation of a foil by a laser pulse representative of a LMJ quad.

In the rest of this chapter, we showed the influence of the magnetic field on the interaction from three points of view: the electrons (heat flux), the ions (hydrodynamics) and the energy balance. From this study it appeared that, in a significant part of the plasma, the electrons are weakly magnetized. The effects of this are easily readable with the Braginskii model ("grey" diffusion): the larger the magnetization, the more the heat is rotated and inhibited. Yet, because of the multi-group form of the non-local model, the effects of the field are much less easy to explain, as it may lead to a relocalization of the heat flux. From the point of view of the hydrodynamics, we showed that despite beta parameters close to unity, the Laplace (Lorentz) force remained negligible. Nonetheless, note that we still account for it in the simulations. Finally, it appeared that the magnetic field represented only a very small fraction of the total system energy (less than a percent). Yet, we showed that the typical dissipation time of the field, through resistive effect, was low compared to the hydrodynamic time scale. As such, it means that the growth of the field results from a competition between the thermo-electric sources and Joule dissipations.

In the last chapter, we studied the reconnection of the magnetic field between two neighboring plasma plumes and their associated magnetic field loops. We started by introducing the concept of magnetic reconnection, as it relies on the MHD framework, which is not often used in laser plasma studies. We presented the simple Sweet-Parker model, which despite its strong assumptions, allows to give an upper limit for the reconnection time. In the case of laser generated plasmas, it has been estimated to be on the nanosecond time scale. We followed with a state of the art of the magnetic reconnection, as it has been mostly studied in astro and space physics. This part has been completed with a review

of the different experimental platforms aiming at the study of magnetic reconnection. In particular, we presented the different results that can be found in the literature: the Omega and Rutherford experiments.

This led us to the different types of code that have been used to interpret these experiments. From this we summarized the study that has been conducted with the Heckle code, showing the importance of an initial angle between the reconnecting magnetic field loops. Indeed, it showed that a “Hall” quadrupolar out-of-plane magnetic field forms prior to the reconnection. If, because of the angle, an anti-Hall magnetic field is present (out-of-plane B-field of opposite polarization), it could delay the reconnection and reduce its rate.

In order to test this numerical result, we have carried two experiments. The first one has been performed with co-planar targets at the Phelix laser facility. It showed that the reconnection does indeed occur over a nanosecond time scale, as no change in the proton dose pattern has been observed during the 1.8 ns laser irradiation. As a consequence, during the following LULI2000 experiment, 4 ns laser pulses have been used, along co-planar but also “pro-Hall” and “anti-Hall” target geometries. This experiment has been interpreted with a post-processed Heckle simulation. From this, our preliminary interpretation is that the reconnection was faster with the aluminum targets and that, with “anti-Hall” bended targets, the reconnection rate was smaller, as predicted by the Heckle simulations.

Perspectives

Proton radiography has proven to be a difficult diagnostic because of the integrated measurement. Yet, because of its unique ability to probe electro-magnetic fields deep within solid targets, it is *de facto* the best diagnostic for the study of electro-magnetic fields in laser–solid interaction. Moreover, many nanosecond laser facilities now provide at least a short pulse laser, allowing to use this diagnostic without too much constrains. Therefore, as presented at the end of the fourth chapter, our team will conduct an experiment on LMJ-Petal. This will allow to complete the validation of the FCI2’s non-local with B-field model, with laser parameters of interest for ICF. The same holds for the reconnection study. Moreover, because of the larger focal spots, the speckle statistics should be better, which along with the smoothing methods should reduce the turbulent background seen on aluminum targets. Finally, still in context of the validation of the non-local model, the kinetic code ALADIN now includes hydrodynamics. Further comparisons will thus be performed, but this time accounting for the plasma’s expansion.

Bibliography

- [1] S. Atzeni and J. Meyer-ter Vehn, *The Physics of Inertial Fusion: Beam-Plasma Interaction, Hydrodynamics, Hot Dense Matter.*, Vol. 125 (Oxford University Press, 2004).
- [2] R. P. Drake, *High-energy-density physics: fundamentals, inertial fusion, and experimental astrophysics* (Springer Science & Business Media, 2006).
- [3] B. Remington, R. Drake, and D. Ryutov, *Reviews of Modern Physics* **78**, 755 (2006).
- [4] J.-M. Rax, *Physique des tokamaks* (Editions Ecole Polytechnique, 2011).
- [5] M. D. Rosen, *Physics of Plasmas* **6** (1999).
- [6] P. Gauthier, F. Chaland, and L. Masse, *Physical Review E* **70**, 055401 (2004).
- [7] E. L. Dewald, M. Rosen, S. H. Glenzer, L. J. Suter, F. Girard, J. P. Jadaud, J. Schein, C. Constantin, F. Wagon, G. Huser, P. Neumayer, and O. L. Landen, *Physics of Plasmas* **15**, 072706 (2008).
- [8] M. Vandenboomgaerde, J. Bastian, A. Casner, D. Galmiche, J.-P. Jadaud, S. Laffite, S. Liberatore, G. Malinie, and F. Philippe, *Physical Review Letters* **99**, 065004 (2007).
- [9] O. Hurricane, D. Callahan, D. Casey, P. Celliers, C. Cerjan, E. Dewald, T. Dittrich, T. Döppner, D. Hinkel, L. B. Hopkins, *et al.*, *Nature* **506**, 343 (2014).
- [10] J. Lindl, *Physics of Plasmas* **2**, 3933 (1995).
- [11] G. Zimmermann and W. Kruer, *Comments on Plasma Physics and Controlled Fusion* **2**, 51 (1975).
- [12] D. S. Clark, M. M. Marinak, C. R. Weber, D. C. Eder, S. W. Haan, B. A. Hammel, D. E. Hinkel, O. S. Jones, J. L. Milovich, P. K. Patel, H. F. Robey, J. D. Salmonson, S. M. Sepke, and C. A. Thomas, *Physics of Plasmas* **22**, 022703 (2015).
- [13] L. Biermann and A. Schlüter, *Physical Review* **82**, 863 (1951).
- [14] T. H. Kho and M. G. Haines, *Physical Review Letters* **55**, 825 (1985).
- [15] A. Nishiguchi, T. Yabe, M. Haines, M. Psimopoulos, and H. Takewaki, *Physical Review Letters* **53**, 262 (1984).

- [16] D. Froula, J. Ross, L. Divol, N. Meezan, A. MacKinnon, R. Wallace, and S. Glenzer, *Physics of Plasmas* **13**, 052704 (2006).
- [17] P. Holstein, D. Babonneau, C. Bowen, F. Chaland, C. Cherfils, E. Dattolo, S. Depierreux, D. Galmiche, P. Gauthier, J. Giorla, *et al.*, *Nuclear fusion* **44**, S177 (2004).
- [18] M. Yamada, R. Kulsrud, and H. Ji, *Reviews of Modern Physics* **82**, 603 (2010).
- [19] L. Spitzer Jr and R. Härm, *Physical Review* **89**, 977 (1953).
- [20] S. I. Braginskii, *Transport Properties in a Plasma* (Review of Plasma Physics, Consultants Bureau, vol. 1, pp. 205-311, 1965).
- [21] J. F. Luciani, P. Mora, and J. Virmont, *Physical Review Letters* **51**, 1664 (1983).
- [22] G. P. Schurtz, P. D. Nicolai, and M. Busquet, *Physics of Plasmas* **7**, 4238 (2000).
- [23] M. Borghesi, D. H. Campbell, A. Schiavi, O. Willi, A. J. Mackinnon, D. Hicks, P. Patel, L. A. Gizzi, M. Galimberti, and R. J. Clarke, *Laser and Particle Beams* **20**, 269 (2002).
- [24] R. Smets, N. Aunai, G. Belmont, C. Boniface, and J. Fuchs, *Physics of Plasmas* **21**, 062111 (2014).
- [25] S. Atzeni, *Plasma Physics and Controlled Fusion* **27**, 1535 (1987).
- [26] J. J. Duderstadt and G. A. Moses, *Inertial Confinement Fusion* (John Wiley & sons, 1982).
- [27] A. Decoster, "Formation code hydrodynamique laser," Tech. Rep. (CEA, 2008).
- [28] T. N'kaoua and R. Sentis, *Chocs* **3**, 25 (1991).
- [29] M. Busquet, *Physics of Fluids B* **5**, 4191 (1993).
- [30] R. F. Schmalz, J. Meyer-ter Vehn, and R. Ramis, *Physical Review A* **34**, 2177 (1986).
- [31] Y. Saillard, P. Arnault, and V. Silvert, *Physics of Plasmas* **17**, 123302 (2010).
- [32] J. Sanz, R. Betti, V. A. Smalyuk, M. Olazabal-Loume, V. Brean, V. Tikhonchuk, X. Ribeyre, and J. Feugeas, *Physics of Plasmas* **16**, 082704 (2009).
- [33] T. W. Johnston, *Physical Review* **120**, 1103 (1960).
- [34] R. Kingham and A. Bell, *Journal of Computational Physics* **194**, 1 (2004).
- [35] I. Shkarofsky, T. Johnston, and M. Bachyinski, *The particle kinetics of plasmas*. (Addison-Wesley, 1966).
- [36] A. Decoster, B. Perthame, and P. Marcowich, *modeling of collisions*. (Series in applied Mathematics, 1988).

-
- [37] R. J. Goldston and P. H. Rutherford, *Introduction to plasma physics* (CRC Press, 1995).
- [38] M. N. Rosenbluth, W. M. MacDonald, and D. L. Judd, *Physical Review* **107**, 1 (1957).
- [39] P. Nicolai, M. Vandenboomgaerde, B. Canaud, and F. Chaigneau, *Physics of Plasmas* **7**, 4250 (2000).
- [40] D. Gray, J. Kilkenny, M. White, P. Blyth, and D. Hull, *Physical Review Letters* **39**, 1270 (1977).
- [41] D. Shvarts, J. Delettrez, R. McCrory, and C. Verdon, *Physical Review Letters* **47**, 247 (1981).
- [42] R. Fabbro, E. Fabre, F. Amiranoff, C. Garban-Labaune, J. Virmont, M. Weinfeld, and C. Max, *Physical Review A* **26**, 2289 (1982).
- [43] T. G. Cowling, *Proc. R. Soc. London Sec. A* **183**, 453 (1945).
- [44] I. P. Shkarofsky, *Can. J. Phys* **39**, 1619 (1961).
- [45] E. M. Epperlein and M. G. Haines, *Physics of Fluids* **29**, 1029 (1986).
- [46] W. Hubbard, *Astrophys. J.* **146**, 858 (1966).
- [47] Y. T. Lee and R. M. More, *Physics of Fluids* **27**, 1273 (1984).
- [48] P. Mellor, Tech. Rep. (CEA, 2005).
- [49] J.-M. Rax, *Physique des plasmas* (Dunod, 2005).
- [50] J. F. Luciani, P. Mora, and R. Pellat, *Physics of Fluids* **28**, 835 (1985).
- [51] J. R. Albritton, E. A. Williams, I. B. Bernstein, and K. P. Swartz, *Physical Review Letters* **57**, 1887 (1986).
- [52] E. M. Epperlein and R. W. Short, *Physics of Fluids B* **3**, 3092 (1991).
- [53] A. V. Brantov, V. Y. Bychenkov, V. T. Tikhonchuk, and W. Rozmus, *Physics of Plasmas* **5**, 2742 (1998).
- [54] J.-L. Feugeas, P. Nicolai, X. Ribeyre, G. Schurtz, V. Tikhonchuk, and M. Grech, *Physics of Plasmas* **15**, 062701 (2008).
- [55] A. Marocchino, M. Tzoufras, S. Atzeni, A. Schiavi, D. Nicolai, Ph. J. Mallet, V. Tikhonchuk, and J.-L. Feugeas, *Physics of Plasmas* **20**, 022702 (2013).
- [56] D. Del Sorbo, J.-L. Feugeas, D. Nicolai, Ph. M. Olazabal-Loumé, B. Dubroca, S. Guisset, M. Touati, and V. Tikhonchuk, *Physics of Plasmas* **22**, 082706 (2015).
- [57] P. L. Bhatnagar, E. P. Gross, and M. Krook, *Physical Review* **94**, 511 (1954).
- [58] C. Boniface, K.-C. Le Thanh, and P. Mellor, Tech. Rep. (CEA, 2012).

- [59] P. D. Nicolai, J.-L. A. Feugeas, and G. P. Schurtz, *Physics of Plasmas* **13**, 032701 (2006).
- [60] L. Lancia, B. Albertazzi, C. Boniface, A. Grisollet, R. Riquier, F. Chaland, K.-C. Le Thanh, P. Mellor, P. Antici, S. Buffechoux, S. N. Chen, D. Doria, M. Nakatsutsumi, C. Peth, M. Swantusch, M. Stardubtsev, L. Palumbo, M. Borghesi, O. Willi, H. Pépin, and J. Fuchs, *Physical Review Letters* **113**, 235001 (2014).
- [61] R. Kingham and A. Bell, *Journal of Computational Physics* **194**, 1 (2004).
- [62] A. B. Langdon, *Physical Review Letters* **44**, 575 (1980).
- [63] E. Epperlein, G. Rickard, and A. Bell, *Physical review letters* **61**, 2453 (1988).
- [64] V. V. Korobkin and R. V. Serov, *ZhETF Pis'ma* **4**, 103 (1966).
- [65] I. H. Hutchinson, *Principles of plasma diagnostics* (Cambridge university press, 2005).
- [66] G. A. Askar'yan, M. S. Rabinovich, A. D. Smirnova, and V. B. Studenov, *ZhETF Pis'ma* **5**, 116 (1967).
- [67] J. Stamper, K. Papadopoulos, R. Sudan, S. Dean, E. McLean, and J. Dawson, *Physical Review Letters* **26**, 1012 (1971).
- [68] A. Nishiguchi, T. Yabe, M. G. Haines, M. Psimopoulos, and H. Takewaki, *Physical Review Letters* **53**, 262 (1984).
- [69] A. Nishiguchi, T. Yabe, and M. G. Haines, *Physics of Fluids* **28**, 3683 (1985).
- [70] A. Nishiguchi and T. Yabe, *Journal of Computational Physics* **52**, 390 (1983).
- [71] S. C. Wilks, A. B. Langdon, T. E. Cowan, M. Roth, M. Singh, S. Hatchett, M. H. Key, D. Pennington, A. MacKinnon, and R. A. Snavely, *Physics of Plasmas* **8**, 542 (2001).
- [72] C. K. Li, F. H. Séguin, J. A. Frenje, J. R. Rygg, R. D. Petrasso, R. P. J. Town, P. A. Amendt, S. P. Hatchett, O. L. Landen, A. J. Mackinnon, P. K. Patel, V. A. Smalyuk, J. P. Knauer, T. C. Sangster, and C. Stoeckl, *Review of Scientific Instruments* **77**, 10E725 (2006).
- [73] C. A. Cecchetti, M. Borghesi, J. Fuchs, G. Schurtz, S. Kar, A. Macchi, L. Rognani, P. A. Wilson, P. Antici, R. Jung, J. Osterholtz, C. A. Pipahl, O. Willi, A. Schiavi, M. Notley, and D. Neely, *Physics of Plasmas* **16**, 043102 (2009).
- [74] J. A. Stamper and B. H. Ripin, *Physical Review Letters* **34**, 138 (1975).
- [75] M. Borghesi, A. MacKinnon, A. Bell, R. Gaillard, and O. Willi, *Physical Review Letters* **81**, 112 (1998).

-
- [76] C. K. Li, F. Séguin, J. Frenje, J. Rygg, R. Petrasso, R. Town, P. Amendt, S. Hatchett, O. Landen, A. Mackinnon, P. Patel, V. Smalyuk, T. Sangster, and J. Knauer, *Physical Review Letters* **97**, 135003 (2006).
- [77] C. K. Li, F. Séguin, J. Frenje, J. Rygg, R. Petrasso, R. Town, P. Amendt, S. Hatchett, O. Landen, A. Mackinnon, P. Patel, M. Tabak, J. Knauer, T. Sangster, and V. Smalyuk, *Physical Review Letters* **99**, 015001 (2007).
- [78] C. K. Li, F. Séguin, J. Rygg, J. Frenje, M. Manuel, R. Petrasso, R. Betti, J. Delettrez, J. Knauer, F. Marshall, D. Meyerhofer, D. Shvarts, V. Smalyuk, C. Stoeckl, O. Landen, R. P. Town, C. Back, and J. Kilkenny, *Physical Review Letters* **100**, 225001 (2008).
- [79] R. Petrasso, C. K. Li, F. Seguin, J. Rygg, J. Frenje, R. Betti, J. Knauer, D. Meyerhofer, P. Amendt, D. Froula, O. Landen, P. Patel, J. Ross, and R. Town, *Physical Review Letters* **103**, 085001 (2009).
- [80] C. K. Li, F. Séguin, J. Frenje, R. Petrasso, P. Amendt, R. Town, O. Landen, J. Rygg, R. Betti, J. Knauer, D. Meyerhofer, J. Soures, C. Back, J. Kilkenny, and A. Nikroo, *Physical Review Letters* **102**, 205001 (2009).
- [81] C. K. Li, F. H. Séguin, J. A. Frenje, M. Manuel, D. Casey, N. Sinenian, R. D. Petrasso, P. A. Amendt, O. L. Landen, J. R. Rygg, R. P. J. Town, R. Betti, J. Delettrez, J. P. Knauer, F. Marshall, D. D. Meyerhofer, T. C. Sangster, D. Shvarts, V. A. Smalyuk, J. M. Soures, C. A. Back, J. D. Kilkenny, and A. Nikroo, *Physics of Plasmas* **16**, 056304 (2009).
- [82] C. K. Li, F. H. Séguin, J. A. Frenje, M. Rosenberg, R. D. Petrasso, P. A. Amendt, J. A. Koch, O. L. Landen, H. S. Park, H. F. Robey, R. P. J. Town, A. Casner, F. Philippe, R. Betti, J. P. Knauer, D. D. Meyerhofer, C. A. Back, J. D. Kilkenny, and A. Nikroo, *Science* **327**, 1231 (2010).
- [83] C. K. Li, F. H. Séguin, J. A. Frenje, M. J. Rosenberg, H. G. Rinderknecht, A. B. Zylstra, R. D. Petrasso, P. A. Amendt, O. L. Landen, A. J. Mackinnon, R. P. J. Town, S. C. Wilks, R. Betti, D. D. Meyerhofer, J. M. Soures, J. Hund, J. D. Kilkenny, and A. Nikroo, *Physical Review Letters* **108**, 025001 (2012).
- [84] L. Romagnani, J. Fuchs, M. Borghesi, P. Antici, P. Audebert, F. Ceccherini, T. Cowan, T. Grismayer, S. Kar, A. Macchi, P. Mora, G. Pretzler, A. Schiavi, T. Toncian, and O. Willi, *Physical Review Letters* **95**, 195001 (2005).
- [85] S. H. Glenzer, W. E. Alley, K. G. Estabrook, J. S. D. Groot, M. G. Haines, J. H. Hammer, J. D. Moody, W. Rozmus, L. J. Suter, T. L. Weiland, and E. A. Williams, *Physics of Plasmas* **6**, 2117 (1999).
- [86] M. André, *Chocs* **1**, 19 (1991).

- [87] T. Massard and P. Mora, *2005–2014: 10 years of LIL/ILP open campaign* (Institut Lasers et Plasmas, 2014).
- [88] G. Schurtz, S. Gary, S. Hulin, C. Chenais-Popovics, J.-C. Gauthier, F. Thais, J. Breil, F. Durut, J.-L. Feugeas, P.-H. Maire, *et al.*, *Physical Review Letters* **98**, 095002 (2007).
- [89] L. Lancia, *Study of non-linear effects on laser propagation and electron transport in plasmas*, Ph.D. thesis, École Polytechnique and Università di Roma La Sapienza (2010).
- [90] L. Lancia, C. Fourment, J. Fuchs, J.-L. Feugeas, P. Nicolai, S. Bastiani-Ceccotti, M. Gauthier, S. Hulin, M. Nakatsutsumi, M. Rabec-Le-Gloahec, J. Santos, and G. Schurtz, *Laser and Particle Beams* **31**, 653 (2013).
- [91] B. Albertazzi, *Plasmas Lasers et Champs Magnétiques*, Ph.D. thesis, École Polytechnique and Université du Québec (2014).
- [92] T. Vinci and A. Flacco, <https://github.com/aflux/neutrino>.
- [93] A. C. Kak and M. Slaney, *Principles of computerized tomographic imaging* (Society for Industrial and Applied Mathematics, 2001).
- [94] E. Buresi, J. Coutant, R. Dautray, M. Decroisette, B. Duborgel, P. Guillaneux, J. Launspach, P. Nelson, C. Patou, J. M. Reisse, and J. P. Watteau, *Laser and Particle Beams* **4**, 531 (1986).
- [95] E. Clark, K. Krushelnick, M. Zepf, F. Beg, M. Tatarakis, A. Machacek, M. Santala, I. Watts, P. Norreys, and A. Dangor, *Physical Review Letters* **85**, 1654 (2000).
- [96] A. Maksimchuk, S. Gu, K. Flippo, D. Umstadter, and V. Y. Bychenkov, *Physical Review Letters* **84**, 4108 (2000).
- [97] R. Snavely, M. Key, S. Hatchett, T. Cowan, M. Roth, T. Phillips, M. Stoyer, E. Henry, T. Sangster, M. Singh, *et al.*, *Physical Review Letters* **85**, 2945 (2000).
- [98] A. J. Mackinnon, P. K. Patel, R. P. Town, M. J. Edwards, T. Phillips, S. C. Lerner, D. W. Price, D. Hicks, M. H. Key, S. Hatchett, S. C. Wilks, M. Borghesi, L. Romagnani, S. Kar, T. Toncian, G. Pretzler, O. Willi, M. Koenig, E. Martinolli, S. Lepape, A. Benuzzi-Mounaix, P. Audebert, J. C. Gauthier, J. King, R. Snavely, R. R. Freeman, and T. Boehlly, *Review of Scientific Instruments* **75**, 3531 (2004).
- [99] W. H. Bragg and R. Kleeman, *The London, Edinburgh, and Dublin Philosophical Magazine and Journal of Science* **8**, 726 (1904).
- [100] J. A. Frenje, C. K. Li, F. H. Séguin, D. G. Hicks, S. Kurebayashi, R. D. Petrasso, S. Roberts, V. Y. Glebov, D. D. Meyerhofer, T. C. Sangster, J. M. Soures, C. Stoeckl, C. Chiritescu, G. J. Schmid, and R. A. Lerche, *Review of Scientific Instruments* **73**, 2597 (2002).

-
- [101] N. Sinenian, M. J. Rosenberg, M. Manuel, S. C. McDuffee, D. T. Casey, A. B. Zylstra, H. G. Rinderknecht, M. Gatu Johnson, F. H. Séguin, J. A. Frenje, C. K. Li, and R. D. Petrasso, *Review of Scientific Instruments* **82**, 103303 (2011).
- [102] D. Strickland and G. Mourou, *Optics Communications* **55**, 447 (1985).
- [103] M. G. Haines, M. S. Wei, F. N. Beg, and R. B. Stephens, *Phys. Rev. Lett.* **102**, 045008 (2009).
- [104] S. C. Wilks, A. B. Langdon, T. E. Cowan, M. Roth, M. Singh, S. Hatchett, M. H. Key, D. Pennington, A. MacKinnon, and R. A. Snavely, *Physics of Plasmas* **8**, 542 (2001).
- [105] A. Mancic, J. Robiche, P. Antici, P. Audebert, C. Blancard, P. Combis, F. Dorchie, G. Faussurier, S. Fourmaux, M. Harmand, R. Kodama, L. Lancia, S. Mazevet, M. Nakatsutsumi, O. Peyrusse, V. Recoules, P. Renaudin, R. Shepherd, and J. Fuchs, *High Energy Density Physics* **6**, 21 (2010).
- [106] P. Bolton, M. Borghesi, C. Brenner, D. Carroll, C. D. Martinis, F. Fiorini, A. Flacco, V. Floquet, J. Fuchs, P. Gallegos, D. Giove, J. Green, S. Green, B. Jones, D. Kirby, P. McKenna, D. Neely, F. Nuesslin, R. Prasad, S. Reinhardt, M. Roth, U. Schramm, G. Scott, S. Ter-Avetisyan, M. Tolley, G. Turchetti, and J. Wilkens, *Physica Medica* **30**, 255 (2014).
- [107] D. S. Kershaw, “Computer simulation of superthermal transport for laser fusion,” Tech. Rep. (California Univ., Livermore (USA). Lawrence Livermore Lab, 1979).
- [108] R. Dautray and J.-P. Watteau, “Codes numériques en fci,” in *La fusion thermonucléaire inertielle par laser* (Eyrolles, 1993).
- [109] N. L. Kugland, D. D. Ryutov, C. Plechaty, J. S. Ross, and H.-S. Park, *Review of Scientific Instruments* **83**, 101301 (2012).
- [110] L. Gao, P. M. Nilson, I. V. Igumenshchev, M. G. Haines, D. H. Froula, R. Betti, and D. D. Meyerhofer, *Physical Review Letters* **114**, 215003 (2012).
- [111] F. Chaland, Tech. Rep. (CEA, 2013).
- [112] P. Antici, Ph.D. thesis, École Polytechnique (2007).
- [113] A. Ciardi, T. Vinci, J. Fuchs, B. Albertazzi, C. Riconda, H. Pépin, and O. Portugall, *Physical review letters* **110**, 025002 (2013).
- [114] B. Albertazzi, A. Ciardi, M. Nakatsutsumi, T. Vinci, J. Béard, R. Bonito, J. Billette, M. Borghesi, Z. Burkley, S. Chen, *et al.*, *Science* **346**, 325 (2014).
- [115] P. M. Nilson, L. Willingale, M. C. Kaluza, C. Kamperidis, S. Minardi, M. S. Wei, P. Fernandes, M. Notley, S. Bandyopadhyay, M. Sherlock, R. J. Kingham, M. Tatarakis, Z. Najmudin, W. Rozmus, R. G. Evans, M. G. Haines, A. E. Dangor, and K. Krushelnick, *Physical review letters* **97**, 255001 (2006).

- [116] P. M. Nilson, L. Willingale, M. C. Kaluza, C. Kamperidis, S. Minardi, M. S. Wei, P. Fernandes, M. Notley, S. Bandyopadhyay, M. Sherlock, R. J. Kingham, M. Tatarakis, Z. Najmudin, W. Rozmus, R. G. Evans, M. G. Haines, a. E. Dangor, and K. Krushelnick, *Physics of Plasmas* **15**, 092701 (2008).
- [117] N. A. Gross and W. J. Hughes, *Space Weather* **13**, 606 (2015).
- [118] R. Giovanelli, *Nature* **158**, 81 (1946).
- [119] J. Dungey, *The London, Edinburgh, and Dublin Philosophical Magazine and Journal of Science* **44**, 725 (1953).
- [120] H. Ji and W. Daughton, *Physics of Plasmas* **18**, 111207 (2011).
- [121] R. Samtaney, N. F. Loureiro, D. A. Uzdensky, A. A. Schekochihin, and S. C. Cowley, *Physical Review Letters* **103**, 105004 (2009).
- [122] N. F. Loureiro, A. A. Schekochihin, and S. C. Cowley, *Physics of Plasmas* **14**, 100703 (2007), <http://dx.doi.org/10.1063/1.2783986>.
- [123] P. A. Sweet, in *Electromagnetic phenomena in cosmical physics*, Vol. 6 (1958) p. 123.
- [124] E. N. Parker, *The Astrophysical Journal Supplement Series* **8**, 177 (1963).
- [125] H. Ji, M. Yamada, S. Hsu, R. Kulsrud, T. Carter, and S. Zaharia, *Physics of Plasmas* **6**, 1743 (1999).
- [126] M. Yamada, H. Ji, S. Hsu, T. Carter, R. Kulsrud, N. Bretz, F. Jobes, Y. Ono, and F. Perkins, *Physics of Plasmas* **4**, 1936 (1997).
- [127] R. M. Close, C. E. Parnell, D. W. Longcope, and E. R. Priest, *The Astrophysical Journal Letters* **612**, L81 (2004).
- [128] K. C. Shibata, S. Masuda, M. Shimojo, H. Hara, T. Yokoyama, S. Tsuneta, T. Kosugi, and Y. Ogawara, *The Astrophysical Journal Letters* **451**, L83 (1995).
- [129] S. Masuda, T. Kosugi, H. Hara, S. Tsuneta, and Y. Ogawara, *Nature* **371**, 495 (1994).
- [130] M. G. Kivelson and C. T. Russell, *Introduction to space physics* (Cambridge university press, 1995).
- [131] J. W. Dungey, "Origins of the concept of reconnection and its application to the magnetopause: A historical view," in *Physics of the Magnetopause* (American Geophysical Union, 2013).
- [132] G. Frank, A, In: Neutral current layers in a plasma.(A75-22979 09-75) Moscow, Izdatel'stvo Nauka, 1974, p. 108-166. **1**, 108 (1974).
- [133] L. Stenzel, R and W. Gekelman, *Journal of Geophysical Research* **86**, 649 (1981).

-
- [134] L. Stenzel, R. W. Gekelman, and N. Wild, *Journal of Geophysical Research* **87**, 111 (1982).
- [135] M. Yamada, Y. Ono, A. Hayakawa, M. Katsurai, and F. W. Perkins, *Physical Review Letters* **65**, 721 (1990).
- [136] M. Yamada, F. Perkins, A. MacAulay, Y. Ono, and M. Katsurai, *Physics of Fluids B: Plasma Physics* **3**, 2379 (1991).
- [137] C. K. Li, F. Séguin, J. Frenje, J. Rygg, R. Petrasso, R. Town, O. Landen, J. Knauer, and V. Smalyuk, *Physical Review Letters* **99**, 055001 (2007).
- [138] M. J. Rosenberg, J. S. Ross, C. K. Li, R. P. J. Town, F. H. Séguin, J. A. Frenje, D. H. Froula, and R. D. Petrasso, *Physical Review E* **86**, 056407 (2012).
- [139] M. J. Rosenberg, C. K. Li, W. Fox, I. Igumenshchev, F. H. Séguin, R. P. J. Town, J. A. Frenje, C. Stoeckl, V. Glebov, and R. D. Petrasso, *Nature communications* **6** (2015), 10.1038/ncomms7190.
- [140] M. J. Rosenberg, C. K. Li, W. Fox, I. Igumenshchev, F. H. Séguin, R. P. J. Town, J. A. Frenje, C. Stoeckl, V. Glebov, and R. D. Petrasso, *Physics of Plasmas* **22**, 042703 (2015).
- [141] M. J. Rosenberg, C. K. Li, W. Fox, A. B. Zylstra, C. Stoeckl, F. H. Séguin, J. A. Frenje, and R. D. Petrasso, *Physical Review Letters* **114**, 205004 (2015).
- [142] G. Fiksel, W. Fox, A. Bhattacharjee, D. H. Barnak, P.-Y. Chang, K. Germaschewski, S. X. Hu, and P. M. Nilson, *Phys. Rev. Lett.* **113**, 105003 (2014).
- [143] A. S. Joglekar, A. G. R. Thomas, W. Fox, and A. Bhattacharjee, *Phys. Rev. Lett.* **112**, 105004 (2014).
- [144] A. G. R. Thomas, R. J. Kingham, and C. P. Ridgers, *New Journal of Physics* **11**, 033001.
- [145] W. Fox, A. Bhattacharjee, and K. Germaschewski, *Physical Review Letters* **106**, 215003 (2011).
- [146] W. Fox, A. Bhattacharjee, and K. Germaschewski, *Physics of Plasmas* **19**, 056309 (2012).
- [147] J. Birn, J. F. Drake, M. Shay, B. N. Rogers, R. E. Denton, M. Hesse, M. Kuznetsova, Z. W. Ma, A. Bhattacharjee, and A. Otto, *Journal of Geophysical Research* **106**, 3715 (2001).
- [148] P. L. Pritchett, *Journal of Geophysical Research* **106**, 3783 (2001).
- [149] S. Skupsky, R. Short, T. Kessler, R. Craxton, S. Letzring, and J. Soures, *Journal of Applied Physics* **66**, 3456 (1989).

List of Figures

0.1	<i>Energy variation in the hot-spot and position of the maximum reaction rate.</i>	5
0.2	<i>FCI2 simulation of an indirect drive ICF experiment.</i>	7
0.3	<i>Illustration of the self-generation of the magnetic field.</i>	8
0.4	<i>Illustration of the laser irradiation in a former LMJ design.</i>	8
1.1	<i>1D scheme of the irradiation of a solid foil by a nanosecond laser pulse.</i>	17
1.2	<i>FCI2 simulation (Mylar): Density and electron temperature.</i>	18
1.3	<i>FCI2 simulation (Mylar): Internal and kinetic energy density.</i>	19
1.4	<i>FCI2 simulation (Gold): Density and electron temperature.</i>	20
1.5	<i>FCI2 simulation (Gold): Internal and kinetic energy density.</i>	21
1.6	<i>Normalized differential heat flux $q(v)$ from (Eq. 1.20).</i>	24
1.7	<i>Sharp (solid) and harmonic (dashed) cut-off.</i>	25
1.8	<i>Braginskii's vectorial notations.</i>	27
1.9	<i>X_{\perp}, X_{\wedge} and $\sqrt{X_{\perp}^2 + X_{\wedge}^2}$ as a function of the magnetization.</i>	29
1.10	<i>Thermoelectric coefficients as a function of the magnetization.</i>	34
1.11	<i>LMV delocalization kernel</i>	35
1.12	<i>Lineout of $\ \mathbf{Q}_{NL}\ / \ \mathbf{Q}_{SH}\$.</i>	35
1.13	<i>Lineout of $f \simeq \ \mathbf{Q}_{z,NL}\ / \ \mathbf{Q}_{z,FS}\$.</i>	36
1.14	<i>Scheme of the coupling between the magnetic field and the heat flux</i>	36
1.15	<i>Scheme of the thermo-electric source of magnetic field</i>	37
1.16	<i>Spitzer-Härm and Fokker-Plank electric fields.</i>	39
1.17	<i>$(1 - a_1)$, a_2, $3\lambda_1/\lambda$ and $3\lambda_2/\lambda$ as a function of the Hall parameter</i>	41
1.18	<i>Target's density profile in Epperlein's test.</i>	46
1.19	<i>Laser intensity profile in Epperlein's test.</i>	46
1.20	<i>Magnetic field and electron temperature with ALADIN.</i>	47
1.21	<i>Magnetic field color maps with Nernst velocity vector plots.</i>	48
1.22	<i>Electron Temperature color maps with heat flux vector plots.</i>	49
1.23	<i>Lineouts of the Hall parameter.</i>	51
1.24	<i>Evolution over 100 ps of the magnetic field.</i>	52
1.25	<i>Electron temperature with different heat flux models in a hohlraum.</i>	55
2.1	<i>Scheme of the Korobkin and Stamper's experiments</i>	62
2.2	<i>Results from Nishiguchi et al.'s study.</i>	63

2.3	<i>Scheme of the experimental setup of the LULI2000 campaign (2008).</i>	65
2.4	<i>Visualization of the JLF-Titan campaign setup (2011).</i>	67
2.5	<i>Angular averaged of the JLF-Titan focal spot.</i>	68
2.6	<i>General scheme of a proton radiography experiment.</i>	69
2.7	<i>Scheme of the optical diagnostic line.</i>	70
2.8	<i>Abel transform.</i>	72
2.9	<i>Scheme of a Normarski interferometer.</i>	73
2.10	<i>Measured interferometry result.</i>	75
2.11	<i>Simulated interferometry result.</i>	76
2.12	<i>Knudsen number.</i>	77
2.13	<i>Measured polarimetry result.</i>	79
2.14	<i>Simulated polarization rotation.</i>	80
2.15	<i>Simulated polarimetry result.</i>	81
2.16	<i>Scheme of an X-ray pinhole.</i>	82
2.17	<i>Measured x-ray pinhole result.</i>	83
2.18	<i>Simulated x-ray pinhole result.</i>	84
2.19	<i>Scheme of backlighter capsule proton source.</i>	85
2.20	<i>Scheme of the proton radiography.</i>	86
2.21	<i>Magnetics field topologies used for tests</i>	88
2.22	<i>Case 1</i>	89
2.23	<i>Case 2</i>	89
2.24	<i>Case 3</i>	90
2.25	<i>Case 4</i>	91
2.26	<i>Synthetic transmission of an EBT type RCF</i>	92
2.27	<i>Effect of the scattering</i>	93
2.28	<i>Effect of the protons' energy</i>	94
2.29	<i>Effect of the laser's power</i>	95
2.30	<i>Effect of the laser's focal spot</i>	96
2.31	<i>Estimation the scattering.</i>	97
2.32	<i>Error bar of the proton radiography.</i>	97
2.33	<i>Radiochromic films</i>	98
2.34	<i>Modulation of the proton dose.</i>	99
2.35	<i>Radius of the accumulation ring over time.</i>	100
2.36	<i>Proton dose modulation from the LULI2000 experiment</i>	101
2.37	<i>FCI2 simulation of the LULI2000 experiment: B-field</i>	102
2.38	<i>FCI2 simulation of the LULI2000 experiment: Te</i>	103
3.1	<i>Magnetic field color map.</i>	108
3.2	<i>Scheme of the "waist" of the plasma plume.</i>	110
3.3	<i>Lineout of the magnetic field.</i>	110

3.4	<i>Magnetic field source color map.</i>	111
3.5	<i>Electron temperature color map.</i>	113
3.6	<i>Double ablation front.</i>	114
3.7	<i>Lineouts of $-U$, T_e, N_e, B (log).</i>	115
3.8	<i>Lineouts of β and R_m.</i>	116
3.9	<i>Laser variation : Reference case.</i>	117
3.10	<i>Laser variation : High energy case.</i>	118
3.11	<i>Laser variation : Flat-top case.</i>	119
3.12	<i>Laser variation : High intensity case.</i>	120
3.13	<i>Laser variation : 3ω case.</i>	121
3.14	<i>Hall parameter (magnetization).</i>	123
3.15	<i>Ratios Braginskii / Spitzer-Härm.</i>	124
3.16	<i>Ratios with / without B-field for non-local heat flux.</i>	125
3.17	<i>Thermal β parameter.</i>	127
3.18	<i>Kinetic β parameter.</i>	128
3.19	<i>Density map (Reference case).</i>	129
3.20	<i>Density map (Reconnection experiment).</i>	130
3.21	<i>Lineouts of χ, P and T_e (Reconnection experiment).</i>	130
3.22	<i>Energy balance.</i>	132
3.23	<i>Sources of internal energy.</i>	133
3.24	<i>Laser variation : LMJ case.</i>	134
3.25	<i>Sources of internal energy.</i>	136
4.1	<i>Illustration of the laser irradiation of a hohlraum</i>	139
4.2	<i>Scheme of two near-by irradiation spots on a solid target.</i>	140
4.3	<i>Scheme of the reconnection region.</i>	142
4.4	<i>Scheme of the Sweet-Parker model.</i>	143
4.5	<i>Image of the Sun in the XUV range.</i>	146
4.6	<i>Scheme of the coronal mass ejection model.</i>	147
4.7	<i>Scheme of the magnetosphere.</i>	148
4.8	<i>Stenzel and Gekelman's experiment</i>	149
4.9	<i>Cross section of the MRX</i>	151
4.10	<i>Scheme of the electro-magnetic fields and currents in the reconnection region.</i>	156
4.11	<i>Cartoon of the Heckle simulations' geometry</i>	158
4.12	<i>Heckle: initial profiles.</i>	159
4.13	<i>Co-planar case: $\ \mathbf{B}_z\$, $\ \mathbf{E}_{xy}\$ and j_z.</i>	159
4.14	<i>Reconnection rate with $\Psi = 24^\circ$.</i>	160
4.15	<i>Visualization of the reconnection experiments.</i>	161
4.16	<i>Photograph of the Phelix interaction chamber.</i>	162
4.17	<i>Phelix experiment: proton radiography.</i>	163

4.18	<i>FCI2 simulation, Phelix experiment.</i>	164
4.19	<i>Scheme of the North + North-bis configuration on the LULI2000.</i>	165
4.20	<i>Geometry of the pro- and anti-Hall targets during the LULI2000 campaign.</i>	165
4.21	<i>FCI2 simulation, LULI2000 experiment (gold).</i>	166
4.22	<i>FCI2 simulation, LULI2000 experiment (Aluminum).</i>	167
4.23	<i>LULI2000 experiment: proton radiography (gold).</i>	169
4.24	<i>LULI2000 experiment: proton radiography. (aluminum)</i>	170
4.25	<i>Post-processing of the Heckle simulation using the code ILZ.</i>	172
4.26	<i>Post-processing of the Heckle simulation, with scattering.</i>	173
4.27	<i>Magnetic field map from the Heckle simulation.</i>	174
4.28	<i>Visualization of the LMJ-Petal experiment.</i>	177

Role of the author

This thesis is the result of the collaboration between different groups, as it presents both experimental and numerical results. The CEA/DAM team brought its competence in hydro-radiative simulations, both for the numerical development and the use of the simulation for the design and interpretations of experiments. The LULI team brought its strong experience in management and experiments in “user” facilities such as LULI2000, JLF-Titan and Phelix. Finally, the LPP brought its competence in the reconnection of the magnetic field and its hybrid code.

Therefore, we will detail here the role of each and every one in the work presented in this thesis, such as to clarify the work of the author.

The original non-local model in FCI2 has been developed by G. Schurtz, P. Nicolai and M. Busquet. Latter on, the MHD has been included by P. Mellor. The ALADIN code has been developed by D. Deck and K.-C. Le Thanh. The validation of the “NLSH” non-local model, compared to the “NLBR” has been a shared work between A. Grisollet and the author: A. Grisollet ran the ALADIN simulations and the author participated to the discussions on which non-local models to compare (as the SNB “formalism” allows many ways to couple the heat-flux and the magnetic field) and the interpretation of the results.

The JLF-Titan experiment has been performed before this thesis, by J. Fuchs and B. Albertazzi (and others). The author analyzed the experimental results with B. Albertazzi and performed the post-processed results later on. The interferometry and polarimetry post-processors have been coded by the author, the proton-radiography post-processor embedded in FCI2 has been adapted by F. Chaland and the ILZ code has been developed by the author, such as to provide a simple and flexible tool (E, B or E+B fields, multiple geometries *etc.*). The sensitivity study of the proton radiography, performed with ILZ and FCI2’s post-processor has been performed by the author. The comparisons of the different models with the LULI2000 results involved the CEA-DAM and LULI teams, as well as L. Lancia who performed the experiment during her thesis.

The author ran the laser-foil FCI2 simulations presented in this thesis (450 simulations over 3 years) and, under the guidance of C. Boniface first and A. Grisollet then, improved the meshing, which proved to be of first importance for this kind of “brutal” interactions. The laser variation study, as well as the study of the effect of the field on the interaction

(chapter 3) has been performed by the author. Finally, the author wrote the many scripts used to produce the figures shown in this thesis, which are now used by other FCI2 users.

The original study with Heckle of the effect on the reconnection rate of an angle between the two magnetic loops has been conducted by R. Smets, who ran the Heckle simulations presented here. The design of the reconnection experiments presented here is the results of discussions between the CEA-DAM, LULI and LPP teams. These experiments have been conducted by J. Fuchs and the author (and others). The ILZ post-processing of the Heckle simulations, as well as the analysis and interpretation of these experimental results has been performed by the author.

The author was supervised in this work by J. Fuchs at LULI and by C. Boniface and A. Grisolle at CEA.

List of publications and presentations

Publications

- B. Albertazzi, A. Ciardi, M. Nakatsutsumi, T. Vinci, J. Béard, R. Bonito, J. Billette, M. Borghesi, Z. Burkley, S. N. Chen, T. E. Cowan, T. Herrmannsdorfer, D. P. Higginson, F. Kroll, S. A. Pikuz, K. Naughton, L. Romagnani, C. Riconda, G. Revet, R. Riquier, H.-P. Schlenvoigt, I. Yu. Skobelev, A.Ya. Faenov, A. Soloviev, M. Huarte- Espinosa, A. Frank, O. Portugall, H. Pépin, and J. Fuchs.
Laboratory formation of a scaled protostellar jet by coaligned poloidal magnetic field. Science **346**, 325 (2014).
- S. N. Chen, M. Gauthier, D. P. Higginson, S. Dorard, F. Mangia, R. Riquier, S. Atzeni, J.-R. Marquès, and J. Fuchs.
Monochromatic short pulse laser produced ion beam using a compact passive magnetic device. Review of Scientific Instruments **85**, 4 (2014).
- D.P. Higginson, Ph. Korneev, J. Béard, S.N. Chen, E. d’Humières, H. Pépin, S. Pikuz, B. Pollock, R. Riquier, V. Tikhonchuk, and J. Fuchs.
A novel platform to study magnetized high-velocity collisionless shocks. High Energy Density Physics **17**, 190 (2015)
- D. P. Higginson, G. Revet, B. Khair, J. Béard, M. Blecher, M. Borghesi, K. Burdonov, S. N. Chen, E. Filippov, D. Khaghani, K. Naughton, H. Pépin, S. Pikuz, C. Riconda, R. Riquier, S. N. Ryazantsev, A. Soloviev, I. Yu. Skobelev, M. Stardubtsev, T. Vinci, O. Willi, A. Ciardi, and J. Fuchs
Temporal stability and fidelity of astrophysically-relevant magnetically collimated jets in the laboratory. to be submitted to Physics of Plasmas.
- L. Lancia, B. Albertazzi, C. Boniface, A. Grisollet, R. Riquier, F. Chaland, K.-C. Le Thanh, Ph. Mellor, P. Antici, S. Buffechoux, S.N. Chen, D. Doria, M. Nakatsutsumi, C. Peth, M. Swantusch, M. Stardubtsev, L. Palumbo, M. Borghesi, O. Willi, H. Pépin, and J. Fuchs.
Topology of megagauss magnetic fields and of heat-carrying electrons produced in a high-power laser-solid interaction. Physical Review Letters **113**, 235001 (2014).
- A. Grisollet, R. Riquier, C. Boniface, K.-C. Le Thanh, F. Chaland, Ph. Mellor, L. Lancia, B. Albertazzi, H. Pépin, and J. Fuchs.

Modeling magnetic field growth, evolution and transport in high power laser-produced plasma. to be submitted to Physics of plasmas.

- R. Riquier, B. Albertazzi, A. Grisollet, C. Boniface, F. Chaland, L. Lancia, R. Smets, H. Pépin, and J. Fuchs.

Interplay between the self-generated magnetic-field and laser plasma hydrodynamic. to be submitted to Physics of plasmas.

Presentations

- LaB workshop, Princeton, 2015
- ToIFE workshop, Oxford, 2014
- Ion transport workshop, CEA-DAM, 2013

Posters

- ICHED, San-Diego, 2015
- NIF-JLF user meeting, Livermore, 2014 & 2015
- ECLIM, Paris, 2014
- SFP-Plasma, Toulouse, 2014
- Forum ILP, Orsière, 2014
- HEDP summer school, Ohio state univ., 2013
- SFP, Marseille, 2013
- Omega user meeting, Rochester, 2013

Remerciements

Une thèse ne pouvant se faire sans l'aide et le soutien d'un certain nombre de personnes, le temps est maintenant venu de les remercier.

Tout d'abord, je voudrais remercier ceux qui m'ont accueilli dans leurs unités respectives : François AMIRANOFF puis Patrick AUDEBERT pour le LULI, et Erik LEFEBVRE au CEA/DAM.

Bien entendu, un grand merci à mon directeur de thèse, Julien FUCHS, pour son énergie et pour m'avoir transmis ses compétences expérimentales. Merci également à mes encadrants au CEA : Claude BONIFACE pour sa passion et son enthousiasme, Alain GRISOLLET pour son savoir inépuisable sur les méthodes numériques.

Mes plus grands remerciements à mes rapporteurs, pour avoir envoyé leurs rapports dans un délai si bref ! Thank you Robert CAUBLE, grazie Stephano ATZENI.

Merci à tous ceux qui se sont impliqués dans ce projet et m'ont aidé à réaliser ce travail : Drew HIGGINSON lors des expériences, Roch SMETS pour la reconnexion, Fabrice CHALAND et Phillippe MELLOR pour les simus hydro-rad.

Merci à "l'élite à BIII" pour leur humour et pour leur aide pour les repét' de la soutenance : Pascal, Stéphane, Olivier, Laurent, Max, Marc, Laurent et Marion.

Merci aux équipes techniques du LULI, pour leur aide et leur bonne humeur, en particulier : Mathieu, Yohann, Fabien, Émilie, Olivier, Frédéric, Joanna, Edouard, Julie et Élodie

Il est temps d'attaquer la grande famille des doctorants du LULI. Pour commencer, merci à mes aîeux pour m'avoir montré l'exemple : Livia, Bruno, Maxence, Floriane, Clément et Vincent. Merci à mes contemporains : Adrien, Laura, Vincent, Kevin, Roman et Anaïs. Enfin, merci et bon courage aux "petits jeunes" : Claire, Maylis, Cédric, Alexandre, Thomas, Guilhem et Simon.

Pour en finir avec le LULI, Merci à Jean-Raph', Lorenzo et Frédéric.

Un grand merci aux doctorants du CEA : Lucile, Christelle, Tony, Nicolas, Guillaume, Clément, Sophie et bien sûr mes co-bureaux Alan, Thibaud et Alexis pour le soutien et les blagues.

Merci aussi aux amis du master : Alexandre, Andréa, Basil, Dimitri, Florian, Laura, Mai, Nicolas et Thibault.

Enfin, merci au coloc', Nicolas. Dommage qu'on ait raté nos soutenances respectives après un cursus universitaire de 8 ans en parallèle !

Et bien entendu, merci à mes parents et à ma sœur pour leur soutien.

page left blank

Titre : Champ magnétique dans les plasmas laser : transport électronique non-local et reconnexion

Mots clés : Fusion par confinement inertiel, FCI, plasmas à haute densité d'énergie, HEDP, laser, champs magnétiques, transport électronique, flux de chaleur, reconnexion.

Résumé : Dans le cadre de la fusion par confinement inertiel, une capsule contenant un combustible de deutérium-tritium est implorée soit par irradiation laser (attaque directe, interaction laser – cible de numéro atomique faible), soit par un rayonnement de corps noir émis par une cavité convertissant le rayonnement laser (attaque indirecte, interaction laser – cible de numéro atomique élevé).

Dans les deux cas, une modélisation correcte du transport électronique est cruciale pour rendre les simulations hydro-radiatives prédictives. Cependant, il a été montré très tôt que les hypothèses d'un mécanisme de transport linéaire ne sont pas adaptées dans le cadre de l'irradiation d'une cible solide par un laser de puissance ($I \sim 10^{14}$ W/cm²). Cela est dû à des gradients de température très importants (effets cinétiques dits « non-locaux ») ainsi qu'à la présence d'un champ magnétique auto-généré par effet thermo-électrique. Enfin, le flux de chaleur et le champ magnétique sont fortement

couplés au travers de deux mécanismes : le transport du champ magnétique par le flux de chaleur (effet Nernst) et la rotation et inhibition du flux de chaleur par la magnétisation du plasma (effet Righi-Leduc).

Dans ce manuscrit, nous commençons par exposer différents modèles de transport électronique, et en particulier le modèle non-local en présence de champ magnétiques implémenté dans le code hydro-radiatif FCI2. Par la suite, nous cherchons à valider ce modèle par des comparaisons avec un code cinétique, puis avec une série d'expériences lors desquelles le champ magnétique a été mesuré par radiographie proton. Nous détaillons ensuite des simulations FCI2 afin d'expliquer les phénomènes de création et de transport du champ, ainsi que son effet sur l'interaction.

Enfin, nous étudions la reconnexion du champ magnétique, lors de l'irradiation d'une cible par deux faisceaux laser.

Title : Magnetic field in laser plasmas: non-local electron transport and reconnection

Keywords : Inertial confinement fusion, ICF, High energy density plasmas, HEDP, laser, magnetic fields, electron transport, heat flux, reconnection.

Abstract : In the framework of the inertial confinement fusion, a pellet filled with a deuterium-tritium fuel is imploded, either through laser irradiation (direct drive, laser – low atomic number target interaction) or by black body radiations from a cavity converting the laser radiation (indirect drive, laser – high atomic number target interaction).

In both cases, a correct modeling of the electron transport is of first importance in order to have predictive hydro-radiative simulations. Nonetheless, it has been shown early on that the hypothesis of the linear transport are not valid in the framework of a solid target irradiated by a high power laser ($I \sim 10^{14}$ W/cm²). This is due to very steep temperature gradients (kinetic effects, so-called « non-local ») and because of a magnetic field self-generated through the thermo-electric effect. Finally, the heat flux and the magnetic field are

strongly coupled through two mechanisms: the advection of the field with the heat flux (Nernst effect) and the rotation and inhibition of the heat flux by the plasma's magnetization (Righi-Leduc effect).

In this manuscript, we first present various electron transport models, particularly the non-local with magnetic field model included in the hydro-radiative code FCI2. Following, in order to validate this model, we compare it first against a kinetic code, and then with experiments during which the magnetic field has been probed through proton radiography. Once the model validated, we use FCI2 simulations to explain the source and transport of the field, as well as its effect on the interaction.

Finally, the reconnection of the magnetic field, during the irradiation of a solid target by two laser beams, is studied.

